PROCEEDINGS OF THE

SYNTHETIC

APERTURE

RADAR

TECHNOLOGY CONFERENCE

March 8-9-10, 1978

Las Cruces, NM

Sponsored by

NASA

CONDENSED PROGRAM

TUESDAY, MARCH 7, 1978

1730 - 2100	Registration at Holiday Inn, Best Western, and Mission Inn

WEDNESDAY, MARCH 8, 1978

0700 - 0730	Registration at Motels
0730 - 0815	Buses from motels to PSL
0730 - 0815	Registration at PSL
0830 - 0930	OPENING SESSION
1000 - 1200	SAR CALIBRATION TECHNIQUES
1200 - 1320	Lunch -- buses to Corbett Center
1330 - 1700	IMAGE SIMULATION AND INTERPRETABILITY
1700 - 1715	Buses to motels
1815 - 1830	Buses from motels to reception at Holiday Inn
1830 - 2100	Reception
2000	Early bus to motels
2100	Late bus to motels

THURSDAY, MARCH 9, 1978

0715 - 0745	Buses to PSL
0730 - 0800	Late Registration at PSL
0800 - 1200	ANTENNAS
1200 - 1330	Lunch -- Buses to/from Corbett Center
1330 - 1720	DATA PROCESSING
1730	Buses to motels

FRIDAY, MARCH 10, 1978

0715 - 0745	Buses to PSL
0800 - 1120	SYSTEM DESIGN
1130 - 1230	SUMMARY SESSION
1400	Early bus to El Paso Airport
1340 - 1600	Tour of PSL facilities & bus to El Paso Airport

PROCEEDINGS OF THE

1978
SYNTHETIC APERTURE RADAR
TECHNOLOGY CONFERENCE

March 8-10, 1978
New Mexico State University
Las Cruces, New Mexico

Sponsored by

NASA

Johnson Space Center

Physical Science
Laboratory

FOREWORD

The purpose of the 1978 Synthetic Aperture Radar Technology Conference
is to identify key problems in the development of calibration techniques,
antenna designs, image simulation and interpretability methods, data pro-
cessing algorithms, and system designs. This proceedings is the first of its
kind in the SAR field; it complements and updates the excellent compilation of
SAR resource papers on Synthetic Aperture Radar as compiled by John J. Kovaly
and published in 1976 by Artech House, Inc. Many of the papers in this volume
discuss the SEASAT and SIR-A design approaches, thus emphasizing the move-
ment of SAR platforms from aircraft to spacecraft and the concomitant problems
of increased antenna size, etc. Although the conference is unclassified, and
has therefore resulted in the exclusion of a few classified papers, the
papers included in this proceedings identify and articulate the current state
of SAR technology.

I wish to express my appreciation for the dedicated efforts of both the
authors and the SAR Technology Conference Technical and Proceedings Committees
in producing this proceedings.

Keith R. Carver
Technical Committee Chairman
February 9, 1978

TABLE OF CONTENTS

WEDNESDAY, MARCH 8, 1978

TABLE OF CONTENTS

---

*Not included in this volume.

TABLE OF CONTENTS

THURSDAY, MARCH 9, 1978

TABLE OF CONTENTS

FRIDAY, MARCH 10, 1978

---

*Not included in this volume   **Withdrawn

TABLE OF CONTENTS

VII. SUMMARY SESSION (11:30 - 12:30), Chairman: K. R. Carver, New Mexico
      State University, Physical Science Laboratory.

Panel Members: R. H. Duncan
                R. K. Moore
                R. G. Fenner
                F. T. Barath
                D. Held

I. OPENING SESSION, (8:30 - 9:30), Chairman: K. R. Carver,
                    New Mexico State University, Physical Science
                    Laboratory

    1. Welcome to New Mexico State University - Gerald W. Thomas,
        President, NMSU.

    2. "A Perspective of SAR for Remote Sensing," Merrill I. Skolnik,
        Superintendent, Radar Division, Naval Research Laboratory.

    3. "Applications of Space- orne SAR Data," Fawwaz T. Ulaby, Director,
        Remote Sensing Laboratory, University of Kansas.

WEDNESDAY, MARCH 8, 1978

II. SAR CALIBRATION TECHNIQUES (10:00 - 12:00), Chairman: Richard H. Duncan,
                                Chief Scientist, White Sands Missile Range,
                                New Mexico.

SAR ANTENNA CALIBRATION TECHNIQUES

KEITH R. CARVER
PHYSICAL SCIENCE LABORATORY
NEW MEXICO STATE UNIVERSITY
LAS CRUCES, NEW MEXICO

ALLEN C. NEWELL
ANTENNA SYSTEMS METROLOGY SECTION
NATIONAL BUREAU OF STANDARDS
BOULDER, COLORADO

SUMMARY

Calibration of SAR antennas requires a measurement of gain, elevation and azimuth pattern shape, boresight error, cross-polarization levels, and phase vs. angle and frequency. For spaceborne SAR antennas of SEASAT size operating at C-band or higher, some of these measurements can become extremely difficult using conventional far-field antenna test ranges. Near-field scanning techniques offer an alternative approach and for C-band or X-band SARs, give much improved accuracy and precision as compared to that obtainable with a far-field approach.

1.0 INTRODUCTION

1.1 RATIONALE FOR ANTENNA CALIBRATION

Focused SAR antennas have a two-way synthetic power gain pattern given by

$$G(\theta) = \frac{\left| \sum_{n=1}^{N} A_n e^{j(\beta n \sin \theta + \phi_n)} \right|^2}{\left| \sum_{n=1}^{N} A_n \right|^2} G_r^2(\theta) \qquad (1)$$

where N is the number of elements in the synthetic array, A_n is the processor-controlled amplitude weighting factor, $\beta = 4\pi VT/\lambda$, V = velocity, VT = distance between elements, θ is the angle from beam center, and ϕ_n is the residual uncompensated phase error from the nth element. $G_r^2(\theta)$ is the two-way pattern of the real aperture. This relationship assumes that the return amplitude of a reflector is essentially constant during the integration time NT. Equation (1) is normalized so that the synthetic aperture gain is equal to the real aperture gain if there are no uncompensated phase errors ϕ_n.

Calibration of the real-aperture antenna pattern is necessary to predict image quality and also to determine the minimum detectable σ^0. Such a calibration requires the measurement of antenna gain, sidelobe levels,

cross-polarization levels, boresight errors, and far-field phase behavior. For example, the signal-to-noise ratio is proportional to the gain and thus the minimum detectable σ^o is directly related to the gain. As another example, random phase errors in the far-field pattern are equivalent to the uncompensated phase errors ϕ_n in (1) above; large values of ϕ_n cause synthetic beam broadening and gain reduction, along with beam tilt and increased sidelobe levels. Table 1 is a partial list of measured antenna pattern characteristics and their principal effect on SAR system performance. Specific cause-effect relationships are to be found in the literature on SAR technology.

TABLE 1

SAR ANTENNA CALIBRATION FACTORS

Pattern Characteristics	Effect on SAR System Performance
1. Peak gain	1. SNR; minimum detectable σ^o
2. Pattern shape (amplitude)	2. Ambiguities
a. range sidelobe level	a. range ambiguity level
b. azimuth sidelobe level	b. azimuth ambiguity level
3. Cross-polarization level	3. Ability to cleanly differentiate between σ^o_{hh} and σ^o_{hv}
4. Boresight error	4. Position of antenna beam relative to zero Doppler plane; rate of change of that position
5. Far-field phase pattern deviation from spherical	5. Beam broadening and tilt; gain reduction; increased sidelobes and ambiguity levels

This relationship of antenna pattern characteristics to SAR system performance requires attention to accuracy in measured antenna gain, sidelobe level, cross-polarization level, and boresight error and emphasis on precision in the measurement of phase.

1.2 CALIBRATION TECHNIQUES FOR SPACEBORNE SAR ANTENNAS

Large spaceborne SAR antennas pose special calibration problems not encountered with other antenna systems, primarily as a result of increased measurement accuracy and precision required for these electrically large radiators. For example, as the SAR frequency is increased to C-band, X-band or higher, the range length required can increase to considerably more than a mile so that very few far-field test facilities qualify for an adequate measurement. Moreover, spaceborne SAR antenna support structures are designed for deployment in a 0 G environment so that earth-bound ranges produce handling problems including static stresses, wind, etc.

An alternative test approach makes use of near-field planar scanning techniques and circumvents nearly all of the problems encountered with far-field ranges. The measurement accuracy for nearly every electrical performance parameter is improved with near-field test techniques and antenna handling becomes greatly simplified. The principal disadvantage is psychological, since the method is relatively new and requires numerical inversion of the raw data to produce far-field patterns.

2.0 FAR-FIELD TEST TECHNIQUES

2.1 CANDIDATE FAR-FIELD TEST RANGES

Typical far-field antenna test ranges use two towers separated by distances ranging from 10 m to 2000 m; a transmitting antenna, usually a paraboloidal dish, is mounted on one tower and is used to provide an incident quasi-plane wave illuminating the test antenna which is operated in the receive mode on the other tower. The test antenna is normally exposed to the wind and weather, although it is possible to cover the test zone with a large thin inflated rubberized airdome which then protects the test antenna from environmental effects. Antenna test engineers often use the rule-of-thumb relation $R = 2 D^2/\lambda$, although this is quite arbitrary; this rule, which corresponds to a 22.5^o quadratic phase taper over the test aperture, is inadequate for pattern measurements in connection with spaceborne SAR antennas.

Both the SEASAT and SIR-A antennas are planar arrays approximately 10 m x 3 m in size; Table 2 compares various range separation criteria for a 10 m

TABLE 2

FAR-FIELD RANGE DISTANCES FOR 10 m APERTURE

RANGE DISTANCE

FREQUENCY	$2D^2/\lambda$ (22.5°)	$4D^2/\lambda$ (11.25°)	$8D^2/\lambda$ (5.63°)
L-band (1.275 GHz)	850.00 m (2788')	1700.01 m (5576')	3400.02 m (2.11 mi)
C-band (5.000 GHz)	3333.33 m (2.07 mi)	6666.71 m (4.14 mi)	13,333.41 m (8.28 mi)
X-band (9.700 GHz)	6466.67 m (4.02 mi)	12,933.41 m (8.03 mi)	25,866.82 m (16.07 mi)

aperture length at L-band, C-band, and X-band. It is useful to compare these distances with some existing well-known far-field antenna test ranges; the characteristics of these ranges are summarized in Table 3 and Fig. 1.

TABLE 3

SOME EXISTING LONG FAR-FIELD TEST RANGES

Name	Location	Range Length	Comment
1. PSL, New Mexico State University	Las Cruces, N. M.	732 m	too short for SEASAT, SIR-A
2. JPL, West Mesa Range	Pasadena, Calif.	1007 m	marginal length for phase test
3. Hughes Aircraft Co. Carbon Canyon Range	Fullerton, Calif.	1156 m	marginal length for phase test
4. Lockheed Santa Cruz	Santa Cruz, Calif.	1829 m	used for SEASAT-A antenna test (airdome protection)
5. Rome Air Development Center Range	Newport, N. Y.	2287 m	weather can be a problem

The 1829 m Lockheed Santa Cruz range has been used for far-field amplitude pattern tests of the SEASAT L-band SAR antenna, and offers protection from wind and weather by means of a large inflatable airdome which covers the
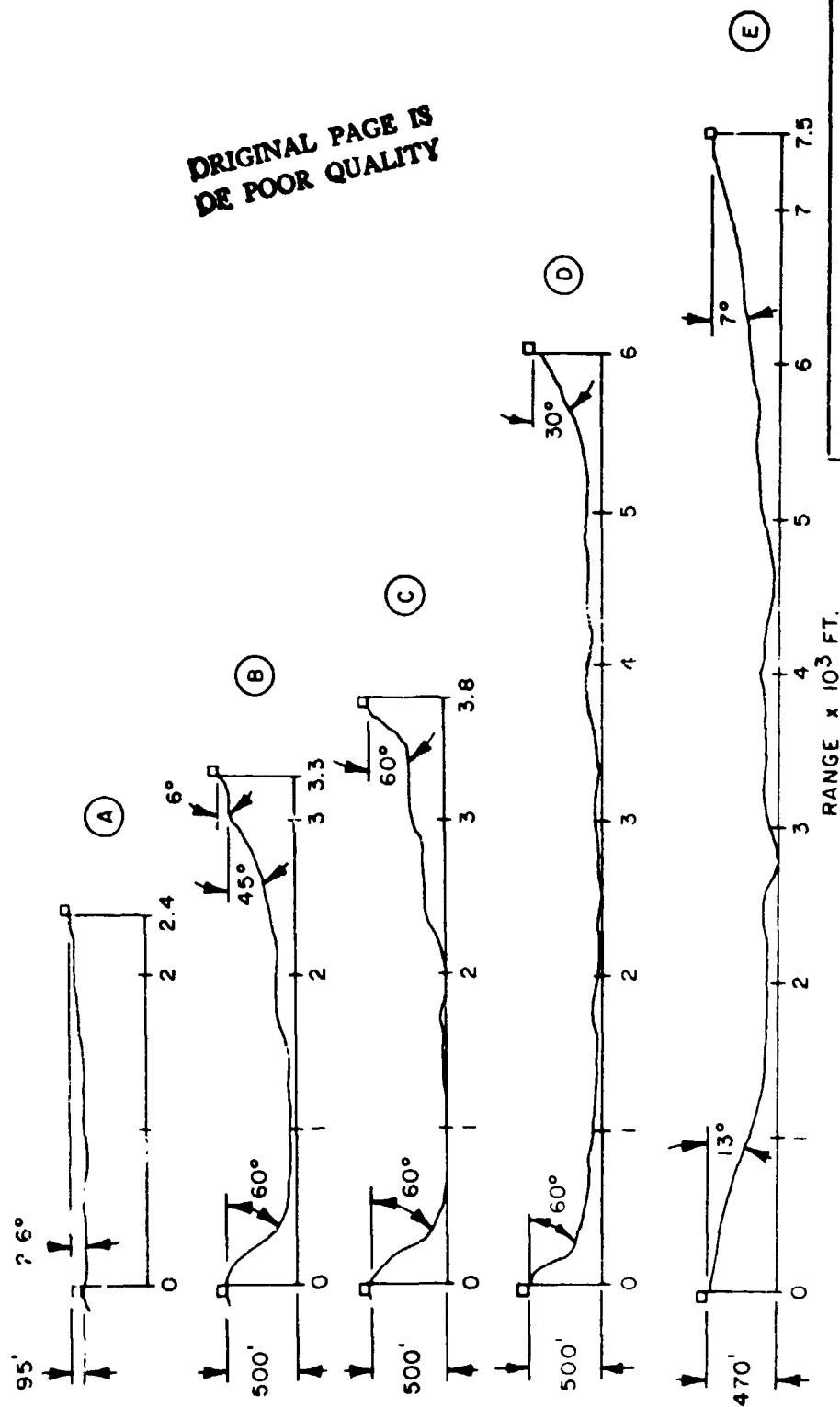
Figure 1. Vertical profiles of long baselength far-field antenna ranges.

(A) — PSL/NMSU, TORTUGAS MT. AUX RANGE, LAS CRUCES, N.M.
(B) — JPL/CIT, WEST MESA LONG RANGE, PASADENA, CA.
(C) — HUGHES A/C CO., CARBON CANYON RANGE, FULLERTON, CA.
(D) — LOCKHEED SANTA CRUZ RANGE, SANTA CRUZ, CA.
(E) — ROME ADC/USAF RANGE, NEWPORT, N.Y.

RANGE × 10³ FT.

II-3-5

positioner, test antenna, etc. This range is slightly longer than $4D^2/\lambda$ at L-band.

2.2 REQUIRED MEASUREMENT ACCURACY FOR SIR-A ANTENNA

As an example of typical spaceborne SAR antenna performance parameters and specified measurement uncertainties, consider the 10 m x 3 m SIR-A antenna with specifications as listed in Table 4 (1).

TABLE 4

SIR-A ANTENNA PERFORMANCE SPECIFICATIONS
AND MEASUREMENT UNCERTAINTY
FREQUENCY = 1.27 GHz

Parameter	Nominal Value	Measurement Uncertainty
Gain	33 dBi	$\pm$ 0.7 dB
Elevation Sidelobe Level	-14.5 dB	$\pm$ 0.4 dB
Azimuth Sidelobe Level	-14.5 dB	$\pm$ 0.4 dB
Cross-Polarization Level	-25 dB	unspecified
Azimuth Far-field Phase	***	3.5° rms over -8 dB beamwidth
Maximum Total Boresight Error	$\pm$ 2.0°	0.1°
Voltage Amplitude vs. Freq. (over 7 MHz bandwidth)	***	8% rms w.r.t. best linear fit
Voltage Phase Delay vs. Freq. (over 7 MHz bandwidth)	***	5° rms w.r.t. best quadratic fit
VSWR	1.5 max	unspecified
Payload Bay RFI	2 V m^{-1}	unspecified

2.3 PERFORMANCE CRITERIA FOR FAR-FIELD RANGES

From Table 4, the principal SAR antenna parameters to be measured are (1) gain, (2) pattern shape and sidelobe level, (3) cross-polarized level, (4) boresight, (5) phase vs. angle over azimuth pattern to - 8 dB, (6) phase

vs. frequency over the bandwidth, and (7) amplitude vs. frequency over the bandwidth.

2.3.1 GAIN MEASUREMENT ERROR BUDGET: FAR-FIELD TECHNIQUES

In a far-field gain measurement made by comparison to a standard antenna, there are nine principal sources of error; these are briefly discussed here.

1. Accuracy of gain standard

Using extrapolation techniques developed by NBS (Boulder) it is possible to measure the gain of a reference standard horn to $\pm$ 0.10 dB. This is discussed further in Section 3.3.1.

2. Range reflections

Reflections from specular zones on the terrain between towers and from antenna support structures cause multipathing and therefore a variation of the field over the region occupied by the test SAR antenna. If the ratio of maximum to minimum field is R, then the reflectivity is given by

$$F = 20 \log \ (R - 1)/(R + 1) \tag{2}$$

A reflectivity of -39 dB corresponds to R = 1.023 or a 0.20 dB excursion in incident power density levels over the quiet zone. At L-band, and for a 10 m x 3 m quiet area, this $\pm$ 0.20 dB value can be considered to typify a good far-field range.

3. Cross-polarized return error

Cross-polarized incident waves resulting either from the source antenna or from depolarized multipath signals can cause errors in the measured gain. Assuming an intrinsic range cross-polarized level of - 35 dB and a test SAR antenna cross-polarized level of -30 dB (with respect to beam peak principal-polarization level), the equivalent cross-polarized component is -65 dB with respect to the beam peak. Using a relation similar to that in (1), we can show that this produces a gain error of $\pm$ 0.01 dB in the gain of the principal-polarization component.

4. Boresight inaccuracy

By examining the slope sensitivity of the azimuth pattern of the SIR-A antenna to angle, it can be shown that an error of 0.1^{o} in positioning angle will cause the pattern to roll off by 0.05 dB at L-band.

5. Detector nonlinearity

If a 17 dBi standard-gain horn is used for gain comparison, this is 16 dB

below the peak gain of the SIR-A antenna. If an attenuator-compensation technique is used, nonlinearity errors can be reduced to ± 0.05 dB.

6. Detector-antenna mismatch

Assuming that the VSWR into the antenna or into the detector does not exceed 1.1, it can be shown that the gain error due to mismatch is ± 0.049 dB. This can be reduced if the phase of the reflection coefficients is known.

7. Short-term instabilities : ± 0.01 dB, estimated

8. Inadequate receiver-transmitter separation

A finite length range produces a quadratic phase taper of the illuminating wave with respect to plane, and thus causes a reduction in apparent gain over that obtained with a truly plane wave. The reduction in gain can be estimated by

$$\Delta G = 10 \log e^{-(\delta/2)^2} \tag{3}$$

where δ is the maximum quadratic phase error, given by

$$\delta = (2\pi/\lambda)(D^2/8R) \tag{4}$$

For a range length of 1829 m (e.g., Lockheed Santa Cruz range) and a 10 m aperture dimension, this corresponds to a gain reduction of 0.036 dB at L-band and 2.115 dB at X-band.

9. Roll-off of source antenna pattern

By an appropriate choice of source antenna diameter, this source of error can be reduced to less than 0.001 dB; this dictates that a sufficiently small diameter dish be used and must be balanced with the additional requirement that the source antenna beamwidth be large enough to keep the range reflectivity to the order of -39 dB.

2.3.2 GAIN MEASUREMENT ERROR SUMMARY FOR FAR-FIELD TECHNIQUE

Table 5 summarizes the principal sources of gain error and the RSS net error.

2.3.3 CROSS-POLARIZATION LEVEL

Assuming a -35 dB residual range cross-polarization level, the error in measuring a nominal -30 dB SAR antenna cross-polarization component would be (+3.9 dB, -7.2 dB); if the nominal antenna cross-polarization level were -20 dB, the measurement error would then decrease to ± 0.27 dB.

2.3.4 SIDELOBE LEVEL

Assuming a range reflectivity of -39 dB, the error in measurement of a first sidelobe level at a -15 dB nominal value would be ± 1.10 dB.

TABLE 5
ESTIMATES OF ERROR IN ON-AXIS GAIN USING FAR-FIELD TECHNIQUES

Source of Error	Error in Gain at L-band
1. Accuracy of gain standard	+ 0.10 dB
2. Range reflections	+ 0.20 dB
3. Cross-polarized returns	+ 0.01 dB
4. Boresight inaccuracy	- 0.05 dB
5. Detector nonlinearity	+ 0.05 dB
6. Detector-antenna mismatch	+ 0.05 dB
7. Short-term instabilities	+ 0.01 dB
8. Finite range-length	- 0.04 dB
9. Roll-off of source pattern	0.00 dB
RSS uncertainty	+ 0.24 dB

2.3.5 PHASE VS. ANGLE

In a far-field range measurement of phase, the test ante a is positioned so
as to rotate about the apparent phase center. This point of rotation mini-
mizes the variation of phase vs. angle over the main beam. For an ideal
antenna with a fixed point phase center, the phase fronts are spherical so
that in principle there is no variation of phase with angle as the antenna
is rotated about the phase center. In practice, however, the apparent
phase center wanders as the look angle is changed.

Errors in the phase measurement result from (1) an inadequate range separa-
tion distance (vide Table 2) and (2) interference effects caused by range
reflections. Consider, for example, the Lockheed Santa Cruz range (Table 3)
of 1829 m length; for the 10 m dimension of SIR-A, this finite length would
introduce a quadratic phase taper over the test aperture with a maximum of
10.4^o at the aperture edges. Assuming a -40 dB range reflectivity (equiva-
lent spurious field is 0.01 times direct-wave field), the additional phase
error incurred is $\pm 0.57^o$ maximum on the beam peak. At the -8 dB level on
the main beam the effective reflectivity is -32 dB, and the range reflectivity
contribution to the phase error increases to $\pm 1.44^o$. Under these conditions,
the worst-case phase error over the -8 dB beamwidth is therefore $\pm 11.8^o$.

This is about three times the phase error tolerance specified in the
Functional Requirements Document for the SIR-A antenna (Table 4). If the
range length ʾ increased in order to reduce the quadratic phase taper error,
the ground scʋˑ ˑˑ will increase and thus will begin to dominate the phase
error budget. It appears thaʈ no available far-field range can measure the
phase pattern to within 3.5° rms error for the SIR-A antenna.

2.4 SUMMARY OF FAR-FIELD RANGE REQUIREMENTS FOR SIR-A

Table 6 summarizes the performance required of far-field ranges in order to
meet the error limits discussed previously. Although these are specifically
for SIR-A, they may be taken as representative of other spaceborne SAR
antenna range calibration requirements.

TABLE 6

FAR-FIELD TEST RANGE REQUIREMENTS FOR SIR-A

Characteristic	Performance Level
1. Frequency range	1264 - 1286 MHz
2. Minimum range length	1800 m
3. Range reflectivity	-39 dB over test volume
4. Gain accuracy	$\pm$0.7 dB (worst case)
5. Boresight accuracy	$\pm$0.1°
6. Mechanical stability	wind below 2 mph

3.0 PLANAR NEAR-FIELD TEST TECHNIQUES

3.1 ADVANTAGES OF NEAR-FIELD MEASUREMENTS FOR SIR-A

Because of the special problems posed in the calibration of an electrically
large SAR antenna, planar near-field (PNF) measurement techniques offer an
attractive alternative to conventional far-field measurements. The required
accuracies can be achieved in a measurement environment that is more com-
patible with the large lightweight antenna designed to operate in zero
gravity. It is not subject to the effects of wind, weather, or motion of the
antenna during measurement which can cause distortion in the antenna
surface and, therefore, degrade the reliability and accuracy of the results.

In PNF measurements the antenna under test (AUT) remains stationary while a probe moves over a plane area very close to the aperture. Measurements are made approximately every half wavelength in both x- and y-directions of the amplitude and phase of the signal received by the probe. The resulting matrix of data, $B_1(x,y)$ is recorded on magnetic tape or disc for future processing. Normally the probe is essentially polarization matched to the AUT during the above measurement, and in order to obtain complete polarization results, a second measurement is performed with an independent probe, usually the original probe rotated about its axis by 90°. The two data arrays $B_1(x,y)$ and $B_2(x,y)$ are computer processed to obtain the angular spectra, correct for the directive and polarization patterns of the probe, and calculate the usual far-field parameters for the AUT. It should be emphasized that in the measurements and data processing, the only approximations are that multiple reflections between the probe and AUT are small enough to neglect, and the measurement area is truncated to a finite size. Neither the AUT or probe need possess special pattern/polarization properties, or be reciprocal, and the numerical techniques involved do not introduce small angle or other approximations. In short, the technique is based on a very general and powerful theory, and is capable of producing high accuracy results. This capability has been demonstrated in a number of ways on a large variety of antennas.

3.2 SPECIAL TECHNIQUES REQUIRED FOR SIR-A

Because of the large dimensions of the SIR-A antenna, the usual PNF measurement techniques must be modified slightly in order to use existing facilities. In general, measurements must be made over an area somewhat larger than the dimensions of the AUT. The length of the scan in the x-direction L_x, the corresponding antenna dimension a_x, and the probe-to-AUT distance D, determine the maximum angle for which the computed results are reliable through the relationship

$$\theta_s = \arctan \frac{L_x - a_x}{2d} \tag{5}$$

A similar relation holds for the y-direction. Assuming d = 40 cm, a_x = 10 m, a_y = 3 m, and θ_s = 60° requires a scan length of approximately 11.4 m by 4.4 m. The largest planar scanner presently in operation is shown in Fig. 2 and has a measurement area of 3.85 m by 4.5 m. To accomodate the SIR-A
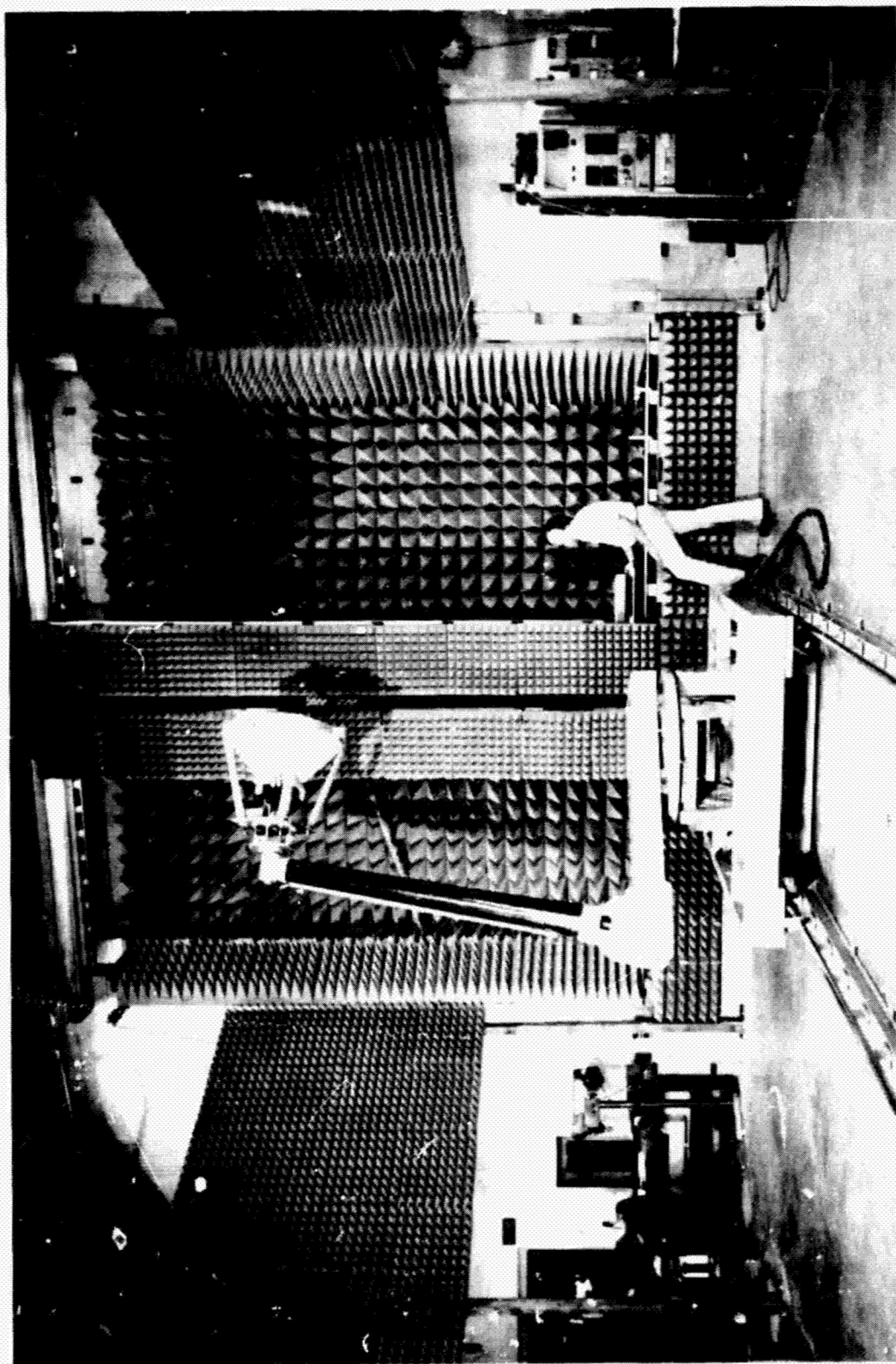
Figure 2. Planar near-field measurement facility at the National Bureau of Standards.

antennas, the measurement must be performed in three parts with the antenna translated in the x-direction in increments of 3.8 m between each scan as shown in Fig. 3. This requires careful angular and translational indexing to maintain the SIR-A in the same measurement plane after translation and re-establish the correct x- and y-positions. Similar realignments have been done in the past using an optical autocollimator for angular rotation sensing, and a laser interferometer for translation measurement, and the requirements here do not appear to be unreasonable.

3.3 ESTIMATES OF ERROR IN RESULTS FROM PNF MEASUREMENTS

Extensive work has been done to study the effect of errors in the measured near-field data upon the calculated results. This has included comparisons with other measurement techniques, computer simulation of var   types of errors, and mathematical analysis. The mathematical analysis i   most general application because it provides equations in terms of simple antenna parameters and estimes of error in the PNF system from which upper bound errors may be determined. For instance, the error in dB in on-axis gain due to maximum probe position errors of Δ_x, Δ_y, and Δ_z respectively in the x-, y-, and z-directions is given by

$$\Delta G = \frac{8.7}{n} \left[\frac{\Delta_x}{L_x} + \frac{\Delta_y}{L_y} \right] + \frac{43}{\sqrt{n}} \left[\frac{\Delta_z}{\lambda} \right]^2 \tag{6}$$

In the above, n is the antenna aperture efficiency, λ the wavelength, L_x and L_y the antenna dimensions. Similar expressions have been derived for errors in sidelobe level, monopulse difference null, bearwidth, boresight direction, main beam phase, and cross-polarization level in terms of the above position errors as well as errors arising from receiver nonlinearity, multiple reflections, measurement area truncation, probe pattern uncertainty, and amplitude normalization.

In the following estimates, we have used the uncertainties associated with the National Bureau of Standards near-field measurement facility. The maximum probe position errors in all three directions are $\pm$ 0.013 cm, the receiver amplitude error is ± 0.005 dB/dB, and the receiver phase error is $\pm$ 5 degrees. Multiple reflections produce a ripple in the measured data of
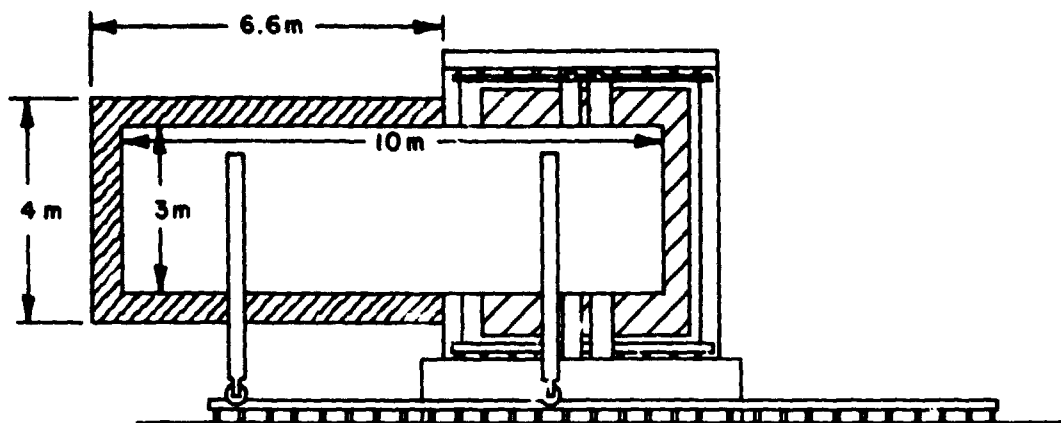
SIR ANTENNA ON NEAR-FIELD SCANNER, POSITION 1
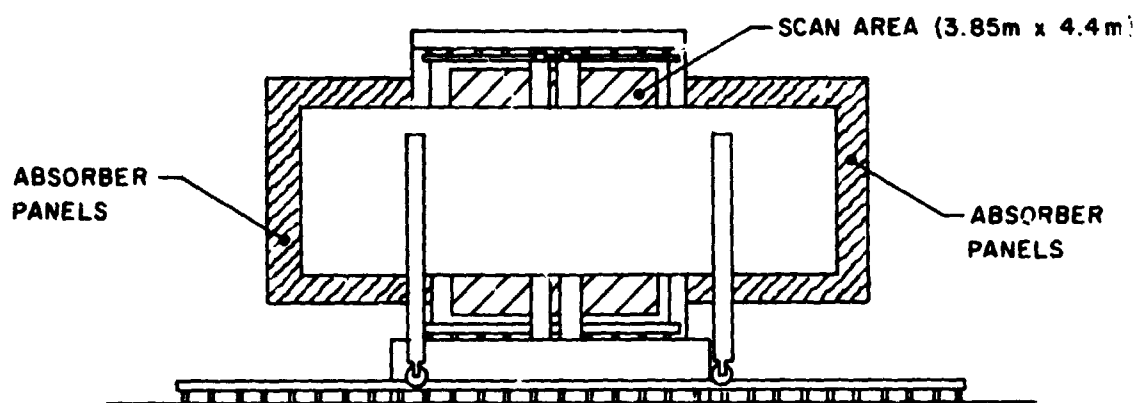
SIR ANTENNA ON NEAR-FIELD SCANNER, POSITION 2
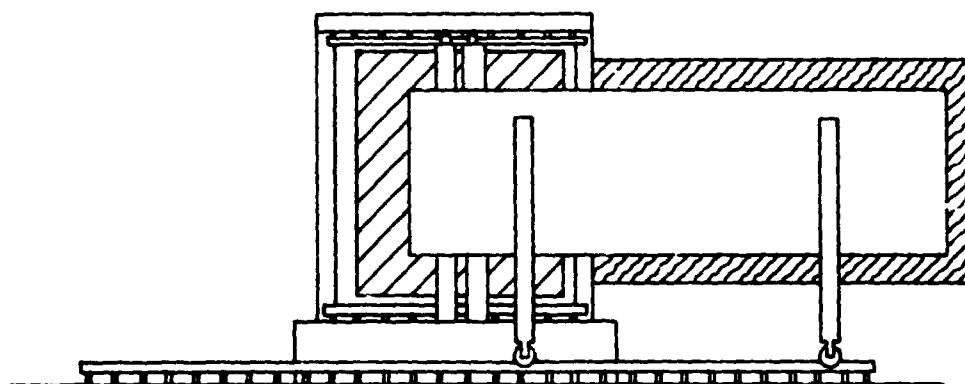
SIR ANTENNA ON NEAR-FIELD SCANNER, POSITION 3

Figure 3.   Schematic of SIR antenna in three positions for PNF measurement.

II-3 14

+0.1 dB, the probe gain is accurate to within ± 0.10 dB, and the amplitude normalization uncertainty is ± 0.05 dB. It is further assumed for estimating the effect of area truncation that the measured amplitude at the extremes of the scan area is at least 30 dB below the peak near-field amplitude.

3.3.1 GAIN MEASUREMENT ERROR BUDGET: NEAR-FIELD TECHNIQUES

Table 7 below summarizes the errors in on-axis gain for both the L-band and X-band of a 10 m x 3 m SAR planar array.

TABLE 7

ESTIMATES OF ERROR IN ON-AXIS GAIN USING PLANAR NEAR-FIELD TECHNIQUES

Source of Error	Error in Gain in dB	
	L-Band	X-Band
1. Amplitudes nonlinearity	± 0.12	± 0.12
2. Probe gain uncertainty	± 0.10	± 0.10
3. Multiple reflections	± 0.05	± 0.05
4. Normalization amplitude	± 0.05	± 0.05
5. Area truncation	± 0.02	± 0.003
6. Receiver phase	± 0.01	± 0.02
7. z-position	< 0.001	< 0.001
8. x-position	< 0.001	< 0.001
9. y-position	< 0.001	< 0.001
RSS uncertainty	± 0.17 dB	± 0.17 dB

3.3.2 CROSS POLARIZATION UNCERTAINTIES

All of the above sources of error contribute to the error in cross polarization with the exception of the probe gain. The absolute gain of the probe does not enter into the polarization calculation, but the probe polarization does in much the same way that the polarization of the source antenna enters into far-field measurements. Usually the polarization of the probe is measured along with its gain in a generalized 3-antenna measurement to an uncertainty of approximately ± 0.05 d   er dB of axial ratio. The net effect of all sources of error is that the cross polarizat ~ of the AUT is uncertain

to $\pm$ 1.1, $\pm$ 3.3, and $\pm$ 10.2 dB for cross component levels of -20, -30 and
-40 dB below the main component. These values are for both on-axis and
sidelobe regions.

3.3.3 SIDELOBE LEVEL UNCERTAINTIES

In this case, it is the probe gain and normalization amplitude uncertainties
which do not effect sidelobe levels, but a knowledge of the relative probe
pattern is important as it enters into the probe correction of the measured
data. When all sources of error are considered, the uncertainties in side-
lobe pattern levels are, respectively, $\pm$ 0.6, $\pm$ 1.2, and $\pm$ 2.7 dB for -20,
-30, and -40 dB sidelobes.

3.3.4 PHASE VERSUS ANGLE

In the mathematical error analysis, the relative change in the amplitude of
the far-field $\Delta E/E$ has been computed for various sources of error in the
measured near-field data. If ΔE is in phase with E, the amplitude change will
be a maximum, while if ΔE is 90^0 out of phase with E, the effect will be to
alter the phase of the computed far-field. Errors in far-field phase may,
therefore, be obtained from the amplitude error equations by

$$\Delta\phi = \arctan\frac{\Delta E}{E} = \frac{180}{\pi}\frac{\Delta E}{E} \tag{7}$$

Using this modification in the error equations, one finds that the most
serious errors are due to receiver amplitude and phase nonlinearity and to a
lesser extent, multiple reflections and z-position errors. The net effect is
to produce an error in the phase at the -6 dB level on the main beam of about
4 degrees.

3.3.5 PHASE AND AMPLITUDE VERSUS FREQUENCY

This requirement implies a swept-frequency measurement of the antenna response
in the on-axis or maximum gain direction and is one measurement where near-
field techniques are more difficult than far-field measurements. Near-field
measurements are by nature fixed frequency measurements, and swept-frequency
results must be obtained from a series of near-field measurements made at
closely spaced frequencies. These measurements can be accomplished during
one physical scan if the source and receiver are stepped through the

frequencies as the probe moves between data points.

4.0 COMPARISON OF FAR-FIELD AND NEAR-FIELD MEASUREMENT UNCERTAINTIES

Table 8 compares the uncertainties obtained through far-field and near-field approaches to a measurement of an L-band SAR antenna which is 10 m x 3 m in area. A far-field range reflectivity of -39 dB over the quiet zone is assumed.

TABLE 8

COMPARISON OF FAR-FIELD AND NEAR-FIELD MEASUREMENT UNCERTAINTIES

Parameter	Uncertainty	
	Far-field	Near-field
1. Gain	± 0.24 dB	± 0.17 dB
2. Sidelobe Level (-15 dB)	± 1.10 dB	
(-20 dB)	± 1.96 dB	± 0.60 dB
(-30 dB)	± 6.44 dB	± 1.20 dB
3. Cross-polarization level		
(-30 dB)	+ 3.9 dB - 7.2 dB	± 0.15 dB
4. Phase vs. angle over -6 dB beamwidth	± 11°	± 4°
5. Phase/amplitude vs. freq.	?	?

It is seen from this table that the near-field measurement is generally superior from an electrical parameter measurement uncertainty viewpoint. Also, it should be emphasized that the handling of large SAR antennas designed for zero gravity environments is greatly simplified with the near-field approach.

5.0 REFERENCE

1. Elachi, C., J. M. Vickers, R. Jordan, and J. Granger, "Space Shuttle Functional Requirements for SIR-A," Spec. FM51174, Rev. A, Jet Propulsion Laboratory, Pasadena, California, Nov. 23, 1977.

A SIGNIFICANT POST-LAUNCH CALIBRATION
EXPERIMENT FOR THE SEASAT-A SAR

ROBERT C. BEAL
APPLIED PHYSICS LABORATORY
THE JOHNS HOPKINS UNIVERSITY
LAUREL, MARYLAND 20810

SUMMARY

This paper outlines a technique for periodically monitoring the impulse response function of the Seasat-A Synthetic Aperture Radar (SAR). The technique will directly yield most of the significant contributors to the overall instrument transfer function, and in addition will yield several diagnostic side benefits. The essential measurement involves exciting the total SAR system at L-band with a strong point source scatterer of radar cross section -10^7 m^2, receiving via the normal S-band analog data link, and finally sampling and processing only a small subset of data in the immediate vicinity of the strong point source.

Depending upon the details of the data handling, a number of key system parameters can be extracted:

(1) Resolution of the entire system, or of the system devoid of optical processor contamination, as obtained by the effective width of the point source response.

(2) Optimum phase and amplitude compensation for minimizing either the width of the impulse response or the sidelobe energy.

(3) Real aperture antenna pattern, by collecting several successive passes of data, and employing range compression. Such information might be essential for post-launch analysis of the actual antenna deployment and for an evaluation of the sources of image contrast degradation resulting from excessive sidelobe energy.

(4) Long term radiometric calibration, relative and perhaps absolute, by using the stable S-band pilot tone in the data link as a reference throughout the life of the experiment.

(5) Absolute geometric calibration, by comparing the actual measured range and azimuth position of the strong scatterer with predicted location using Seasat Project-generated instrument predicts, again throughout the life of the mission. Such information might be essential for characterizing and removing positional biases.

(6) Data link contamination, by locating the strong scatterer in a region of overlapping station coverage, and comparing the quality of the impulse response at low station elevation angles.

1.0 THE CONCEPT OF AN IDEAL ACTIVE RADIOMETER

1.1 PERSPECTIVE

Even though practical microwave synthetic apertures have existed for about twenty years, our ability to extract quantitative, scientifically useful information has been substantially lagging. Perhaps part of this lag is understandable. Many of the early applications of SAR were of a reconniassance nature, and were successful merely because of the ability of the technique to pierce cloudcover and darkness. As more sophisticated applications are sought, however, such as the space-borne measurements of ocean wave spectra, ice thickness and structure, soil moisture, and vegetation classification, it becomes imperative that we expand our understanding of the total instrument transfer function, that is, the effect of the total instrument on the quantity to be measured. The Seasat-A SAR can provide the ideal opportunity from which to gain this understanding.

1.2 AN IDEAL SYSTEM DEFINITION

The Seasat-A SAR, from a radar measurement (as opposed to applications) point of view, has a purpose which is simply stated: it should produce an absolute radar backscatter map of certain areas of the earth's surface at an incidence angle of 20 degrees, wavelength of 23 cm, spatial resolution of 25 m, and radiometric resolution of 3 dB. If the instrument were "perfect", it would yield an image of a backscatter map uniquely related to the actual

surface distribution of the radar backscatter at a known instant in time. In this perfect system, not only is the mapping function unique, it is also known. As a result, the image is error-free in position, magnitude, and time for any value of backscatter. Such a system, of course, cannot exist.

1.3 BASIC IMAGE DESCRIPTORS

There are literally dozens of significant contamination sources in a real system which prevent perfection. These sources manifest themselves, however, in a relatively small number of ways in the output imagery. It is therefore possible to specify and describe the measurement system with a relatively small number of basic image descriptors. The following set is offered as being more or less complete and orthogonal.

Spatial resolution, or the spatial width of the half intensity points resulting from an ideal impulse excitation. This definition, although convenient, does not account for sidelobe structure which also affects the ability of the system to discriminate between closely spaced targets.

Radiometric resolution, or the "just-detectable difference" in input backscatter, σ_o, sometimes referred to as "noise equivalent $\Delta\sigma_o$". For any real system, radiometric resolution can always be traded against spatial resolution by varying either the detection or the processing bandwidth.

Dynamic range, or the range of absolute input backscatter values which produce output changes. Usually only a small fraction of the total dynamic range is linear, and SAR systems with instantaneous dynamic ranges in excess of 20 dB are rare.

Radiometric accuracy, or the probable error in mapping a point in the output image back into an absolute value of backscatter. Reference to an absolute standard is necessary.

Geometric accuracy, or the probable error in mapping a point in the output image back to an absolute position.

Temporal invariance, or the extent to which all of the above descriptors remain invariant with time.

It is possible to express other common descriptors such as "signal-to-noise ratio" and "contrast" as variations of these six basic descriptors. Signal-to-noise ratio (for a particular input, σ_o) for example, is a function of both the "noise-equivalent σ_o" at the lower end of the absolute dynamic range, and the noise equivalent $\Delta\sigma_o$. Similarly, "contrast" can be related to both spatial resolution and instantaneous dynamic range. To first order, then, modifications of the above six descriptors can be defended as containing the necessary and sufficient information for a complete image quality description.

2.0 SOME POSSIBLE CONTAMINATION SOURCES IN SEASAT-A

As mentioned above, there are several potential contamination sources in the Seasat-A SAR which will determine the final image quality. Some of these sources are predictable and measurable with sufficient pre-launch testing. Others can only be anticipated, and require a precisely controlled set of post-launch measurements for their determination. Some of the more significant potential sources of contamination are discussed here.

2.1 RANGE AND AZIMUTH RESOLUTION

In the Seasat-A SAR, range resolution is fundamentally limited by a combination of geometry and bandwidth in the front end of the sensor. From then on, the information must be preserved with adequate bandwidth while preventing the introduction of additional noise. A resolution calculation : r the Seasat-A SAR based only on front-end parameters yields about 20 m at the near-range point. If no significant degradation occurs in the remainder of the system, the 25 m specification will be satisfied. In the optical processor, however, significant sources of degradation can easily occur. Similarly, either short term oscillator instabilities or an improperly deployed antenna can cause azimuth correlation difficulties with resulting resolution and contrast degradation.

2.2 RADIOMETRIC RESOLUTION

The least-detectable difference in σ_o for a SAR is chiefly a by-product of its coherent radiation source. Rayleigh scattering produces multiplicative noise yielding a variance in output power proportional to its mean. This contamination source results in a variance of 6 dB for a single sample of dimension one resolution element. For the Seasat-A parameters, spatial

integration in azimuth by a factor of four can result in a factor of two increase in radiometric resolution, to 3 dB, if the four samples (or "looks") are statistically independent. Spatial integration beyond 25 m can further increase the radiometric resolution. Normally the Rayleigh-produced variance is a sufficiently large contamination source that it alone determines the radiometric resolution, except at low scattering values where other sources, such as thermal noise, begin to predominate. Consider, for example, a SAR system having a linear operating range of 20 dB, with only four independent samples per resolution element (very close to the Seasat-A SAR situation). Such a system could resolve with respectable confidence only about seven "grey scales", or values of input backscatter. This example illustrates the challenge of SAR remote sensing, when compared with more common visible remote sensors, typically having a radiometric resolution of twenty to one hundred grey scales.

2.3 DYNAMIC RANGE

There are at least three separate and distinct values of dynamic range for most SAR systems. For extended sources, the lower end of the dynamic range is limited by thermal noise. For the Seasat-A SAR, this equivalent thermal noise corresponds to an area-normalized scattering coefficient, σ_o, of approximately -27 dB in the highest receiver gain setting. Conversely, the upper end of the extended source dynamic range is usually limited by saturation levels in electronic components. In Seasat, the data link saturation limits the extended source dynamic range to -20 dB. The instantaneous dynamic range of the system, however, is much less, and is determined by the amount of energy which spills over from its intended position into adjacent elements. The most common cause of this contamination is random phase and amplitude noise preventing optimum correlation. In Seasat, the instantaneous dynamic range will probably be about 10 dB, unless these random contamination sources are much stronger than expected.

Finally, there is a point source dynamic range. Radars which use pulse expansion (to reduce peak power) and doppler discrimination (to accomplish aperture synthesis) effectively spread the energy from the point source over many equivalent resolution elements until, in the act of processing, matched filtering compresses the energy close to its original spatial extent. The

Seasat-A SAR expands the range energy by a factor of 600, and the azimuth energy by a factor of 160 (when processing to 25 m resolution), for a total energy dispersion of 10^5. This energy dispersion quality of the SAR allows point sources of extremely large backscatter relative to the average to pass through the system unaffected. The dynamic range for point sources, therefore, is typically much larger than that for extended sources, 50 dB larger for the Seasat-A SAR.

2.4 RADIOMETRIC ACCURACY

As mentioned briefly at the beginning of this paper, imaging radar will not yield its full scientific potential until it can provide a calibrated map of radar backscatter. Moreover, within a single pass of the Seasat-A SAR, at least three separate contamination sources will act to impede absolute calibration:

(1) the ability to reference points in the image to an absolute standard,

(2) small scale local errors caused by, for example, strong sources contaminating adjacent regions containing weak sources.

(3) large scale systematic but unknown variations in the system transfer function, caused by, for example, antenna pattern uncertainties.

In addition to these three, the absolute measurement will be foiled by the Rayleigh scattering discussed in 2.2 and by temporal variations to be discussed in 2.6. Unfortunately, even if complete knowledge of each of the above contamination sources were available, an extremely sophisticated and non-linear algorithm would be required to map output amplitude back to input backscatter coefficient. In general, all but a fraction of the knowledge necessary to create this algorithm is lacking. In Seasat-A, for example, the SAR antenna pattern is sufficiently sharp that a spacecraft roll of one degree can result in a change of several dB in system gain at a particular range. In addition, the backscatter function itself (for a homogeneous partially specular target) is varying rapidly with angle, especially at angles near nadir. Consequently, even for attitude control systems accurate

to 0.3 degrees, the steeply varying antenna pattern combined with the initial uncertainty in the measurement of that pattern can result in errors of several dB.

In spite of these inherently difficult problems, however, a number of major error sources can be reduced or even eliminated by formulating a proper calibration philosophy.

2.5 GEOMETRIC ACCURACY

Every imaging system forms its image with a unique perspective. If the mapping from object to image is one-to-one, with a known mapping function, then no information is lost, and it might be said that the geometry is absolutely accurate. The synthetic aperture radar also has its own perspective, making measurements of time delay and doppler frequency, from which geocentric latitude and longitude must be inferred. Any discussion of geometric accuracy, therefore, must be centered about the ability to make this inference.

Assume a spacecraft in a perfectly circular orbit around a perfectly homogeneous stationary spherical Earth. The spacecraft velocity and altitude are therefore constant. Finally, assume that the orbital parameters of the spacecraft are known, so that its position in terms of geocentric coordinates is a known function of time. In this ideal situation, the mapping between SAR parameters and geocentric coordinates is trivial. For vacuum, the radar time delay is uniquely related to range from the spacecraft. Therefore, a particular time delay defines a sphere of unique radius centered on the spacecraft. Similarly, a particular doppler frequency shift defines a unique angle with respect to the spacecraft velocity vector, the locus of which is a cone. The full universe of range and doppler frequencies measured by the radar, therefore, can be visualized as concentric families of spheres and cones centered on the spacecraft. The intersections of these spheres and cones with the spherical earth result in a corresponding family of circles and hyperbolae, and allow a unique mapping from "range-doppler" space to geocentric coordinates. In particular, if processing is performed about "zero-doppler", i.e., the position of a point is defined by the time at which it has no radial velocity component, then the only concern need be

with the intersection of circles with a plane normal to the velocity vector (the degenerate form of the hyperbola).

In reality, the spacecraft is in a non-circular orbit, and the earth is neither stationary nor spherical. A non-circular orbit implies a rate of change of altitude and a zero-doppler plane which no longer passes through the sub-satellite point. In Seasat-A, for example, a 1-m/s altitude rate produces nearly a 100-m shift in the zero-doppler plane at the surface of the earth. It is, therefore, necessary to know and correct for altitude rates of 0.25 m/s to limit geometric errors caused by this source to 25 m.

The rotating earth produces an angular offset to the zero-doppler plane of about four degrees at the equator, sinusoidally decreasing to zero as a function of latitude. For Seasat-A geometry, at twenty degrees from nadir, this rotation amounts to a lateral shift of about 150 m.

The non-spherical earth distorts the family of range and doppler curves according to the local figure and terrain (or tidal) properties. Much of this error can be eliminated by using the proper earth model. Local terrain variations, however, are generally unknown a priori, and will introduce significant displacements. A mountain whose peak is 1 km higher than the surface of the corresponding earth model will, in the Seasat-A geometry, be apparently displaced by 3 km.

In addition to these distortions caused by the geometry, additional errors result in the deduction of range from time delay unless electronic-system delays are calibrated frequently. In Seasat-A, this problem is compounded by the fact that the system time delay is a strong function of temperature, which in itself is varying at nearly a constant rate throughout a typical pass.

In summary, a number of significant error sources will drive the system geometric-location accuracy on Seasat-A to at least 100 m, and, more likely, several hundred meters. The final performance will depend largely on to what extent post-launch calibration can remove systematic contamination sources.

2.6 TEMPORAL INVARIANCE

For a meaningful calibration, each of the above image quality descriptors must be either invariant with time or a known function of time. In general, the spacecraft environment is relatively benign, and one might expect few problems in this regard. There are, however, two areas in which the SAR may be particularly succeptible. Short term temperature variations (within a pass) can affect radiometric accuracy (via electronic gain changes) and geometric accuracy (via electronic time delay changes). Attitude and altitude drifts and uncertainties can similarly result in radiometric and geometric errors. A good fraction of this contamination can be eliminated with proper ground testing, but post-launch calibration will be essential to determine the time variance of the total transfer function as well as the actual in-orbit antenna pattern.

3.0 A COMPREHENSIVE POST-LAUNCH CALIBRATION TECHNIQUE

3.1 RATIONALE AND CONCEPTUAL DESCRIPTION

In view of all the potential sources of contamination in the Seasat-A SAR, periodic post-launch calibration of the system transfer function is clearly imperative Fortunately, because the system is linear to first order, its impulse response function is a very powerful and nearly complete descriptor.

This section outlines a technique for periodically monitoring the impulse response function of the Seasat-A SAR. The technique will directly yield quantitative measures of each of the six basic image quality descriptors discussed in Section 2.0. In addition, simple modifications of either the experiment strategy or the data analysis will allow the monitoring of

    (1)   possible resolution degradation resulting from the use of an optical processor,

    (2)   the optimum phase and amplitude compensation functions for range correlation

    (3)   the real aperture antenna pattern, and

    (4)   contamination effects of the data link versus elevation angle.

Figure 1 is a schematic representation of all of the major components of the Seasat-A SAR system in the proposed calibration mode. The information flow as well as the majority of the actual hardware is identical to that planned for a typical SAR receiving station. (See reference [1] for detailed system characteristics.) Note the following significant deviations, however:

(1) the receiving antenna is serving an additional function of a cali- brated, constant amplitude, geometrically fixed point source reference,

(2) the demodulated video output is immediately range compressed and equalized, and only a small fraction of the inherent data is digi- tized and buffered at an easily manageable data rate for only about two seconds, and

(3) azimuth compression is accomplished via computer by using the actual phase and amplitude history of the point source, rather than relying on supplementary position and attitude information.

3.2 DESCRIPTION OF THE SYSTEM

Any large tracking antenna equipped with a wideband (1 GHz to 3 GHz) feed structure would be suitable for use simultaneously as both the strong point source and the data link receiving aperture. For example, $\_$ $\_$ $\_$ $\_$ ng the feed of a 20 meter diameter antenna selectively at 1.275 GHz (Seasat-A SAR operating frequency), a point source reflector can be created of cross-section [2]

$$\sigma = \frac{4\pi A^2}{\lambda^2} \eta^2 \tag{1}$$

where

σ = radar cross section, m^2

A = antenna aperture = $(\pi/4)(20)^2$ m^2

λ = radar operating wavelength = 0.23 m

η = antenna efficiency = 0.5

Substituting, $\sigma \approx 6 \times 10^6$ m^2 along the axis of the antenna.

Fig. 1 SEASAT-A SAR POST-LAUNCH CALIBRATION CONCEPT

This extremely bright target should still be slightly below saturation for the Seasat-A SAR. The expected minimum detectable cross-section is approximately 2 m^2 for the SAR in its highest receiver gain setting (i.e., when the noise is front-end limited). Assuming a range compression of 600, an azimuth compression of 160, and a linear dynamic range (for extended targets prior to compression) of 20 dB, the system should saturate for point sources of approximately 2×10^7 m^2.

A particularly intriguing idea for precisely adjusting the amplitude of the point source involves the simple substitution of a calibrated attenuator for the short at 1.275 GHz. The total dynamic range possible (i.e., ratio of "on" to "off" scattering cross-section) is unclear, but depends largely upon the perfection of the feed assembly. It is possible, however, that switching the scatterer "off" for alternate looks (every 0.5 second) during the two second SAR integration time would provide an effective method of reducing background emanating from sources such as buildings and trees, by differencing sequential single-look images.

By shorting or attenuating the tracking antenna feed selectively only at 1.275 GHz, the antenna can simultaneously be used as a receiver for the S-band analog data. Thus, all the normal data link hardware is utilized through the demodulator. The output of the demodulator, however, is followed by modifications to existing hardware in order to contain the data rate and total data per pass to only a very small fraction of that obtained in the actual system. Since the total information of interest is almost surely confined to an area of ~1 km^2 about the point source, the information rate can be held to only about 1% of that inherent at the instrument output by performing range compression, and then sampling only in the immediate vicinity of the point source. The complete azimuth phase history of the 1 km^2 region will require only about 1.6 M bits of storage. If azimuth processing to only 25 m is desired, the total storage requirement is a factor of four less.

The only remaining step required to produce the two-dimensional point spread function is a cross-correlation in azimuth. For the limited data set described above, an attractive alternative procedure which eliminates the

dependence on supplementary position and attitude information involves a simple autocorrelation of the strong point source phase history.

3.3 SOME FINAL CONSIDERATIONS

The power of the impulse response function to totally describe the SAR system is a direct result of our need to build quantitative remote sensing systems. In this sense, the degree to which the impulse response function is not a complete descriptor is a measure of the design shortcomings. The one-to-one mapping from image space back into radar backscatter space, so essential for scientific deduction, is possible only if the response function is reasonably unique, amplitude-independent, and time-invariant. A well designed calibration experiment should at a minimum, therefore,

(1) utilize a calibration source with well-known and dependable characteristics,

(2) verify the extent to which the impulse response function is both unique and amplitude-independent, and

(3) provide frequent opportunities for calibration to confirm the time invariance of the impulse response function.

For Seasat-A, the optimum geographic location of the calibrated source is tied to several factors, perhaps the most significant of which are the particular characteristics of the orbit. As observed from a fixed location on the earth, the baseline orbit will appear to precess toward the east at a rate of about 18 km at the equator every three days [3]. For either ascending or descending passes, therefore, a particular fixed target will present opportunities for calibration every three days until it passes out of the SAR swath of 100 km, yielding a total of five or six opportunities over a 15 day period. The cycle repeats approximately five months later. Moreover, by positioning the point source at particularly favorable latitudes, sets of ascending and descending passes can be phased to yield sets of 15 day opportunities spaced at 2.5 month intervals. Such favorable locations exist, for example, at latitudes of approximately 32°N, 39°N, and 46°N.

4.0 REFERENCES

1. Jordan, R. L. and D. H. Rodgers, "Seasat-A Synthetic Aperture Imaging Radar System", paper presented at 1976 Wescon, September 1976.

2. Inferred from Skolnik, M. I., Radar Handbook, 1970, McGraw Hill, p. 27-16, eq. (10).

3. Private communication with W. T. K. Johnson, Jet Propulsion Laboratory, Pasadena, California.

WEDNESDAY, MARCH 8, 1978

III.   IMAGE SIMULATION AND INTERPRETABILITY (1:30 - 5:20), Chairman: R.K.
                                    Moore, Remote Sensing Laboratory, University
                                    of Kansas

FEATURE DISCRIMINATION/IDENTIFICATION BASED UPON SAR RETURN VARIATIONS

WILLIAM A. RASCO, SR. AND ROY PIETSCH
AEROSPACE TECHNOLOGY DIVISION
APPLIED RESEARCH LABORATORIES
THE UNIVERSITY OF TEXAS AT AUSTIN
P. O. BOX 8029, AUSTIN, TEXAS 78712

SUMMARY

A study of the statistics of the look-to-look variations in the returns re-corded in-flight by a digital, realtime SAR system is being conducted for the Avionics Laboratory, Radar Branch, WPAFB, under USAF Contract F33615-77-C 1169. The study objectives include the determination of whether these variations demonstrate class-unique information content adequate to allow the use of some measure of that variance in discriminating between or identifying any or all of various classes of objects and features mapped by the SAR system. This paper briefly discusses the data, their source, the techniques employed in sampling, and some measures under study and presents a demonstration of the positive results thus far obtained toward meeting the objective defined above. The determination that the variations in the look-to-look returns. from different classes do carry information content unique to the classes is illustrated by means of a model based on four variants derived from the four look in-flight SAR data under study. The model was limited to four classes of returns: mowed grass on a athletic field, rough unmowed grass and weeds on a large vacant field, young fruit trees in a large orchard, and metal mobile homes and storage buildings in a large mobile home park in Reedley, California. A data population in excess of 1000 returns, distributed between the four classes, was selected. These returns represent over 250 individual pixels from the four classes. The multivariant discriminant model operated on the set of returns for each pixel and assigned that pixel to one of the four classes, based on the target variants and the probability distribution function of the four variants for each class. The model, the variants used, and the test results are presented.

1.0 OBJECTIVES AND GENERAL APPROACH

1.1 OBJECTIVES

The overall objective of the study is to analyze the look-to-look variations of the multilook SAR returns from selected objects and features to determine whether some measure of that variance can be used in discriminating between or identifying any or all of the features and objects analyzed.

1.2 GENERAL APPROACH

The general approach is to analyze the variations of the returns from each of a number of sets of actual multilook returns representing statistically significant samples of selected classes and subclasses of known objects and features.

These sample sets are comprised of the radar returns associated with single pixels identifiable with known objects and features. The single pixels are selected interior to gross features, scene segments, or objects (i.e., individual trees within an orchard or grove, individual structures within a group or within a cluster of structures or trees, etc.)

Initial designation of classes and subclasses to be sampled was based on a requirement to obtain a realistic spread of variations and power levels. Additional classes and subclasses have been added as the study has progressed. All selections are based on ground truth information to minimize the number of "wild points" which may occur.

2.0 DATA SOURCE AND THE SELECTION PROCESS

2.1 SOURCE OF DATA

The SAR returns used in the study are obtained from digital data recorded in flight on wideband magnetic tapes during the recently concluded, USAF-conducted, 72-flight experimental flight test series with the in-flight, real-time data processing FLAMR (Forward Looking Airborne Multimode Radar) system . This system operated in the 16 to 16.5 GHz band .

Approximately 450 wideband, 30.5 x 2.5 cm (14 x 1 in.), 14-track magnetic tapes were recorded during the flight test program. These tapes and associated data and equipment are now located in the SAR Data Bank at the Applied Research Laboratories, The University of Texas at Austin (ARL:UT). The Data Bank is maintained for purposes of supplying SAR data to qualified, Air Force-

approved members of the technical and scientific community. The Data Base is supported by the Air Force through USAF Contract F33615-77-C-1169 with ARL:UT.

2.2 THE SELECTION PROCESS

The flight data to be examined are identified by review of the documentation, the available ground truth data, and photographs of the imagery associated with various flights.

The next step is to replay the appropriate wideband tape corresponding to the selected leg of a flight. This replay is accomplished by means of the wideband tape drive shown on the right in the photograph in Fig. 1. The recorded imagery is reviewed on the Monitor Display in 16 gray level format. The DBS imagery used in the study is shown on the display in 360 vertical lines comprised of 384 range bins each.
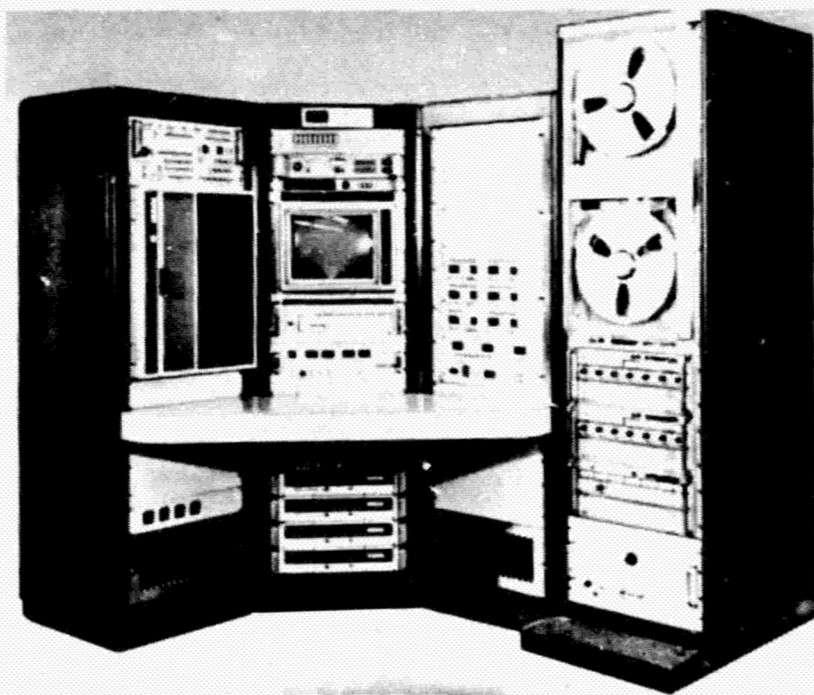
FIGURE 1. SAR DATA BANK FLIGHT DATA RETRIEVAL EQUIPMENT

When the desired map is painted on the display, the image is then "frozen" and the tape drive halted. The desired objects or features to be sampled are then located on the display. To locate the brightest pixel in the case of small discrete objects, the set of gray scale emphasis or deletion switches below the monitor is used. To obtain the azimuth line and range bin numbers of a selected pixel, the manual controls below the display are

used to position a local cursor over the pixel. The desired coordinates are
then read directly from the cursor controls.

After all desired sample pixels on the scan have been identified and coordi-
nates noted, a CCT (Computer-Compatible Tape) is placed on the small tape
drive visible at the left in Fig. 1. The data select/dump controls on the
panel to the right of the display are then set to dump the desired data.
The practice thus far in the study has been to dump the full scan of FM data
(Filter Magnitudes recorded in flight at the output of the Doppler Processor)
and a file of the associated RIOT data (Radar Input-Output data recorded from
the radar-computer I/O bus). The flight data are in computer-compatible
format and are processed on a general purpose computer.

The FM data are next reformatted and five arrays of FM data, similar to those
appearing in Fig. 2, are printed for each selected pixel for use in checking

FM DATA OF TARGET 40 170

MAP LINE NUMBER

R.O. NO.	701	702	703	704	705	706	707		
								- MAP 1	FRQ.04
58	97	107	78	128	110	82	73		
57	84	77	144	174	141	111	82		
56	104	106	144	174	185	113	90		
55	90	105	100	86	85	82	86		
54	84	105	90	83	88	83	78		
								- MAP 2	FRQ.03
58	95	96	125	127	126	73	81		
57	117	81	122	182	181	88	88		
56	115	88	124	174	176	79	95		
55	125	117	115	116	187	85	86		
54	153	105	171	86	78	80	91		
								- MAP 3	FRQ.02
58	95	101	124	81	79	87	72		
57	78	99	112	166	80	90	83		
56	123	81	116	178	86	88	111		
55	95	90	90	75	77	74	92		
54	155	106	108	86	76	81	81		
								- MAP 4	FRQ.01
58	75	125	124	118	111	82	86		
57	80	99	123	181	182	87	73		
56	95	107	152	186	119	105	82		
55	118	110	108	76	83	88	83		
54	103	84	86	65	87	94	90		
								- MAP 1234	
58	93	113	118	121	115	81	78		
57	133	92	131	166	153	101	86		
56	113	100	141	(148)	142	107	101		
55	118	108	108	100	93	88	88		
54	108	137	108	82	84	89	86		

FIGURE 2. FM PRINTOUT FOR 35-PIXEL SECTIONS OF THE FOUR
SINGLE-FREQUENCY AND THE COMPOSITE 4:1 MAPS

and finalizing the selection and coordinates for the sample pixels. The
FM values appearing in Map 1234, the composite 4:1 overlaid map, are examined
to verify that the selected coordinates of the center point of the printout
array represent, for the case of a small discrete, the brightest return from

III-1-4

the discrete. If an immediately adjacent pixel has a higher FM value, then the coordinates are changed to the coordinates of the brighter pixel. Thus far in the study, no further effort to correct for range/Doppler straddling has been made. After the coordinates are finalized, they are used with computer programs and the two data tapes, FM and RIOT, to combine the returns data and other required information on a punched card for each sample pixel. The punched cards are then used as the data base for analysis.

2.3 THE TEST CASE

A photograph of the imagery from which the sample sets treated in this paper were obtained is shown in Fig. 4. This imagery is one of the DBS scans made during a mapping flight in the San Joaquin Valley area of California near the town of Reedley. This scan was chosen for sampling because of the diversity of terrain, vegetation, and cultural features and the large Data Bank stock of photographs of various portions of the town and nearby countryside. Figure 3(A) is a photograph of a mowed grass athletic field located just above and to the right of the two bridges visible in the upper left corner of Fig. 4. The samples comprising sample class 201 were obtained from this location on the imagery.

Figure 3(B) is a photograph of a large vacant field covered with rough grass and weeds and located to the right of the group of bright returns from the buildings located just left of center at the extreme top edge of Fig. 4. The samples from this field comprise class 202. It was anticipated that there would be substantial overlap between the variants for classes 201 and 202, and the two similar features were selected for this reason.

Class 102 is comprised of fruit trees from the orchard shown in Fig. 3(C). This orchard is the large triangular area located just above the river in the lower right quadrant of Fig. 4.

Class 9000 was selected from the rectangular cluster of bright returns just below the sharp bend in the river in the lower right corner of Fig. 4. These returns are from a large mobile home park, visible in Fig. 3(D).

A. CLASS 201

B. CLASS 202

C. CLASS 102

D. CLASS 9000

FIGURE 3. PHOTOGRAPHS OF TEST SAMPLE SOURCE AREAS

3.0 THE DATA

3.1 FORMATION AND COMPOSITION OF THE FIVE MAPS

Since the I and Q data available   the Data Bank have not yet been studied, only the FM data will be discussed here. As shown in the printout of FM data illustrated in Fig. 2, there are five arrays of 5 x 7 FM values each, a total of 35 pixels. Each array carries a MAP number and an FRQ value code to the right of the array, with the exception of the array at the bottom of the figure. The column of numbers on the left edge of the picture contains the range bin coordinate for the associated row of pixels, and the map line numbers above the top array denote the azimuth coordinate for the associated column of pixels. The arrays for maps 1, 2, 3, and 4 are obtained from the four complete 1:1 overlay ratio, single frequency maps formed in the process of producing the 4:1 overlay map from which the bottom array is obtained.

FIGURE 4

SAR MAP OF REEDLEY, CALIFORNIA,
DBS 4:1 OVERLAY
(SAMPLE AREA FOR TEST CASE)

Note that each pixel with a given range bin and azimuth line set of coordinates is represented in all five arrays.

```
ARRAY No.  |← Array-1  →| |← Array-5  →| |← Array-9  →|
LINE No.    1 2 3 4 5 6 7 8 1 2 3 4 5 6 7 8 1 2 3 4 5 6 7 8 - - - - - - - -
MAP-1
FREQ.=f_0   | | | | | | | | | | | | | | | | | | | | | | | |

ARRAY No.     |← Array-2  →| |← Array-6  →| |← Array-10 →|
LINE No.       1 2 3 4 5 6 7 8 1 2 3 4 5 6 7 8 1 2 3 4 5 6 7 8 - - - - - -
MAP-2
FREQ.=f_1      | | | | | | | | | | | | | | | | | | | | | | | |

ARRAY No.     |← Array-3  →| |← Array-7  →| |← Array-11 →|
LINE No.       1 2 3 4 5 6 7 8 1 2 3 4 5 6 7 8 1 2 3 4 5 6 7 8 - - - -
MAP-3
FREQ.=f_2      | | | | | | | | | | | | | | | | | | | | | | | |  !

ARRAY No.      |← Array-4  →| |← Array-8  →| |← Array-12 →|
LINE No.        1 2 3 4 5 6 7 8 1 2 3 4 5 6 7 8 1 2 3 4 5 6 7 8 - -
MAP-4
FREQ.=f_3       | | | | | | | | | | | | | | | | | | | | | | | |

4:1 Overlaid
LINE No.        1 2 3 4 5 6 7 8 9 10 12  14  16  18  20  22  24 - -
MAP-1234        | | | | | | | | | | | | | | | | | | | | | | | |

                x x x x x x x x x x x x x x x x x x x x x x x x
PIXEL No.       1 2 3 4 5 6 7 8 9 10 12  14  16  18  20  22  24
  Return
time sequence   f_0 f_1 f_2 f_3 f_0 f_1 f_2 f_3 f_0 f_1 f_2 f_3

                f_1 f_2 f_3 f_0 f_1 f_2 f_3 f_0 f_1 f_2 f_3 f_0

                f_2 f_3 f_0 f_1 f_2 f_3 f_0 f_1 f_2 f_3 f_0 f_1

                f_3 f_0 f_1 f_2 f_3 f_4 f_1 f_2 f_3 f_0 f_1 f_2
```

FIGURE 5 - FORMATION OF MAP OVERLAY LINES WITH
ASSOCIATED FREQUENCY SEQUENCE OF RETURNS

The FRQ value given for each of the 1:1 overlay maps represents the transmitter frequency used in the formation of that map for this particular scan. This frequency varies from flight to flight and from scan to scan, but its cycle of occurrence does not vary. The cycle sequence is in order of descending frequency (i.e., 16.4, 16.3, 16.2, 16.1, or any combination such as 16.3, 15.2, 16.1, 16.4, and so on). When the "frequency hop" mode was employed, as it often was, the transmitter frequency changed for each 8-azimuth-line array formed.

III-1-8

The method of overlay employed in forming the separate 1:1 maps and the composite 4:1 overlay map is illustrated in Fig. 5. The key datum which the authors wish to convey here is the association of a particular frequency sequence with each pair of azimuth lines in the composite 4:1 overlay map, which is formed by averaging together the appropriate pixels from the four 1:1 maps, 1, 2, 3, and 4. Note that three 8-line arrays are presented for each of the four 1:1 maps and that each array bears an array number, representing the order in which the arrays are formed by the system. Array No. 1 is formed first, then array No. 2 is formed but with an azimuth displacement of two azimuth lines to the right. Next come arrays No. 3 and No. 4, respectively, each with an additional 2-line displacement relative to the preceding array.

After the first four arrays are formed, note that there are only two azimuth lines of the 4:1 map that can be formed by averaging together the corresponding lines of the four 1:1 maps. Thus, lines 7,8 of array No. 1, lires 5,6 of array No. 2, lines 3,4 of array No. 3, and lines 1,2 of array No. 4 correspond in azimuth and, averaged together, form lines 1,2 of the 4:1 map.

The row of x's below the 4:1 map denotes pixels on each map azimuth line. The column of f's below each pair of x's denotes the time order in which each return frequency will be received by the SAR. For pixels 1 and 2, the first transmitter frequency illuminating these points was f_0, then, in order f_1, f_2, and f_3. For the next pair of pixels the first frequency will be f_1, from lines 7 and 8 of array No. 2. The rest of the sequence is f_2 from lines 5,6 of array No. 3, f_3 from lines 3,4 of array No. 4, and finally, f_0 from array No. 5. These sequences continue to cycle throughout the map. This varying frequency sequencing has been found to be quite important in the study of variants and the study of its effects is continuing.

3.2 SCINTILLATION

Four enlarged 1:1 map strips of the mobile home park and adjoining fields shown previously in Figs. 3(D) and 4 are presented in Fig. 6. Note the map-to-map variations in the pattern of returns from the structures in the park and the surrounding fields. Gray level 8 was emphasized in these pictures and the higher gray shades were deleted to better illustrate the variations.

FIGURE 6   MOBILE HOME PARK AND ADJACENT FIELDS

These variations are also apparent in the FM arrays printed in Fig. 2.
Note the variation in FM values between pixels with corresponding range
bin and line coordinates. It has been discovered that the information con-
tent in these variations is significant in feature discrimination as is
demonstrated in the final sections of this paper.

4.0 SAMPLE VARIANTS

Four variants were generated from the 4-look FM data discussed previously.
The four sequential values representing each pixel, converted to power units,
were used to generate four variants employed in the classification model.
The FM values are related to power by $M=8 \log_2 P$ plus a constant so the
conversion to power from the log filter magnitudes is given by

$$P = K(2^{M/8}) \quad , \tag{1}$$

where K is a calibration factor which may change from scan to scan or within
a single scan. To illustrate the classification model, data were selected
from regions within the scan over which K remained constant.

The four target variants based on measurement are the mean, Z_1; sample
variance, Z_2; fast variation, Z_3; and slow variation, Z_4, defined as

$$Z_1 = \frac{1}{4} \sum P_i \tag{2}$$

$$Z_2^2 = \frac{1}{3} \sum (P_i - Z_1)^2 \tag{3}$$

$$Z_3 = [|P_1 - P_2| + |P_2 - P_3| + |P_3 - P_4|]/3 \tag{4}$$

$$Z_4 = [|P_1 - P_3| + |P_2 - P_4| + |P_1 - P_4|]/3 \tag{5}$$

It should be noted in the above relations that variants 1 and 2 do not
involve time sequence of the data whereas the variants, fast variation and
slow variation, do involve the time sequence of the returns. Other measures
of dispersion investigated, but not reported here include average deviation,
color, deviation from color, total variation, spread, and slope.

5.0 STATISTICS OF THE VARIANTS

5.1 DISTRIBUTIONS INVESTIGATED FOR THE VARIANTS

Since the probability distribution function of the measured data or variants derived from the measured data was required in the formulation of the classification model, histograms of the distributions of the various variants were constructed from the sample data sets. Four standard probability distribution functions, which included the Lognormal, the Weibull, the Chi-Square, and the Rayleigh PDF's, were fitted to the data. It was found that the Lognormal and Weibull PDF's generally fitted the test data well with the Weibull PDF giving a better fit than the Lognormal PDF.

The Lognormal and the Weibull distributions are written as

$$p(X) = \frac{1}{\sqrt{2\pi}X\sigma_{LN}} \exp\left\{-(\ln(X/M))^2/2\sigma_{LN}^2\right\} \tag{6}$$

and

$$p(X) = \frac{n}{\sigma_W} (X/\sigma_W)^{n-1} \exp\left\{-(X/\sigma_W)^n\right\} \tag{7}$$

respectively, where M is the median of X, σ_{LN} is the standard deviation of $\ln(X/M)$, σ_W is a scale factor, and n is a shape parameter.

5.2 EXAMPLE HISTOGRAMS AND CURVE FITS

Histograms of unnormalized power for samples of rough grass and mobile homes along with the corresponding Lognormal curve fits are shown in Fig. 7 for returns from individual SAR maps for each of the four looks with 1:1 overlay. It should be noted that there is little change in the distribution curves between maps for the two extremes of power levels represented by the two classes. The distribution and curve fits, both Lognormal and Weibull, are also shown in the same figure. The Lognormal, in general, appears to fit the histogram data but, for some data, does not appear to be well centered about the histogram data. This apparent anomaly occurs whenever σ_{LN} is large (on the order of 1.50). Histograms and Lognormal distributions for received power for the four target types are shown in Fig. 8. These curves show that the Lognormal distribution is a good representation for the PDF for the four sample classes.
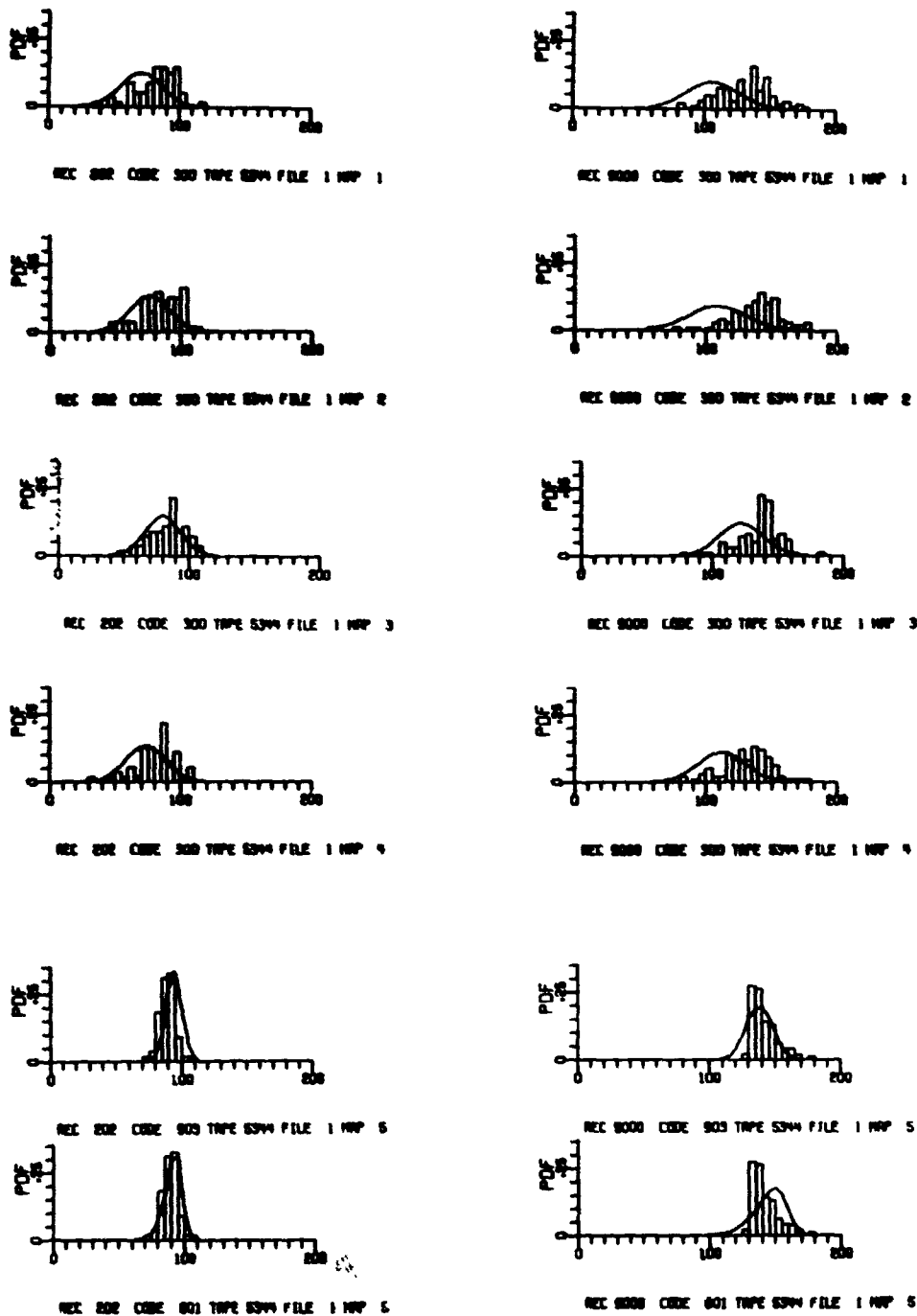
FIGURE 7

RECEIVED POWER DISTRIBUTION - HISTOGRAMS AND FITTED LOGNORMAL FUNCTIONS
FOR TWO TARGET TYPES SHOWING TYPICAL VARIATION BETWEEN MAPS. THE LOWER
SET WHICH SHOWS THE 4-MAP MEANS ALSO SHOWS A COMPARISON BETWEEN THE WEIBULL
AND LOGNORMAL PDF.

FIGURE 8

SINGLE MAP RETURN POWER DISTRIBUTIONS FOR FOUR CLASSES OF TARGETS
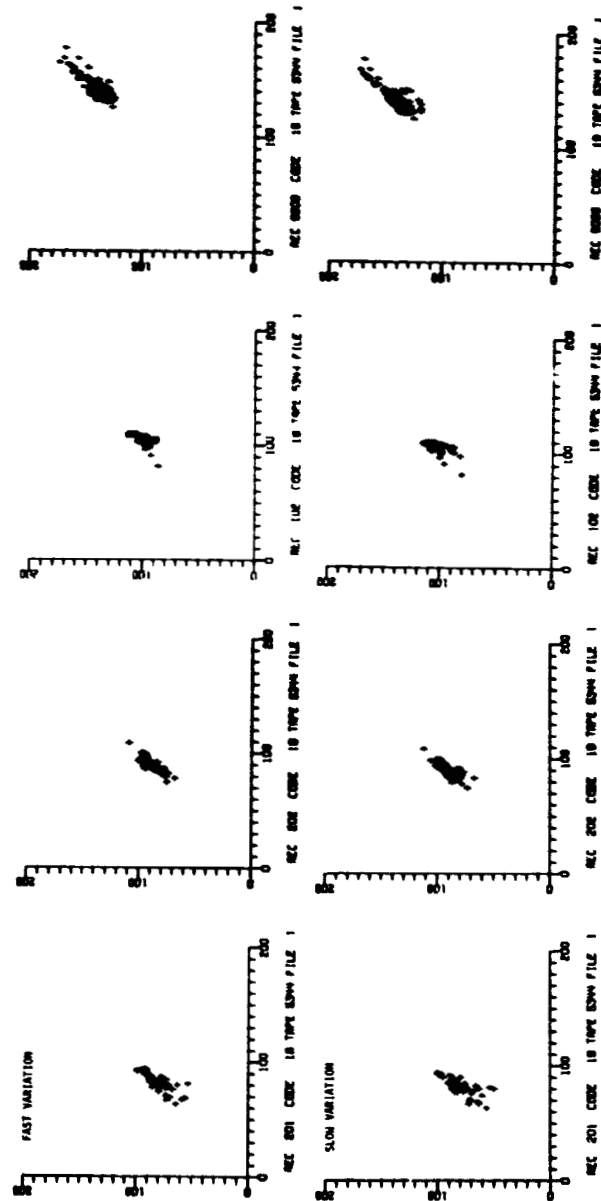
FIGURE 9

SCATTERGRAMS OF FAST VARIATION IN POWER VERSUS MEAN POWER AND OF SLOW
VARIATION IN POWER VERSUS MEAN POWER FOR FOUR CLASSES OF TARGETS

To further illustrate the dispersion of the variants between sample classes, a sample set of crossplots of the variants, fast and slow variation, versus mean power is shown in Fig. 9 for the four classes..

6.0 A MULTIVARIANT DISCRIMINANT MODEL AND RESULTS WHEN APPLIED TO A TEST CASE

6.1 CHOICE OF THE CLASSIFICATION MODEL

To demonstrate the utility of several of the variants currently being studied for discrimination, a classification model based on the statistics of selected variants derived from the SAR return data was formulated and applied to the test sample. Four variants and four classes of objects were used to demonstrate the effectiveness of the Discriminant Model; however, it should be noted here that the model is by no means limited to these dimensions.

Although the Weibull PDF (Probability Distribution Function) fitted the variants for all four classes comprising the test sample, the Shape Factors were large numbers for some targets, thereby making the Weibull PDF less suitable than the Lognormal PDF for construction of the classification model. Consequently, the Lognormal distribution was chosen for constructing the classification model.

6.2 DESCRIPTION OF THE MODEL

The variants, (Z_1, Z_2, Z_3, Z_4), derived from one set of measurements are assumed to belong to one of four sample classes comprising the test sample. Since these quantities have a Lognormal distribution, the PDF of Z, when Z belongs to class T_i, is represented by $p(Z|T_i)$ and for the vector Z is given by the following:

$$p(Z|T_i) = \frac{1}{(2\pi)^2 |C_i|^{1/2} Z_{pi}} \exp\left\{-\frac{1}{2}(Z' \ C_i^{-1} \ Z)\right\} \tag{8}$$

where

$$Z = [\ln(Z_1/M_{i1}) \ , \ \ln(Z_2/M_{i2}) \ , \ \dots \ln(Z_4/M_{i4})]$$

Z' is the transpose of Z, and

$$Z_{pi} = \Pi \ (Z_r/M_{ir})$$

M_{ir}, for $r=1,2,3,4$, are the medians of Z_r when Z_r belongs to T_i. C_i is the covariance matrix of Z. A decision function is formed that assigns each vector Z to one of the sample classes. This function will assign Z to class T_i if the following condition

$$p(Z|T_i) > p(Z|T_j) \qquad (9)$$

is met for all j not including i.

Inserting the expression

$$r_{ij} = \ln \frac{p(Z|T_i)}{p(Z|T_j)} \qquad (10)$$

into the ratio of two probability density functions, one obtains a decision function as follows

$$r_{ij} = -\frac{1}{2}\left[\left(\ln \frac{Z_i}{M_i}\right)' C_i^{-1} \left(\ln \frac{Z_i}{M_i}\right) - \left(\ln \frac{Z_j}{M_j}\right)' C_j^{-1}\left(\ln \frac{Z_j}{M_j}\right)\right]$$

$$+ \frac{1}{2}\ln \frac{C_j}{C_i} + \sum_r \ln\left(\frac{M_{jr}}{M_{ir}}\right) \qquad (11)$$

A decision is now made, based on Eq. (11), as to which class Z belongs. By Eq. (9), Z is assigned to Class T_i if $r_{ij} > 0$, and is not assigned to T_i if $r_{ij} < 0$.

For the selected example given here, only the diagonal terms in the covariance matrices were retained. The off-diagonal terms were set to zero. All combinations for r_{ij} were computed and Z was placed in class k when the condition $r_{kj} > 0$ was met for all j.

6.3 TEST RESULTS

Employing the data representing the four sample classes described in section 4, the model was tested against each data point for several combinations of measurement vectors Z. The result of one test is shown in Table I when the four variants--Mean$_{pwr}$, Standard Deviation$_{pwr}$, Fast Variation, and Slow Variation--were employed in the model. As is shown in Table I, data points of class 102 (young fruit trees in an orchard) were identified

TABLE I

NUMBER OF CORRECT AND INCORRECT CLASSIFICATIONS
FOR EACH PIXEL VERSUS EACH CLASS

Class	Class Description	Number of Samples	Number of Classifications per Class			
			102	201	202	9000
102	Fruit Trees	50	34	5	11	0
201	Mowed Grass Field	49	0	44	5	0
202	Unmowed Grass & Weed Field	54	1	40	14	0
9000	Metal Mobile Homes	37	0	0	0	37

correctly by a ratio of slightly better than 2:1 over incorrect classifica-
tions as belonging to the grass classes 201 and 202. The ratio of correct
to incorrect classifications for the mowed grass class (201) was nearly 9:1
and here the incorrectly classified pixels were classified as belonging to
the rough grass class. The ratio of correct to incorrect for the rough grass
pixels (202) was about 1:4, a poor showing. However, the grasses were
initially selected to test the variants for two very similar subclasses.
Considering this fact, the model did surprisingly well. All class 9000
(metal structures) were correctly classified, a 100% performance.

6.4 CONCLUSIONS

Since the results presented here are preliminary , no optimization or
detailed analysis of the model or variants has been accomplished . How-

ever , it is believed that the evidence presented in this paper indicates
that map to map scintillations for the type SAR studied do contain potential-
ly valuable object and feature classifier information .

7.0 ACKNOWLEDGEMENTS

8.0 REFERENCES

1. G. Hahn and S. S. Shapiro, Statistical Models in Engineering, John Wiley and Sons, 1967.

2. W. J. Szajnowski, Estimators of Log-Normal Distribution Parameters, IEEE Trans. on Aerospace and Electronics Systems, Vol. AES-13, No. 5, September 1977.

3. W. J. Szajnowski, Discrimination Between Log-Normal and Weibull Clutter, IEEE Trans. on Aerospace and Electronics Systems, Vol. AES-13, No. 5, September 1977.

4. Julius T. Tou and R. G. Gonzales, Pattern Recognition Principles, Addison-Wesley Publishing Co., 1974.

↓ N78-30455

IMAGE SYNTHESIS FOR SAR SYSTEM, CALIBRATION AND PROCESSOR DESIGN

J.C. HOLTZMAN, J.L. ABBOTT, V.H. KAUPP, V.S. FROST
REMOTE SENSING LABORATORY
UNIVERSITY OF KANSAS
LAWRENCE, KANSAS 66045

SUMMARY

The "Point Scattering Method" of simulating radar imagery is an efficient, cost-effective technique which rigorously models all aspects of the imaging radar phenomena. The model is valid for incoherently degraded SAR, PPI and real aperture systems. The target behavior, the radar antenna and signal processing equipment, and the storage of radar data on photographic film are incorporated although digital image storage can easily be accomodated. This method does not presuppose the existence of radar imagery; rather, its computational algorithms operate on a symbolic representation of the terrain test site to calculate such parameters as range, angle of incidence, resolution cell size, etc. Empirical backscatter data and elevation data are utilized to model the terrain. Additionally, the important geometrical/propagation effects such as shadow, foreshortening, layover, and local angle of incidence are rigorously treated.

Applications of radar image simulation to SAR system, calibration, and processor design problems are discussed. For example, data or images generated by the Point Scattering Method will display various degrees of interpretability depending upon the configuration of the imaging system being modeled. Therefore, the results can be used to establish optimum design parameters: frequencies, polarizations, angle of incidence, allowable fading, resolution, antenna pattern, and so on. Two tasks of a proposed calibrated SAR system are highlighted: soil moisture detection and vegetation discrimination. This simulation technique in conjunction with test sites containing these types of targets may be applied to establish baseline quality images. Subsequently, system error degradation studies can be performed using classification and detection algorithms to develop quantifiable performance criteria.

1.0 INTRODUCTION

The successful application of airborne imaging SAR and ground-based back-scatter measurement systems to the tasks of soil moisture detection and crop discrimination has received considerable publicity. It has been proposed that a spaceborne SAR be designed to accomplish these same goals on a large scale. The proponents of the design cite as evidence that the proposed system will succeed, that the average σ^0 trends for the targets of interest exhibit considerable separation. SAR system designs have been proposed for orbital platforms capitalizing on the current state of knowledge. However, the degree to which these designs will accomplish the desired goals is not clear. Calibration problems, variability in system components, degradation due to navigational and structural problems (e.g., antenna performance) all must be considered as to their impact on the ultimate performance which can only be assessed in terms of the intended application. For instance, the problem of measuring soil moisture involves discriminating features within a narrow range (<6,7 dB) which clearly calls for a calibrated system having a measurement accuracy on the order of 1 dB. These and other conjectures can be investigated by rigorously modeling the imaging radar "closed-system" and by simulating imagery. The closed-system consists of the target terrain, atmosphere, antenna, signal processing equipment, and data storage medium. The interpretability or information content of the simulated images, as determined by either a human or automated classifier, would be useful in deciding whether the spaceborne SAR can perform the desired discriminations.

A cost-effective, efficient technique which has been developed for imaging radar simulation, and which is well-suited to the above SAR problems is the "Point Scattering Method" of Holtzman, et al. [1]. This method incorporates all aspects of the imaging phenomena, i.e., each component of the closed-system and its effects on the resulting image have been modeled. The present capabilities of digital implementations of the PSM allow simulation of SAR, PPI, and real aperture imagery. Both qualitative (visual) and quantitative (image cross-correlation measurements, real versus simulated imagery) validation tests have been performed for the PSM simulations, with excellent results [2]. The model accurately predicts the radar return by taking into account the propagation/geometrical effects and radar system parameters as well as the

image medium. The signal/target interaction is described in terms of σ^o, the differential scattering cross-section; empirical or theoretical values of σ^o are used in the simulation process.

2.0 THE POINT SCATTERING METHOD : A BRIEF OVERVIEW

In order to produce imagery comparable to that which would be produced by a real radar traversing the atmosphere or space above the desired ground swath, it is necessary to obtain a representation of the terrain at microwave frequencies, and to sample its properties. These properties are electromagnetic and geometric; therefore, the microwave reflectivity and elevation of the site are sampled. Empirical backscatter data are utilized in combination with the relief data to model both the coarse and fine scale characteristics of the terrain. Backscatter data implicitly contain information about the texture and type of terrain, and its use complements elevation sampling which alone is insufficient for modeling the ground as a component of the imaging radar closed system. The digital data base which describes the ground site is in the form of a rectangular matrix, and each of the locations of this matrix contain x- and y-coordinate, elevation, and backscatter category (e.g., 15 cm green wheat over rough moist soil). A matrix of empirical σ^o data, taken from the literature and from the Remote Sensing Laboratory agriculture/soil moisture data bank, is contained on tape for each distinct distributed target found to exist in the test site. Specular reflectors are either treated symbolically or by the optical technique of Holtzman, et al. [3].

After the ground truth data base (terrain feature model) of the desired site has been specified, the reflectivity (σ^o) data for the various categories included in the data base have been obtained, and the complex geometry relating the radar platform to the scene has been determined, then the imaging model, i.e. the final computational algorithm of the PSM is used to calculate the signal reradiated from the ground back to the radar for each resolution element in the scene. It calculates the ground-return signal exiting the receiver, and then converts this into the appropriate density of silver grains in the exposed and developed image. This algorithm determines the shade of gray of each pixel in the image, and hence, is called the graytone equation. The graytone equation produces the final result, drawing upon all preceding data and calculations. It relates the ground to the radar and

to the image. When the desired storage medium of the SAR is not photographic
film but magnetic tape, the PSM can be adapted to reflect this change. The
final computational algorithms of the Point Scattering Model can reflect
a linear, log, or other signal receiver and signal quantizer. The input to
the quantizer is most often the output of a phase detector, that is, the
bipolar video data of a coherent radar receiver. The PSM algorithms can be
modified to this chain of events for further digital processing.

As an example of the most recent results of the Point Scattering Model, an
image was simulated for a site (35° 04' N by 88° 15' W) through which the
Tennessee River flows. Goodyear 3 m resolution SAR imagery was purchased for
comparison purposes. The actual radar data were not employed in the construc-
tion of the ground truth data base, nor in decisions about the terrain reflec-
tivity model. Thus, some misidentification of the scattering categories can
occur since the source intelligence material for delineating categories was
high resolution aerial photography. Because radar and optical imagery differ
so much with respect to each other in the response to terrain features, and
especially moisture content and ground roughness, 100% accurate microwave
response categorization would require more kinds of source intelligence data
than just optical imagery in future studies. Some minor differences be-
tween the real and simulated imagery were caused by misidentification of
categories because only optical intelligence data were used. Figure 1 is
a side by side comparison of 3 m SAR imagery and 18 m resolution PSM simu-
lated imagery (lower swath). The simulation parameters were set to match
as closely as possible those for the actual radar system and flight path.
Table 1 lists several of the system and flight parameter for the situations.

TABLE 1
FLIGHT AND RADAR PARAMETERS

Parameter	APD - 10	Simulated
Altitude	8900 m	8900m
Near Range Angle of Incidence	66.7^O	66.7^O
Far Range Angle of Incidence	71.3^O	71.3^O
Heading	116.4^O Magnetic	116.4^O Magnetic
Look Direction	Southwest	Southwest
Frequency/Polarization	X Band HH	X Band HH

LOOK DIRECTION
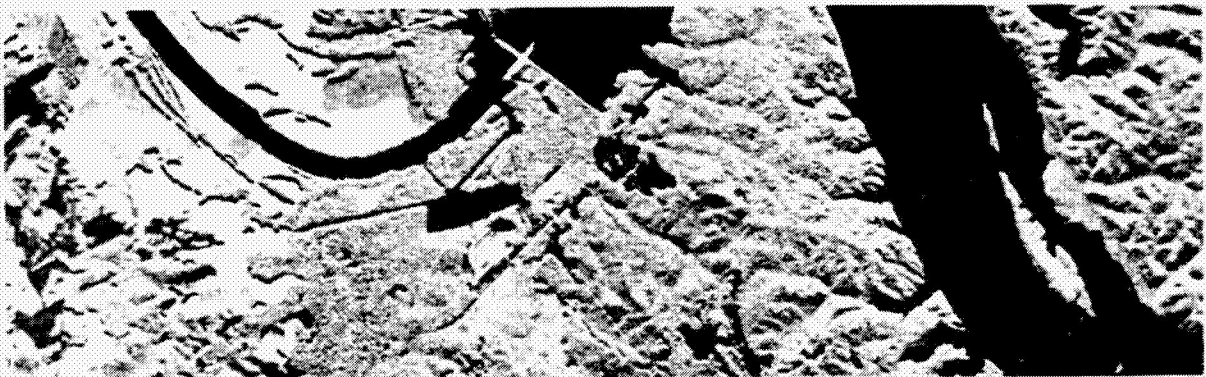
APD - 10 IMAGERY

SIMULATED IMAGERY

FIGURE 1.   COMPARISON OF APD - 10 SAR IMAGERY
AND PSM SIMULATED IMAGERY.

III-2-5

Note that because identical flight paths with respect to the ground were employed, there should be a direct correspondence between feature locations in the two images. Shadows should be of the same lengths, and oriented similarly. Fidelity in the ground truth data base in addition to correct simulation methods account for the favorable similarities in these respects. As secondary points of comparison, the relative gray shades and texture may be employed, but with caution. The deciduous trees in the test region were modeled as having a mean height of 21 meters, and a standard deviation of 3 m. The resulting texture adds to the resemblance between the imagery.

Gray tone comparisons can be made in a relative manner. When the tone of a field "A" with respect to field "B" is lighter in the real radar image, then such a relationship should exist in the simulated version. There are few instances in the swaths of Figure 1 that fail to meet this criteria. These discrepancies are explained by one of two possibilities; either a mislabeling of radar scattering category has occurred, or else the terrain reflectivity model at that particular angle of incidence does not suitably describe the regions's behavior. We cannot attach a number to depict the accuracy of the simulated radar image shown, for such a comparison cannot be construed as absolute or quantitative, but the overall visual effect, in the opinion of trained radar interpreters is very good [4].

3.0 SAR SYSTEM, CALIBRATION, AND PROCESSOR DESIGN

Radar image simulation (especially the PSM) has already been shown to be invaluable in assessing and solving defense department problems [2]. In this section we propose extensions of proven technology (PSM) to a different class of problems. Consider two of the potential applications of a spaceborne SAR: soil moisture detection, and vegetation discrimination. Radar image simulation can serve as an important research tool in the implementation of a calibrated SAR for these two (and other) particular objectives. Simulation offers a way to evaluate all aspects of a spaceborne SAR program from preliminary design through mission planning via the most graphic method possible; the final image product and resultant discrimination analyses. Perturbations of recorded data,created by processor design trade-offs, operating parameters trade-offs, antenna design and degradations, calibration requirements and degradations, etc., can be predicted and the effects analyzed through the use

of radar simulation.

A well-designed candidate program utilizing radar simulation would require developing a data base for a suitable site, surveying the soil moisture and vegetation properties of the site, and collecting supportive scatterometry data and airborne radar images of the site. Before the radar simulation model would be used to evaluate the SAR questions, it would be validated by producing simulations of the airborne images and comparing them to the actual images. This would lend credence to the use of the simulation model to evaluate the SAR. After completion of these preliminary activities the PSM would be applied to evaluate the potential problems (both design and calibration) of a spaceborne SAR.

For instance, the PSM could be employed to confirm the design of the candidate SAR system. One way this could be accomplished is through comfirmation of the optimum frequencies, polarizations, and angles of incidence for either soil moisture detection or vegetation monitoring. Another way this could by accomplished is through verifying the design parameters of the hardware. Design variants and their impacts on ultimate data, interpretability, and discriminations could be assayed easily. Candidate receiver/processor models could be implemented in the PSM, statistical degradations introduced, and resultant images formed. These images could be interpreted and the effects measured.

In addition, the PSM could be applied to answer questions about the design of the SAR system through the easily implemented resolution versus averaging (to reduce fading, data rates,etc.) trade-off studies. With a very fine resolution ground truth data base the effects of sacrificing r   ,tion for speckle reduction could be appraised by human interpreters or automated classification schemes. The significance of the savings in terms of data processing expense could be large, yet the loss of information content of the imagery could be strictly monitored through such a systematic study.

The importance of antenna design and performance for a spaceborne SAR is significant. Radar image simulation as performed by implementation of the PSM can be applied to determine the effect of antenna configuration (e.g.,flatness) under orbital conditions upon the final image and ultimately the effects on interpretability of the data.

In order to accomplish the goals in soil moisture detection the SAR will have
to be a calibrated instrument. While conventional statistical techniques
can be used to estimate the effect of component variations, orbital trajec-
tory errors etc., on the return video signal it is only through simulation
of the final data products that an assessment can be made as to the effect
on the ability to interpret the images. It is suggested, therefore, that
simulated imagery be produced for typical soil moisture (and agricultural)
targets to test different calibration techniques, as well as to evaluate
the variability. The simulated images would be compared to baseline simula-
tions and the resulting classification would establish the expected success
under the tested conditions.

Simulation can also play a vital role in "real-time" calibration of the
orbital sensor. It is anticipated that calibrated ground-based measurements
taken simultaneously with orbital overflights will be performed to "calibrate"
the SAR. Rather than calibrate on a few fields, simulated imagery could be
produced to mimic the conditions at the time of the overflight incorporating
the ground measurements and then could be used to calibrate the identical
imagery produced by the spaceborne SAR. This experiment is analogous to
the S193 exercise of comparing pre-flight antenna patterns with antenna pat-
terns measured from space (APEX Experiment [5]) to validate system perform-
ance and to obtain the final calibration of the S193 data.

Calibration has many ramifications as to the final success of an orbital SAR.
Conjectures as to the performance, precision, and accuracy of the SAR must
be answered at an early date. Simulation, especially using the PSM as a
vehicle, can play an important role in ending the conjectures, leading to
definitive results.

Assuming a design is finalized for the proposed SAR, the value of image combi-
nations, for example, spaceborne SAR with LANDSAT could be evaluated. Human
interpreter studies and/or automated multivariate classification analyses
could be performed on the superposition to determine the usefulness of such
a combination. In the event that a multifrequency/multipolarization SAR
design is proposed or later chosen, then corresponding simulated images
could be digitally processed, optically filtered, superimposed, etc., before
the SAR becomes operational .

Needless to say, there are many techniques which will be employed in the design and operation of a spaceborne SAR assigned to accomplish the tasks of soil moisture detection and vegetation analysis. Simulation of radar imagery is one feasible, cost-effective and efficient method. It should be combined with others, e.g., observation of existing SAR imagery and empirical σ^o data. There may be glaring objections to the use of a single method when such an enormous number of factors contribute to the success or failure of the mission. Choosing design parameters from radar imagery alone is probably insufficient because (1) the lack of space radar imagery of natural terrain surfaces, (2) the absence of numerous data collected by a single, calibrated system, and (3) the "individuality" of resultant images produced by existing commercial and government radars.

4.0 CONCLUSIONS

The Point Scattering Method for radar image simulation has been briefly reviewed and some strip-image format results were shown as a means to assess quality of the products generated. Space does not permit either a full theoretical development of the PSM or a complete analysis of the results. The interested reader can find such details in the referenced documents [1,2].

Simulation traditionally has been an important research tool in all engineering and scientific disciplines but has not been available to the radar designer to the extent being discussed here. Certainly simulations of systems and components have been employed but not the complete imaging simulation represented by the PSM. This newly emerging area, radar image simulation, has been successfully applied to defense-related problems [2] and now offers its capabilities to evaluate problems and answer questions regarding a spaceborne SAR designed to measure soil moisture or to monitor vegetation.

Sample studies of a well-designed program employing radar simulation for evaluation of SAR system, processor design, and calibration are proposed. Space prohibits a definitive statement about the application of radar simulation to address specific system problems, so only the major goals and objectives, and potential rewards are discussed.

REFERENCES

1. Holtzman, J.C.,V.H. Kaupp, R.L. Martin, E.E. Komp, and V.S. Frost, "Radar Image Simulation Project: Development of a General Simulation Model and an Interactive Simulation Model, and Sample Results," ETL TR-0047, U. S. Army Engineer Topographic Laboratories, Fort Belvoir, Virginia, February, 1976.

2. Holtzman, J.C., V.H. Kaupp, J.L. Abbott, V.S. Frost, E.E. Komp, and E.C. Davison, "Radar Image Simulation: Validation of the Point Scattering Model," Volume I, ETL TR-0117, U. S. Army Engineer Topographic Laboratories, Fort Belvoir, Virginia, June, 1977.

3. Holtzman, J.C., V.S. Frost, J. L. Abbott, and V.H. Kaupp, " A Mathematical Model for a Terrain-Imaging Radar and its Potential Application to Radar Image Simulation," Remote Sensing Laboratory Technical Report 319-6, University of Kansas, Lawrence, Kansas, November, 1976.

4. L. F. Dellwig, personal communication.

5. Kaupp, V.H., J.C. Holtzman, "Skylab Program Earth Resources Experiment Package, Sensor Performance Report, S193 RAD/SCAT Final Report," Remote Sensing Laboratory Technical Report 236-4, University of Kansas, Lawrence, Kansas, July, 1975.

$D_5 (32$

DESCRIPTION OF A COMPUTER SIMULATION
OF AN ORBITAL SAR SYSTEM

GARY LYNN CROW
RADIO SCIENCIES DIVISION
APPLIED RESEARCH LABORATORIES
THE UNIVERSITY OF TEXAS AT AUSTIN
AUSTIN, TEXAS 78712

SUMMARY

In order to predict the performance of a synthetic aperture radar (SAR) for
a wide variety of system and environmental parameters a computer simulation
of the SAR system has been developed. This model is a detailed description
of the SAR imaging process on a pulse-by-pulse basis. The simulation is im-
plemented as seven computer programs for a CDC Cyber 171 digital computer.
The first of these programs is the simulation controller. This program co-
ordinates communication between the other programs and between the user and
the simulation. It is also responsible for computing certain parameters,
like the map start time, that will be needed by the other programs. The
second program discussed in this paper specifies the model of the terrain to
be mapped. The terrain can consist of discrete scatterers or extended homo-
geneous areas. The homogeneous areas are represented by a collection of
many discrete targets. The density of the discrete targets per unit area
is under user control but the scatterers are placed so as to insure several
per SAR resolution cell. Representing homogeneous areas as collections of
point reflectors enables the simulation to support the phenomenon of co-
herent speckle which is characteristic of some monochromatic SAR imagery.
The third program discussed computes the range between each scatterer in the
terrain and the phase center of the antenna. These calculations are made on
a pulse-by-pulse basis for each pulse in the simulated time interval. The
range is a function of the location of the terrain on the planet surface,
the rotation and shape of the planet, the orbital parameters of the satellite
carrying the SAR and the location of the antenna phase center with respect
to the center of mass of the satellite. This program also weights the re-
ceived echo strength in accordance with the antenna gain pattern. The
fourth program computes the IPQ (In Phase and Quadrature) video signal by

convolving the radar impulse-response and the echo time histories. The fifth program handles motion compensation. It applies the Doppler phase corrections for each pulse to effect SAR beam steering and range focusing. The sixth program is the SAR processor. It weights the IPQ video and computes the fourier transform to produce the complex output image. The seventh and last program is the post processor. It computes the image log magnitude levels, assigns grey shade levels and displays the resultant image. The output of the simulation is a fully processed SAR image displayed on a high resolution CRT.

1.0 PURPOSE AND STATUS

In general the simulation is designed to permit investigators to assess the effect of various radar and geometric parameters on the quality of the SAR imagery produced. In particular it will be used to investigate the following:

1. To assess the effect of various antenna patterns on the SAR image,
2. To assess the effect of various SAR parameters on the system's ability to detect small differences in the radar cross section of adjacent homogeneous areas.
3. To assess the effect of mapping geometry on SAR image quality.

The first SAR simulation produced at ARL:UT modeled an airborne SAR scenario. This simulation has been completed and results obtained from this first simulation indicate that our approach was feasible. The simulation of the orbital case, on a faster computer, is nearing completion.

2.0 PROGRAM STRUCTURE

The structure of the simulation is shown in Figure 1. The simulation control program, SARTREK, is run first. It reads all the user input data, computes various system parameters based on these inputs and stores these data in an area which is accessible to the other programs. As the other programs in the simulation are executed they will produce other parameters necessary to subsequent programs. These data are also stored in the "control parameter" area. The user supplies input data which specifies the antenna pattern, terrain parameters, SAR radar and processor parameters, orbital parameters and a description of the planet being mapped. After SARTREK the data flow is from left to right in Figure 1. Each program is run in turn
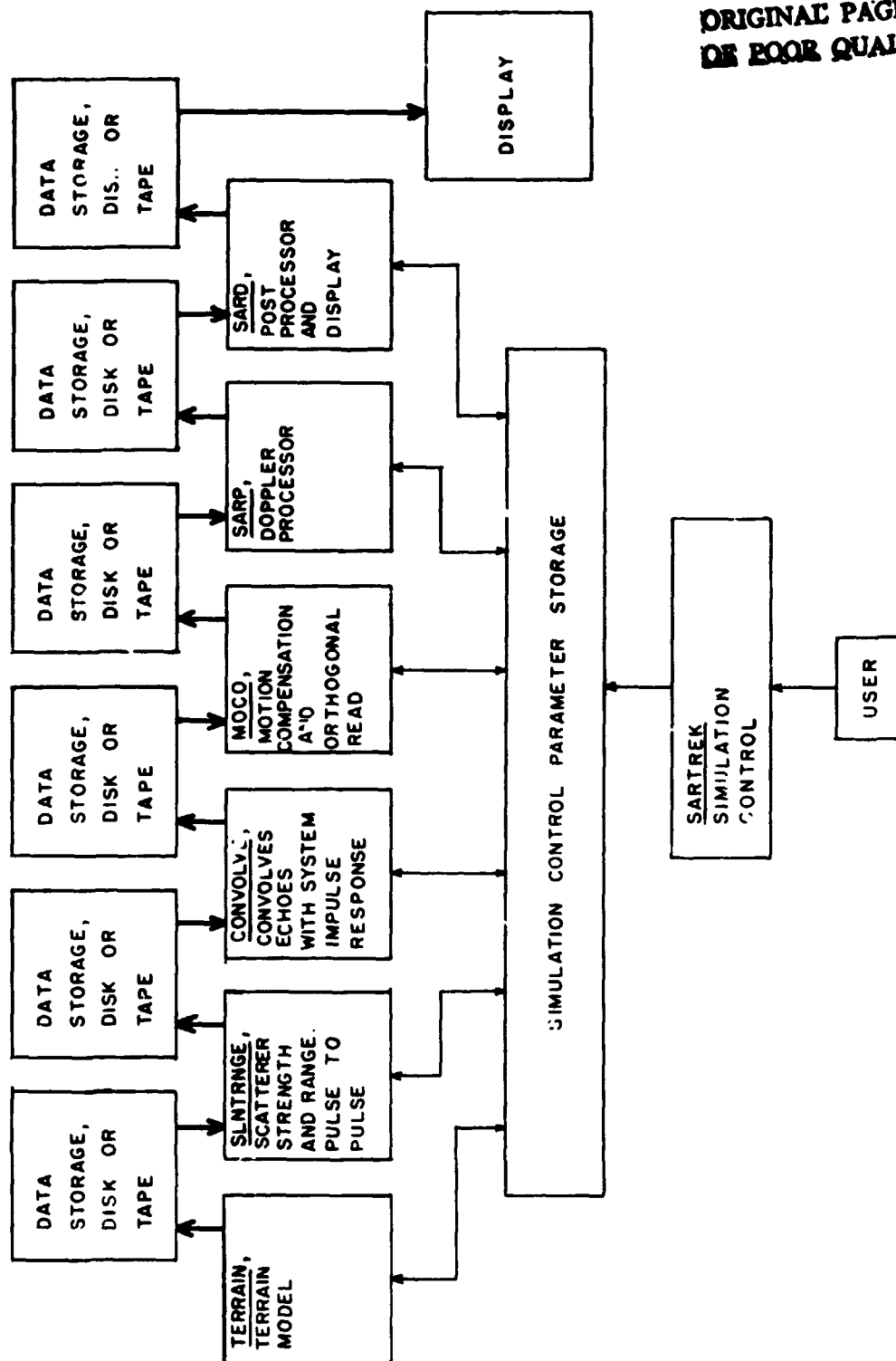
PROGRAM STRUCTURE FOR SAR SIMULATION

FIGURE 1

and its output is stored on tape or disk. The output of one program forms
the input to the next. This technique has two advantages. First, it re-
duces the amount of computer time one must use in a single block. Second,
it yields a considerable savings in computer time since the investigator can
change parameters in a given program and rerun the simulation without having
to rerun the program upstream from where the changes were made. For example,
the user can investigate the effect of changes in Doppler processor para-
meters (SARP) without rerunning the four programs which precede it. The
output of the program is a fully processed SAR map of the modeled terrain
displayed on a high resolution CRT.

3.0 SARTREK - THE SIMULATION CONTROLLER

Program SARTREK forms the communication link between the user and the simula-
tion and between the various programs within the simulation itself. SARTREK
performs four major functions; it reads the user specifications of the
simulation to be run, it computes the mapping start time for the conditions
specified; it computes the change in incident angle during the formation of
the SAR map and it computes the range of useable pulse repetition frequen-
cies (prf). Each of these functions will be discussed in turn.

Program SARTREK reads the specification of the simulation parameters su -
plied by the user. These specifications are listed below. The user speci-
fies certain parameters describing the planet about which the SAR is
orbiting. These parameters are;

1. Planet Name,
2. Planet Equatorial Radius,
3. Planet Eccentricity,
4. Planet Gravitational Constant,
5. Planet Rotational Rate and
6. Time of Prime Meridian Passage.

The planet name is used simply as an identifier for the set of data which
describes the planet. The equatorial radii, and the planet eccentricity
determine the shape of the planet. The length of the radius vector from
the center of the planet to a point on it's surface is a function of lati-
tude. The planet is assumed to be symmetric in longitude. By modeling the
planet in this manner one can investigate the degradation in a SAR map due

to assuming it to be a spherical planet. The planet gravitational constant
is necessary to define the satellite orbit. The planet rotational rate and
radius at the point being mapped are necessary ingredients in the computa-
tion of the distance between scatterers in the terrain and the antenna phase
center on a pulse-to-pulse basis. Unlike the aircraft case, the terrain
cannot be considered stationary in the orbital situation. Planet motion
influences the Doppler shift observed from the terrain and introduces range
gate positioning problems. The time of prime meridian passage is the time
at which the planet's prime meridian crosses a fixed reference point in
inertial space. For the earth this reference is the point at which the
vernal equinox occurs.

The user specifies the orbital parameters to be used. They are listed below;

    1. Orbit Identification,

    2. The Semi-Major axis of the orbit,

    3. The Orbit Eccentricity,

    4. The Inclination of the Orbit,

    5. The Argument of the Perigee,

    6. The Longitude of the Ascending Node and

    7. The Time of Perigee Passage.

Again the orbit identification is a serial number used to identify the set
of parameters with which it is associated. The semi-major axis of the orbit
ellipse determines the scale of the orbit. The orbit eccentricity deter-
mines the shape of the orbit. An eccentricity of 0 specifies a circular
orbit and an eccentricity of one specifies a parabola. Eccentricities bet-
ween zero and one yield an elleptical orbit. The inclination of the orbit
specifies the angle between the plane of the orbit and the equatorial plane
of the planet being orbited. The longitude of the ascending node specifies
the orientation of the orbital plane about the north-south axis of the
planet. The argument of the perigee specifies the orientation of the major
axis of the orbit ellip in the plane of the orbit. Lastly, the time of
perigee passage determines the location of the radar platform in the speci-
fied orbit at a given time.

The user specifies the parameters of the terrain model. These include;

1. The latitude of the terrain,

2. The number, cross section and location of discrete scatterers,

3. The number, size and location of each homogeneous fields and

4. The scatterer density and strength within each homogeneous field.

These parameters will be discussed in detail in the section which describes the terrain model.

The user also specifies the SAR radar and processor parameters. The parameters are listed below;

1. Radar configuration identification,

2. Radar wavelength,

3. Ground range sample interval,

4. Azimuth resolution,

5. Azimuth sampling interval,

6. Radar impulse response shape,

7. Doppler weighting functions,

8. Pulse repetition frequency and

9. Overlay ratio.

The radar configuration identifier is a serial number used to denote the set of parameters with which it is associated. Most of these parameters need no additional explanation. The user specifies the ground range sample interval desired. Once SARTREK has determined the mapping geometry it determines and reports to the user the slant range sample interval required to yield the desired results. The radar impulse response shape, which determines the system range resolution, is specified in terms of the slant range sample interval.

The user specifies the mapping geometry by indicating the desired nadir and squint angle and the swath width.

The radar platform is specified by the orientation of the platform body axis at the start of mapping and the platform roll, pitch and yaw rates.

The antenna is specified by the following;

1. Antenna identification,

2. Antenna gain pattern,

3. Location of the antenna phase center with respect to the platform body axis coordinate system, and

4. Orientation of the antenna coordinate system with respect to the platform body axis coordinate system.

Again, the antenna identification is just a number used to identify a particular set of antenna parameters. The antenna gain pattern is read as a table of values which specify antenna gain as a function of the boresight angle through which the energy passes to and from the antenna. By permitting the user to separate the phase center of the antenna and the center of mass of the platform, the simulation can be used to model the effects of improper stabilization of the radar platform on the image. Similarly, the orientation of the antenna coordinate system can be used to study the effects of antenna pointing errors.

Program SARTREK also computes the map start time and the length of the SAR array. The user has specified the platform orbit, the planet, the latitude at which the terrain to be mapped is located and the mapping geometry. The programs takes these parameters and computes those times in the satellite orbit for which the specified conditions are met. SARTREK produces the plot shown in Figure 2. This plot is used to provide the user with a general view of the results of his specifications. The ground track of two orbits are shown. In the figure shown the orbit is circular and inclined at 45° to the equator. The user has set the terrain at 45° north latitude, the nadir angle at 60° and the squint angle at 90° to the left of the velocity vector. The program begins plotting the ground track at start of the first mapping time. For the case illustrated the ground track starts just over northwestern Turkey. The program also draws a line from the ground track to the center of the map. For this case the line is perpendicular to the satellite ground track reflecting the 90° squint angle specified. Note that the program locates three other mapping locations which satisfy the requirements during the two orbits. The simulation uses the first one found.

Program SARTREK also computes and reports to the user the change in incident angle which occurred during the time of map formation. The program computes
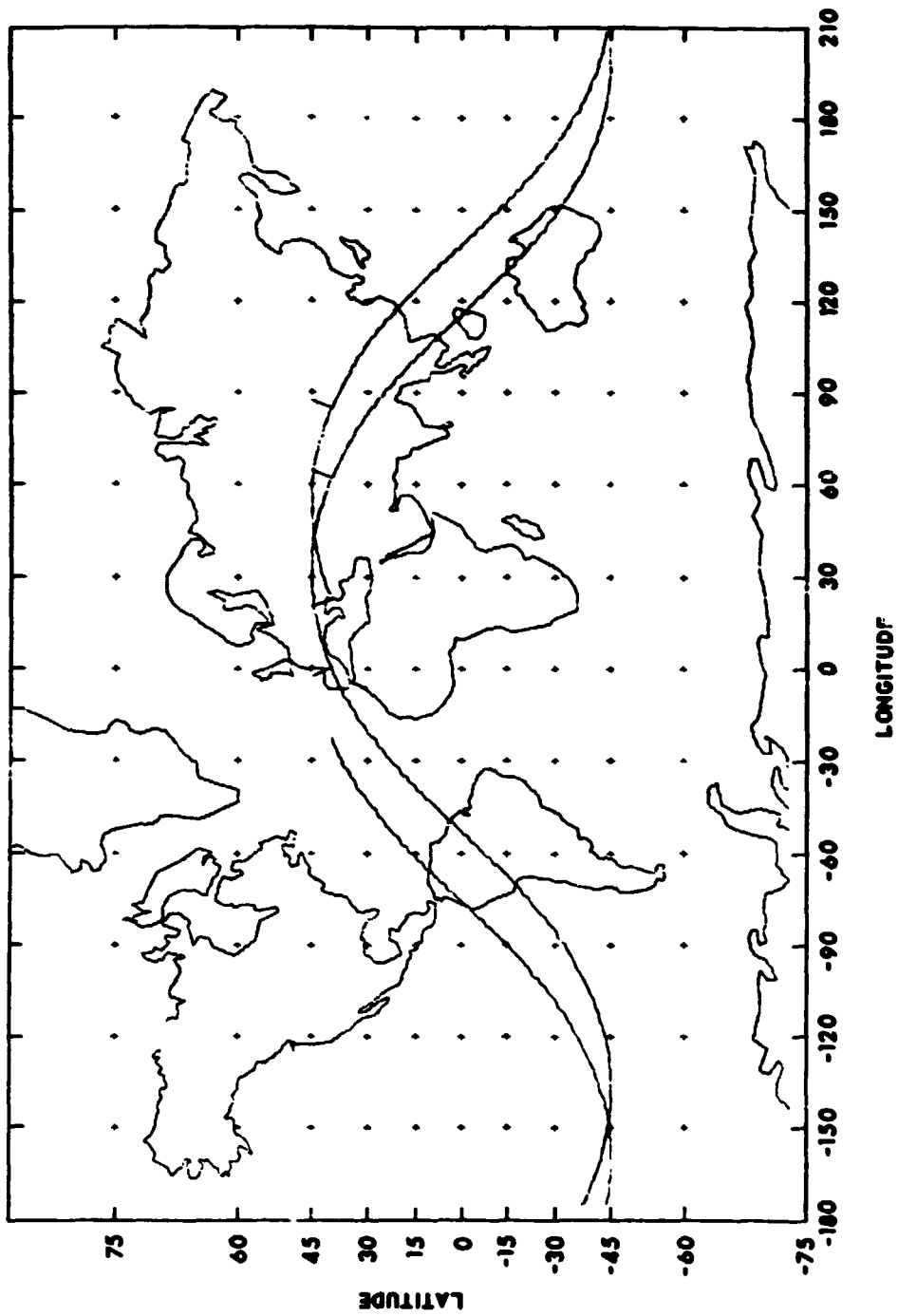
FIGURE 2
ORBIT No. 1

ECCENTRICITY = 0 INCLINATION = 45° TIME OF PERIGEE PASSAGE = 0
SEMI-MAJOR AXIS = 6678 km LONGITUDE OF ASCENDING NODE = -30°
ARGUMENT OF PERIGEE = 0 MAP START LATITUDE = 45°
NADIR ANGLE = 60° SQUINT ANGLE = -90°

the length of the array necessary to provide the desired resolution and from this and the geometry of the given mapping situation computes the change of incident angle during the map. This information is passed to the terrain simulation to be used there to change the reflectivity of the terrain if the change in incident angle is large enough to warrant such a change.

SARTREK also computes a suggested range of prf's to the user. These prf ranges are based on the following criteria. First, the prf must be high enough to permit at least two pulses per resolution cell. Second, the prf should be low enough to preclude range ambiguities within the range extent of the antenna main lobe footprint on the ground. Thirdly, the prf should be high enough to preclude azimuth ambiguities within the cross range extent of the antenna mainlobe footprint. Fourthly, the prf must preclude eclipsing, that is, the system must not emit a pulse during the time echoes are being received from the desired swath. Prf ranges which satisfy these requirements are reported to the user. However, the user is free to select whatever prf he desires.

4.0 TERRAIN - THE TERRAIN MODEL

Program TERRAIN produces a set of data which represent the terrain. In general terrain can be divided into two types of scatterers, discrete and extended. Discrete or point scatterers were usually relatively small objects, often man-made such as automobiles, buildings, etc., any object that is characterized by strong, specular, localized reflection. The extended or homogeneous scatterer is a larger target such as a forest or wheat field. The cross section of an extended target is fairly uniform within a given area. For many purposes the cross section of an extended target is specified as cross section per unit area. This leads to simulating such a target as a bounded area, the interior of which is set to some cross section per unit area. This representation is not sufficient for representing homogeneous targets in the SAR application. As a result of coherent processing, homogeneous areas of a SAR image can exhibit an effect known as coherent speckle. Coheren speckle appears in the SAR image as dark winding trails of various lengths. The origin of coherent speckle lies in the fact that backscatter from a "homogeneous" area is really due to reflection from many

scatter points within each resolution cell. For a coherent processor the received power from each cell depends on the complex sum of the echoes from the many discrete scatterers in each resolution cell. Thus two resolution cells containing the same number of identical scatterers would yield different received power due to differences in the spacing of the scatterers within the resolution cell. The degree to which coherent speckle affects the image is a function of the width of the mainlobe response with respect to spacing of the scatterers within the resolution cell, the sampling interval and the amount and type of incoherent integration. The presence of coherent speckle increases the variance in the measurement of cross section in a homogeneous field and thus increases the error in the estimate of cross section. Since one purpose of the simulation is to assess the effect of various SAR parameters on the system's ability to detect small differences in cross section of adjacent homogeneous areas, it is necessary that the simulation support the origin and propagation of coherent speckle. For this reason the terrain program models homogeneous areas as a collection of many point scatterers. The user specifies each homogeneous field as a rectangular area. The center and extent of the area is specified with respect to the center of the terrain. The user also specifies the strength of the scatterers and the number per resolution cell. Program TERRAIN then computes the required number of scatterers and places them at random within the extent of the field. The user may specify up to nine such homogeneous areas. Up to fifty discretes may also be specified. Note that the location of each scatter is specified with respect to the center of the terrain being modeled. Placement of the terrain on the planet surface is accomplished by the next program in the chain. This permits the terrain to be placed at any desired latitude without rerunning program TERRAIN. At the user's option TERRAIN produces a plot of the terrain for inspection. Such a plot, showing a single homogeneous field and four discrete scatterers is shown in Figure 3.

5.0 SLNTRNGE - THE SLANT RANGE COMPUTATION

The program SLNTRNGE has three functions. The first of these is to compute, for each pulse, the slant range between each scatterer in the terrain and the phase center of the antenna. Figure 4 indicates the geometry involved.
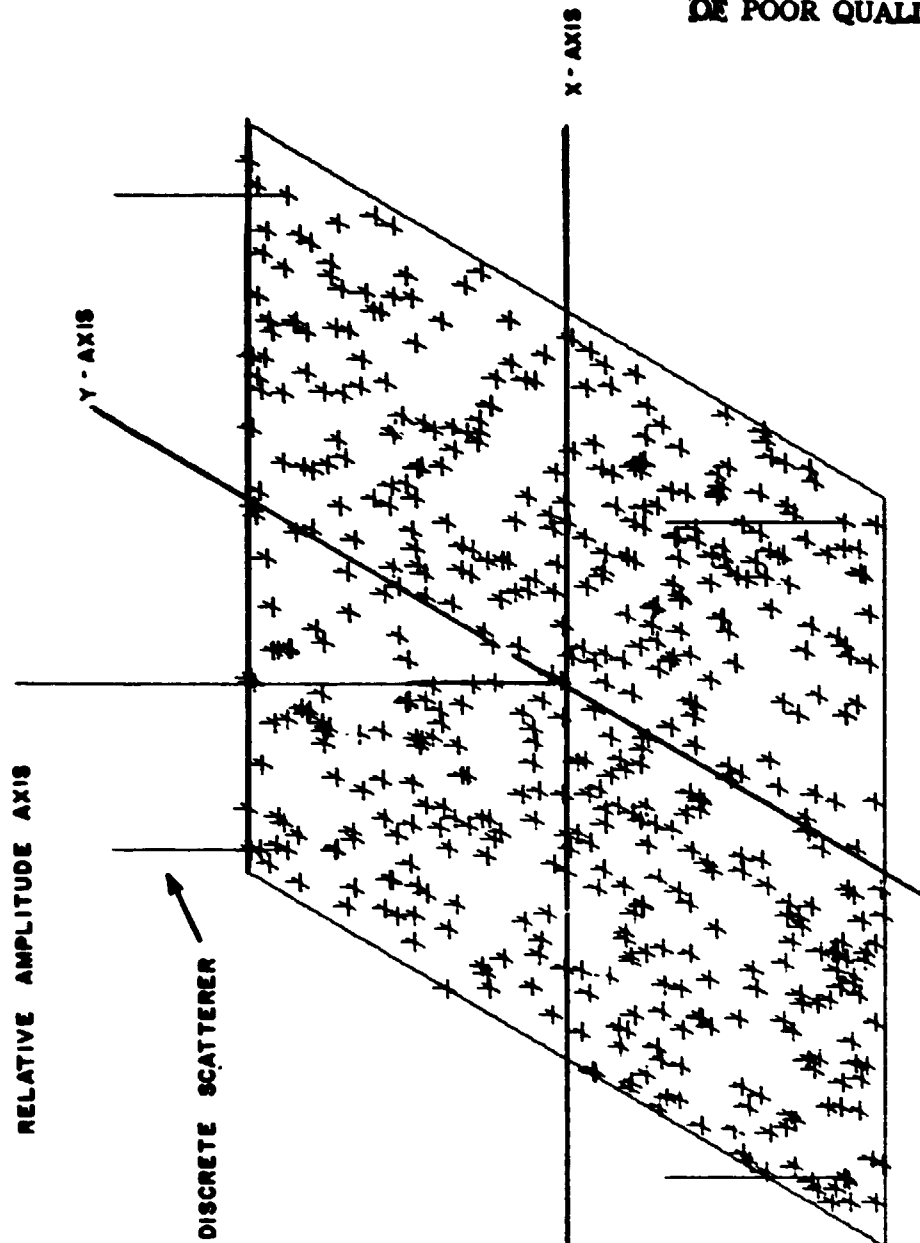
FIGURE 3

TERRAIN OUTPUT
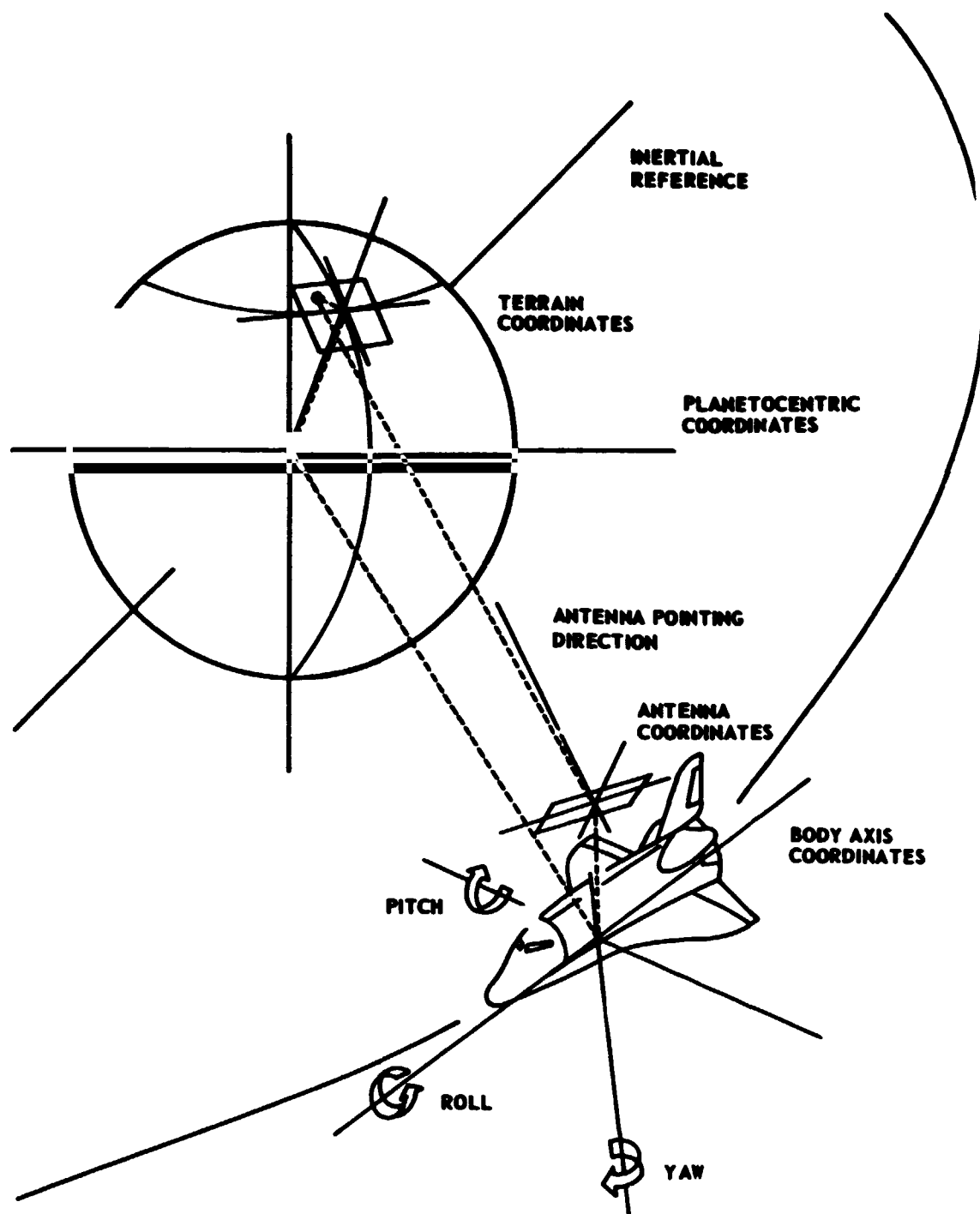
HOMOGENEOUS FIELD AND FOUR DISCRETE SCATTERERS

FIGURE 4
SLANT RANGE GEOMETRY

The location of each scatterer is known with respect to the terrain co-ordinate system. The location of the center of the terrain is known relative to the planet center since the user has specified the latitude of the terrain and SARTREK has computed the longitude at which it must be placed to be mapped from the given orbit and geometry. The latitude and longitude yield the direction of the vector from the planet center to the terrain center. The radius of the planet at the latitude indicated gives the length of the vector. The orbital parameters yield the vector from the planet center to the center of mass of the SAR platform. The vector from the platform mass center to the phase center of the antenna is dependent on the location of the antenna with respect to the mass center and the orientation of the platform body axis. The vector between the scatterer and the antenna phase center can be found once the other four vectors are known. This computation involves several coordinate transformations repeated for each scatterer and each pulse. Much attention has been given to making the code that accomplishes this as efficient as possible.

A other function of SLNTRNGE is to compute the angle between line-of-sight t each scatterer and the antenna boresight. The gain to be associated with this angle is looked up in the antenna gain pattern table. This gain is then applied to the scatterer strength. This also is a potentially time consuming task. Time has been saved in this area by computing the antenna angles subtended by the terrain patch for ea pulse and restricting the gain pattern search within these bounds.

The final function of SLNTRNGE is to reduce the echo strength in accordance with the space loss over the slant range.

The output of SLNTRNGE is a set of slant ranges and their associated echo strengths for each scatterer on each pulse. Note that for each pulse SLNTRNGE computes the range to all the scatterers. These ranges change on a pulse-to-pulse basis as the satellite moves. It is this range change with time that appears as a Doppler frequency in the SAR processor. Program SLNTRNGE will plot the range profiles for a given pulse at the user's option. Figure 5 shows two examples of these plots. The upper plot was produced from a terrain model which contained seven discrete targets. The lower plot was produced from a terrain model consisting of a single homogeneous
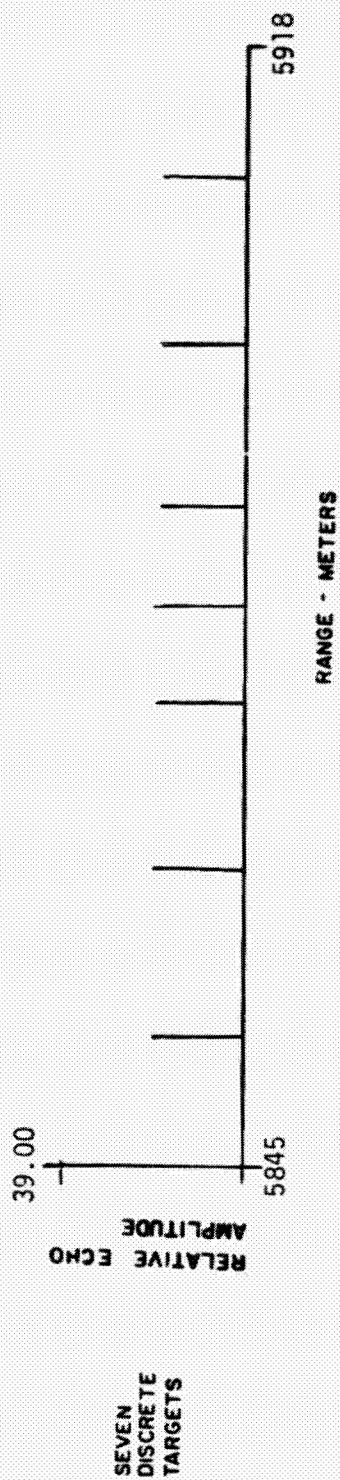
FIGURE 5

SLANT RANGE OUTPUT

SEVEN DISCRETE TARGETS

HOMOGENEOUS FIELD

field. The reduction is density of the scatterers at the near and far edge
of the terrain is caused by mapping the field from a diagonal aspect. Both
of these plots were produced by the airborne SAR simulation.

6.0 CONVOLVE - THE PRODUCTION OF THE IPQ VIDEO.

The objective of Program CONVOLVE is to compute the interaction between the
radar signal, the terrain and the radar receiver to produce the IPQ video
signal to be processed by the SAR processing portion of the simulation. The
overall simulation can be divided into two parts. The first part starts
with the terrain and progresses to the IPQ video (Programs TERRAIN, SLNTRNGE
and CONVOLVE). The second part begins with the IPQ video and moves back to
a representation of the terrain which is the SAR map (Programs MOCO, SARP
and SARD).

The antenna and radar are assumed to be linear networks. Under this assump-
tion the output of the radar receiver is the convolution of the received
signal and the radar impulse response,

$$H(x) = F(x) \ast G(x), \tag{1}$$

where

$F(x)$ is the input signal in the time domain,

$G(x)$ is the radar impulse response function,

$H(x)$ is the IPQ video and

$\ast$ is the convolution operator.

The input signal, $F(x)$, has been computed by SLNTRNGE and the radar impulse
response function has been specified by the user. The convolution can be
computed directly or by using Fourier transform theory. Recall that the
convolution of two functions is the transform of the product of their trans-
forms. Using bars to denote Fourier transforms,

$$\overline{H(x)} = \overline{F(x)} \cdot \overline{G(x)} \tag{2}$$

This formulation greatly speeds the convolution process. The convolution
must be computed once for each pulse. The impulse response function does
not vary with time so $\overline{G(x)}$ need only be computed once. Figure 6 shows the
result of this process. Diagram a shows the impulse response and diagram b
shows the output of SLNTRNGE. Diagrams c and d are the I and Q components
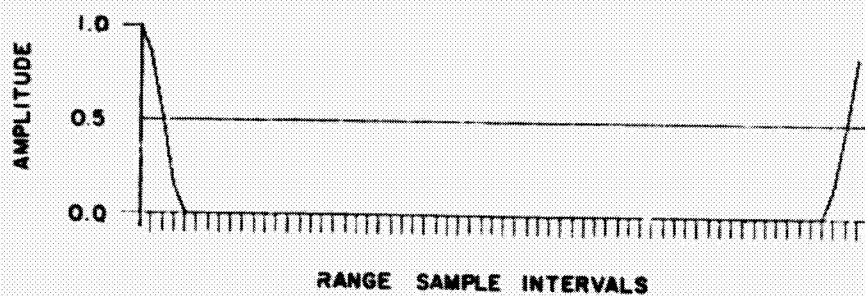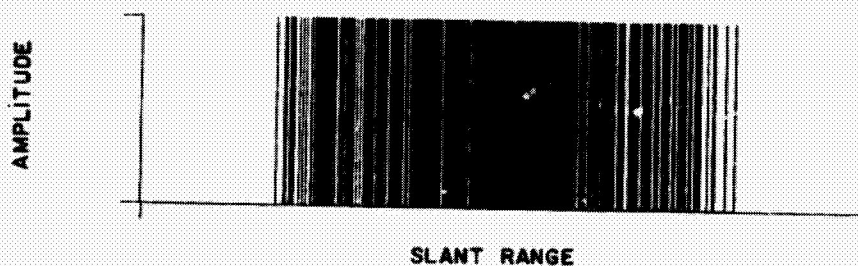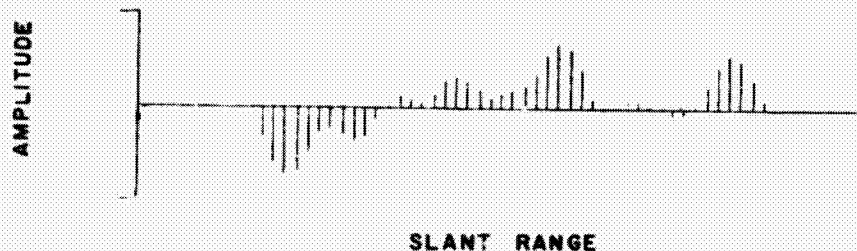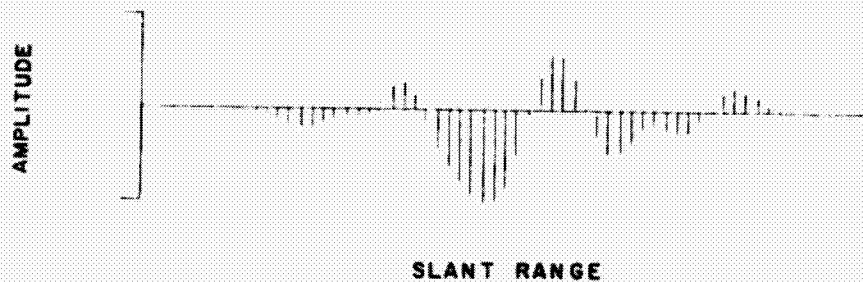
FIGURE ◦

PROGRAM CONVOLVE OUTPUT
THE MODELED TERRAIN CONSISTS
OF A HOMOGENEOUS FIELD

of the IPQ video obtained from the convolution.

7.0 MOCO - MOTION COMPENSATION

Program MOCO has two objectives. The first is to introduce the effects of motion compensation or focusing on the IPQ video waveform. The second objective is to accomplish the orthogonal read or "memory corner turning" necessary to further processing of the SAR signal. Focusing the synthetic array on a point in space is accomplished by adjusting the phase of the IPQ signal for each pulse so that the total time required for a signal to travel from the focus point to the phase center of the antenna is the same for all pulses. In the simulation the location of the scatterer with respect to the antenna phase center is known exactly. Thus perfect motion compensation or focusing is possible. In real systems this is .. + the case. Errors in the location of the antenna phase center with respect to the map center can be introduced into MOCO to study the effects of errors in motion compensation.

The second function of MOCO is the orthogonal reordering of the data. SAR data are accumulated on a pulse-to-pulse basis. Each pulse contains a sample at each range interval. The Doppler processor needs the data presented in range bin order. That is, the processor needs the time histories of each range bin.

8.0 SARP - THE SAR PROCESSOR

In one sense of the word, this portion of the SAR model is not a simulation at all. The digital Doppler processor in this simulation differ from an operational SAR processor mainly in the machine on which it is implemented. Program SARP is a basic Fourier transform processor. The IPQ video from MOCO is weighted by the function of the user choice. These data are then transformed range bin by range bin and resultant spectrum is passed to the next program in the simulation. If the user desires, program SARP will produce a perspective plot of the filter magnitudes for each range bin. Figure 7 shows such a plot for a terrain model consisting of seven discrete targets.

III-3-17

THE TERRAIN MODEL CONSISTS OF SEVEN DISCRETE TARGETS
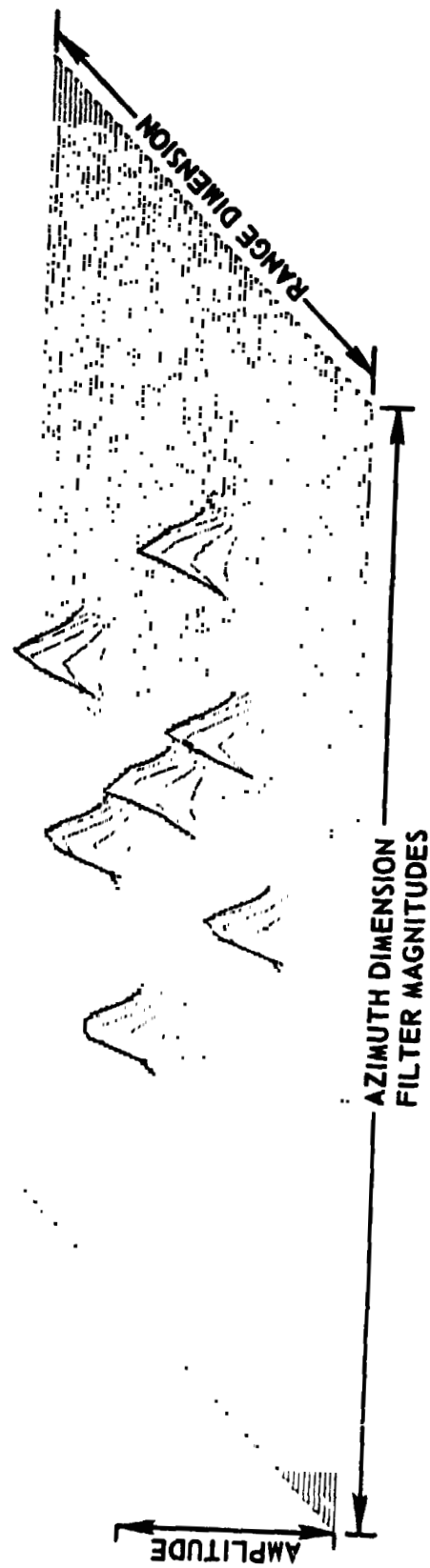
FIGURE 7
PERSPECTIVE VIEW OF FILTER BANK MAGNITUDES
THIS IS AN OPTION OUTPUT OF PROGRAM SARD

III-3-18

9.0 SARD - THE SAR DISPLAY

The purpose of program SARD is to display the filter magnitude data as the final SAR map. The program has three basic functions. The first is to overlay the filter magnitudes if the overlay option is selected by the user. If overlay is selected the corresponding filter magnitudes from the maps involved are averaged and the result becomes the filter magnitudes displayed. The purpose of this noncoherent integration is to reduce coherent speckle and the effect of sampling grid placement.

The second function is to convert the filter magnitudes to grey shade levels. The high resolution has 16 grey shades. The grey shade assignments involve mapping the filter magnitude values into grey shades in accordance with the user's specifications.

The final function of SARD is to communicate the grey shade data from the computer to the display memory where it is transferred to the CRT. Figure 8 shows photographs of various modeled terrains. These images were produced by the airborne SAR simulation. The radar was illuminating the terrain from a near diagonal aspect. Detail "a" shows the SAR image for a terrain model consisting of seven discrete scatterers arranged along the front and back sides of a square with one scatterer in the center. For these images the resolution cell was not square, this led to the deformation of the image that can be observed in the figure. Detail "b" is the image from a single, square homogeneous field. Detail "c" is the image for a homogeneous field with large discretes at each corner.

10.0 ACKNOWLEDGEMENTS

11.0 REFERENCES

1. Beckner, F. L. and G. L. Crow, Definition Of A Mathematical Model For An Orbiting Imaging Radar, Applied Research Laboratories Technical Report No. ARL-TR-77-6, 1977.

RANGE

AZIMUTH

DETAIL - C

HOMOGENEOUS FIELD AND
FOUR DISCRETE SCATTERERS

RANGE

AZIMUTH

DETAIL - B

HOMOGENEOUS FIELD

RANGE

AZIMUTH

DETAIL - A

SEVEN DISCRETE
TARGETS

FIGURE 8

IMAGES PRODUCED BY THE SAR SIMULATION

EFFECT OF PIXEL DIMENSIONS ON SAR PICTURE QUALITY

JOHN R. PIERCE
VIJAYA N. KORWAR
DEPARTMENT OF ELECTRICAL ENGINEERING
CALIFORNIA INSTITUTE OF TECHNOLOGY
PASADENA, CALIFORNIA 91125

SUMMARY

In an SAR mapping system, the pixel size for best picture quality is not
always known. Here we investigate whether it is worthwhile looking at small
pixels if it turns out after processing that such fine resolution was not
necessary and that several adjacent pixels therefore need to be combined.
The product of looks per pixel and number of pixels in the scene is kept
constant. Assuming that the returns from all the resolution cells obey
Rayleigh statistics, the expression for pixel SNR incorporating both speckle
and additive white Gaussian noise is derived. We conclude that it is pos-
sible to use fine resolution and leave the large-area estimate slightly but
not much worse than if the larger pixel size had been initially decided upon.

1.0 INTRODUCTION

Speckle reduction in SAR requires incoherent averaging over several inde-
pendent looks at each pixel. [1]. [2], [3]. If we can settle in advance on
the best pixel size, we should take the maximum allowable looks at pixels
of that size to get speckle reduction. But suppose we aren't sure what the
best pixel size is, which might happen in mapping unknown surfaces. Might
it not be better to design the system to take fewer looks at smaller pixels?
(We ignore additional processing requirements which would arise for digital,
though not for optical, proces*ors, but do consider that the system power
is fixed.) Suppose a large area G is divided into n = M/k resolvable sub-
areas (n, M, k integers) and k looks are taken at each sub-area and the
average of the k reflectivities is taken as the estimate of reflectivity for
that sub-area. If it is later decided that an estimate of the reflectivity
of area G is required, this can be obtained by averaging over the estimates
for the n sub-areas. In the following, we define pixel SNR in the presence
of speckle and additive white Gaussian noise as in [1] and derive the

expression for pixel SNR as a function of n. The return from each sub-area is assumed to obey Rayleigh statistics.

2.0 PIXEL SNR FOR k LOOKS AT n = M/k AREAS

Let A_1, A_2, $\cdots$ A_n be the mean power returns from the n sub-areas. Each component (in-phase (I) and quadrature (Q)) of the return amplitude from the jth look at the ith sub-area is (after Butman and Lipes [1]):

$$r_{Iij} = a_{Iij} + n_{Iij} \tag{1}$$

$$r_{Qij} = a_{Qij} + n_{Qij} \tag{2}$$

where the a's are the signal components and the n's are noise components, i.e. the n_{Iij} and n_{Qij} are statistically independent white Gaussian noise with variance $N_o/2$ and the a_{Iij}, a_{Qij} are statistically independent Gaussian random variables with zero mean and variance $A_i/2$.
The power return is

$$P_{ij} = r^2_{Iij} + r^2_{Qij} \tag{3}$$

which is exponentially distributed with mean $(A_i + N_o)$ and variance $(A_i + N_o)^2$, for each j from 1 to k.
The estimate of power return from the ith sub-area, after averaging over k looks is

$$p_i = \frac{1}{k} \sum_{j=1}^{k} p_{ij} \tag{4}$$

The variance of p_i, for independent looks is

$$N_i = \frac{1}{k} \cdot \left[A_i + N_o \right]^2 \tag{5}$$

In the absence of noise, the mean signal power in p_i is $\frac{1}{k}$ times the sum of the mean signal powers for the p_{ij}, i.e.

$$\bar{p_i}\Big]_{N_o = 0} \equiv S_i = \frac{k}{k} A_i = A_i \tag{6}$$

so that the pixel SNR which incorporates both noise and speckle is

$$SNR = \frac{\sqrt{k} \, A_i}{A_i + N_o} \tag{7}$$

This gives the pixel SNR that can be expected in the estimate of the power return or reflectivity of the ith sub-area (which has size G/n if all n

III-4-2

sub-areas are equal). But now suppose that an estimate of the reflectivity of the large resolution cell of size G is required, after having processed the data to give a resolution size of G/n. This can be obtained by averaging over the estimates for the n sub-areas.

In this case the estimate of power from the whole area is

$$p = \frac{1}{n} \sum_{i=1}^{n} p_i \tag{8}$$

where p_i is exponentially distributed with mean $(A_i + N_o)$ and variance $(A_i + N_o)^2/k$.

Now the pixel SNR becomes

$$SNR]_G = \frac{S}{\sqrt{N}} = \frac{\sqrt{k}\left[A_1 + \cdots + A_n\right]}{\sqrt{(A_1+N_o)^2 + \cdots + (A_n+N_o)^2}} \tag{9}$$

We assume now that there is available a total power MP which is incident on the n sub-areas in k looks. Thus, in one look, a total power $\frac{MP}{k}$ is incident on the whole area G and, if the n sub-areas are equal, $\frac{MP}{kn} = \frac{MP}{M} = P$ is incident on each sub-area G; let the mean return power in each look in this case be A. Thus, in the case where power P is incident on each of $n > 1$ sub-areas G/n, a total power nP is incident on the area G and the mean return must therefore be nA.

Therefore,

$$nA = A_1 + A_2 + \cdots + A_n \tag{10}$$

where $A_1, \cdots A_n$, as defined before, are the mean power returns from the n sub-areas.

Now consider two n-dimensional vectors

$$\underline{a} = ((A_1+N_o)(A_2+N_o) \cdots (A_n+N_o)) \quad \text{and} \tag{11}$$

$$\underline{b} = (\, 1 \quad\quad 1 \quad \cdots \quad 1 \,). \tag{12}$$

Then Schwartz's inequality

$$a \cdot b \leq |a||b| \tag{13}$$

gives

$$n(A+N_o) \leq \sqrt{n}\sqrt{(A_1+N_o)^2 + \cdots + (A_n+N_o)^2} \tag{14}$$

Let

$$n(A+N_o) = r\sqrt{n}\sqrt{(A_1+N_o)^2 + \cdots (A_n+N_o)^2} \tag{15}$$

where $r \leq 1$.

Then Eq. (9) becomes

$$SNR]_G = \sqrt{k} \cdot r \frac{\sqrt{n} \cdot A}{A + N_o} = r \frac{\sqrt{kn} A}{A + N_o} = r \frac{\sqrt{M} A}{A + N_o} \qquad (16)$$

where

$$r = \frac{\frac{1}{n} \sum_{i=1}^{n} (A_i + N_o)}{\sqrt{\frac{1}{n} \sum_{i=1}^{n} (A_i + N_o)^2}} \qquad (17)$$

3.0 SPECIAL CASES

(1) When $n = 1$, we get $r = 1$, and

$$SNR]_G = \frac{\sqrt{M} A}{A + N_o} \qquad (18)$$

so that taking M looks at the large area G and averaging gives the best estimate of the reflectivity of the large area G.

(2) If the area G has uniform reflectivity so that the A_i's are all equal, then the equality sign holds in Eq. (14) and again $r = 1$, irrespective of what n is.

If the A_i's are not equal, then $r < 1$ so that we sacrifice something in pixel SNR by not having decided on the coarser resolution.

(3) When $N_o = 0$, i.e., no noise is present,

$$SNR]_G = r\sqrt{M}; \qquad r = \frac{\sum_{i=1}^{n} A_i}{\sqrt{n} \sqrt{\sum_{i=1}^{n} A_i^2}} \qquad (19)$$

which is unaltered if all A_i's are multiplied by a common factor, so that the variation of $SNR]_G$ with n is independent of the power incident on area G.

4.0 CONSEQUENCES FOR VARIOUS DISTRIBUTIONS OF A_i FOR $N_o = 0$

(1) For the most extreme case where all but one of the A_i are zero:

$$r = \frac{1}{\sqrt{n}} \qquad (20)$$

When $n = M$, this gives $r = \frac{1}{\sqrt{M}}$, so that $SNR]_{G_{(n=M)}} = 1$ while if we had $n = 1$,

it would have been $SNR]_{G_{(n=1)}} = \sqrt{M}$, which is expected since we are getting only one non-zero return in all the M looks and thus effectively taking only one look at the whole area. On the other hand, if all the return comes from only one of the M sub-areas, that in itself would be of considerable interest.

(2) <u>Uniform distribution of the A_i's:</u> If we assume that most scenes of interest can be classified as having A_i that are independent and uniformly distributed between 0 and A_m, then we can get the expected value of r as a function of n.

$$r^2(n) = \frac{(\frac{1}{n} \sum_{i=1}^{n} A_i)^2}{\frac{1}{n^2} \sum_{i=1}^{n} A_i^2} \tag{21}$$

The numerator is a random variable with mean equal to $(\frac{A_m}{2})^2$ and a variance that becomes very small as $n \to \infty$ while the denominator is a random variable with mean $\frac{A_m^2}{3}$ and negligible variance as $n \to \infty$, so that

$$\lim_{n \to \infty} \overline{r(n)} = \frac{\sqrt{3}}{2} = 0.866 \tag{22}$$

For finite n, $\overline{r^2(n)}$ is given by

$$\overline{r^2(n)} = \int \frac{(\alpha_1 + \cdots \alpha_n)^2}{\alpha_1^2 + \cdots + \alpha_n^2} p_{A_i}(\alpha_i) \cdots p_{A_n}(\alpha_n) d\alpha_i \cdots d\alpha_n \tag{23}$$

(where $p_{A_i}(\alpha_i)$ = probability density function of A_i)which is difficult to evaluate explicitly for general n. However, for n = 2, this can be evaluated for the uniform A_i distribution case, and gives

$$r(2) = \sqrt{\frac{1 + \ln 2}{2}} = 0.92 \tag{24}$$

(3) <u>Exponential distribution of the A_i's:</u> If the A_i's are independent and exponentially distributed with a mean value of A_m, then for $n \to \infty$, we have the numerator of Eq. (21) tending to A_m^2 and the denominator to $2A_m^2$ so that

$$\lim_{n \to \infty} r(n) = \frac{1}{\sqrt{2}} = 0.707 \tag{25}$$

Since all these values of r calculated in Eqs. (22), (24), (25) are not significantly different from 1, we conclude that, for a realistic distribution of the A_i's, the pixel SNR does not get much worse if n is doubled or quadrupled. It might be worthwhile doubling n for the sake of improved small-area resolution, (especially if k, the number of looks at each small area, is large enough to compensate for speckle) while leaving the estimate of the large area G if later desired, almost as good.

5.0 CONCLUSIONS

If we are not sure what the best pixel size is, it seems to be better to design the system to take fewer looks each at smaller pixels. If the chosen (larger) pixel size is indeed correct, we will have sacrificed something in SNR. But if a smaller pixel size is better, we can at least get some (noisier) information about the smaller pixels, and we still have almost as good information about the larger pixels as if we had looked at the whole large pixels only.

6.0 REFERENCES

1. Butman, S. A. and Lipes, R. G., "The effect of noise and diversity on SAR imagery," Deep Space Network Progress Report 42-29, Jet Propulsion Laboratory, Pasadena, California, p. 46, July and August, 1975.

2. Goodman, J. W., "Some fundamental properties of speckle," JOSA, 66, pp. 1145-1150, Nov. 1976.

3. Porcello, L. J., et al, "Speckle reduction in SARs," JOSA, 66, pp. 1305-1311, Nov. 1976.

EFFECT OF AMBIGUITIES ON SAR PICTURE QUALITY

VIJAYA N. KORWAR
DEPARTMENT OF ELECTRICAL ENGINEERING
CALIFORNIA INSTITUTE OF TECHNOLOGY
PASADENA, CALIFORNIA 91125

RICHARD G. LIPES
JET PROPULSION LABORATORY
CALIFORNIA INSTITUTE OF TECHNOLOGY
4800 OAK GROVE DRIVE
PASADENA, CALIFORNIA 91103

SUMMARY

In this paper, we investigate and simulate the degradation of picture qual-
ity in a high-resolution, large-swath SAR mapping system caused by speckle,
additive white Gaussian noise and range and azimuthal ambiguities occurring
because of the non-finite antenna pattern produced by a square aperture
antenna. The effect of the azimuth antenna pattern was accounted for by
calculating the azimuth ambiguity function. Range ambiguities were ac-
counted for by adding, to each pixel of interest, appropriate pixels at a
range separation corresponding to one pulse repetition period, but attenu-
ated by the antenna pattern. A method of estimating the range defocussing
effect which arises from the azimuth matched filter being a function of
range is shown. The resulting simulated picture was compared with one de-
graded by speckle and noise but no ambiguities. It is concluded that azi-
muth ambiguities don't cause any noticeable degradation (for large time
bandwidth product systems, at least) but range ambiguities might. However,
this latter degradation can also be removed by picture enhancement if the
variation of terrain intensity as a function of range is not too great.

1.0 INTRODUCTION

Range and azimuth ambiguities caused by the antenna pattern not being finite
degrade the quality of pictures obtainable in an SAR mapping system. So do
speckle and white Gaussian noise added by the receiver. When fine azimuthal
resolution as well as large range swath are desired, range ambiguities be-
come serious. We consider the worst case where the swath is so large that
the time between successive pulses is just sufficient to accomodate the

return from the terrain between the 6 dB points of the antenna range pattern.
A square antenna aperture is assumed, so the two-way antenna amplitude pattern is a $(sinc)^2$ function for both range and azimuth. Thus, the first sidelobe is about 26 dB down below the main lobe and the response from pixels lying outside the mainlobe are considered negligible. The points halfway between the beam direction and the first zero of the $(sinc)^2$ function have an amplitude of $(\frac{2}{\pi})^2$ which is approximately 1/2, so the 6 dB beamwidth was, for simplicity, considered to be half the width between the first zeros on either side. A lunar picture of 256 (azimuth) x 512 (range) 8-bit pixels was taken and each pixel degraded as described below. Each pixel is assumed to correspond to a just-resolvable square cell. First, each pixel intensity was replaced by a pair of Gaussian random variables to account for speckle and additive white noise. The azimuth ambiguity was accounted for by calculating the azimuth ambiguity function and superposing it on the picture. Range ambiguities occur because of returns from previous and succeeding pulses not being sufficiently attenuated by the antenna pattern. These were suitably added. The process of generating random numbers and adding appropriate multiples of ambiguous pixels was repeated for 40 looks and the final picture compared with one having speckle and noise but no ambiguities. Range curvature and the effects of rotation of the terrain were neglected.

2.0 THE SIMULATION

2.1 SPECKLE AND NOISE

According to the model developed by Butman and Lipes [1], a given pixel is formed by envelope-detecting an in-phase and quadrature signal which are contaminated by receiver noise, so that each pixel is represented by I and Q components

$$V_I = a_I + n_I \tag{1}$$

$$V_Q = a_Q + n_Q \tag{2}$$

where a_I, a_Q = I and Q components of voltages in the pixel in the absence of noise and

$$n_I, n_Q = \text{noise voltages}$$

All four are statistically independent (S.I.) zero-mean Gaussian random variables (G rvs) with a_I,a_Q being identically distributed with variance = $\frac{1}{2}$ x pixel intensity and n_I,n_Q being identically distributed with variance = $\frac{1}{2}$ x noise power. The pixel power that is obtained after correlation is

$$P_i = \nu_I^2 + \nu_Q^2 \tag{3}$$

which is an estimate of the actual pixel power

$$s = a_I^2 + a_Q^2 \tag{4}$$

After M looks the estimate of pixel power is

$$p = \frac{1}{M}\sum_{i=1}^{M} P_i \tag{5}$$

2.2 AZIMUTH AMBIGUITIES

Let $\sigma(x)$ describe the complex reflectivity of the ground as a function of position x of the spacecraft at slant range r_o and let the wavelength be λ. Then the signal return obtained after heterodyning with the carrier is

$$O(x) = \int_{-\infty}^{\infty} \sigma(x') \ C(x-x') \ A(x-x')dx' \tag{6}$$

where

$$C(x) = e^{2\pi i \frac{x^2}{r_o \lambda}} \tag{7}$$

$A(x)$ = azimuth antenna pattern

$$= \{(\sin H(x))/H(x)\}^2 \tag{8}$$

and

$$H(x) = \frac{\pi D}{\lambda} \cdot \frac{x}{r_o} (1+x^2/r_o^2)^{-\frac{1}{2}}$$

where D = length (or width) of antenna aperture.

The output after matched filtering is

$$G(x) = \int_{-\infty}^{\infty} O(x+x'') \ C(x'') \ A(x''') \ dx''$$

$$= \int_{-\infty}^{\infty}\int_{-\infty}^{\infty} \sigma(x') \ C(x''+x-x') \ A(x''+x-x') \ C(x'') \ A(x'') \ dx'dx''$$

$$= \int_{-\infty}^{\infty} \sigma(x') \ \rho(x-x') \ dx' \tag{9}$$

where $\rho(\tau)$ is the correlation function of the $A(x)$ $C(x)$, i.e. of the azimuth chirp modulated by the two-way antenna pattern which is a $(\text{sinc})^2$ function. (This latter function is hereafter referred to as the chirp $(\text{sinc})^2$ function.)

The correlation function $\rho(x)$ can be calculated by two methods:

(a)   the method of stationary phase

(b)   computer simulation

For method (a) we consider $x/r_o \ll 1$ and prop. 2.19, p. 45 of [3] which gives the power spectrum of

$$f(x) = e^{-2\pi i x^2/r_o\lambda}\left(\frac{\sin(\frac{\pi Dx}{\lambda r_o})}{\frac{\pi Dx}{\lambda r_o}}\right)^2 = e^{-\frac{1}{2}ikx^2}\left(\frac{\sin \alpha x}{\alpha x}\right)^2 \tag{10}$$

as $|F(\omega)| \quad \frac{2\pi}{k} \ \frac{\sin \frac{\alpha\omega}{k}}{\frac{\alpha\omega}{k}}^4 \tag{11,}$

for the large time bandwidth product (TBP) case. The inverse of this is the correlation function of $f(x)$ which can be calculated in closed form and is

$$\rho(\tau) = \frac{2}{3}\frac{D^3}{8} - \tau^2\frac{D}{2} + \frac{\tau^3}{2} \qquad (0 \leq |\tau| \leq \frac{D}{2})$$

$$\frac{-\tau^3}{6} + \tau^2\frac{D}{2} - \frac{D^2}{2}\tau = \frac{D^3}{6} \qquad (\frac{D}{2} < |\tau| < D) \tag{.2}$$

and is shown in Fig. 2, after normalizing to $\rho(0) = 1$. Method (b), in which the function $f(x)$ was replaced by its main lobe only and sampled every $D/4$. In this case, the approximation $x \ll r_o$ was dropped (it is not really valid

for large swath). Computer calculation of $\rho(\tau)$ was done for TBP's of 256 and 200,000 and in each case the resulting plot is very close to Fig. 2 with $\rho(\tau)$ falling below 10^{-6} after $\tau = D$.

To allow for the possibility that the correlation function used will be a rect chirp instead of a $(\text{sinc})^2$ chirp, the cross-correlation function of these two was evaluated by methods (a) and (b). So was the auto-correlation function of the rect chirp. This latter is itself a sinc function with zero at $\tau = D/2$ as expected while the cross-correlation of the rect and sinc chirps is intermediate in shape between the auto-correlation functions of the rect chirp and $(\text{sinc})^2$ chirp. Remembering that the basic azimuth resolution cell is of width $D/2$, it seems that in no case do pixels beyond the first on either side of a pixel of interest contribute to the return for that pixel.

The fraction of the adjacent pixel which must be added to the pixel of interest is calculated as follows:
Consider the signal returns from the ground to be discretised with one return intensity accounting for each resolution cell. The I (or Q) component of a signal return is assumed to be

$$z_{ij} = y_{ij} + \alpha(y_{i+1,j} + y_{i-1,j}) \tag{13}$$

for the pixel in the ith azimuth and jth range; y_{ij} is the actual Gaussian random variable for this element and α is an appropriate weight. Similarly,

$$z_{i+1,j} = y_{i+1,j} + \alpha(y_{i+2,j} + y_{ij}) \tag{14}$$

Since all the y's with different subscripts are independent,

$$\overline{z_{ij} z_{i+1,j}} = \alpha(\overline{y_i^2}) + \alpha(\overline{y_{i+1}^2}) \simeq 2\alpha \overline{y_i^2} \tag{15}$$

where bars denote expected value and we assume the intensity of ijth and (i+1)j th pixel is approximately the same

$$\overline{z_i^2} = \alpha^2 \overline{y_i^2} + (\overline{y_{i+1}^2} + \overline{y_{i-1}^2}) \approx (\alpha^2 + 2) \overline{y_i^2} \tag{16}$$

This means the ratio of the correlation between adjacent elements in the picture to the power of the pixel itself is

$$R = \frac{2\alpha}{\alpha^2 + 2} \tag{17}$$

To evaluate σ using the correlation function $\rho(\tau)$ calculated before, we consider the correlated output for the continuous model of the ground (Eq.(9))

$$G(x) = \int_{-\infty}^{\infty} \sigma(x') \, \rho(x - x') dx' \tag{9}$$

We have for the correlation function of $G(x)$,

$$R(x - y) = \overline{G(x) \, G*(y)}$$

$$= \iint_{-\infty}^{\infty} \overline{\sigma(x')\sigma*(y')} \, \rho(x-x') \, \rho*(y-y') \, dx'dy' \tag{18}$$

$$\approx \int_{-\infty}^{\infty} dx' \overline{|\sigma(x')|^2} \, \rho(x-x') \, \rho*(y-x')$$

because $\sigma(x')$ and $\sigma(y')$ are S.I., so that

$$\overline{\sigma(x') \, \sigma*(y')} = |\sigma(x')|^2 \, \delta(x'-y') \tag{19}$$

Now $\rho(x-x')$ and $\rho*(y-x')$ have a very short extent so that unless x and y are close, the integral in (18) is zero. If x and y are close, the integral over x' is nonzero only over a short distance so that $\overline{|\sigma(x')|^2}$ is approximately constant $= \sigma^2$.

$$\therefore \ R(x - y) \approx \sigma^2 \int_{-\infty}^{\infty} dx' \, \rho(x-x') \, \rho*(y-x')$$

$$= \sigma^2 \int_{-\infty}^{\infty} dz \, \rho(\tau) \, \rho*(z+x-y) \tag{20}$$

$$= \sigma^2 \, a(x-y)$$

where $a(\tau)$ is the autocorrelation function of $\rho(\tau)$.

Now if a pixel extends from $-D/4$ to $D/4$, its adjacent one extends from $D/4$ to $3D/4$, so it is centered at $D/2$. Thus, if $x-y = D/2$, $\frac{R(D/2)}{R(0)}$ represents the same ratio as R in Eq. (17).

$$\frac{R(D/2)}{R(0)} = \frac{\sigma^2 a(D/2)}{\sigma^2 a(0)} = \frac{a(D/2)}{a(0)} \tag{21}$$

From Eqs. (17) and (21),

$$\frac{a(D/2)}{a(0)} = \frac{2\alpha}{\alpha^2 + 2} \qquad (22)$$

$\frac{a(D/2)}{a(0)}$ can be evaluated for the chirp $(\text{sinc})^2$ by finding the correlation function of Fig. 2 and is equal to 0.493.

$$\therefore \quad 0.493 = \frac{2\alpha}{\alpha^2 + 2} \qquad (23)$$

$$\text{or} \quad \alpha = 0.268 \qquad (24)$$

for the chirp $(\text{sinc})^2$ function. This is the required weight factor for adjacent pixels in azimuth. The weight factor required if a rect chirp were used in the matched filtering can be similarly calculated but was smaller than 0.268. So in the simulation the worst-case of $\alpha = 0.268$ was used.

2.2 RANGE AMBIGUITIES AND RANGE DEFOCUSSING

No chirp or coding was assumed for the range direction, so adjacent range bins don't contribute to the ambiguity as in the azimuth case. However, there is a more serious effect in this case, because one pulse on either side of the pulse of interest (corresponding to a range bin of interest) is quite intense because it lies in the mainlobe of the antenna range pattern, though outside the central half. Since only the mainlobe is considered, this means that for each range bin there is exactly one range bin that contributes an ambiguity as shown in Fig. 1. The central 256 bins form the desired swath while the ambiguous range bin corresponding to the ith bin is the one at $(i + 256) \mod (512)$. Thus R1' is the ambiguous bin corresponding to R1, and R2' corresponds to R2. We say this kind of ambiguity is more serious than the azimuth type (or the type that would additionally be present in range if range coding or range chirp were used) because while adjacent pixel powers don't vary much, those separated by 256 range bins do.

There is, however, a mitigating effect: each pixel is affected by not just one, but several pixels in the ambiguous range bin. This is because the _azimuthal_ ambiguity function is a function of range that extends over several elements at the ambiguous range bin. If it _did not_ do so, each pixel in the ith range bin would have just the pixel in its azimuthal line in the $(i + 256) \mod (512)$ range bin adding to it and the variation with azimuth of the pixel intensity in the latter range bin would cause widely

varying numbers to be added to the pixel in the ith range bin. The mitigating effect can be calculated as follows (in this calculation, the $(\text{sinc})^2$ modulation in azimuth was neglected). The return from the ambiguous range bin at range r_1 is of the form $e^{-2\pi i\, x^2/r_1\lambda}$ while the azimuth matched filter for the desired range bin at range r_o is $e^{-2\pi i\, x^2/r_o\lambda}$. The magnitude of the cross-correlation function

$$r(\tau) = \left| e^{-2\pi i\, x^2/r_1\lambda} \;*\; e^{-2\pi i\, x^2/r_o\lambda} \right| \tag{25}$$

was evaluated by computer and found to be fairly constant over its extent, though the phase varies rapidly. This rapid phase variation allows another simplification to be made in the simulation: to be accurate, the I and Q random variables for the various elements in the ambiguous range bin weighted by the corresponding components of the cross-correlation function should have been added to the I and Q components of the desired pixel. But this is time-consuming. However, because of the rapid phase variation of $r(\tau)$, this entire process of weighting and summing was replaced by generating just two random variables with zero mean and with variance equal to the sum of the powers of all pixels in a range bin contributing to the ambiguity for a given pixel. That is, if $y_{ik\,I}$ and $y_{ik\,Q}$ are the I and Q components of a pixel of interest, the range ambiguity was represented by adding two S.I. zero mean Gaussian random variables each of variance $\tfrac{1}{2}\,T_{i'k}$

$$\tfrac{1}{2}\,T_{i'k} = \tfrac{1}{2}\,a_{i'}\Sigma_k\,c_k\,P_{i'k} \tag{26}$$

where c_k = squared magnitude of cross-correlation coefficients (i.e., samples of $r^2(\tau)$)

$P_{i'k}$ = powers of pixels in the ambiguous (i'th) range bin contributing to range ambiguity for P_{ik}

and $a_{i'}$ = the attenuation due to the antenna range pattern at the i'th range.

The further approximation made is that the c_k are all equal, which is what the computer calculation of $r(\tau)$ indicates. These simplifications seem justifiable because the resulting pictures seem insensitive to just how many pixels $r(\tau)$ extends over, as long as the area under the $r^2(\tau)$ is kept the same. In the simulated pictures attached (Fig. 3), set III corresponds to the case where $r(\tau)$ extends over 15 elements and set II to that where $r(\tau)$

extends over 7 elements, but otherwise similar. In addition computer print-outs for one range bin were obtained for $r(\tau)$ spread over 25 and 51 elements and were all seen to be very close.

Another result that is obtained from the computer calculation of $r(\tau)$ is that the area under $r^2(\tau)$ is the same as that under the autocorrelation function of the chirp rect, which is normalized to 1. This is to be expected since correlating $e^{-2\pi i x^2/r_o \lambda}$ with $e^{-2\pi i x^2/r_1 \lambda}$ merely spreads the energy of return over several pixels in the ambiguous range instead of focussing it into one pixel as it does if $r_1 = r_o$. Thus, all that needs to be calculated if a quick estimation of $T_{i'k}$ is required without a computer is to find the number n of elements $r(\tau)$ spreads over; then c_k is $1/n$. A quick estimate can be obtained as follows:

Let v = velocity of spacecraft = $\dfrac{x}{t}$

$\quad$ T = time for which the rectangular chirp lasts = $\dfrac{L}{v}$ $\qquad$ (27)

$\quad$ where L = synthetic aperture length = $\dfrac{\lambda r_o}{D}$

Let $k_o = \dfrac{2\pi v^2}{r_o \lambda}$, $\quad k_1 = \dfrac{2\pi v^2}{r_1 \lambda}$, $\qquad$ (28)

$$\therefore \ r(\tau) = e^{-ik_o t^2} * e^{-ik_1 t^2}$$

$$= \int_{-T/2}^{T/2 - |\tau|} e^{ik_o(t+\tau)^2} \, e^{-ik_1 t^2} \, dt$$

$$= e^{ik_o \tau^2} \int_{-T/2}^{T/2 - |\tau|} e^{i(k_o - k_1)t^2} \, e^{i2k_o t\tau} dt \qquad (29)$$

which can be reduced to give

$$|r(\tau)|^2 = fc^2 + fs^2 \qquad (30)$$

where
$$fc = \frac{1}{\alpha} \int_{\alpha\left[-T/2 + k_o \tau/(k_o - k_1)\right]}^{\alpha\left[T/2 + k_o \tau/(k_o - k_1)\right]} \cos\left(\frac{\pi x^2}{2}\right) dx \qquad (31)$$

$$fs = \frac{1}{\alpha} \int_{\alpha\left[-T/2 + k_o \tau/(k_o - k_1)\right]}^{\alpha\left[T/2 + k_o \tau/(k_o - k_1)\right]} \sin\left(\frac{\pi x^2}{2}\right) dx \qquad (32)$$

$$\alpha = \sqrt{\frac{4v^2}{\lambda} \left(\frac{1}{r_o} - \frac{1}{r_1}\right)} \tag{33}$$

It can be seen from tables of Fresnel integrals, that fc^2 and fs^2 are almost constant until both upper and lower limits of integration are $>$ about 4. and then fc^2 and fs^2 start falling.

Thus, $|r(\tau)|^2$ is negligible when

$$\alpha \left(\tau \frac{k_o}{k_o - k_1} - \frac{T}{4}\right) \simeq 4 \tag{34}$$

noting

$$\frac{k_o}{k_o - k_1} = \frac{\frac{1}{r_o}}{\frac{1}{r_o} - \frac{1}{r_1}} \simeq \frac{r_o}{\Delta r} \tag{35}$$

and the time bandwidth product

$$TBP = \frac{L}{D/2} = \frac{vT}{v\tau_o} = \frac{T}{\tau_o} \tag{36}$$

where $\qquad \tau_o = D/2v = $ time between successive pulses $\tag{37}$

we get for the number of elements (of length $D/2$) on each side that $r(\tau)$ extends over,

$$\frac{\tau}{\tau_o} = \frac{\Delta r}{r_o} \cdot \frac{T}{2} \cdot \frac{1}{\tau_o} + \frac{4}{\alpha} \cdot \frac{\Delta r}{r} \cdot \frac{1}{\tau_o}$$

$$= \frac{\Delta r}{r_o} \left[\frac{TBP}{2}\right] + \sqrt{\frac{8}{TBP}} \; \sqrt{\frac{\Delta r}{r_o}} \tag{38}$$

For large TBP only the first term on the right of Eq. (38) needs to be retained. For the simulation, TBP = 256 and we get $\tau/\tau_o = 6$ so that $r(\tau)$ extends over 1. elements on either side of a central one or n = 12 + 1 = 13 elements in all. The computer calculation of $r(\tau)$ gives n = 15.

2.3 OBTAINING THE PICTURES

The simulation was performed by

(i) generating two zero-mean S.I. G rvs for each of the 256 x 256 pixels of interest, with variances equal to ½ the pixel intensity x the range antenna function for the pixel;

(ii) generating two S.I. zero mean G rvs with correct variance

corresponding to range ambiguity, Eq. (26) and adding to the values in (i) above;

(iii) adding the I and Q G rvs respectively of one adjacent pixel on each side with $\alpha = 0.268$ for the azimuth ambiguity, Eq. (24); at this stage the G rvs correspond to a_I and a_Q in Eqs. (1), (2);

(iv) generating two G rvs corresponding to n_I and n_Q, with variance $N_o = 10$ on a 0 - 255 intensity scale (this value of N_o was chosen by finding the mean picture intensity to be 50 and requiring an SNR of 5); we now have v_I and v_Q of Eqs. (1) and (2);

(v) squaring and adding v_I and v_Q to get p_i (Eq. (3));

(vi) repeating (i) to (v) 40 times and averaging p_i to get p of Eq. (5).

Additive white noise N_o merely translates the distribution curve of pixel intensities in the original picture by an amount equal to the noise power, provided the noise is not so large that the variance it introduces into v_I and v_Q is not averaged out by the number of looks taken. By subtracting that value of pixel power in the output below which lie less than 5% of the pixels(in the output picture so far obtained), the noise is effectively removed. In addition, the contrast of the picture was increased by 'stretching' the range of intensities occupied by the picture (both the original and the simulated ones) to extend over as much of the 0 - 255 range as possible.

3.0 PROCESSING AND RESULTS

See Fig. 3. Pictures (a) and (b) are the 256 x 512 original and the 256 x 256 original. The other 9 pictures are divided into sets of 3, each set being in one horizontal line. The topmost, set I, was obtained without azimuth or range ambiguities being added, but the antenna range pattern is superposed on the picture; speckle and noise are present in the picture; i.e., it was obtained as in 2.3 but with $\alpha = 0$ and $T_{i,j} = 0$ in Eq. (26). Sets II and III do have azimuth and range ambiguities as well as speckle and noise; the only difference is that Set II had the range ambiguity spread over 7 elements (n = 7) while set III had n = 15. There is no visible difference between the corresponding pictures of these two sets.

In each set, the left most picture, i.e. (c), (f), (i), was obtained as

described above; the second and third pictures of each set have additional enhancement techniques applied. We notice that all 9 pictures are worse than the original because of speckle, but that major features are still recognizable in the central portions of all of them. However, the upper and lower edges, corresponding to the ends of the range swath, in (c), (f), (i) show the effect of the antenna range pattern attenuation and it is very difficult to distinguish craters and so on in these regions. However, (f) and (i) are almost as good as (a) in recognizability of features showing that ambiguities don't make much difference to the picture quality if further enhancement is not used, because the edges, where range ambiguities are most important, are attenuated in all three sets.

The second picture of each set, i.e. (d), (g), (j), was obtained by dividing each pixel power after 40 looks by the approximate antenna range pattern attenuation, and then subtracting white noise and 'stretching.' In all three cases, the edges now appear too bright--this is because the range ambiguity plus white noise at the edges are now enhanced and distinguishing features at the edges is just as difficult as in (c), (f), and (i).

The third picture of set I, i.e. (e), was obtained by first subtracting the white noise, i.e. 10 on a 0 - 255 scale, from each pixel power after 40 looks and then dividing by the antenna range attenuation function. Then the picture was 'stretched.' Now it is possible to see more features at the edges than before.

In the third pictures of sets II and III, i.e. (h) and (k), the white noise of 10 plus an estimate of range ambiguity was subtracted from each pixel and then this was divided by the antenna range attenuation factor and stretched. The estimate of range ambiguity used was equal to the average picture intensity (= 50) times the antenna pattern attenuation at the ambiguous range bin. In all these pictures, i.e. (e), (h) and (k), the edges are now not too bright or dim and, in addition, (h) and (k) are almost indistinguishable from (e).

4.0 CONCLUSIONS

(i) The effect of azimuth ambiguities seems to be negligible in the pictures since the central areas, where range ambiguities are not important,

are not noticeably different in sets I, II and III. This is expected
from the fact that only adjacent pixels contribute to the ambiguity.
(ii) The effect of range ambiguities, for the particular picture used here,
is more or less removable by enhancement techniques, because the intensity
of the ambiguous ranges is not too different from the mean picture intensity.
But this could easily not be the case and then, since the correct estimate
of ambiguity is not available, the enhancement won't improve quality very
·uch.
('ii) Speckle is the major source of picture degradation, as can be seen
fr·· ·he fact that the pictures with speckle and no ambiguities are
noticeably worse than the original, while the pictures with ambiguities
and speckle are not too different from those without ambiguities but with
speckle.

5.0 OTHER POSSIBILITIES
One way to bring the mean intensity of pixels contributing to range
ambiguities nearer to the mean picture level is by spreading the energy in
the ambiguous return over more elements. (Then the enhancement technique
described can be used to remove the ambiguities.) This can be done by
using equal chirps of opposite sign on alternate pulses so that they don't
correlate. Another way, suggested by Dr. J. R. Pierce, is to use opposite
directions of circular polarization on alternate pulses. This method,
in fact, even reduces the total energy from ambiguous returns, as long as
the ground reflects the signal back more or less circularly polarized.

6.0 ACKNOWLEDGEMENTS
The authors are grateful to Dr. J. R. Pierce for his suggestion.

7.0 REFERENCES
1. Butman, S. A. and Lipes, R. G., "The effect of noise and diversity on
        SAR imagery," Deep Space Network Progress Report 42-29, Jet
        Propulsion Laboratory, Pasadena, California, July and Aug. 1975,
        p. 46.

2. Harger, R. O., Synthetic Aperture Radar Systems: theory and design,
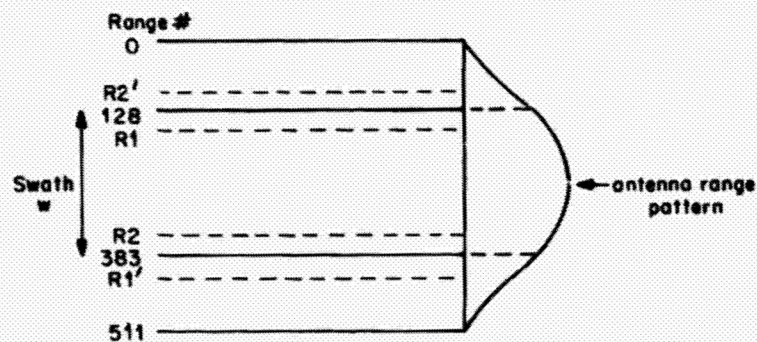   Academic Press, 1970.
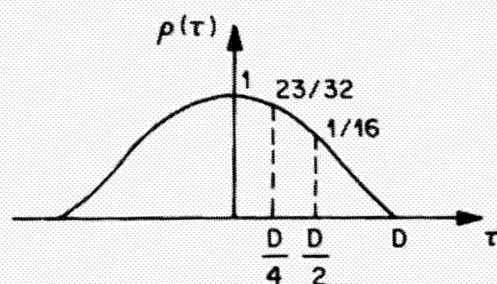
FIG. I ILLUSTRATING RANGE AMBIGUITIES

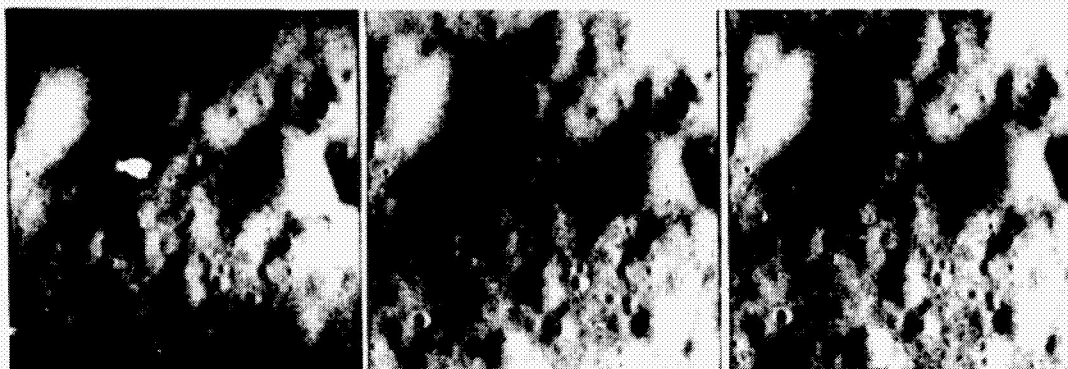FIG. 2 CORRELATION FUNCTION FOR CHIRP $(S...C)^2$ FUNCTION

(a)

(b)

FIG. 3 (a) AND (b): ORIGINAL
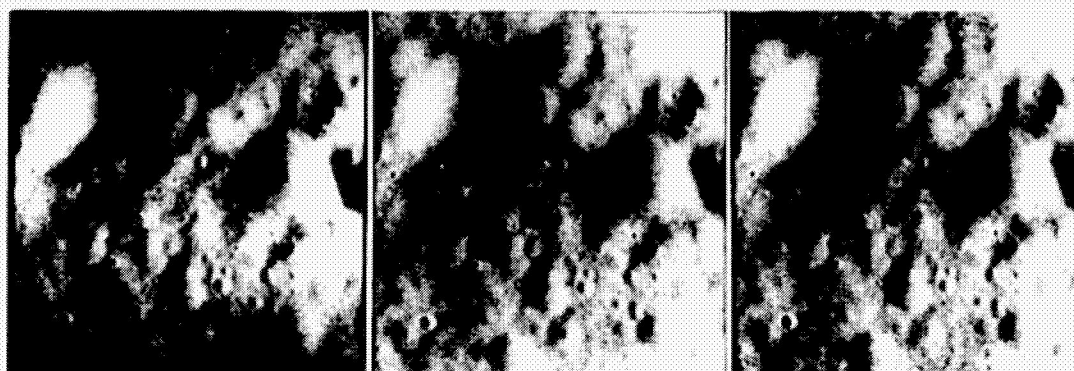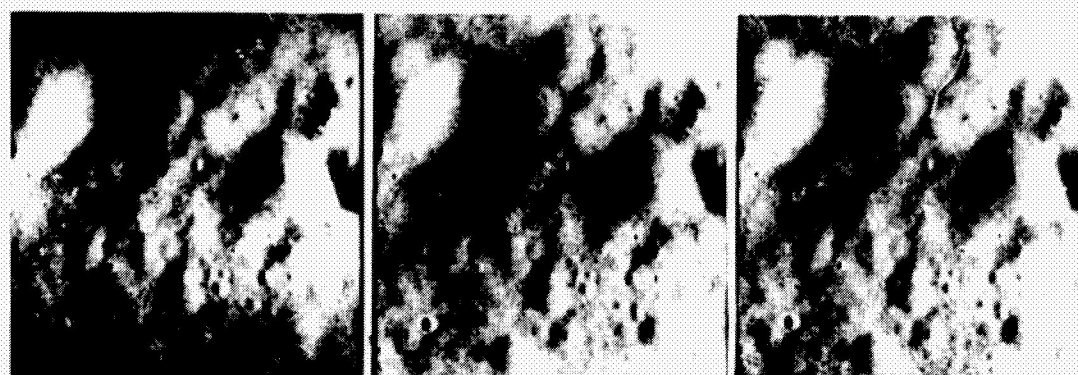PICTURES OF A LUNAR SCENE.

FIG 3 (c) THROUGH (k): SIMULATED PICTURES OF THE SAME SCENE.

SYNTHETIC APERTURE RADAR OPERATOR TACTICAL TARGET ACQUISITION RESEARCH

MICHAEL L. HERSHBERGER AND DAVID W. CRAIG
HUGHES AIRCRAFT COMPANY
CULVER CITY, CALIFORNIA 90230

SUMMARY

A radar target acquisition research study was conducted to access the effects of two levels of 13 radar sensor, display, and mission parameters on operator tactical target acquisition. A saturated fractional-factorial screening design was employed to examine these parameters. Data analysis computed ETA^2 values for main and second-order effects for the variables tested. Ranking of the research parameters in terms of importance to system design revealed four variables (radar coverage, radar resolution/multiple looks, display resolution, and display size) accounted for 50 percent of the target acquisition probability variance.

1.0 INTRODUCTION

Synthetic aperture radar (SAR) operator performance research was begun in the mid-1960's and has continued at a modest level to the present time. Most of this research has been directed towards defining SAR sensor characteristics for locating large, location known, fixed targets. Only recently have SAR sensors systems appeared suitable for operators to locate and designate small tactical targets. There have been several limited initial investigations of SAR operator performance for detection/recognition of small targets [1, 2, 3, 4, 5, 6].

The objective of this research study was to identify the important radar, display, and mission variables in a quick response tactical target acquisition mission. The results of the study would identify variables which have a major affect on operator/system performance and which variables are unimportant. This information would allow designers and mission planners to make better design decisions.

2.0 METHOD

To achieve the research objective, a number of variables must be varied and controlled. Recent work by Simon [7] has resulted in the development of economical multifactor behavioral research designs. The economy is based on the fact that there are very few meaningful interactions beyond the second order in behavioral research. Simon recommends a general behavioral research strategy that proceeds from a large multi-factor screening study to research in which functional relationships are described using central-composite designs and finally to performance prediction using system simulation. The first step of this research strategy was adopted for the present study.

The quick response mission scenario provided the foundation for the ing study in which two levels of 13 parameters were investigated. The study parameters are summarized in Table 1.

2.1 RADAR IMAGERY, TEST EQUIPMENT, REFERENCE MATERIAL AND OPERATORS

High resolution UPD-4 synthetic aperture radar imagery recorded during military maneuvers in West Germany was used. The raw radar signal film was reprocessed to provide the two levels of radar resolution required in the study.

The imagery was screened for selection of 32 simple and complex background scenes in which radar tactical targets were embedded. The composite target scenes were mounted in glass slides and projected with a 12.7 cm optical projector onto a back-projection screen. The focus and projected image size on the screen was adjusted to produce the required levels of display resolution and display size.

Army Map Service (AMS) 1:50,000 topographic charts and mission/target descriptor information on 12.7- by 17.8-cm index cards served as briefing and reference materials. Operator/subjects used the charts during target briefing, and the charts were available during each test trial.

Tactical Air Command F-111 Weapon Systems Officers (WSOs) from Nellis Air Force Base served as radar operators in the study. Eight WSOs were selected from an initial sample of 60.

TABLE 1
STUDY PARAMETERS AND LEVELS

Parameter	Low Level	High Level
Radar Resolution/ Looks	12.2 meters/4 looks	High Res on/ 1 look
Radar Coverage	4572 x 4572 meters	1524 x 1524 meters
Display Resolution	500 x 500 elements	2000 x 2000 elements
Display Size	12.7 x 12.7 cm	25.4 x 25.4 cm
Target Type	Convoy	AAA site
Background Complexity	Complex	Simple
Target Difficulty	Difficult	Easy
Target Intelligence	Low	High
Target Reference Point	No	Yes
Navigation System Error	+610 meters	+91 meters
Navigation Error Cursor Design	Crosshair	Circle
Operator Viewing Distance	71 cm	36 cm
Mission Time Available	20 seconds	60 seconds

2.2 EXPERIMENTAL DESIGN

The effects of 13 variables were examined using a fractional-factorial design. To completely specify the effects of 13 independent variables, each at two levels, and all of their interactions in a full factorial design would require 2^{13} or 8192 observations per subject. Clearly, this was an impracticably large number of conditions and some modification was necessary. In most behavioral research it is reasonable to assume that higher order interactions account for very little variance. With this assumption, a research strategy which, as a first step, examines only the main effects of each variable, is an economical research approach.

Simon [7] describes an economical sampling strategy, referred to as a screening design, which uses a fractional replicate of a 2^{13} factorial design. The basic design consists of 16 selected combinations of the 13 independent variables which is augmented with an additional 16 conditions. The 32 total experimental conditions allow an estimate of the main effects along with a number of aliased two-factor interaction strings.

2.3 PROCEDURES

Each operator received a one-hour familiarization briefing, 32 training trials, and 32 test trials over a two-day period. Each operator was given a verbal briefing which included: 1) a description of the study objectives and an overview of what the operator would be doing, 2) a discussion of the application of SAR to the quick response mission, 3) a description of the radar, display, and mission parameters the operator would experience during the study, 4) a review of the UTM map grid system, and 5) a series of training trials to familiarize the operator with the parameters under investigation. A warm-up trial was given before each test trial because of the large differences in conditions that existed among the test trials due to changes of the 13 study parameters from trial to trial. Target acquisition time, probability, and operator confidence estimates were the performance measures recorded.

3.0 RESULTS

The objective of this study was to determine what parameters are important determiners of operator performance in a simulated tactical strike mission. This screening study with 13 parameters was designed to accomplish this objective. In this type of study the percent of variance attributable to the different study parameters (ETA squared) is the measure used to make this determination. The ETA^2 values for each of the 13 parameters studied are given for the three performance measures--target acquisition time, probability of correct target acquisition, and operator confidence judgment.

The time measure used in the analysis was the percent of time used of the total mission time available. This measure was used to take incorrect target acquisitions into account in the analysis of the time data. If an

operator found the wrong target or ran out of time, the maximum time available, 20 or 60 seconds depending on the mission time available for that trial, was used as the time score. The ratio of time available to time taken to acquire the target was the value used in the analysis.

Operator confidence data were analyzed by assigning a value of 4 for "high" confidence, 3 for "medium" confidence, 2 for "low" confidence, and 1 for trials where the operators ran out of time. Although these values cannot be assumed to be on an interval scale which, strictly speaking, is required by the analysis for ETA^2, they allow an approximate estimation of ETA^2 values for the operator confidence judgment data.

Following the presentation of results for percent of variance attributable to the parameters studied, those parameters determined as important will be discussed.

3.1 VARIANCE ATTRIBUTABLE TO STUDY PARAMETERS

Evaluation of the ETA^2 values indicates that radar coverage, display resolution, and radar resolution were the principal parameters that affected operator target acquisition performance. Radar coverage was the most important variable (smaller coverage produced better performance) accounting for 30.1, 22.2, and 26.6 percent ETA^2 values for the time, probability, and confidence judgment measures. Display resolution, the second most important parameter, accounted for 13.2, 12.5, and 17.6 percent of variance, respectively, for the time, probability, and confidence judgment measures. Radar resolution was the third most important parameter for operator time and probability performance--9.1 and 10.5 percent ETA^2, respectively. Interestingly, radar resolution was not an important parameter in the operator's confidence judgments (0.8 percent ETA^2). The operator's judgments of their acquisition performance were unaffected by presentation of a high resolution/1-look or a 12.2 meter/4-look radar image.

A second group of three parameters had moderate effects on operator performance; these parameters were display size, navigation error, and target type. Display size was the most important of these parameters, accounting for 4.9, 7.0, and 3.9 percent of the variance for time, probability, and confidence judgment measures. Navigation error accounted for 5.6, 3.1, and 2.3 percent

of the variance for the time, probability, and confidence judgment measures. Although target type had a moderate effect on target acquisition time (5.4 percent of the variance), it had a small effect on target acquisition probability (1.4 percent of the variance) and no effect on the operator's confidence judgments (less than 0.1 percent of the variance).

Four of the six remaining parameters that accounted for a small but meaningful (2 to 3) percent of the variance included: navigation error cursor design, target reference point, target difficulty, and mission time available. The two variables having no affect on operator performance were the amount of target intelligence and operator viewing distance.

One second-order interaction which accounted for a relatively large percent of the variance was identified in the study. This was the interaction between radar coverage and display resolution. Display resolution had a much greater effect on time and probability performance with the large radar coverage. At the small coverage, the 2000-line display resolution was only slightly superior to the 500-line display.

In the remainder of this discussion of results, those parameters determined to be of major or moderate importance will be addressed separately. The implication of the results to SAR tactical strike systems design will be discussed, and recommendations for additional research to establish quantitative functional relationships among the parameters and operator performance will be made.

3.2 OPERATOR PERFORMANCE OBTAINED WITH THE STUDY PARAMETERS
The performance estimates that will be discussed for each of the two levels of the parameters are averaged across the high and low levels of the other 12 parameters.

3.2.1 RADAR COVERAGE
The 1524-meter coverage resulted in the best performance. The large effect of radar coverage in favor of the smaller coverage was a surprising result. Past SAR tactical target acquisition research [3] found a small effect due to radar coverage in favor of larger coverage.

Inspection of radar scenes at the two coverages indicates that scale factor is probably the underlying cause. At the 4572-meter coverage, the individual target returns that made up the linear and pattern targets are small and difficult to see; even the complete target made up of several radar returns was small at the 4572-meter coverage. With the 1524-meter coverage, the targets are much easier to see. The increased performance obtained with the larger display size, discussed later, supports this hypothesis. For small targets, displayed scale factor of the SAR scenes is an important design consideration, which would argue for a small radar coverage.

3.2.2 DISPLAY RESOLUTION

The second most important parameter was display resolution. The 2000-line display resolution was determined to be considerably better than the 500-line resolution display. Previous research [4] found that operator acquisition of large targets was not affected by variation of display resolution; although, qualitative evaluation of tactical targets in that same study indicated that tactical targets might be affected by display resolution.

In the current study, display resolution was varied by defocusing the optical projection system and adding TV line structure to the radar images. Therefore, two factors were varied in the two display resolutions-- resolution and line structure. The interaction between display resolution and radar coverage indicates that line structure was probably the more important factor. At 1524-meter coverage, there was only a small performance advantage for the 2000-line resolution display over the 500-line display, while at the 5472-meter coverage performance was significantly better with the 2000-line resolution display.

The hypothesis is that the coarse line structure of the 500-line resolution display interferred with the target patterns at the 4572-meter radar coverage, because the line structure was large relative to the size of the target returns. The line structure of the 2000-line resolution display was small relative to the target patterns at the 4572-meter coverage and hence did not interfere with target patterns. At 1524-meter coverage, the line structure of the 500-line resolution display did not interfere with the

target return patterns, and performance was only slightly poorer compared to the 2000-line resolution display.

3.2.3 RESOLUTION/MULTIPLE LOOKS

As expected, resolution/multiple looks had a major effect on operator target acquisition. The high resolution/1-look condition resulted in substantially improved performance over the 12.2-meter resolution/4-look condition. Future research should be conducted to establish functional relationships among radar resolution, radar multiple looks, and operator target acquisition performance for use by radar system designers. The high resolution/ 1-look and 12.2-meter/4-look conditions represent reasonable upper and lower bounds for such research.

3.2.4 NAVIGATION SYSTEM ERROR

The $\pm$91-meter and $\pm$610-meter navigation errors investigated had a moderate affect on operator performance. The smaller navigation error, as one would expect, resulted in more rapid operator target acquisition and higher probability of correct target acquisition.

3.2.5 DISPLAY SIZE

All other things being equal, a large display size allows SAR video to be displayed at a larger scale factor than a small display size. As discussed previously, displayed SAR video scale factor may be an important factor in SAR operator tactical target acquisition. The 25.4-cm (larger scale factor) display resulted in better performance than did the 12.7-cm display.

Display size coupled with display resolution, radar coverage, radar resolution, and operator viewing distance determine the operator's ability to extract displayed sensor information. In this screening study, it was not possible to determine the potentially complex interactions among these parameters. Since the scale factor of the displayed SAR video appears to be an important factor in SAR operator target acquisition performance and since cockpit real estate is precious in attack aircraft, it is important that future research be conducted to determine the relationships among display size, radar coverage, radar resolution, and operator viewing distance. If aircraft cockpit considerations dictate a small display, other design

options may have to be exercised to avoid unnecessarily limiting the operator's performance potential. The suggested research would provide the data to make intelligent design decisions.

3.2.6 TARGET TYPE

Target/background characteristics are known to be major sources of variance in ground mapping sensor target acquisition studies. Target type, background complexity, and target difficulty were controlled variables in this study, primarily to extract and measure this source of variance. Of these three variables, target type caused the most performance variation. The extended targets (convoys) were acquired faster and more often than were the pattern targets (AAAs). Post hoc analysis of the radar images leads us to conclude that scene clutter and raster structure tended to interfere more with the perception of the pattern targets than the linear targets, hence the poorer performance obtained with pattern targets.

4.0 CONCLUSION

This research was performed to establish the relative importance among radar sensor, display, and mission variables on operator tactical target acquisition performance for application to the quick response mission. The results of the research provided the data necessary to identify which were the important variables as a first step towards defining a viable system and future research requirements.

REFERENCES

1. Hershberger, M. L. and Craig, D. W. Synthetic array radar utilization and display, Tech. Rpt. AFAL-TR-69-367. Wright-Patterson Air Force Base, Ohio: Air Force Avionics Laboratory, April 1970. (Secret)

2. Hershberger, M. L. and Craig, D. W. A preliminary simulation of an advanced weapon delivery system for low altitude bombing, Tech. Mem. TM72-03. Culver City, California: Hughes Aircraft Company, Display Systems Laboratory, February 1972.

3. Humes, J. M., Craig, D. W., Poplawski, T. C., Guerin, D. F. and Hershberger, M. L. Synthetic array radar operator performance simulation studies, Tech. Rpt. AFAL-TR-74-63. Wright-Patterson Air Force Base, Ohio: Air Force Avionics Laboratory, August 1974. (Confidential)

4. Humes, J. M., Craig, D. W., Poplawski, T. C. and Hershberger, M. L. Synthetic array radar operator performance evaluation studies, Tech. Rpt. AFAL-TR-74-158. Wright-Patterson Air Force Base, Ohio: Air Force Avionics Laboratory, November 1974. (Confidential)

5. Lamonica, G. L. The effects of image quality on synthetic aperture radar operator performance, Tech. Rpt. AFAL-TR-74-333 Volume II. Wright-Patterson Air Force Base, Ohio: Air Force Avionics Laboratory, March 1975. (Confidential)

6. Hershberger, M. L., Scanlan, L. A., and Craig, D. W. Crew size evaluation for all weather strike aircraft, Tech. Rpt. AFAL-TR-76-79. Wright-Patterson Air Force Base, Ohio: Air Force Avionics Laboratory, June 1976.

7. Simon, C. W. Economical multifactor designs for human factors engineering, Tech. Rpt. P73-326. Culver City, California: Hughes Aircraft Company, Display Systems Laboratory, June 1973.

DEFINITION STUDY OF THE SHUTTLE IMAGING RADAR-A (SIR-A) ANTENNA ON THE SECOND SPACE SHUTTLE MISSION (OFT-2)

HAROLD A. NITSCHKE, NASA JOHNSON SPACE CENTER, HOUSTON, TX
JOHN W. KIEREIN, BALL BROTHERS RESEARCH CORPORATION, BOULDER, CO
THOMAS A. METZLER, BALL BROTHERS RESEARCH CORPORATION, BOULDER, CO

SUMMARY

The study resulted in the definition of an antenna configuration fixed-mounted high in the payload bay on the hybrid OFT-2 pallet which is compatible with Orbiter interface requirements. Tests showed that the combination of the selected panels and the designed corporate feed will meet the SIR-A performance requirement of 33 dB gain. The effects of Orbiter structure proximity on performance were determined by scale model tests to be negligible. The potential for improved performance during subsequent reflights includes a multiple-beam capability and dual polarization.

1.0 INTRODUCTION

A study was conducted to define the concept and preliminary design of the SIR-A antenna. Operational Flight Test Number 2 (OFT-2) is the first mission to include scientific experiments in the payload bay and SIR-A is the highest priority experiment approved for flight. It is presently scheduled for flight during the second half of 1979.

The primary consideration of the study was to provide the concepts for the antenna, supporting structure, and corporate feed at the lowest possible cost, while meeting the performance requirements and Orbiter interface requirements. The antenna was constrained to fit in the area forward of the Development Flight Instrumentation (DFI) without protruding from the payload bay envelope. The antenna points to the north side of the orbital track while the Orbiter flies with the payload bay opening facing the earth. This orientation is intended to thermally qualify the Orbiter to fly in this attitude for long durations. Results of the study included definition of the location in the payload bay, selection of antenna panels, design and selection of the corporate feed, design of supporting structure, and performance projections. The study has been followed by a program of detailed design, manufacturing, and test of the system.

2.0 CONFIGURATION

The SIR-A antenna design relies heavily upon previous SEASAT technology and the utilization of standard components in an effort to minimize cost and risk factors while

optimizing system performance. Seven honeycomb microstrip antenna panels, identical to the panel developed and tested for the SEASAT Engineering Model Unit (EMU), are arrayed to form a 9.38m x 2.08m planar, longitudinally polarized, radiating surface. A unique coaxial corporate feed distributes power to each panel in-phase, but with a stepped amplitude taper such that the center three panels each radiate one-sixth of the total power and the outer four panels each one-eighth. Power to each radiating patch on the panel is carried by a microstrip feedline network etched on the face of the panel.

The antenna panels and corporate feed, as shown in Figure 1, are mechanically supported and aligned to a planar surface by a fixed strongback truss. An installation truss, with adjustable fittings to the OFT-2 spacelab-hybrid pallet, supports the antenna/strongback in a fixed high-in-the-payload bay location and allows vernier adjustment of the antenna boresight pointing angle to 47 degrees from nadir.

Initial truss concepts were constructed with graphite epoxy material, but reduction in the pallet-mounted, structural fundamental frequency requirements has permitted the use of less costly, aluminum trusswork. With either material, thermal and mechanical distortions of the truss structure are sufficiently small to cause the array to deviate less than +0.635cm from a planar surface during on-orbit operations. Multilayer aluminized mylar on the trusswork and teflon-impregnated quartz cloth on the radiating panels provide passive thermal control. The multilayer insulation is covered with the quartz cloth to reduce the surface reflectivity, thus avoiding potential glare to the crew.

3.0   ANTENNA PANELS

The 1.34m x 2.08m EMU panel combines microstrip array techniques with a unique fiberglass honeycomb construction [1] to yield an efficient, lightweight, monolithic antenna. All radiating elements and feedlines are precision photo-etched on a copper laminate and supported above a bonded copper ground plane by the honeycomb structure, thus significantly reducing dielectric losses. The complete EMU array is illustrated in Figure 2, with nominal measured performance for individual panels tabulated below. Low development and manufacturing costs, rugged construction, and adequate performance made the EMU design particularly attractive for application to the SIR-A antenna. Only minor attachment fitting modifications have been made in this SEASAT design for the SIR-A program.

TEFLON-IMPREGNATED QUARTZ CLOTH (TIQC) OR EQUIVALENT

ANTENNA PANELS (7 NEW EMU)

7-WAY CORPORATE FEED

MULTILAYER ALUMINIZED MYLAR (MLI) WITH TIQC OUTBOARD COVER

STRONGBACK TRUSS (GRAPHITE EPOXY)

MLI WITH TIQC OUTBOARD COVER

INSTALLATION TRUSS (GRAPHITE EPOXY)

PREFERRED ELECTRONICS LOCATION

ADJUSTABLE PALLET INTERFACE FITTINGS (4)
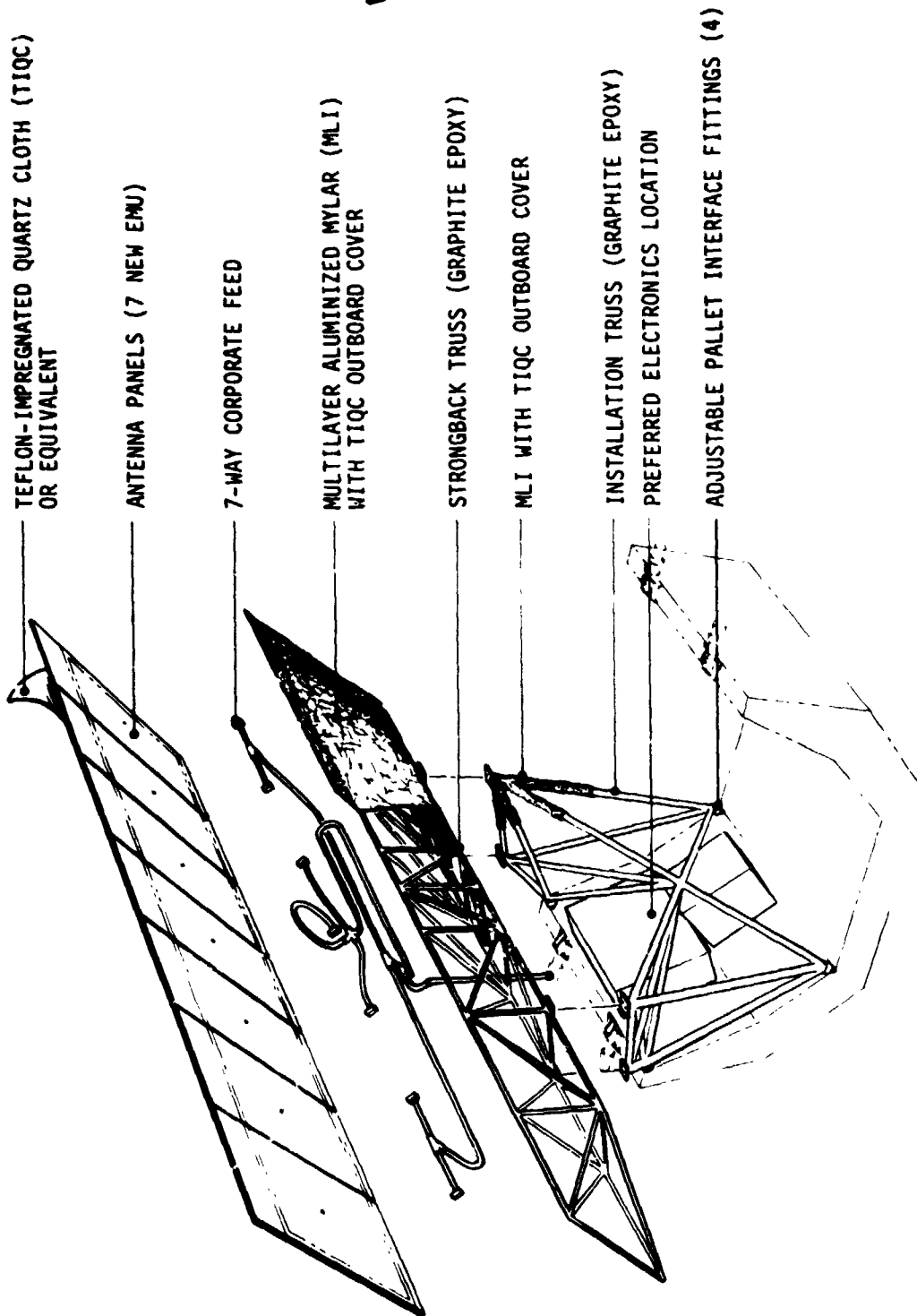
FIGURE 1

SIR-A BASELINE CONFIGURATION
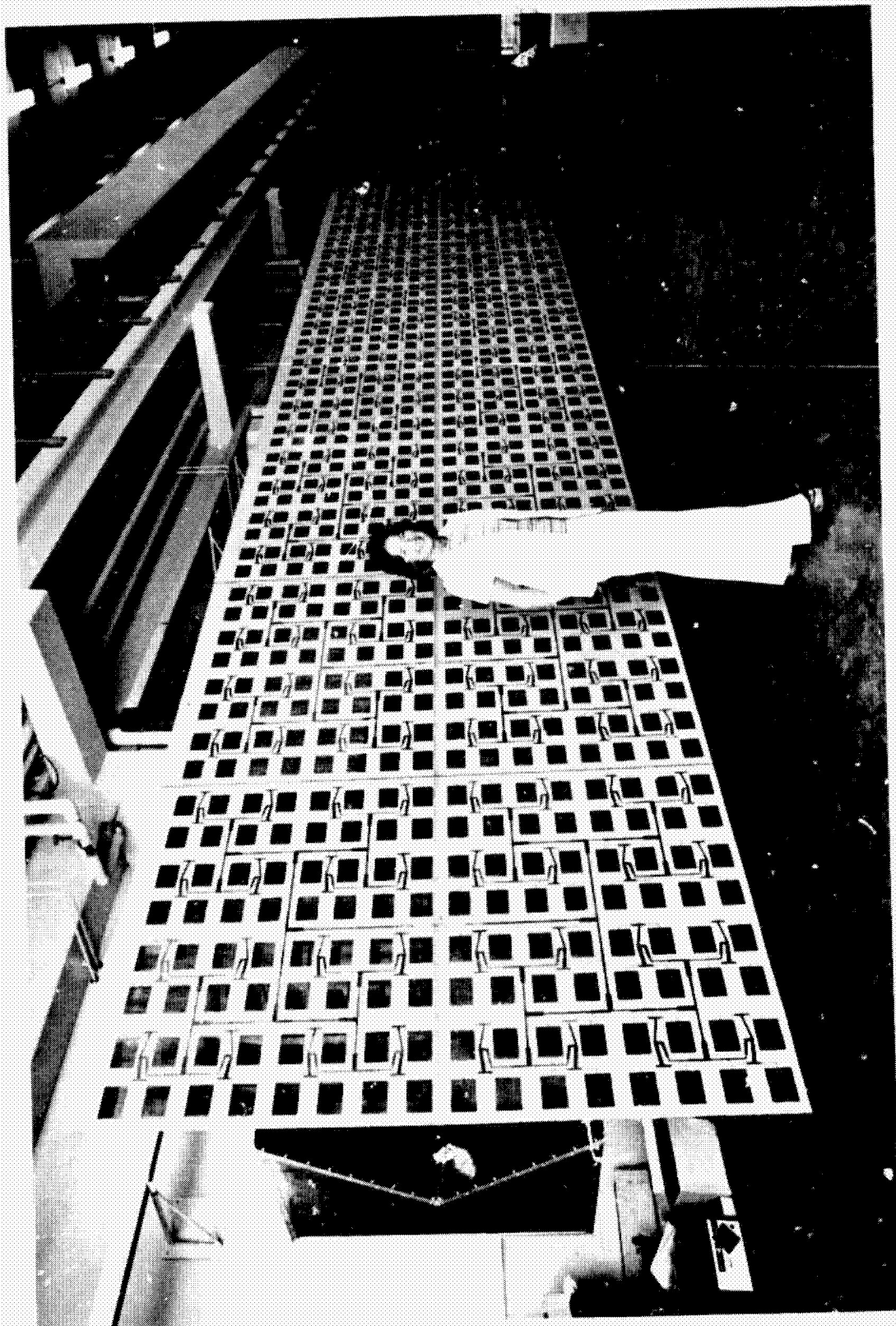
FIGURE 2
SEASAT EMU ARRAY

TABLE 1
EMU PANEL CHARACTERISTICS

PARAMETER	PERFORMANCE
Gain	25.9 dB
Sidelobes	
E-Plane	<-12.5 dB
H-Plane	<-16.0 dB
Beamwidth	
E-Plane	9.1°
H-Plane	6.2°
VSWR	< 1.3:1

4.0 CORPORATE FEED

A seven-way corporate feed, composed of standard air-loaded coaxial line and reactive power dividers, efficiently distributes power to the array panels and implements the required phase and amplitude distribution. As depicted in Figure 3, the power divider configuration theoretically yields a "natural" amplitude taper across the array. If required, minor power distribution variations due to load mismatches in the reactive network can be compensated by modifying the power split of the first reactive divider, the only nonstandard electrical component. Equal phase illumination is ensured by trimming similar lines to equivalent electrical lengths and critically phasing the 127 inch line shown in Figure 3, such that the electrical length from input to panel terminations is equivalent for all ports. Multipactor breakdown considerations dictate the use of TNC-type connectors and dielectrically loaded power dividers. A 3 dB multipactor margin is maintained throughout the system. Based on vendor data, system insertion is calculated as less than 0.7 dB.

A prototype SIR-A feed system composed of Andrews H5550 7/8" coaxial cable with N-type connectors and Microlab D2TN power dividers was constructed and tested during this study in order to establish confidence in the proposed design. The feed exhibited good control over the amplitude distribution and total system insertion loss was 0.3 dB with input VSWR less than 1.15 < 1. Theoretical insertion loss for the prototype system was 0.2 dB.

5.0 SYSTEM PERFORMANCE

Projected nominal performance of the SIR-A antenna is shown in Table 2. When the array of seven EMU panels is uniformly illuminated, the E-Plane beamwidth (-8 dB) is
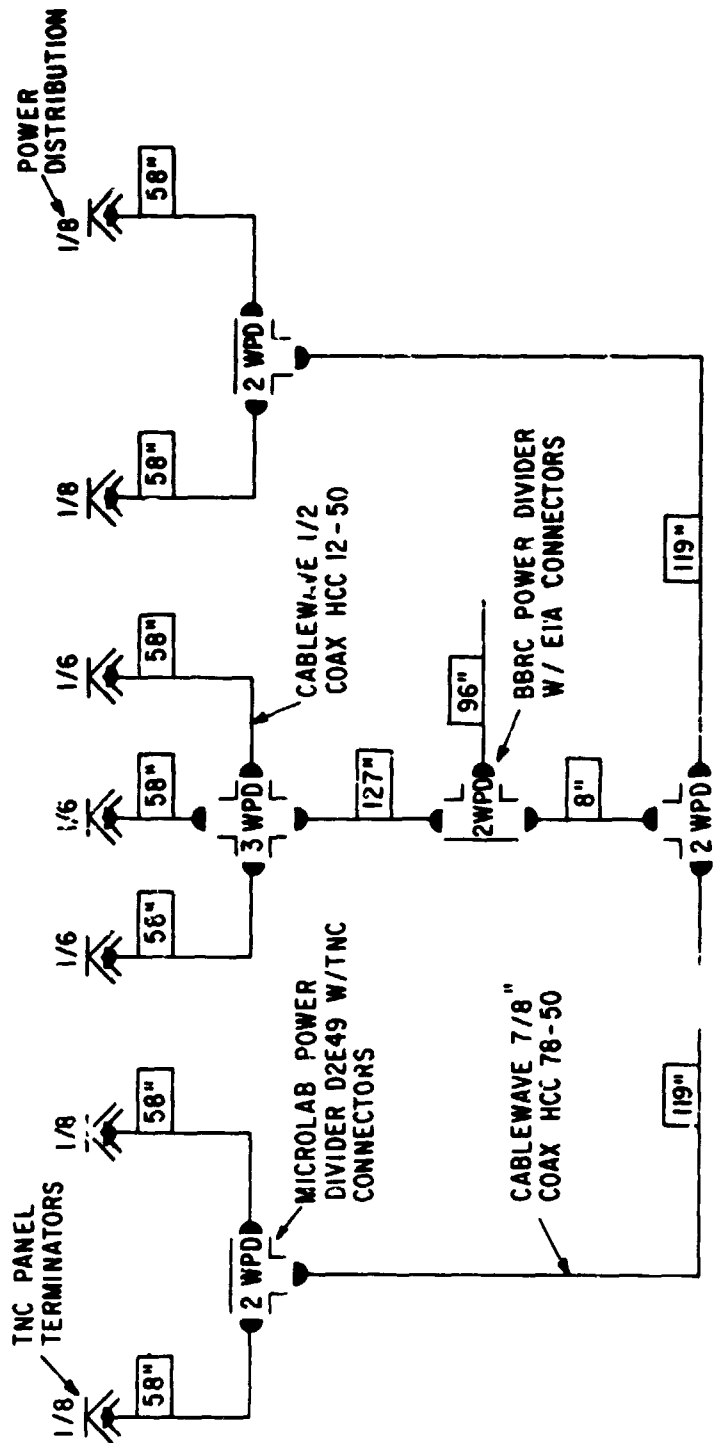
FIGURE 3
SIR-A CORPORATE FEED

theoretically 1.99 degrees with 13 dB sidelobes, but the amplitude taper implemented by the corporate feed increases this beamwidth to 2.07 degrees and potentially reduces sidelobes to -15.2 dB. Array distortions, and particularly phase and amplitude errors in the feed, will cause deviations from these nominal values [2].

The panel gain (25.9 dBi), plus the seven-element array factor gain of 8.45 dB, yields a theoretical 34.35 dBi gain for the SIR-A antenna array; however, several nominal directivity and efficiency losses must be considered (Table 2).

TABLE 2
DIRECTIVITY AND EFFICIENCY LOSSES

E-Plane Taper	-0.02
Feed Network	-0.70
Mechanical Distortions	-0.08
Feed Phase and Amplitude Errors	-0.13
Thermal Blanket	-0.05
Frequency and Temperature Effects	-0.2
NET LOSS	-1.18

Thus, the nominal projected gain of the seven-panel SIR-A antenna array is 33.17 dBi.

Due to the proximity of the SIR-A antenna to potential reflecting surfaces within the Shuttle payload bay, a 1/10 scale model radiation pattern test at 12.75 GHz was conducted to assess the impact of the Shuttle structural surfaces on the SIR-A antenna performance. The test configuration is depicted in Figure 4. This figure shows the antenna in a scale model payload bay with the DFI pallet installed. The Orbiter radiator panel on the side of the bay is also mocked up. Radiation patterns with the antenna mounted high in the bay, as in Figure 1, indicated no measurable beamwidth variation from free space conditions and only a minor increase (0.8 dB) in one H-Plane sidelobe. Shuttle structural surfaces will not adversely affect SIR A performance.

6.0   POTENTIAL FOR IMPROVEMENT

Because the SIR-A experiment remains inside the Shuttle vehicle and returns to earth, the potential for evolution in system configuration during subsequent reflights is possible. Probable reflights, as yet unscheduled, will provide greater ground coverage than is possible during the 5-day OFT-2 Mission. Improvements in performance could be achieved, with small additional costs, by adding an H-Plane multiple-beam capability to the antenna. Dual polarization could also be added with some
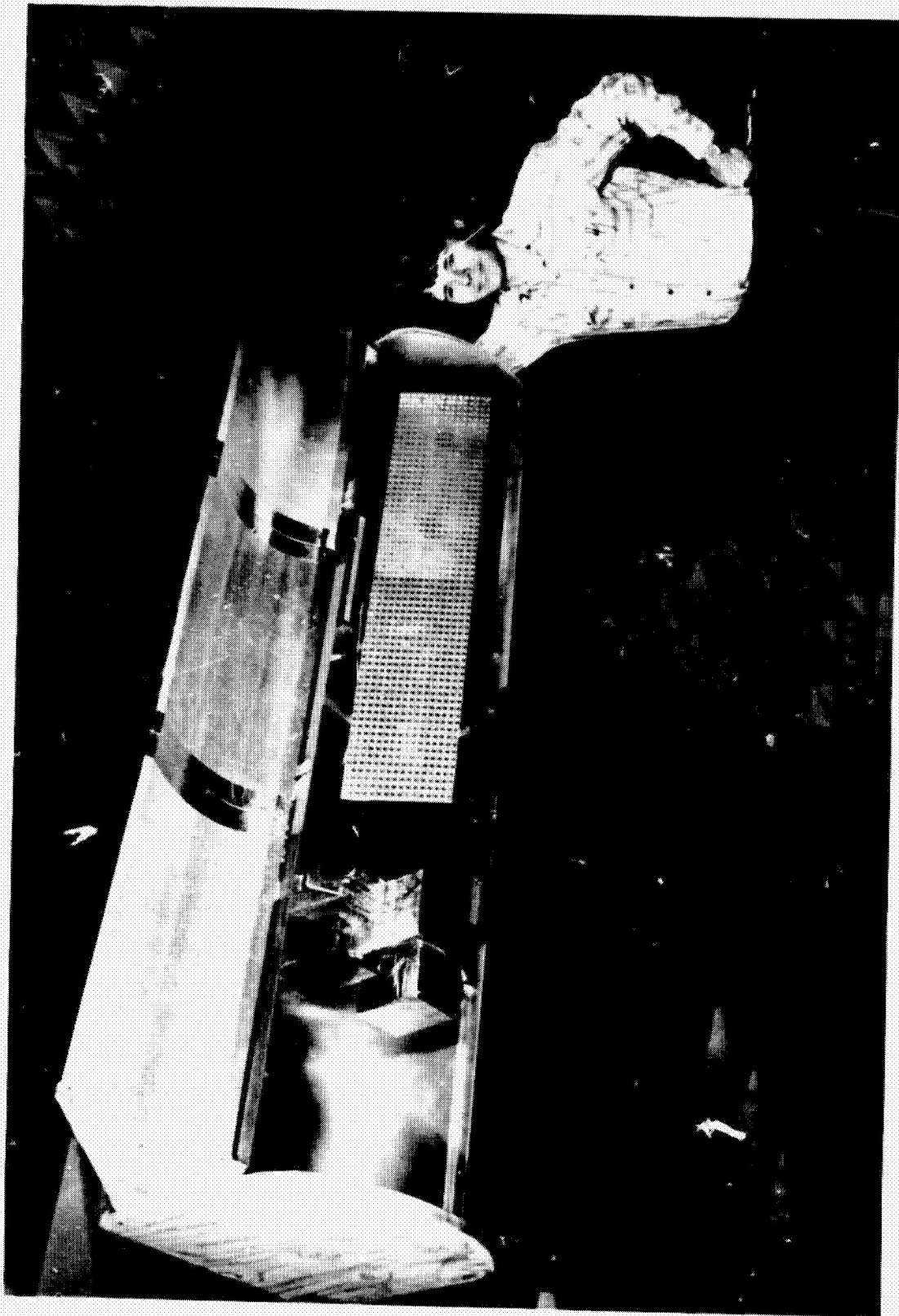
FIGURE 4

1/10 SCALE OPERATIVE MOCK-UP OF THE PROPOSED SIR-A ANTENNA IN THE SHUTTLE BAY

modification to the antenna circuit artw~r~ and transmitter. The antenna could have an on-orbit pointing adjustment capabili. ncorporated. Another improvement would be to fold the antenna so that it occupies approximately the width of one Spacelab pallet during launch and descent, and deploys over the aft payload bay doors during operation. This change would reduce the length of payload bay occupied, without affecting Orbiter thermal radiator performance, thus allowing a larger variety and number of additional other payloads to share the mission. In order to accomplish this, a foldable feed system, as implemented on the SEASAT SAR antenna and a DoD SAR antenna, would be required. Such changes would result in additional scientific data and provide evolutionary improvement.

7.0   REFERENCES

[1]   Brejcha A. G., Keeler L. G., Sanford G. G., "The SEASAT-A Synthetic Aperture Radar Antenna," Synthetic Aperture Radar Technology Conference - 1978.

[2]   Huisjen M. A., "Prediction of Antenna Array Performance from Subarray Measurements," Synthetic Aperture Radar Technology Conference - 1978.

D_{10} (32)

PREDICTION OF ANTENNA ARRAY PERFORMANCE
FROM SUBARRAY MEASUREMENTS

DR. MARTIN A. HUISJEN
SENIOR MEMBER TECHNICAL STAFF
BALL BROTHERS RESEARCH CORPORATION
BOULDER, CO 80306

SUMMARY

Because of the practical difficulties involved in measuring the RF performance of large array antennas such as SEASAT, it is desirable to predict performance based on subarray and feed network measurements. Computer runs have been used at BBRC to determine the effect of mechanical distortions oi array pattern performance. Subarray gain data, along with feed network insertion loss, and insertion phase data can be combined with the analysis of Ruze on random errors to predict gain of a full array. The performance predictions for the full SEASAT array will be compared with test data.

1.0   INTRODUCTION

There are significant practical advantages to be obtained if one is able to successfully predict RF performance of a large antenna array based on measurements of a single subarray. The subarray measurements can be performed on a much more compact range so that it may be possible to use an anechoic chamber. Environmental problems of an outdoor range and mechanical handling problems involved with interfacing a large array to a positioner are eliminated. Design modifications can be incorporated into a single subarray and the results quickly checked out.

1.1   SIMPLEST APPROACH

The full array performance characteristics to be predicted are the gain, beamwidths, and sidelobe levels. The most straightforward approach to predicting these parameters from subarray data is to assume the full array will be uniformly illuminated by a lossless feed network. In such a case the array gain is simply the subarray gain multiplied by the number of subarrays. The beamwidth in each dimension is the subarray beamwidth divided by the number of subarrays in the respective dimension. The sidelobe levels depend on the amplitude taper within each subarray. A best first guess at the first sidelobe levels in the arrayed direction(s) is -13.2 dB, corresponding to the sidelobes of a uniformly illuminated aperture.

Consider the SEASAT Synthetic Aperture Radar Antenna (SARA), sketched in Figure 1, as an example. It is an L-band (1275 MHz) 10.74m by 2.09m array made up of eight panels, each 1.34m by 2.09m. Each panel is a subarray consisting of 8 by 16 radiating elements. The intrapanel feed network is uniform in the E-Plane (8-element) direction and tapered in the H-Plane (16-element) direction to produce -18.2 dB sidelobes. The main feed network distributes power uniformly to each of the eight panels. The approach described above predicts, for the full array, a gain 9 dB above the single panel gain, an E-Plane beamwidth eight times smaller than the single panel E-Plane beamwidth, an H-Plane beamwidth identical to that of a single panel, E-Plane sidelobe levels of -13.2 dB, and H-Plane sidelobes identical to the single panel H-Plane sidelobes.
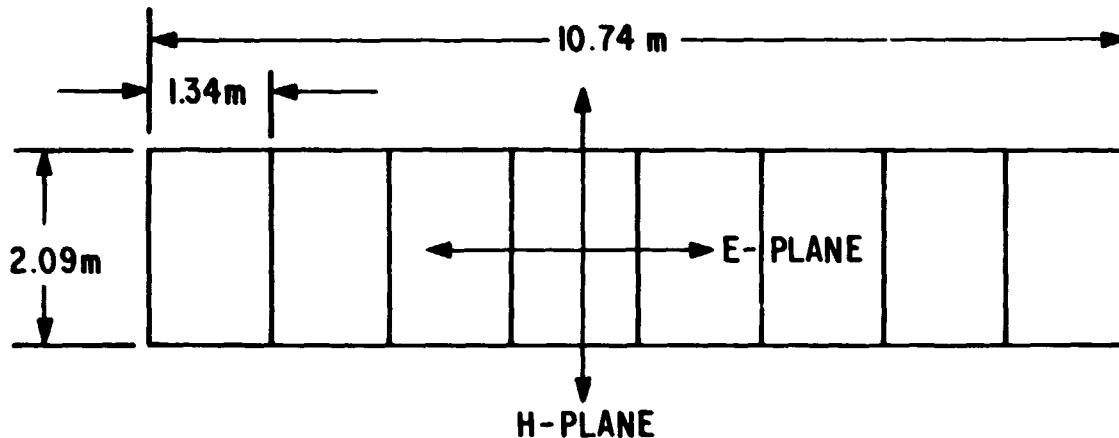
FIGURE 1

SEASAT SAR ARRAY

This simple approach to predicting array performance neglects several complications which should be taken into account in order to make an accurate performance prediction. These complications are:

- Mechanical distortion of support structure which combines subarrays
- Mechanical distortion of subarrays
- Power loss in main feed network
- Power tapers designed into main feed network
- Phase and amplitude errors in main feed network

Methods of dealing with these complications will be described in succeeding sections of this presentation.

2.0   MECHANICAL DISTORTION EFFECTS BY COMPUTER CALCULATION

2.1   DESCRIPTION OF PROGRAM

The effects on RF performance of mechanical distortions of an array can be calculated using a computer program developed at BBRC. The program calculates patterns for linear arrays which can be distorted into a second dimension. The relative gains of various distortion cases are calculated by simply comparing the magnitudes of the computed on-boresight fields for each case. When the program is used for a planar array, it calculates principal plane patterns for deflections out of the plane of the array. It accounts only for deflections within the principal plane being calculated.

2.2   FULL ARRAY DISTORTIONS

Subarrays must be combined on some kind of support structure to form a full planar array. In the case of the SEASAT SARA, the eight panels were supported side by side on a graphite epoxy Extendable Support Structure (ESS). There can be out-of-plane deflections of this structure due to manufacturing tolerances and to thermal effects. Figure 2 shows the results of computer calculations done for parabolic deflections in the long dimension of the ESS. The beamwidths and sidelobe levels are those for the principal E-Plane pattern. Based on these calculations, the ESS was designed to maintain a total deflection less than $\pm 1/4$ inch over its range of operating conditions. This type of analysis can obviously be done for any shape of deflection. Parabolic was chosen as the most likely possibility.

Deflections in the H-Plane (short dimension) of the array are due to deflections of the panels in that dimension. Figure 3 shows the results of computer calculations for parabolic deflections in the H-Plane of the panels. Note that the sidelobes begin at -18.2 dB because of the amplitude taper in the H-Plane.

2.3   SUBARRAY DISTORTIONS

As mentioned in the previous paragraph, deflections in the H-Plane of SEASAT panels are equivalent to deflections in the H-Plane of the entire array. Deflections in the E-Plane of the individual panels, however, produce effects different from deflections of the entire array. Figure 4 shows the results of computer calculations for parabolic deflections in the E-Plane of the panels. Since the E-Plane beamwidth and first sidelobes are determined by the array factor of eight panels, they are not changed to first order by an alteration of the individual panel pattern. The major effect which
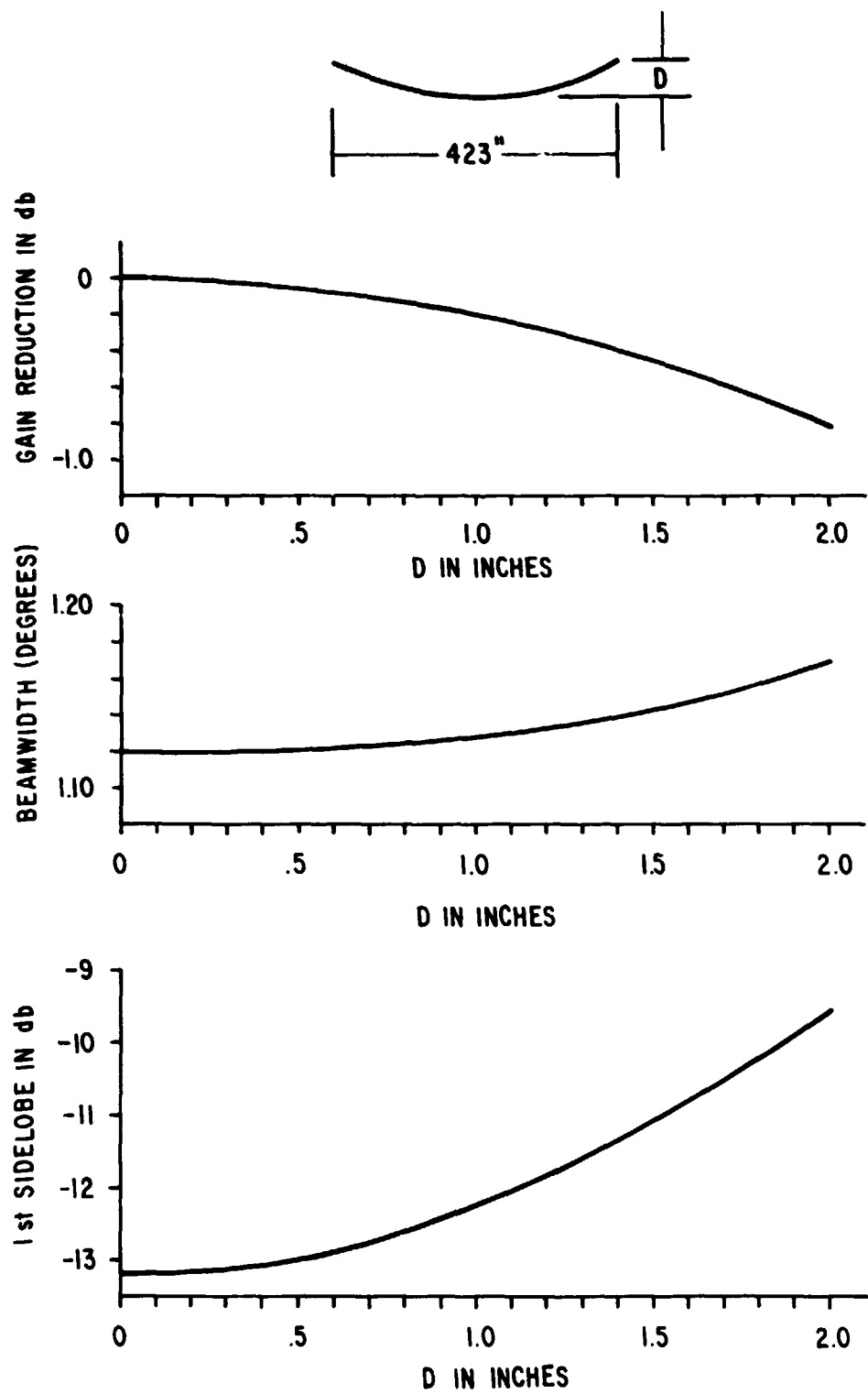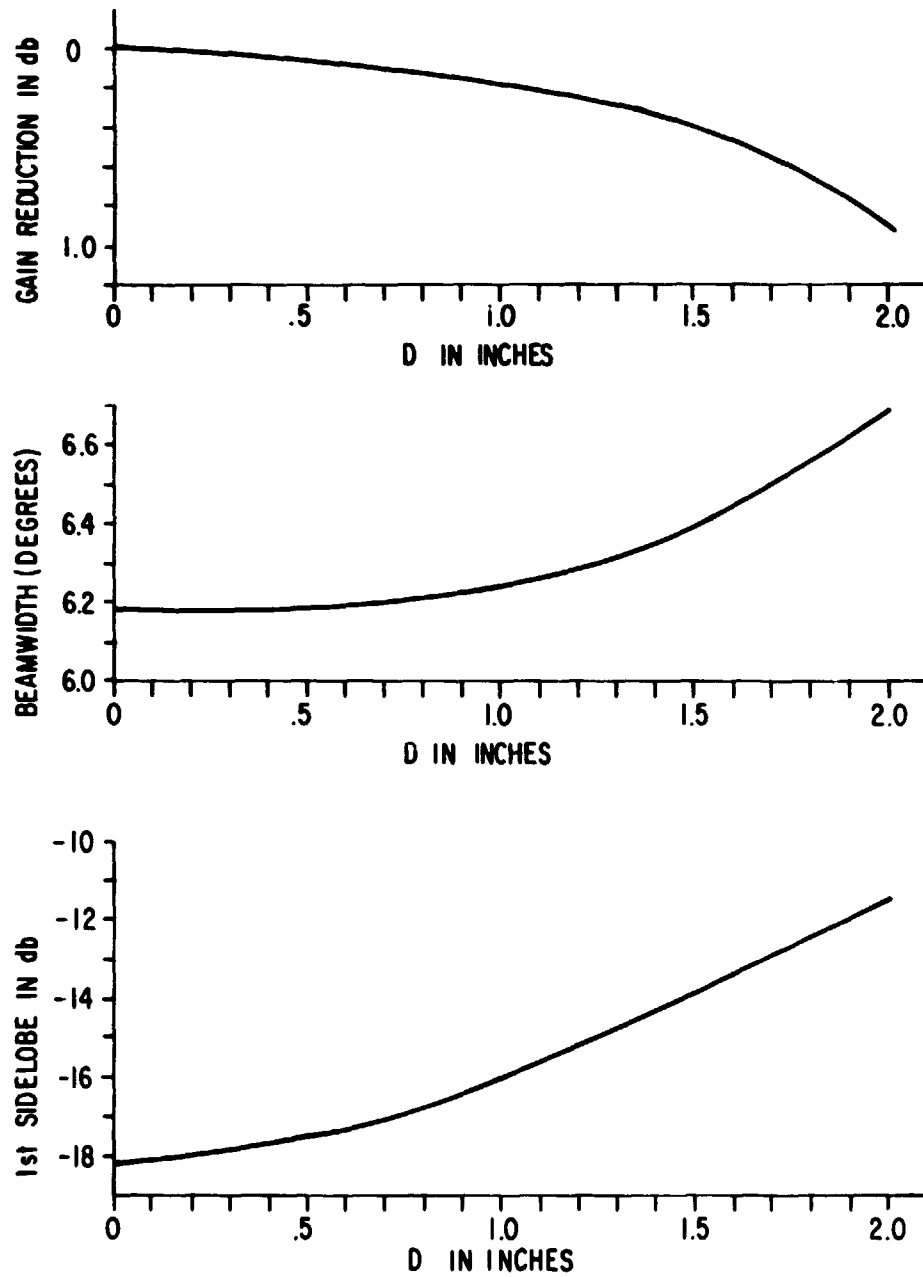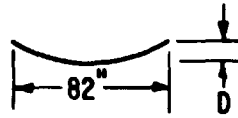
FIGURE 2

PERFORMANCE VS ARRAY E-PLANE DISTORTION

FIGURE 3

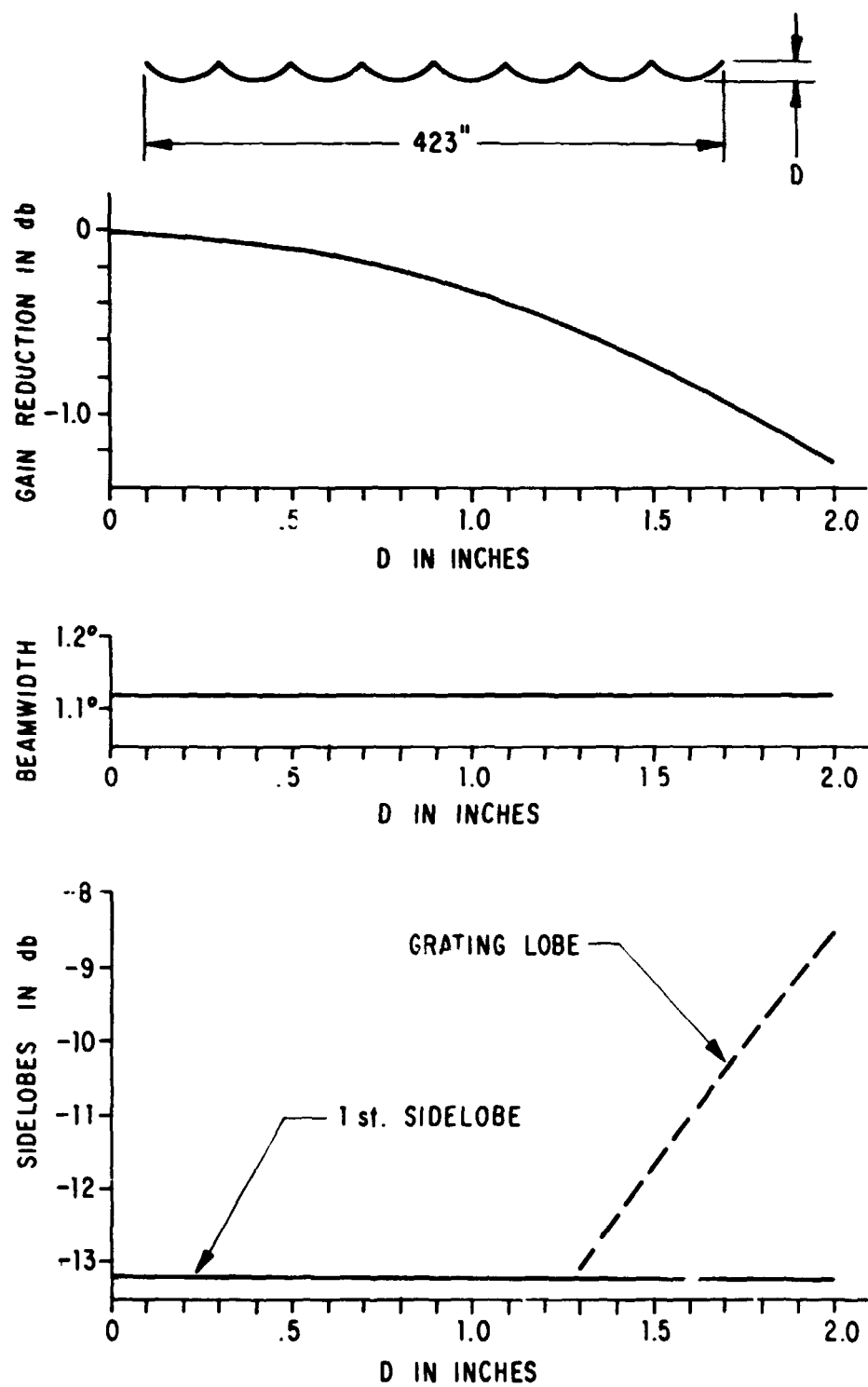PERFORMANCE VS ARRAY H-PLANE DISTORTION

FIGURE 4

PERFORMANCE VS PANEL E-PLANE DISTORTION

occurs is the introduction of a grating lobe at about 10 degrees corresponding to radiating elements separated by one panel width ($10° = \sin^{-1} \frac{\lambda}{1.34m}$). These results were used to establish a design goal of $\pm 1/4$ inch deflection of the antenna panels over their range of operating conditions.

2.4 ALTERNATIVE CALCULATION OF GAIN REDUCTION

In Section 2.1 it was stated that relative gains of the various distortion cases can be calculated by comparing the magnitudes of the computer-calculated on-boresight fields for each case. This is true because the average radiated power remains constant as a function of distortion while the peak radiated power changes due to loss of phase coherence in the broadside direction.

This suggests a method of approximately calculating the gain loss due to mechanical distortions without using a computer. Ruze [1] has analyzed an aperture illuminated with a gaussian distribution of phases of mean square deviation $\overline{\delta^2}$ and found that the gain varies as $e - \overline{\delta^2}$. One can apply this to a mechanically-distorted aperture by treating a distortion d as a phase error $\delta = \frac{2\pi d}{\lambda}$. Although the distribution of phase errors will in general not be gaussian, the mean square error $\overline{\delta^2}$ can be calculated and used to find the relative gain. This approximation to the gain becomes worse as the ratio of distortion to array length increases. As an example, consider a parabolic distortion with a peak-to-peak deflection of $f\lambda$ where f is some fraction. The mean deflection is $1/3 \ f\lambda$, with a mean squared deviation of $4/45 \ f^2 \lambda^2$ corresponding to a mean squared phase error $\overline{\delta^2} = (2\pi)^2 \frac{4}{45} f^2$. Table 1 compares the results of this approximate calculation with the exact computer results for parabolic distortions in the E–Plane of the SEASAT array. The agreement is very good for small distortions.

TABLE 1

COMPARISON OF GAIN CALCULATIONS FOR SEASAT E-PLANE

Pk to Pk Parabolic Deflection f in Wavelengths	Computer-Calculated Gain Change	$10 \log e - \overline{\delta^2}$
0	0 dB	0 dB
1/36	-.01	-.01
1/18	-.05	-.05
1/9	-.20	-.19
2/9	-.81	-.75

3.0 FEED NETWORK EFFECTS

3.1 LOSS

Insertion loss in the RF feed network supplying power to the subarrays is dealt with very simply. Such loss has no effect on the patterns; it decreases the array gain directly by the amount of loss in the feed.

3.2 AMPLITUDE TAPERS

It is often desirable to purposely design the feed network for an unequal power distribution to the subarrays. Usually the power is tapered from the center of the array outward in order to reduce sidelobes. Such tapers affect gain, beamwidths, and sidelobes. The effects on pattern performance can be found by using the previously-described computer program with the appropriate amplitude distribution on the array elements. The gain relative to a uniform power distribution can be found from the equation

$$\Delta G = 10 \log \frac{1}{n} \frac{\left(\sum_{i=1}^{n} A_i \right)^2}{\sum_{i=1}^{n} \left(A_i^2 \right)} \tag{1}$$

where n is the number of subarrays and A_i is the relative amplitude at the i th subarray (proportional to square of power at i th subarray).

3.3 PHASE AND AMPLITUDE ERRORS

Due to manufacturing tolerances and other variables, the power distribution produced by the feed network usually deviates somewhat from the desired distribution; and the phases at each subarray are not exactly equal. Such errors can be dealt with exactly if data have been taken on the relative powers and phases appearing at each output port of the feed network. One problem which should be noted is that the relative powers and phases at each output port may change when connected to the subarrays. The feed network measurements are usually done one output port at a time with matched loads connected to the other ports. Since the subarrays will not in general have the same input impedance as the matched loads, the measurements may not be completely valid. If, however, the subarray impedances are identical and reasonably well matched, the feed network measurements provide a good indication of the power distribution in the array.

The effect of the errors on pattern performance can be found using the computer program with the measured phases and amplitudes applied to the appropriate a ay elements. The gain relative to a uniform power distribution in amplitude and phase is found from an equation very similar to Equation 1,

$$\Delta G = 10 \log \frac{1}{n} \frac{\left(\sum_{i=1}^{n} \overline{A}_i \right)^2}{\sum_{i=1}^{n} A_i^2} \tag{2}$$

where $\overline{A}_i$ is now a phasor accounting for both the amplitude and phase at the i th subarray.

4.0   SEASAT PREDICTIONS COMPARED WITH DATA

For the SEASAT SARA, pattern and gain measurements were taken on four of the eight panels which were combined as the flight unit.   Power split and phase measurements were taken on the main feed network before it was combined with the panels.   These data are used in this section to predict the flight unit RF performance which is then compared with acceptance test data taken at the LMSC Santa Cruz facility.

Figure 5 shows the power split versus frequency measured at the eight output ports of the main feed network.   The numbers on each curve at 1275 MHz indicate P_{out}/P_{in} for each port at the center frequency.   The insertion loss of the feed is found from the equation

$$Loss = 10 \log \frac{\sum_{i=i}^{8} P_{out_i}}{P_{in}} \tag{3}$$

This gives an insertion loss of 0.58 dB at 1275 MHz.   Figure 6 shows the relative phases measured at each output port of the feed network.   Putting the phase and amplitude data into Equation 2, a loss of 0.04 dB is found due to the phase errors and unequal power split in the main feed.

The gains and beamwidths at 1275 MHz for the four flight panels which were measured are given in Table 2.
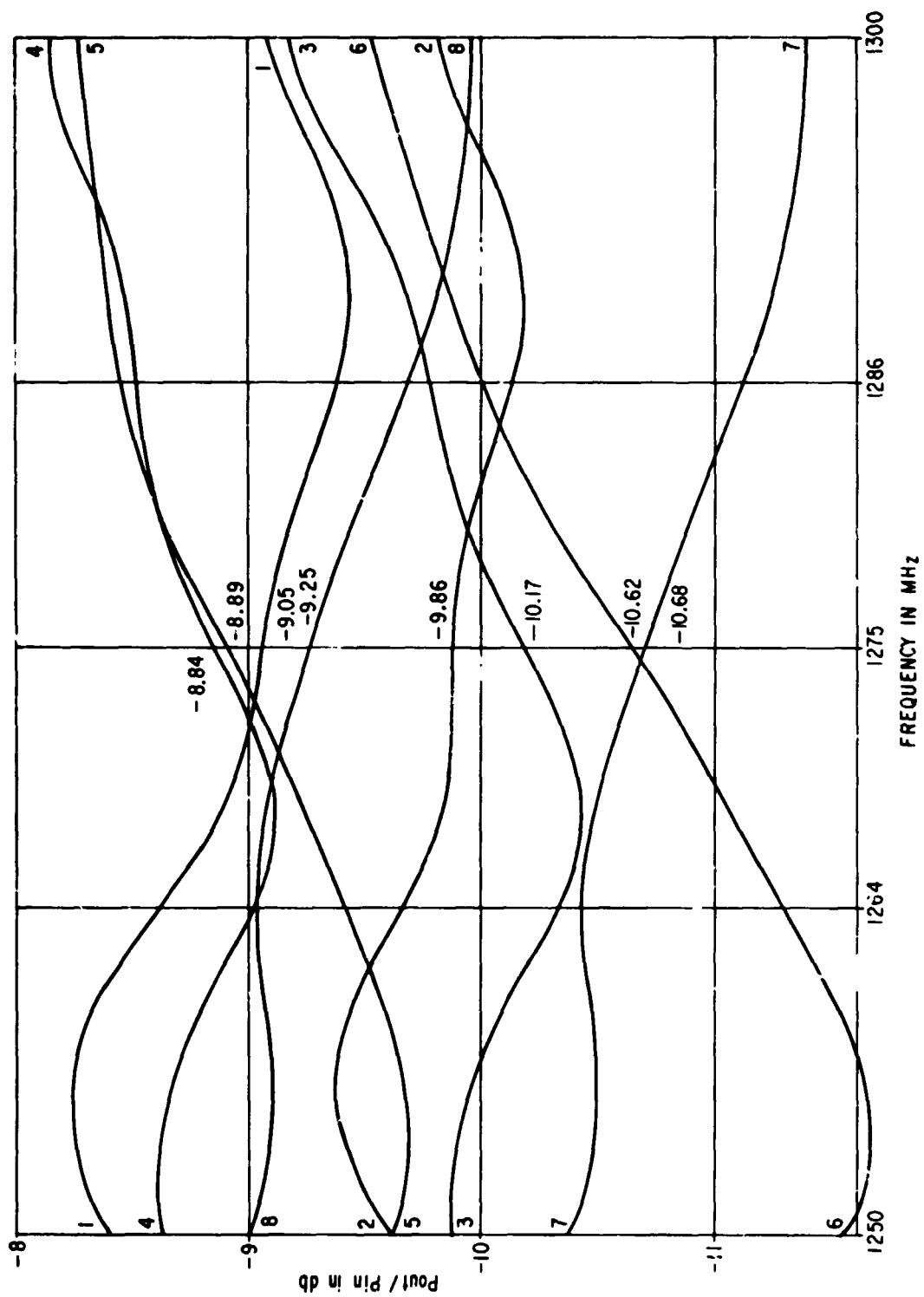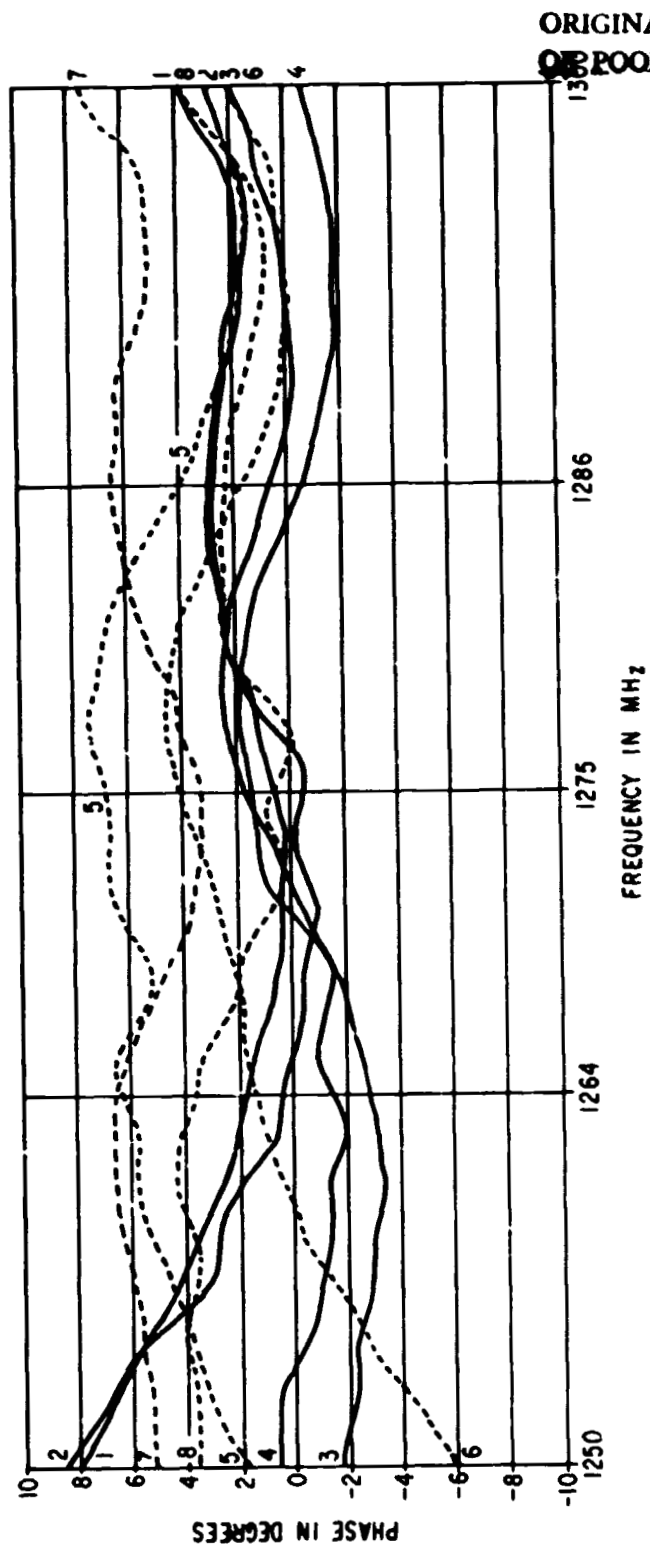
FEED NETWORK POWER SPLIT VS FREQUENCY

FIGURE 5

FIGURE 6

FEED NETWORK PHASE VS FREQUENCY

TABLE 2
SEASAT SINGLE PANEL DATA

Panel No.	Gain (dB)	E-Plane BW (°)	H-Plane BW (°)
F005	26.5	9.03	6.17
F007	26.5	9.00	6.20
F008	26.5	9.07	6.20
F009	26.4	9.02	6.25
Average	26.5	9.03	6.21

After the panels were attached to the ESS and hung on a gravity compensation fixture, they were surveyed to determine the flatness of the array. Six points on each panel were measured. The peak-to-peak deflection of the array was 0.5 inch. The shape of the deflection was not determined, but parabolic is a good assumption for the purposes of performance prediction.

4.1 GAIN

The foregoing data are used in Table 3 to predict the gain of the SEASAT array.

TABLE 3
SEASAT SARA PREDICTED GAIN

	(dB)
Single Panel Gain	26.5
Array Eight Panels	+ 9.03
Feed Network Loss	− .58
Feed Network Errors	− .04
Array Distortion	− .04
Predicted Array Gain	34.87
Measured Array Gain	34.9

The agreement between predicted and measured gain is remarkably good and certainly within measurement error! Mismatch losses have been neglected in the gain prediction since they affect both panel and array gain. (This assumes approximately equal VSWRs for the panels and the array plus feed network.)

4.2 BEAMWIDTHS

The array H-Plane beamwidth prediction is 6.21 degrees, the average of the

beamwidths of the four measured panels. The beamwidth of the array was measured to be 6.25 degrees.

The array E-Plane beamwidth prediction is made using computer calculations. Eight elements were arrayed with a spacing equal to the panel spacing. They were fed with the phases and amplitudes found in the feed network measurements. The element pattern used in the calculations was the E-Plane pattern of a single panel. Figure 7 is a plot of the calculated pattern, while Figure 8 shows the measured E-Plane pattern. The beamwidth from the calculated pattern should be modified to account for the measured 0.5 inch mechanical distortion, but Figure 2 shows that the beamwidth is unaffected by that level of distortion. The predicted E-Plane 3 dB beamwidth is, therefore, the computer-calculated value of 1.13 degrees. This compares very well with the measured value of 1.12 degrees. It should be noted that the average measured panel beamwidth of 9.03 degrees divided by 8 is also 1.13 degrees.

4.3   SIDELOBES

The H-Plane first sidelobes measured for the array are asymmetric with levels of -19.4 and -17.2 dB on either side of the main beam. This behavior could be predicted closely from the single panel measurements which showed asymmetric sidelobes at approximately the same levels. In Section 1.1 it was stated that the H-Plane feed network was tapered to produce -18.2 dB first sidelobes. The measured deviation from this behavior is most likely due to phase and amplitude errors in the intrapanel feed network.

Figure 8 shows that the measured E-Plane sidelobes are also asymmetric with a maximum level of -12.9 dB. The computer-predicted pattern has asymmetric sidelobes, but the maximum sidelobe is at -13.8 dB. About 0.2 or 0.3 dB of this discrepancy can be accounted for by the 0.5 inch distortion of the array. The remaining discrepancy is probably due to an alteration of the feed network phases and amplitudes when the panels were connected.

5.0   CONCLUSION

Methods have been presented for predicting the gain, beamwidths, and sidelobes of an array based on subarray measurements. These methods were used to predict the performance of the SEASAT SAR eight-panel array from single panel measurements. The predicted and measured performance parameters are presented in Table 4.
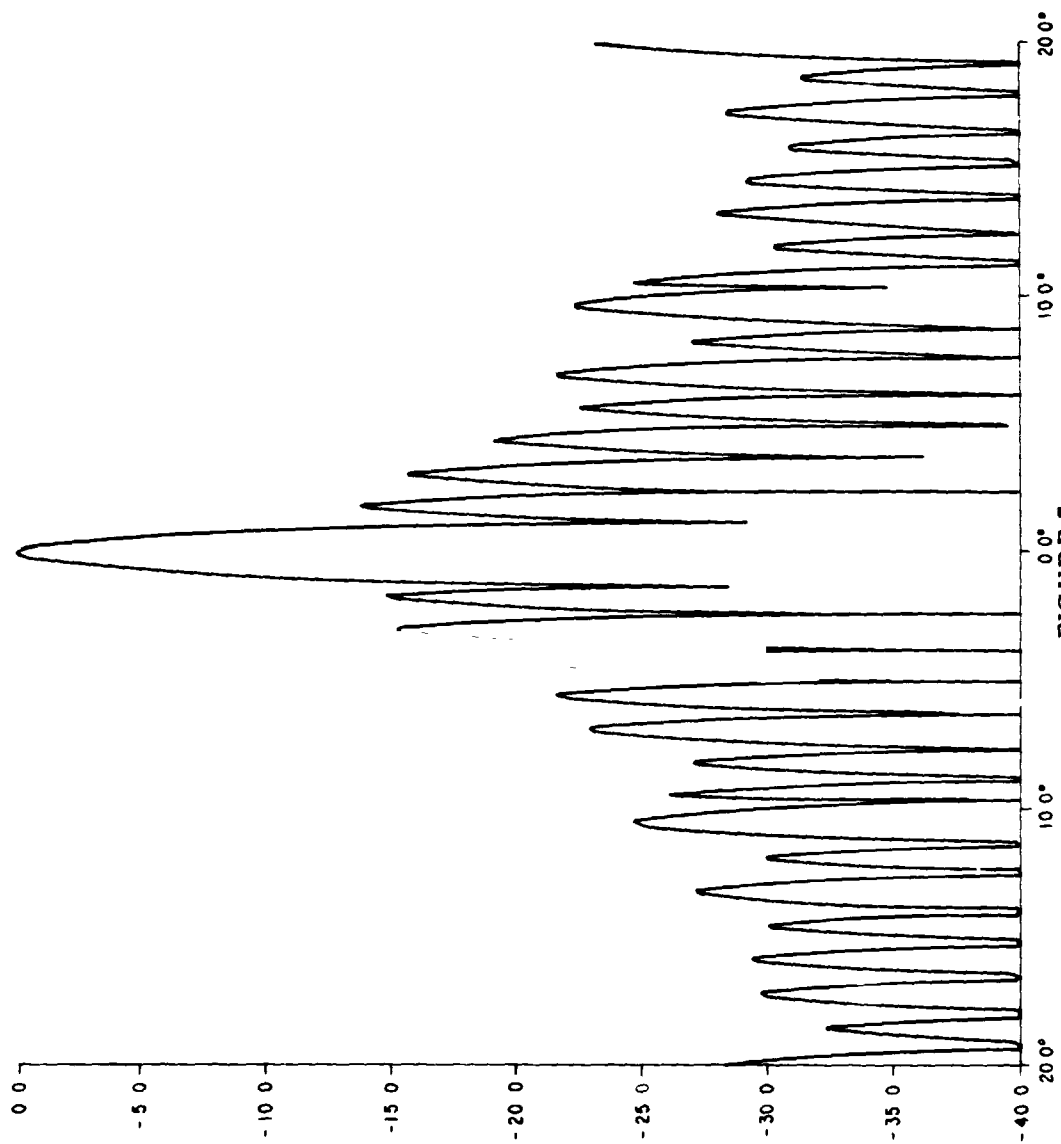
FIGURE 7

CALCULATED E-PLANE PATTERN
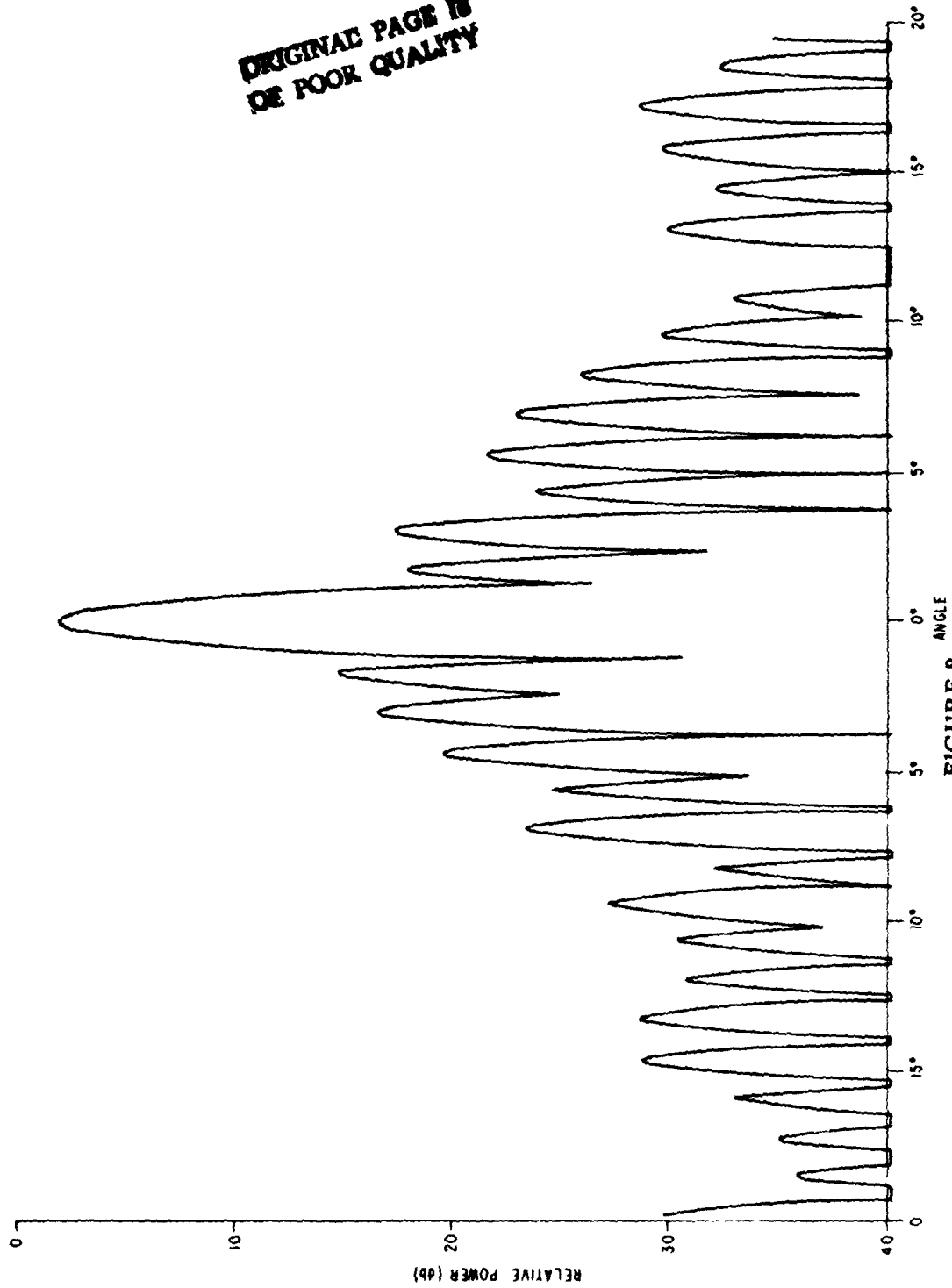
FIGURE 8

MEASURED E-PLANE PATTERN

TABLE 4

SEASAT PREDICTIONS VS ACTUAL PERFORMANCE

Parameter	Prediction	Measured
Gain	34.87 dB	34.9 dB
E-Plane Beamwidth	1.13°	1.12°
H-Plane Beamwidth	6.21°	6.25°
E-Plane Sidelobe	-13.8 dB	-12.9 dB
H-Plane Sidelobe	-17.2 dB	-17.2 dB

6.0   REFERENCES

[1]   J. Ruze, "Antenna Tolerance Theory - A Review," Proc. IEEE, 54, 633–640, 1966.

MATHEMATICAL MODELING AND SIMULATION OF THE SPACE SHUTTLE IMAGING RADAR ANTENNAS

ROSS W. CAMPBELL, KAREN E. MELICK, AND EDGAR L. COFFEY, III
PHYSICAL SCIENCE LABORATORY
NEW MEXICO STATE UNIVERSITY
LAS CRUCES, NEW MEXICO 88001

SUMMARY

Simulations of Space Shuttle synthetic aperture radar antennas under the influence of space environmental conditions have been carried out at L, C, and X-band. Mathematical difficulties in modeling large, non-planar array antennas are discussed, and an approximate modeling technique is presented. Results for several antenna error conditions are illustrated in far-field profile patterns, earth surface footprint contours, and summary graphs.

1.0 INTRODUCTION

Antennas to be used on Space Shuttle missions in the 1980's for synthetic aperture radars are expected to undergo stresses induced by the space environment that may degrade the performance of the radar. For example, thermal gradients across and through the antenna surface may cause the structure to bow. Deployment techniques that rely on unfolding the antenna in one or more places may create surface discontinuities at the fold joints. in addition, feedline lengths may change slightly due to thermal expansion, resulting in phase excitation errors. Power division to different sections of the antenna may be perturbed by non-unity VSMRs. To estimate the effect of these and other antenna errors on overall synthetic aperture radar performance, it is necessary to computer simulate the antenna over a wide range of possible error conditions. Unfortunately, classical methods of analysis, such as computing the array factor as the weighted sum of path length differences, are unmanageable because of the large electrical size of the antenna. A closed-form array factor expression is unobtainable because of the general nature of the mechanical surface errors. To overcome these computational limitations, a compromise modeling method was developed.

2.0 THE MATHEMATICAL MODEL

2.1 MODEL OF MECHANICAL SURFACE FLATNESS ERRORS

The physical array surface is modeled with a number of piecewise bilinear rectangular sections as illustrated in Figure 1. That is, if the array is nominally located in the (x,y)-plane, the z-axis displacement of the array surface is given by

$$z(x,y) = \sum_{m=1}^{M} z_m(x,y) \tag{1}$$

where

$$z_m(x,y) = \begin{cases} a_o^m + a_1^m x_m + a_2^m y_m + a_3^m x_m y_m & \text{in the } m^{th} \text{ section} \\ 0 \text{ elsewhere} \end{cases} \tag{2}$$

and (x_m, y_m) are the local coordinates of the mth section shown in Figure 2. The $\{a_n^m\}$ coefficients may be determined uniquely from the displacements at each of the four corners of the rectangle. Furthermore, the same coefficients give a continuous approximation of the actual antenna surface. These sections need not conform to physical antenna panels. The number of sections needed can be determined by the curvature of the warped surface and the maximum error that can be tolerated. As the number of sections is increased, the approximation becomes more exact, converging to the actual surface in the limit. [4] Of course, the results become exact electrically when each section contains only one element of the array.

2.2 MODEL OF ELECTRICAL ERRORS

Let us suppose the array antenna is divided into M x N subarray sections as illustrated in Figure 3. The far-field pattern of such an antenna may be written as the weighted sum of the contributions from each subarray.

$$\bar{E}(r,\theta,\phi) = \frac{j\beta\eta}{4} \frac{e^{-j\beta r}}{r} \sum_{m=1}^{M} \sum_{n=1}^{N} a_{mn} e^{j\phi_{mn}} \bar{g}_{mn}(u,v) e^{j\Psi} \tag{3}$$

where: $a_{mn}e^{j\phi_{mn}}$ = the complex excitation of the mn^{th} subarray

(u,v,w) = $(\sin\theta\cos\phi, \sin\theta\sin\phi, \cos\theta)$, the cosines of the beam pointing direction with respect to the x, y, and z axes

$\beta = 2\pi/\lambda$ = wave number of the source

$\eta = \sqrt{\dfrac{\mu}{\varepsilon}}$ = intrinsic impedance of the medium

$\overline{g}_{mn}(u,v)$ = vector array factor of the mn^{th} subarray

Ψ = $(x_{mn}u + y_{mn}v + z_{mn}w)$

(x_{mn}, y_{mn}, z_{mn}) = location of the center of the mn^{th} subarray

If the vector subarray factor is known, equation (3) may be used to obtain the far-field pattern. Either measured data or computed data may be used for g(u,v).

Each electrical section may be excited separately in both magnitude and phase. The number of sections needed to obtain a desired accuracy is determined by the severity of the electrical taper.

2.3 SIMULTANEOUS MECHANICAL AND ELECTRICAL ERRORS

If the bilinear rectangular sections of (2.1) are made to conform with the subarray sections of (2.2), then electrical and mechanical errors may be studied simultaneously. The only further approximation needed is in the computation of the subarray factor $\overline{g}(u,v)$ for elements equally spaced over a bilinear surface. A closed-form expression for $\overline{g}$ is not available; however, since all sections are the same physical size, $\overline{g}$ could be computed and tabulated parametrically so that when using equation (3), only a table look-up is necessary.

If the bilinear surfaces are sufficiently flat, an alternative technique is available. The two straight lines formed by projecting the localized coordinate axes onto the bilinear surface of (2) may be used to define an error-minimizing plane.[1] That is, the coefficients of

$$z_m(x_m, y_m) = b_0^m + b_1^m x_m + b_2^m y_m \tag{4}$$

are chosen so that the error

$$\epsilon = \iint\limits_{section} |(a_0 = a_1 x + a_2 y + a_3 xy) - (b_0 + b_1 x + b_2 y)| \, dxdy \tag{5}$$

is a minimum. The superscript "m" has been omitted for clarity. The minimum occurs when

$$b_0 = a_0$$

$$b_1 = a_1 \tag{6}$$

$$b_2 = a_2$$

and the integrated error $\epsilon = A^2/16*|a_3|$, where A is the surface area of one rectangle. A maximum error of $A/4*|a_3|$ occurs at the corners of the rectangle. Consequently, the subarray factor used in calculations is the pattern from a planar rectangular array with average displacement

$$z_{avg} = b_0 \tag{7}$$

whose normal points in the direction (θ_m, ϕ_m) defined by

$$\tan(\alpha_x^m) = b_1^m$$

$$\tan(\alpha_y^m) = b_2^m \tag{8}$$

where

$$\cos(\alpha_x^m) = \sin(\theta_m)\cos(\phi_m)$$

$$\cos(\alpha_y^m) = \sin(\theta_m)\cos(\phi_m)$$

(9)

The array factor for each subarray is the well-known

$$\frac{\sin\frac{M\Psi x}{2}}{M\sin\frac{\Psi x}{2}} \cdot \frac{\sin\frac{N\Psi y}{2}}{N\sin\frac{\Psi y}{2}}$$

(10)

pattern with the angular tilt due to α_x and α_y included in the Ψ-factors.

3.0 SIMULATION RESULTS

A variety of antenna mechanical surface errors and electrical excitation errors have been simulated at 1.5, 4.5, 9.0, 12.0 and 14.0 GHz [2,3], including:

- Antenna panel unfolding errors due to incomplete deployment of a folded panel.

- Various warping conditions due to thermal gradients through the antenna surface.

- Electrical excitation errors occurring from feedline mismatches.

For the antenna panel unfolding errors, a three-panel array was modeled with the outer two panels tilted away from the perfectly flat baseline case. Deflections varied from 0.5 cm to 5.0 cm over the 11.6 m length of the entire array. Figure 3 consists of four graphs which illustrate gain degradation versus frequency, gain degradation versus warp severity, beam pointing error versus warp severity, and side lobe level versus wrap severity.

Parabolic bow mechanical errors caused by the thermal gradients through the antenna were modeled with a twelve-panel array curved to fit a parabola (in azimuth) with maximum deflection ranging from 1 cm to 5 cm. Figure 4 consists of four graphs which depict the azimuth far-field pattern of a uniformly excited 11.6 m antenna at 1.5 GHz for bows ' 1.0, 2.0, 3.0, and 4.0 cm. Two-dimensional Earth surface footprints for the parabolic bow error as well as the unfolding error are shown in Figure 5.

Electrical mismatch errors were studied for the seven panel SIR-A microstrip array antenna for VSWRs of 1.0, 1.1, and 1.2. Results are shown in Figure 6.

4.0 <u>REFERENCES</u>

[1] E. L. Coffey, Interim Report on Antenna Evaluation for the Shuttle Imaging Radar: Phase I (NASA Contract NAS9-95469), Physical Science Laboratory Report No. PA00853, New Mexico State University, Les Cruces, NM, July 1976.

[2] E. L. Coffey and K. R. Carver, Final Report on Antenna Evaluation Study for the Shuttle Multispectral Radar: Phase I (NASA Contract NAS9--5469), Physical Science Laboratory Report No. PA00874, New Mexico State University, Las Cruces, NM, December 1976.

[3] E. L. Coffey and K. R. Carver, Final Report on Antenna Evaluation Study for the Shuttle Multspectral Radar: Phase II (NASA Contract NAS9-95471), Physical Science Laboratory Report No. PA00881, New Mexico State University, Las Cruces, NM, May 1977.

[4] G. Strong and G. J. Fix, <u>An Analysis of the Finite Element Method</u>, Prentice - Hall, New York, 1973, pp. 165-171.
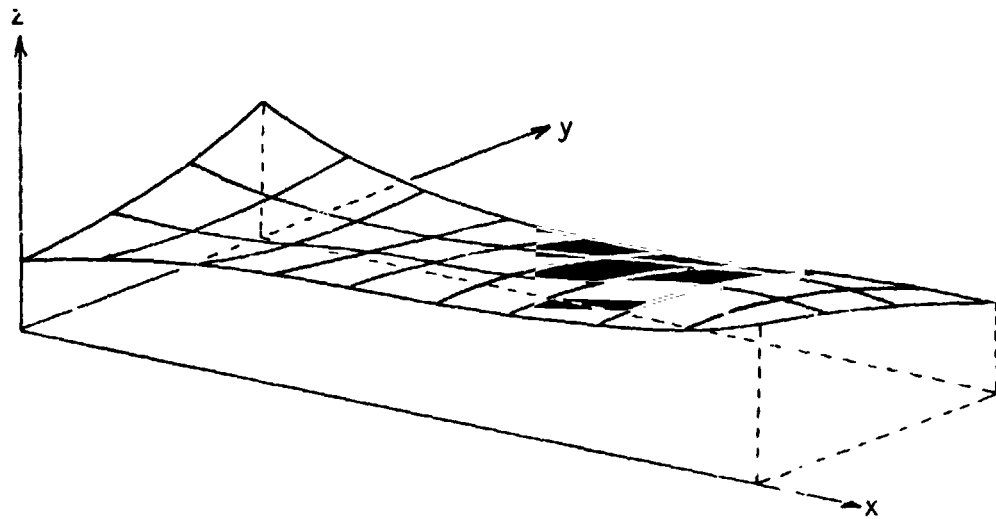
Figure 1a.   Mechanically deformed array surface.
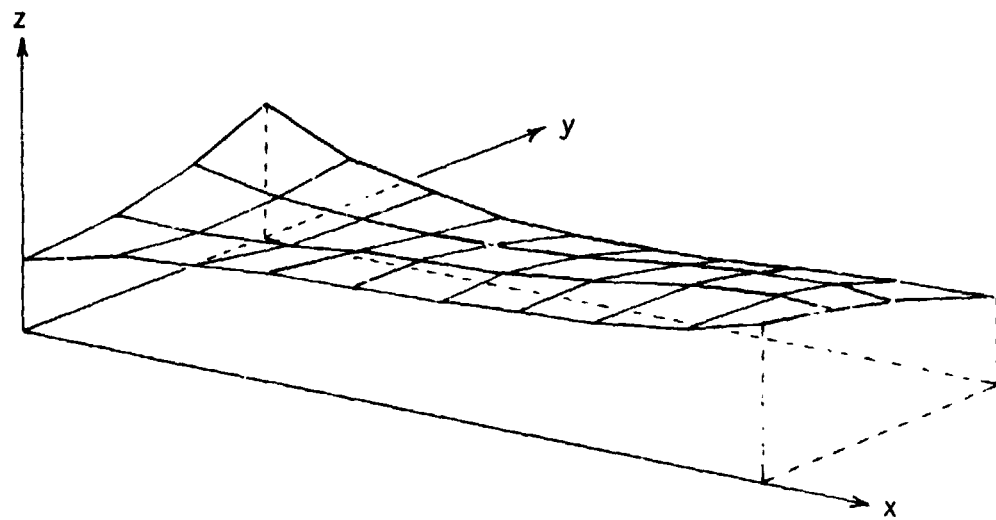
Figure 1b.   Piecewise bilinear approximation.
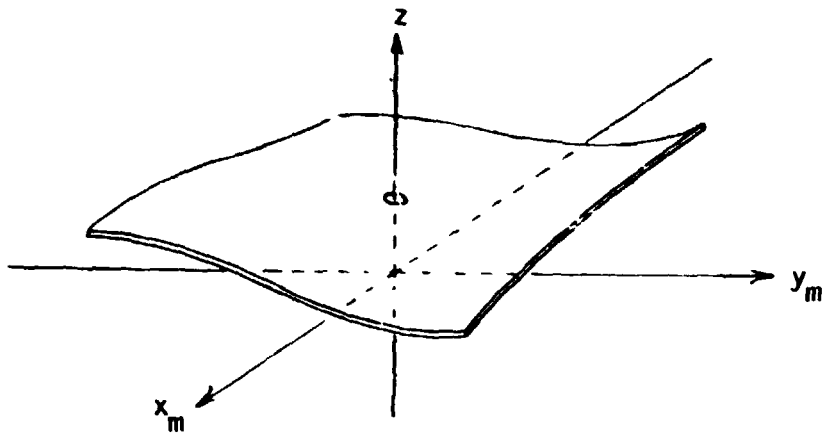
Figure 2a. Original surface.
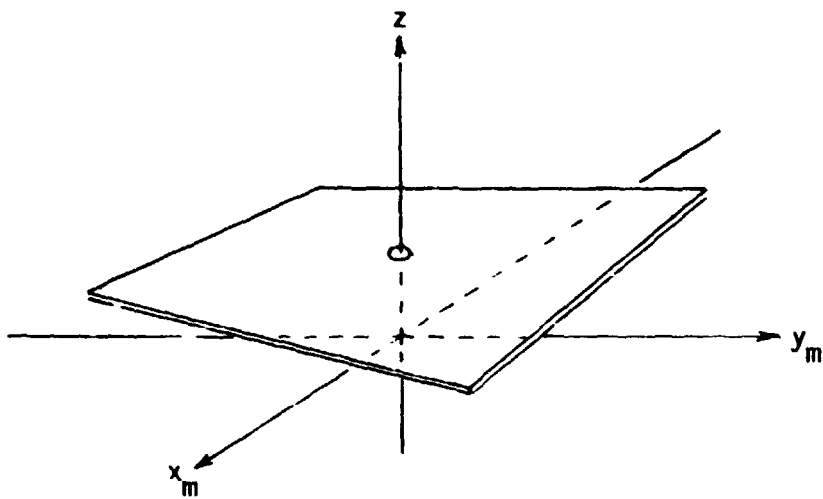
Figure 2b. Bilinear approximation.
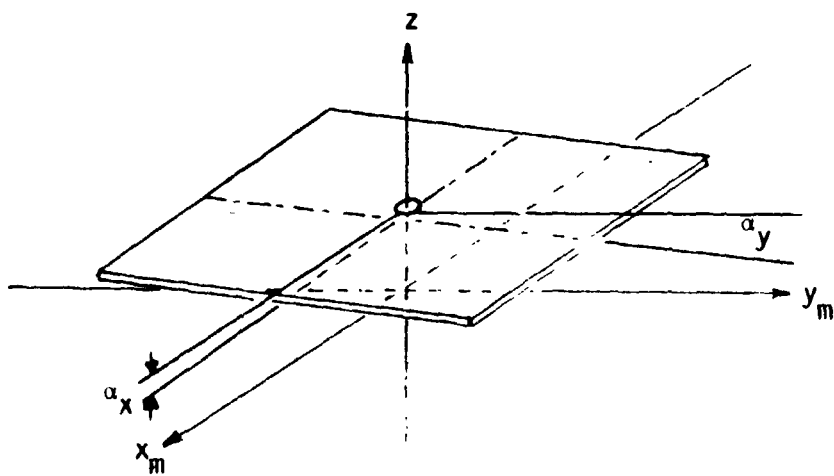
Figure 2c. Planar approximation.

Gain Degradation (dB) vs. Warp Severity (cm) at 1.5 GHz,
10 deg. Tilt, Panel Unfolding Errors

Azimuth Profile Plane Side Lobe Level (dB) vs. Warp Severity
(cm) for Panel Unfolding Errors at 1.5 GHz, 50 deg. tilt
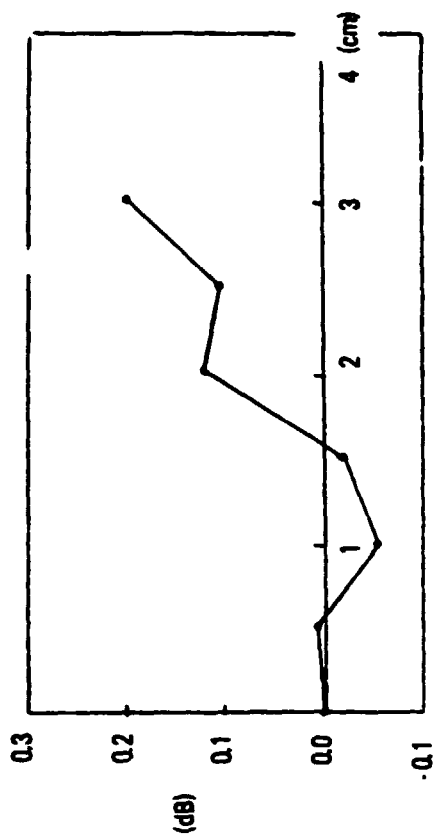
Gain Degradation (dB) vs. Frequency (GHz)
(Panel Unfolding Error: -1.0, 2.0 cm), 50 deg. tilt

Beam Pointing Error (km) vs. Panel Unfolding Error (cm)
at 1.5 GHz, 50 deg. tilt.
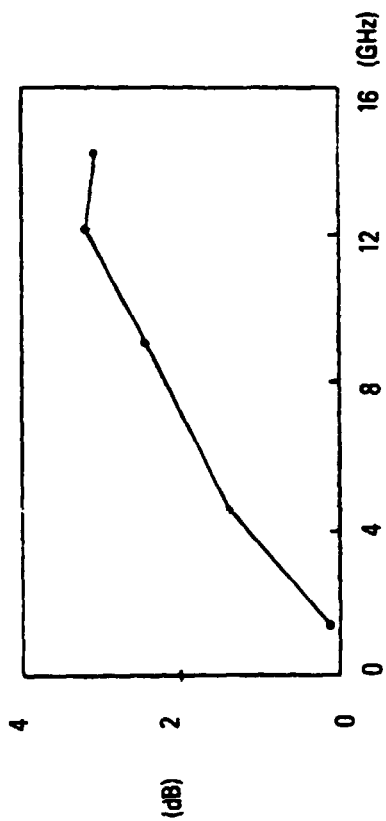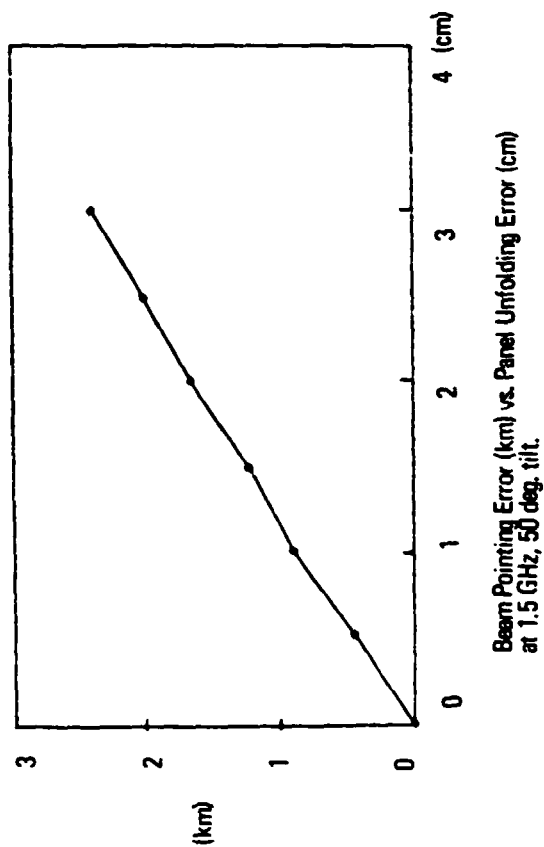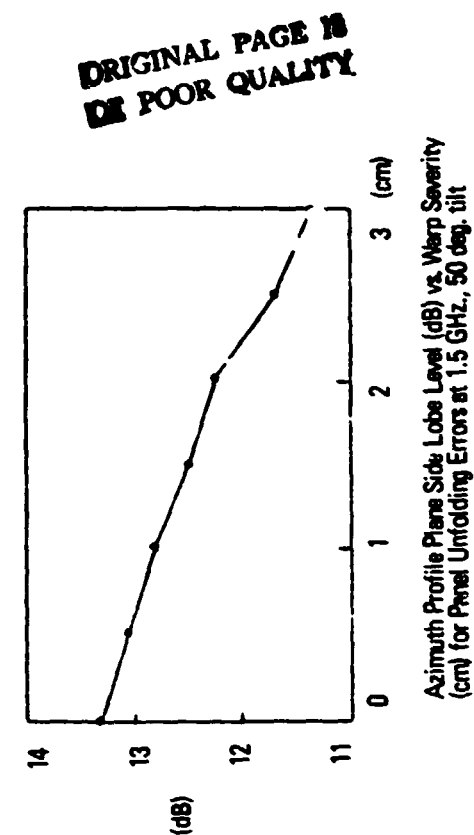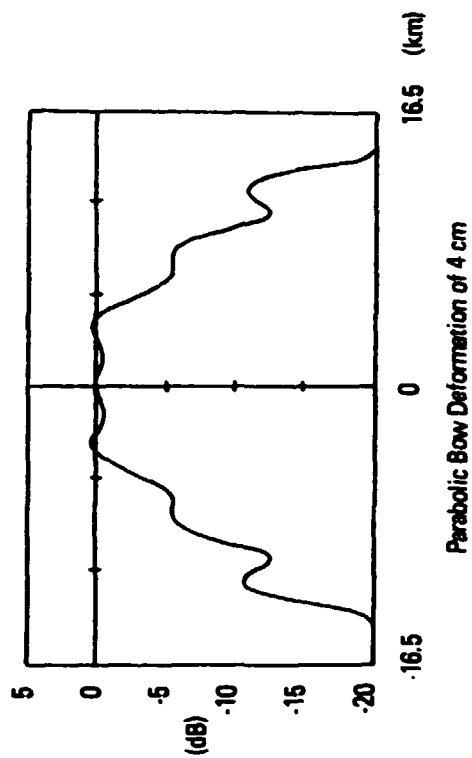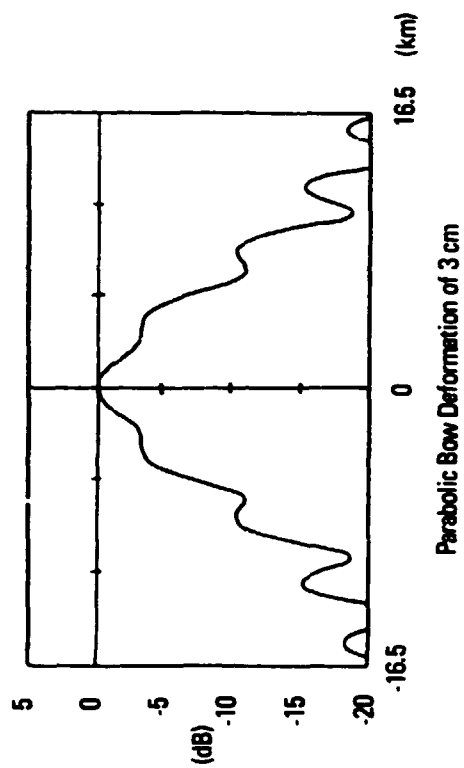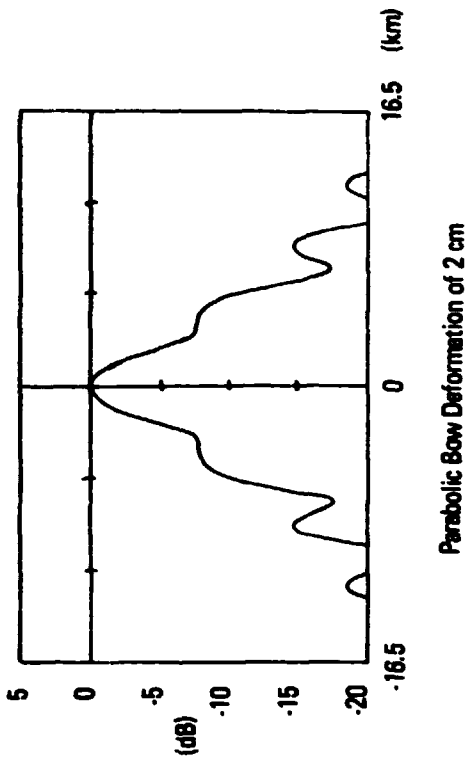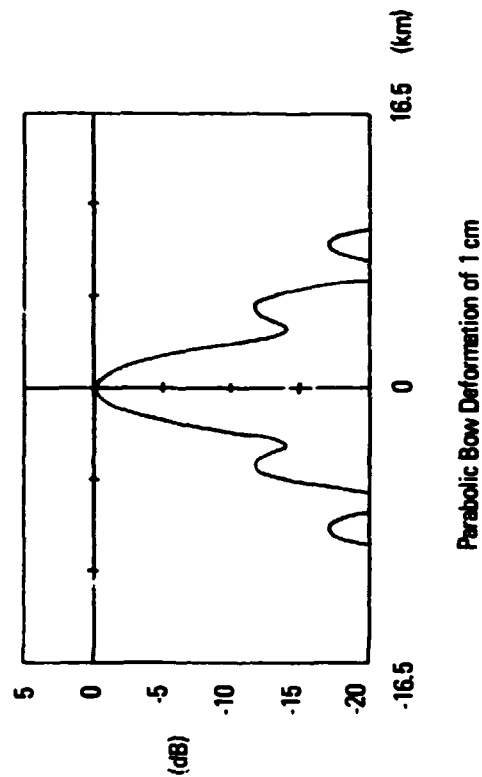
Figure 3.

Figure 4. Azimuth Main Beam Profile vs. Longitudinal Distance: f = 1.5 GHz, Tilt = 50 deg., and altitude = 200 km.
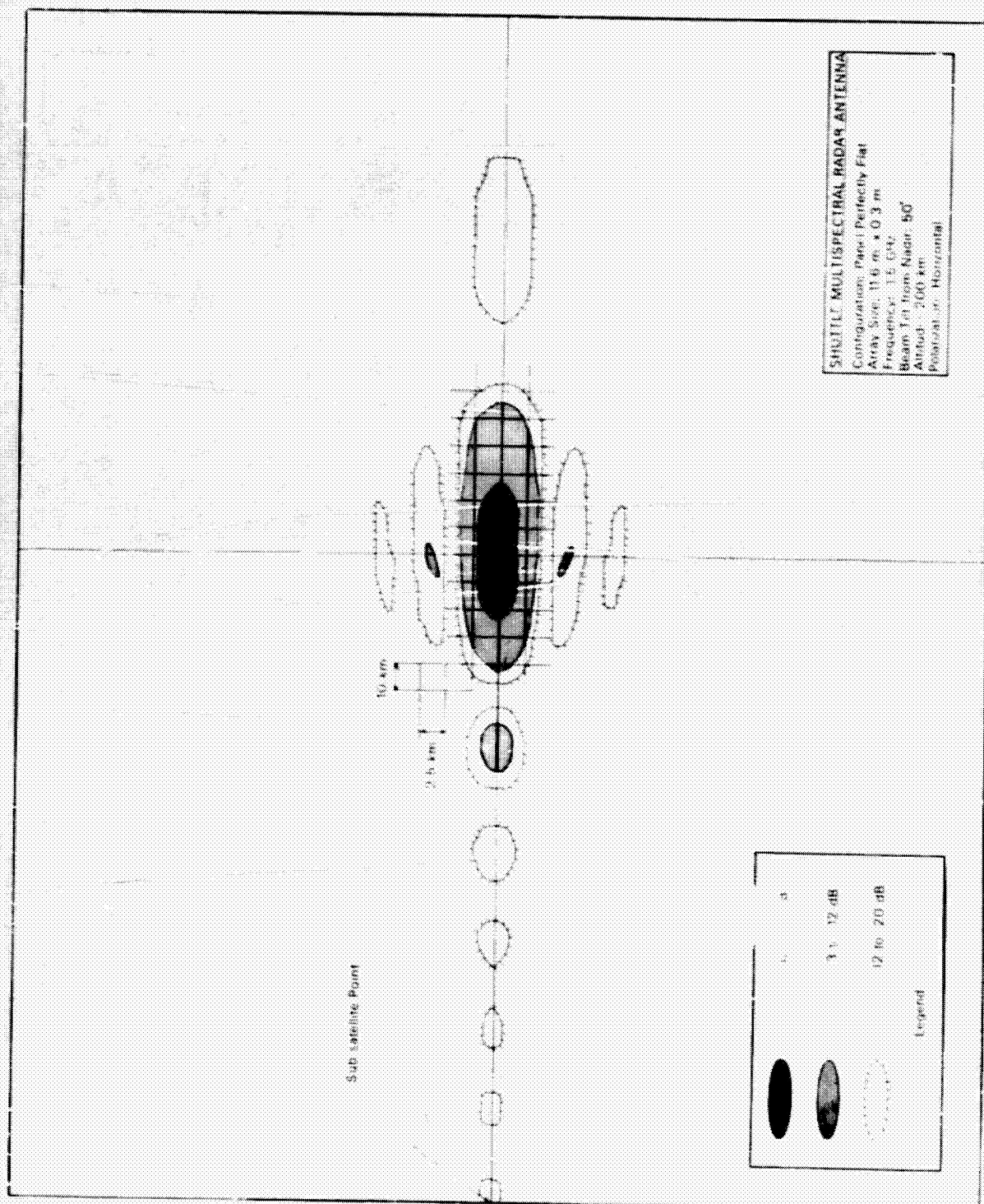
Figure 5a. Earth Surface Footprint - Panel Perfectly Flat.
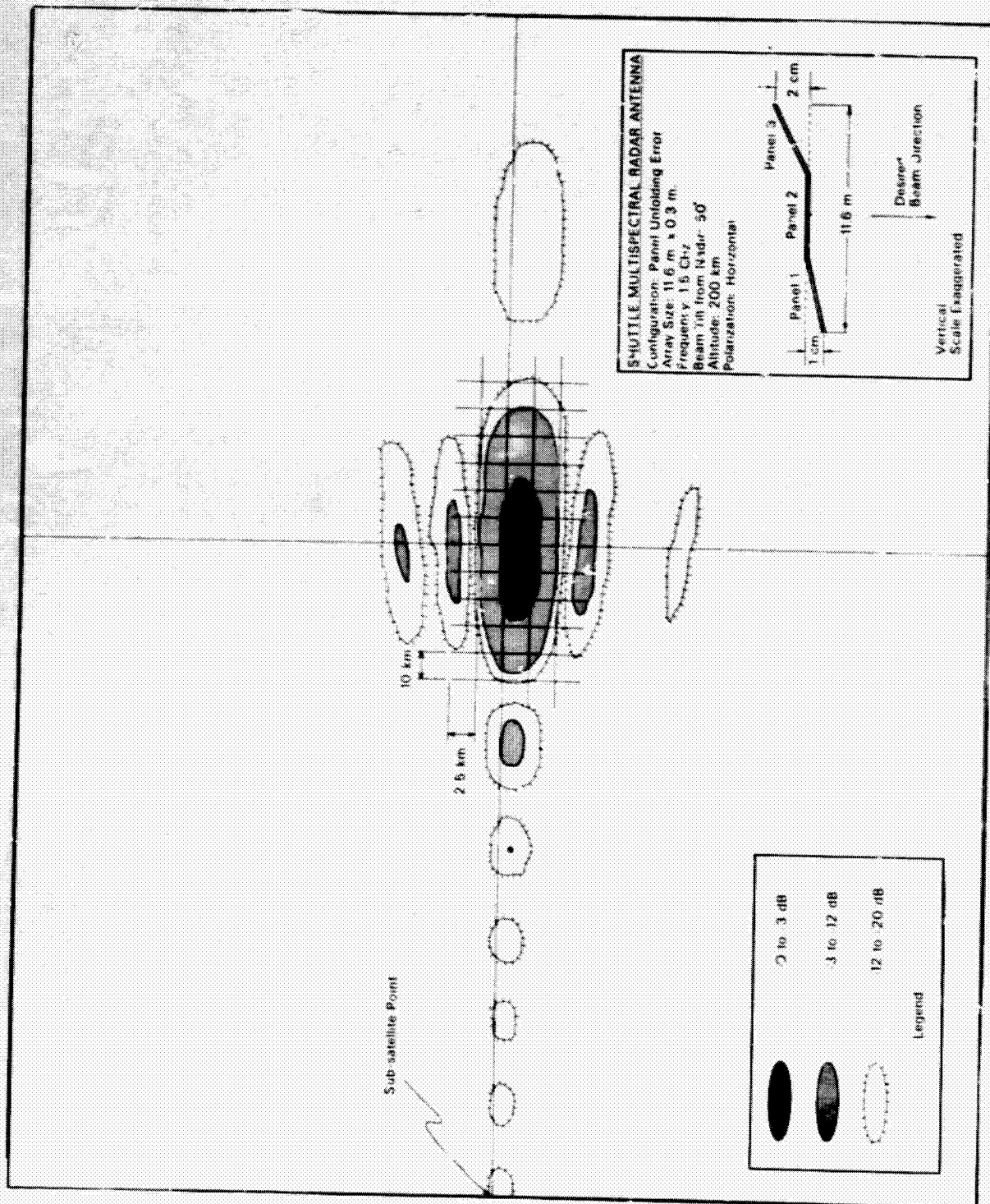
Figure 5b.   Earth Surface Footprint - Panel Unfolding Error.

IV-4-12
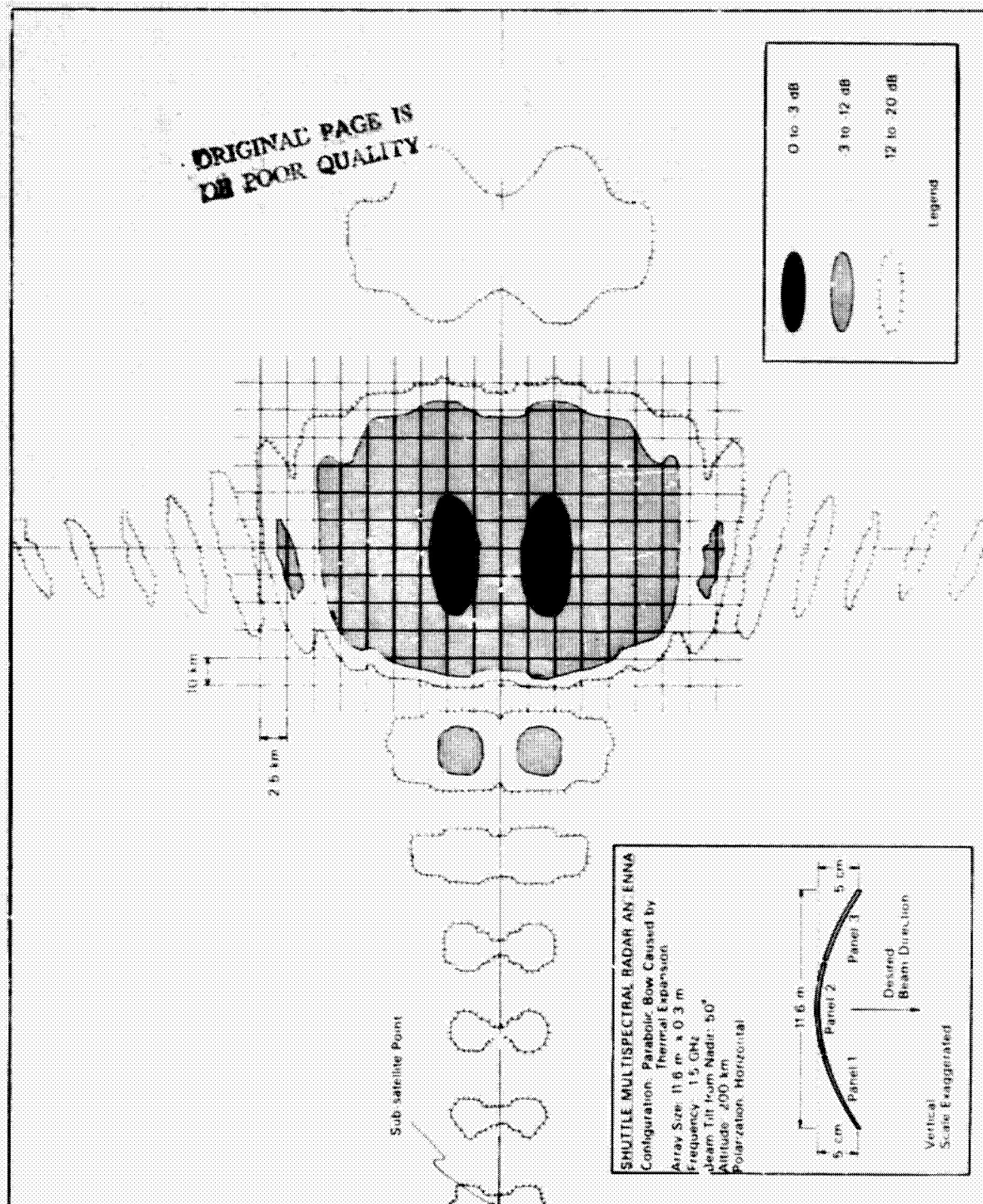
Figure 5c. Earth Surface Footprint - Parabolic Bow Error.

IV-4-13
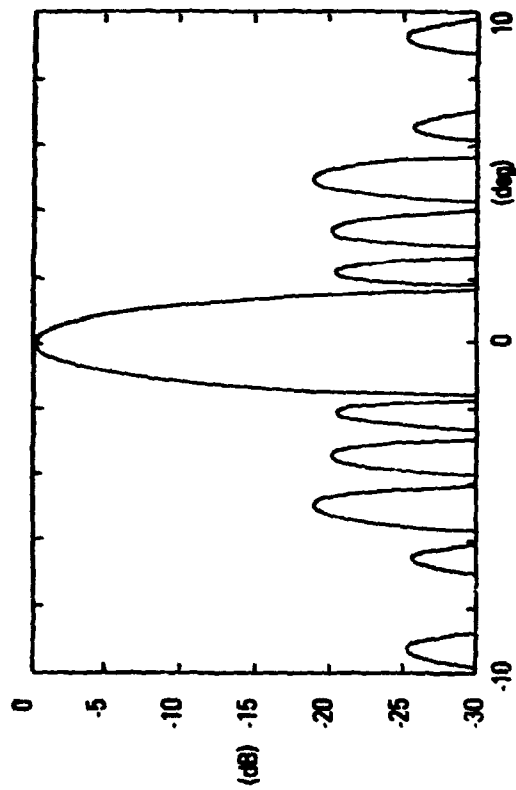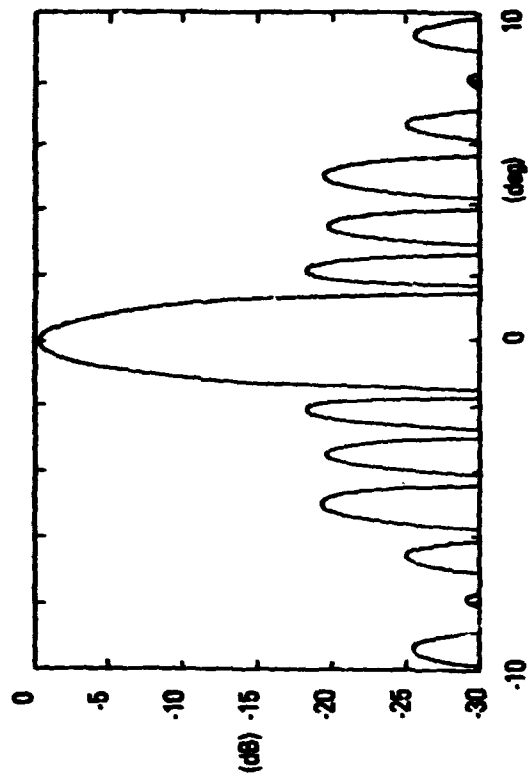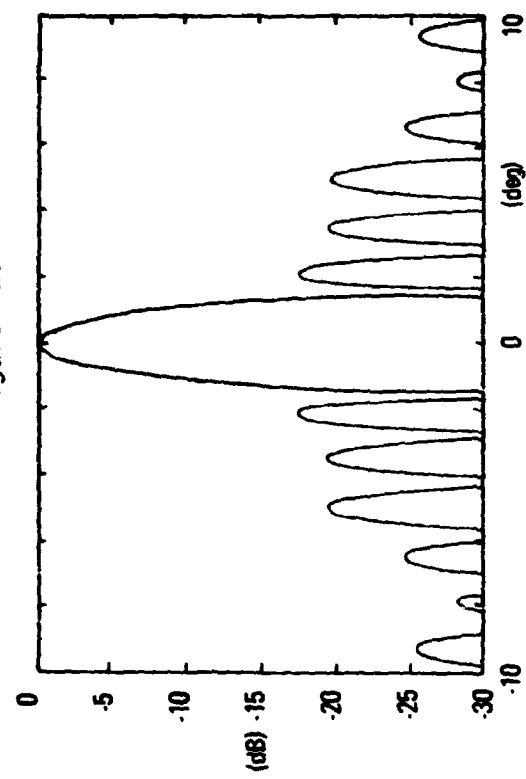
Figure 6b.

Figure 6a.

Figure 6c.

Figure 6a. SIR-A Antenna, Azimuth taper=1.5,
VSWR = 1:1, Baseline configuration.

Figure 6b. SIR-A Antenna, Azimuth taper=1.5,
VSWR = 1.1:1, Baseline configuration.

Figure 6c. SIR-A Antenna, Azimuth taper=1.5,
VSWR = 1.2:1, Baseline configuration

LOW LOSS, FLEXIBLE, LIGHTWEIGHT CORPORATE RF FEED SYSTEM FOR SAR ANTENNA APPLICATION

FRANK SCHIAVONE
SENIOR MEMBER OF TECHNICAL STAFF
BALL BROTHERS RESEARCH CORPORATION
POST OFFICE BOX 1062
BOULDER, COLORADO 80306

SUMMARY

Mechanical and electrical efficiency constraints imposed by the SEASAT-A Synthetic Aperture Radar (SAR) Antenna posed difficult design problems. After consideration of available standard cable and waveguide systems, it was determined that an optimum design could be obtained from a suspended substrate [1] RF feed system. Size and mechanical flexibility constraints forced the design of a flexible, suspended substrate section capable of 180-degree flexure. Original design goal for insertion loss over power division was 1 dB; measured results indicated 0.6 dB maximum across the band. Multipactor testing of system components indicated system breakdown capability in excess of 4 kW compared to a specification input maximum of 1500 W.

1.0   SEASAT SAR STRUCTURE

The basic SEASAT SAR structure is depicted in Figure 1 in an exploded view showing the essential elements. The expandable support structure provides a locking truss capable of holding the eight, 2.16m x 1.34m, lightweight, honeycomb, microstrip antenna panels flat to within 0.63cm (0.25 inch) over the entire 10.75m length. When folded, the panels are separated by 3.43cm (1.35 inches) to provide an overall package volume of 2.16m x 1.34m x 25.4cm exclusive of the tripod structure. To fit the confines of the closed package, the RF feed system lines were constrained to 1.4cm (0.55 inch) in height to allow for thermal blanketing. When the SAR is folded, the connecting RF lines between panels must be capable of 180-degree flexure without any performance degradation for at least 10 cycles. Actual tests provided confidence in performance by flexing over 200 cycles without degradation.

1.1   MICROWAVE FEED SYSTEM FORMATS

During the initial stages of fabrication, approaches using commercial components were considered and tradeoff estimations compared. The tradeoff comparison given in Table 1 was used as the basis for deciding to design a suspended substrate. Four

LAUNCH-RESTRAINT
MECHANISM

BIAXIAL DEPLOYMENT
MECHANISM

EXTENSION STRUTS

EXTENDABLE SUPPORT
STRUCTURE (ESS)
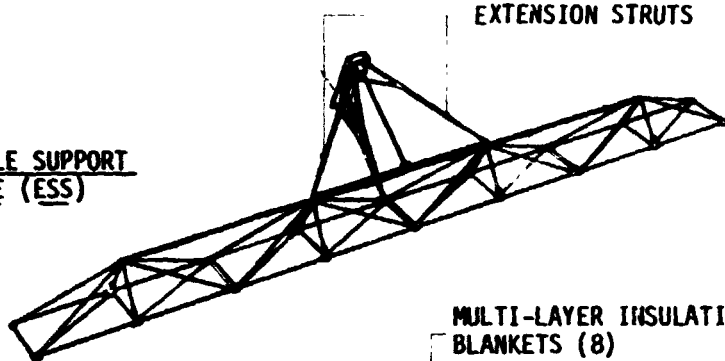
MULTI-LAYER INSULATION
BLANKETS (8)
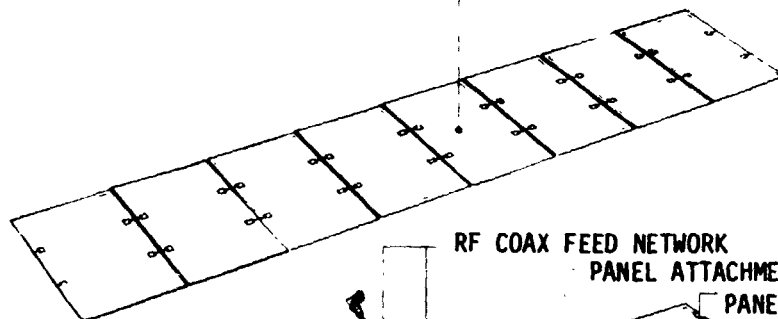
RF COAX FEED NETWORK
PANEL ATTACHMENTS (32)
PANELS (8)

2.16M x 11.0M ANTENNA
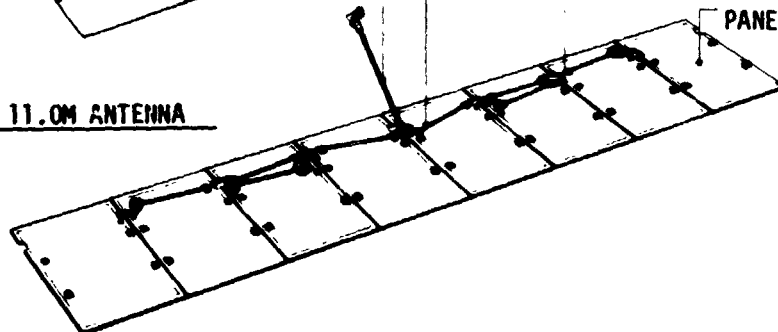
FIGURE 1

BASIC SEASAT LAYOUT

TABLE 1

MICROWAVE FEED SYSTEM TRADEOFFS

	COAX SYSTEMS						
	2,2,2 CORPORATE	5,4 Bi-PUS	8 OCTOPUS	W/ROTARY JOINT	UNSHIELDED MICROSTRIP	SUSPENDED SUBSTRATE	REDUCED HEIGHT WAVEGUIDE
ELECTRICAL							
Loss Budget	1.15	1.10	.95	.85	1.70	.55	.90
Phase Sensitivity (PPM/°C)	Good	Good	Good	Good	Good	Good	Good
Phase Stability	Fair	Fair	Poor	Good	Good	Good	Good
Multipactor Spacing	Poor	Poor	Poor	Fair	Excellent	Excellent	Excellent
Phase Length Trimability	Fair	Fair	Fair	Good	Good	Good	Good
Temp. Insertion Loss Sens.	Poor	Poor	Fair	Good	Excellent	Excellent	Excellent
Transition Loss Level	Poor	Fair	Good	Good	Excellent	Excellent	Excellent
MECHANICAL							
Complexity	Poor	Poor	Poor	Fair	Good	Good	Poor
Hinge Torque	Poor	Poor	Fair	Good	Good	Good	Fair
Packaging & ESS Compatibility	Poor	Poor	Fair	Fair	Excellent	Good	Fair
Weight (lb)	25	25	20	20	5	8	8
Thermal Expansion Loading	Poor	Poor	Poor	Fair	Excellent	Good	Good
Vibration Loading	Poor	Poor	Poor	Fair	Excellent	Good	Good
Vacuum Venting	Poor	Poor	Poor	Fair	Excellent	Good	Good
Mechanical Assembly	Fair	Fair	Fair	Fair	Excellent	Excellent	Excellent
THERMAL							
Power Dissipation	Poor	Poor	Poor	Fair	Good	Good	Excellent
Thermal Cycling Distortion	Poor	Poor	Poor	Fair	Good	Good	Excellent
Predicted RFM Temp. Profile	Poor	Poor	Fair	Good	Good	Good	Good
PROGRAM							
Mechanical Design Risk	Fair	Fair	Poor	Fair	Good	Good	Fair
Electrical Design Risk	Poor	Fair	Good	Good	Good	Excellent	Excellent
Material Availability	Poor	Poor	Poor	Poor	Excellent	Good	Good
Impact on Mechanical Layout	Poor	Poor	Poor	Poor	Excellent	Good	Fair
Impact on Thermal Layout	Good	Fair	Poor	Good	Excellent	Good	Fair

variations of coaxial feed systems were considered with different power split configurations (i.e., 2,2,2 giving 3 levels of 3 dB power splits) along with a microstrip feed system on the panel, and a reduced height waveguide. Within the mechanical, electrical and thermal constraints derived, the suspended substrate system appeared to be the optimal solution.

1.2   FEED SYSTEM REQUIREMENTS

Analysis of system requirements imposed stringent insertion loss and phase error requirements along with difficult mechanical specifications. The required low bellows torque to minimize expandable support system stress was met with considerable margin. Comparison of measured performance with required minimum specification, predicted performance, and measured results shows good agreement (Table 2). The power division tolerance was exceeded during test but not corrected because analysis of effect on antenna performance was shown negligible even with +2 dB amplitude deviation. Power balance within original specification could be achieved by balancing the output terminal mismatches with tunable output connectors.

1.3   FEED SYSTEM LAYOUT

The system layout is shown (Figure 2) with the power divider sections, bellows interconnection points (both valley and apex positions), and the 0.95cm (3/8 inch) air-articulated coaxial cables feeding the microstrip panels. The flexible input section ends in a TNC female connector interface specified by the customer; the outputs are TNC male.

Coaxial cable output lines were chosen to allow bending underneath the truss members to avoid mechanical interference when the SAR is folded.

1.4   MULTIPACTOR CONSIDERATIONS AND TEST RESULTS

Multipactor in high vacuum between electrodes with an RF potential between is a function of the peak field potential, the electrode spacing, and the transit time of the free electrons affected by the RF potential. The sinusoidally varying electric field accelerates the free electrons between electrodes in response to the field to cause collision with the electrodes and subsequent secondary emission. Since the phenomena is transit time induced, regions of multipactor occur dependent on the RF field period and electrode spacing. Thus, very high fields with small spacing relative to a half cycle may not lead to sustained multipactor. The best general rule for design use

SUBSTRATE-CABLE TRANSITION (TYPICAL)

ELBOW ASSEMBLY

APEX

ROUTING UNDER ESS (TYPICAL)

VALLEY

BELLOWS JOINT JUMPER

SUSPENDED SUBSTRATE FEED

3/8-INCH DIAMETER ALUMISPLINE TO REAR PANEL FEED (TYPICAL)

THIRD SECTION FEED

SECOND SECTION FEED

APEX

LMSC RF INTERFACE (TNC CONNECTOR)

INPUT SECTION 54274

FIRST SECTION

ESS (VALLEY)

TYPICAL STOWED TRUSS AND CABLE CROSSING

LMSC INTERFACE

INPUT LAUNCH RESTRAINT

ESS LOWER BRACE

ESS SQUINT ROTATION

POWER DIVIDER

PANEL UNFOLD BELLOWS

NOD AND SQUINT ROTATION FREEDOM

FIGURE 2

SEASAT FEED SYSTEM LAYOUT

TABLE 2
SUSPENDED SUBSYSTEM FEED SYSTEM - FUNCTIONAL REQUIREMENTS

PARAMETER	REQUIREMENT	EXPECTED PERF.	MEASURED PERF.
Insertion Loss—Input Port to Center of Panel	0.9 dB	0.84 dB	.60 dB
Input VSWR Rel. 50Ω			
With Panels Installed	1.5:1	1.5:1	1.5:1
With Ports @ 50Ω	1.3:1	1.2:1	1.2:1
Power Division to Ports	-9 $\pm$ 0.5 dB	-9 $\pm$ 0.5 dB	-9 $\pm$ 1.0 dB
Bandwidth (Basis for all Elect. Perf.)	$\pm$11 MHz	$\pm$11 MHz	$\pm$11 MHz
Center Frequency	1275 MHz	1275 MHz	1275 MHz
Input Power - Peak @ D.S. = .045	1500 W	OK	OK
Average	90 W		
Phase Error (Between Panel Ports)	$\pm$5°	$\pm$5°	$\pm$4°
Weight	15 lbs	12 lbs	
Input Connector Type	TNC Female Recep.	OK	OK
Panel Termination	3/8" Dia. Alumspline Coax	OK	OK
Temperature Range			
Storage	-30 to +140°F	--	OK
Stowed	-40 to +100°F	--	
Operating	-40 to + 80°F	--	
Test-Stowed-Qual	-66 to +176°F	OK	OK
Test-Operating-S/S Acceptance	-40 to + 80°F	OK	OK
Envelope-Rel. to 1/4" thick Panels			
Back-to-Back Panel Spacing-			
Stowed	1 3/8" Max	OK	OK
Front-to-Front Panel Spacing-			
Stowed	1/8" Max	OK	OK
Protrusion Beyond Panel Edges	1" Max	OK	OK
Flex Joint Torque - Per Hinge (Max)	1 ft-lb	1/2 ft-lb	1/30 ft-lb

a .plies a criteria based on the lowest power-spacing combination required to initiate multipactor. This is a functi-:: of the geometry used and is illustrated in curves of multipact·r re;;ions for air-lo·.ded coax lines and parallel plate configurations [2]. Multipactor can be cured by interp·sing high quality dielectric provided that care is used in :illing the void. This is the case where coax cable is used on spacecraft at levels above the critical multipactor ievel. Other ionization phenomena can occur if partial gas entrapment occurs in the RF structure; cauticn should be exercised if dielectric or foam-filled RF systems are employed.

The most useful general formula found for design was provided by Lockheed Aerospace and is given below:

$$P_{BRK} = 6.124 \cdot 10^4 \cdot \frac{Fo^2 \cdot S^2}{Zo} \tag{1}$$

Fo = operating frequency (GHz)

S = electrode spaci.g (cm) -3.951·10^5 f·;·S (IN)

Zo = RF structure   .cteristic impedance (ohm)

This equation has been ir·cu on prcvious multipactor test measurements made on earlier SEASAT-suspended substrate components and appears conservative. Test results are given in Table 3.

Testing is most easily performed by monitoring RF pulse reflected or transmitted power. Reflected power is slightly easic· to monitor for breakdown than insertion i. variation but not sig..ificantly different. Where power division components are tested, multipactor in the output arms would be more evident in the insertion loss monitoring because of the masking effect of the power division.

2.0   REFERENCES

[1]   Dennis L. Gish, "Characteristic Impedance and Phase Velocity of a Dieiectric-Supported Air Strip Transmis.ion Line with Sidewalls," IEEE Trans. Vol. MTT-18, No. 3, March 1970.

[2]   R. Woo, "Final Report on RF Voltage Breakdcwn in Coaxial Transmission Lines," Tech. Report 32-1500, Jet Prooulsion Laboratory, 1 October 1970.

TABLE 3

MULTIPACTOR TEST RESULTS – DEVELOPMENTAL COMPONENTS

Element	Matched Exp. Pk. Pwr.	Spacing Zo	Lockheed Form Multipactor	JPL (Par Plate) Multipactor	Pwr. Level Applied
Antenna (2 x 2)	1.46w	.250"/25Ω	~800w	~1000w	>2-5w No Bkdwn.
High Power (.625")	750w	.3075"/50Ω	1214w	~2700w	>1500w No Bkdwn.
Hi Po Divider (.625")	750w	.3075"/50Ω	1214w	~2700w	>1200w No Bkdwn.

RF FEED PREDICTED BREAKDOWN LEVELS – BASELINE CONFIGURATION

Element	Matched Exp. Pk. Pwr.	Spacing Zo	Lockheed Form Multipactor	JPL (Par Plate) Multipactor	Pwr. Level Applied
Main Lines (.550")	750w	.270"/36Ω	1300w	~4500w	>4500w No Bkdwn.
Input Line (.625")	1500w	.3075"/36Ω	1687w	~4700w	>4500w No Bkdwn.
Panel Mtd. Bellows (.445")	750w	.220"/36Ω	863w	~4500w	>4500w No Bkdwn.
Input Bellows (.625")	1500w	.3075"/36Ω	1687w	~4700w	>4500w No Bkdwn.

A DUAL POLARIZED ANTENNA SYSTEM
USING A MEANDERLINE POLARIZER

HENRY A. BURGER
GOODYEAR AEROSPACE CORPORATION
ARIZONA DIVISION
LITCHFIELD PARK, ARIZONA 85340

Certain applications of synthetic aperture radars, e.g., aerial crop surveying, require transmitting on one linear polarization and receiving on two orthogonal linear polarizations for adequate characterization of the surface. To meet the current need at minimum cost, it was desirable to use two identical horizontally polarized shaped beam antennas and to change the polarization of one of them by a polarization conversion plate. The plate was realized as a four-layer meanderline polarizer designed to convert horizontal polarization to vertical (see Figure 1).

Meanderline polarizers have been used before to convert linear polarization to circular.[1, 2] The linear wave is conceptually split into two components which are separated i- phase by 90 degrees to yield circular polarization. If the phase shift is increased to 180 degrees, linear polarization results in the orthogonal sense from the original wave.

The mechanism used for splitting and separating the components is the meanderline circuit. A plane containing a regular pattern of circuits will be a reactive surface to an incident wave, appearing inductive to any E-field component parallel to the run of the lines and capacitive to any component perpendicular to the lines. A series of such sheets can be modeled as a pair of periodically loaded transmission lines where the capacitive or inductive loadings act to retard or advance the phase of the incident wave. By adjusting the reactance values, the spacings between the sheets, and the angle of the meanderlines with respect to the incident wave E-field, any input polarization may be converted to any output polarization.

The question of nonnormal incidence arises because of the present application. All of the available theory assumes normal incidence on the plane containing the circuits. However, in calculating the effects of wave passage across a dielectric boundary, the properties of the boundary are constant. The incident wave is considered to travel across normal to the surface, and the effects of nonnormal incidence angles are accounted for in the propagation constant and in the free space impedance. Dielectric material properties are invariant with incidence angle. It is therefore reasonable to consider that the same would apply to reactive surfaces.

Laboratory tests have confirmed that the circuit susceptance is independent of incidence angle, at least over the range of angles observed. Tests were made with a standard flat-panel testing table where the phase and amplitude of the transmitted wave were monitored as a function of incidence angle. The measured insertion phase differenc: was compared with computed insertion phase differences assuming that the susceptance of the surface is a constant. The results were virtually identical and well within experimental error (see Figure 4).

A polarizer was constructed using four layers of meanderline sheets separated by precisely machined foam spacers. Because bandwidth was not a criterion in this application, all four layers were identical. The spacers were chosen for the best impedance match for up to 30 degrees incidence angle, considering all glue layers, mylar substrates, etc. The polarizer was then attached to the shaped beam antenna at about a 20-degree angle, as shown in Figure 1.

The performance of the polarizer was very much as expected, except for a high cross-polarized energy level (see Figures 2 and 3). The effect of the conversion on the shape of the shaped beam was negligible, as was the effect on the VSWR. The cross-polarized energy proved to have two sources. One source was a result of the small yet significant reflection

from the polarizer returning to the antenna. As the reflection is also rotated in polarization, some of this energy is reflected from the face of the antenna again, giving rise to a very low Q cavity. Radiation ultimately occurred at the undesired polarization. This component was removed by including a resistive card mode suppressor between the polarizer and the antenna, and actually manufactured as part of the polarizer assembly.

The second source of cross-polarized energy was traced to the existence of surface waves on the polarizer. Two dominant waves could be expected, and these could be expected on the outside of the finished assembly as well as between the sheets. These modes leaked and manifested themselves as a grating lobe structure in the cross-polarized response. Various efforts were made to reduce these modes, including absorber along the edges, staggering the circuit elements, etc., but none had any beneficial effect. Because this response was sensitive to the angle of the polarizer with respect to the antenna, an angle was ultimately selected which minimized the cross-polarized energy.

The two antennas of the dual polarized system were arranged one above the other. Because the shaped beam looked down, the modified antenna was placed on top to avoid interception of energy from the adjacent antenna. This arrangement resulted in a higher cross-polarization level in the modified antenna, but still within acceptable limits.

This research was performed for Johnson Space Center under NASA contract NAS 9-15007.

References:

1. Blakney, T.L., Burnett, J.R., Cohn, S.B.: "A Design Method for Meanderline Circular Polarizers." 22nd Annual Antenna Symposium, October, 1972.

2. Young, L.. Robinson, L.A., Hacking, C.A.: "Meander-Line Polarizer." IEEE Transactions on Antennas and Propagation, May, 1973.
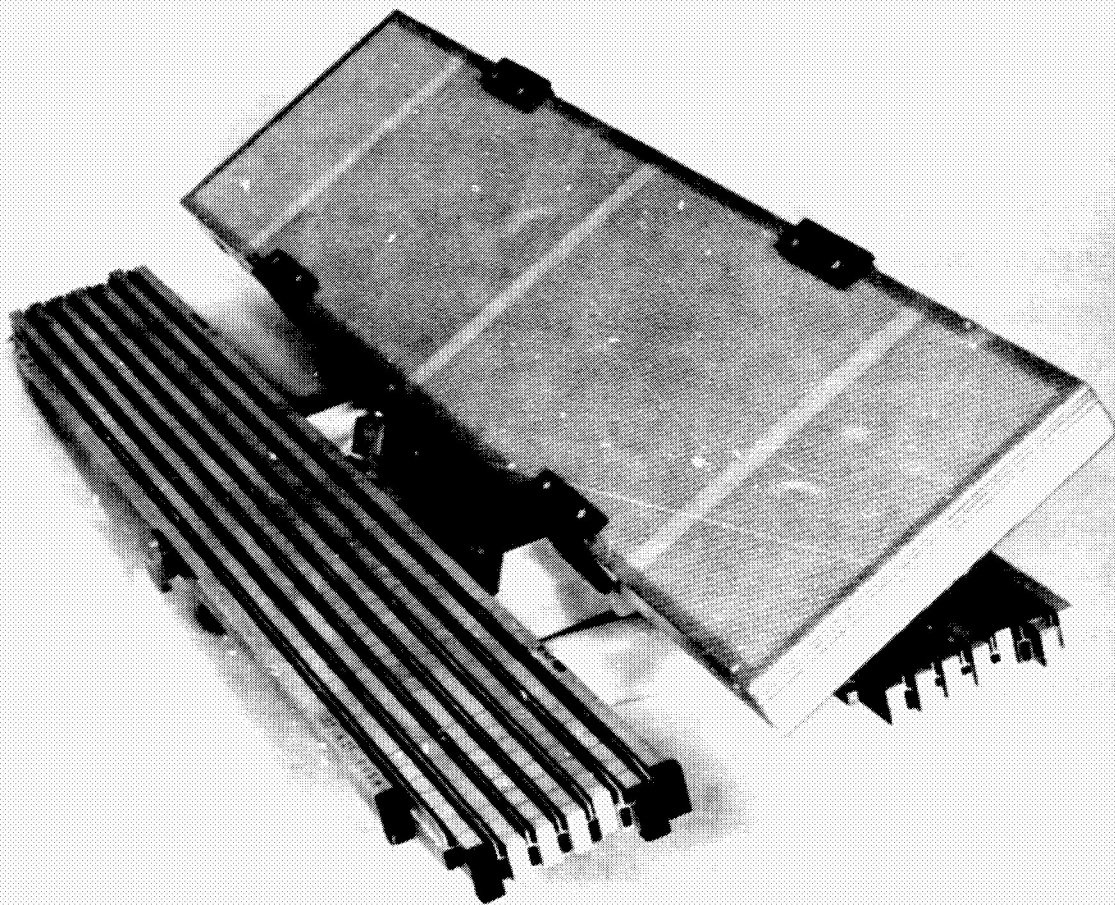
Figure 1 - Dual Polarized Antenna Assembly
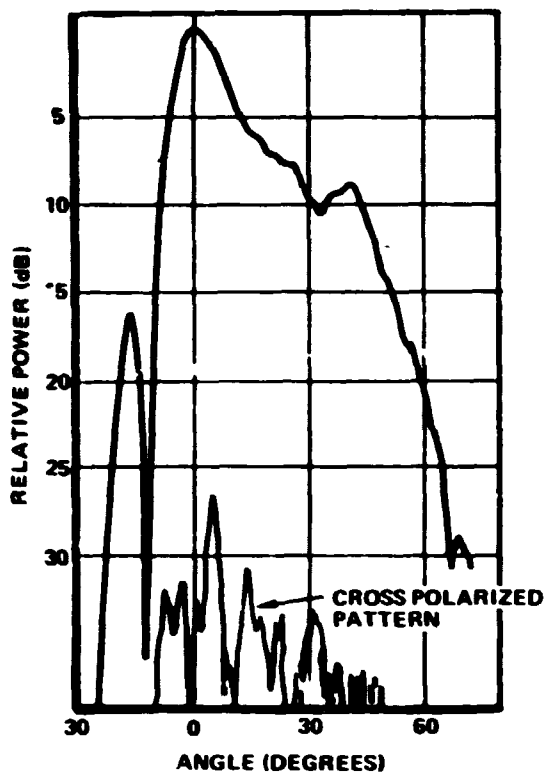
Figure 2 - Horizontally Polarized
Array Elevation Pattern
(Bottom Array)
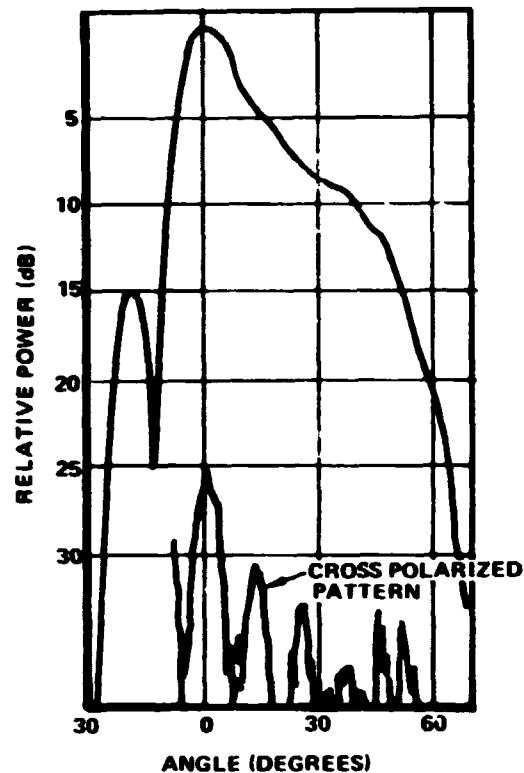
Figure 3 - Vertically Polarized
Array Elevation Pattern
(Top Array with Polarizer)

ORIGINAL PAGE IS
OF POOR QUALITY
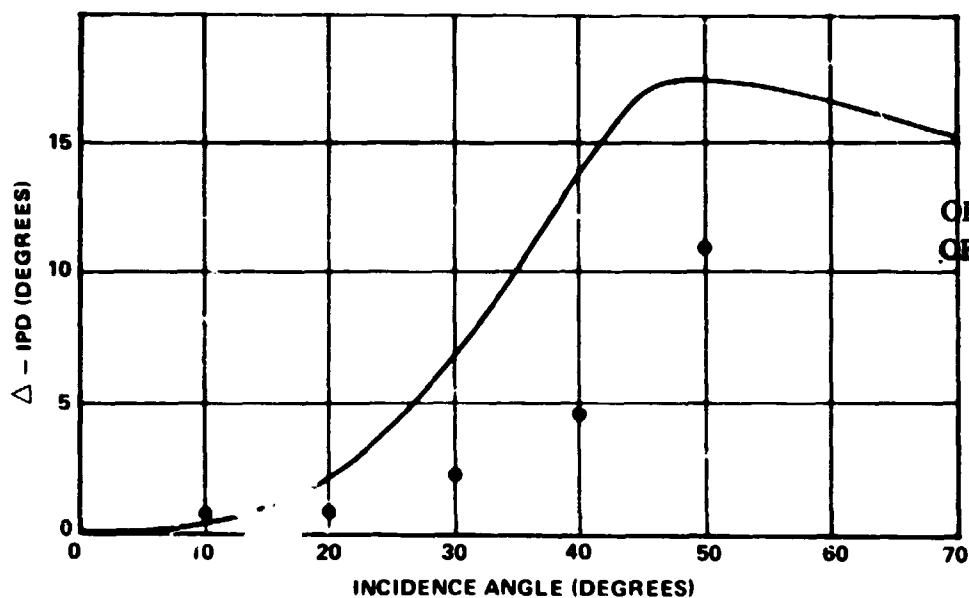
Figure 4 - Expected and Measured Change of Insertion Phase Difference
with Incidence Angle of A Representative Sandwich Assembly

THURSDAY, MARCH 9, 1978

EFFECTS OF RANGE BIN SHAPE AND DOPPLER
FILTER RESPONSE IN A DIGITAL SAR DATA PROCESSOR

CARROLL R. GRIFFIN

APPLIED RESEARCH LABORATORIES
THE UNIVERSITY OF TEXAS AT AUSTIN
AUSTIN, TEXAS 78758

SUMMARY

In calibrating the backscatter coefficient obtained with an imaging synthetic aperture radar (SAR) system to determine absolute values of radar cross-section and reflectivity it is common practice to use a target of known radar cross-section placed within the scene. A corner reflector acts as a point target, but the return from it may not be centered in the resolution cell. It is important, for accurate calibration, to perform straddling corrections based on the range bin and doppler filter response curves.

1.0 THE CALIBRATION PROBLEM

A method commonly used to calibrate the backscatter coefficient in an imaging SAR system is to place a point target of known radar cross-section (RCS), such as a corner reflector, within the imaged area. Without the calibration target, the absolute RCS or σ^0 value can only be inferred. Figure 1 is a SAR map made by the FLAMR (Forward Looking Advanced Multimode Radar) System, a digital processor system using binary phase coded pulse compression and a doppler signal processor with 16 pre-summed doppler filters (sixteen point Complex Fourier Transform). This is a map of a vehicle array at the Marine base near Barstow, California. With a suitable calibration target available in the array, cross-section data on these vehicles may be extracted provided certain corrections are made.

1.1 RESOLUTION CELL STRADDLING

The calibration target, a trihedral corner reflector, may be located within the imaged area, and if its nominal RCS is known as a function of aspect angle, it may be used as a reference, provided it is in the peak response of the range and azimuth filter response, and is not saturating the radar receiver. The corner reflector should also be an isolated point target well

above the surrounding clutter level. Figure 2 is of an array of three corner reflectors positioned in an agricultural scene mapped by the FLAMR SAR. The reference corner reflector for σ^0 and RCS data is the one in the center of the array 45.72 cm (18 in.) on the inside dimension. Figure 3 is the measured response of this target, so that its value may be known, provided its aspect to the radar is known. Frequently, however, the sampling grid of the radar system straddles the point target and it then becomes necessary to correct the observed response in both range and cross-range for such effects. In order to make such a correction, the shape of the range bin and of the doppler filter response must be known. These points may be summarized as follows for the special case of impulse response symmetry, and invariance of the impulse response in azimuth:

Let $\quad f$ = amplitude response of a resolution cell = $f(r, a)$ with r the range dimension, a the azimuth dimension, then

$$|f^2| = \text{power response} = f(a, r_0) \, f(r, a_0) \tag{1}$$

and r_0, a_0 is the point of maximum response. For a point target, power received P_R is

$$P_R = K \, \sigma \, f^2 \, (r_t, a_t), \text{ in which} \tag{2}$$

all the constant radar parameters (including the range, although it may cause a usually negligible error) are lumped into a constant K, and r_t, a_t define the actual position of the scatterer of cross-section σ in the resolution cell. The value of $f^2 \, (r_0, a_0) = 1$. The straddling corrections in azimuth and range are made to effectively convert the value of $f^2 \, (r_t, a_t)$ to unity, so that the result is:

$$\frac{P_R}{f^2 \, (r_t, a_t)} = K \, \sigma \, f^2 \, (r_0, a_0) = K\sigma \tag{3}$$

from which K may be known

$$K = \frac{P_R}{f^2 \, (r_t, a_t)} \tag{4}$$

assuming σ is known for the reference calibration target (corner reflector).

1.2 STRADDLING CORRECTIONS

The process of modifying P_R by the factor f^2 (r_t, a_t) is a two-step one using the range and azimuth straddling correction curves. These are derived from the response curves of a range bin and doppler filter, which are presented in Figure 4. This particular SAR system had 3 nominal resolutions of 6 meters, 12 and 24 meters (20, 40 and 80 feet). The doppler filter shape was constant for the 3 resolutions but the range bin shape was not, as may be observed. Figure 5 indicates how two adjacent range bins overlap and the correction curve which may be derived for straddling corrections.

1.3 THE CORRECTION CURVE

The straddling correction curve is obtained by plotting the difference between the maximum of the response curve and the value at every other point as a function of the difference between one curve and its adjacent neighbor, up to the point of zero difference, both toward, and away from, the radar. From this, it is evident that the maximum correction will be required when the target exhibits equal returns in adjacent range bins. This procedure for obtaining the correction curves may be understood by referring to Figure 5. When the filter response is symmetrical, as it is in azimuth, the correction curve is the same either in the mapping direction or away from it.

2.0 CORRECTION OF OBSERVED DATA

A print-out of the pixel data is useful in making the straddling correction, on a point target. The entire map, which in the FLAMR case consists of 356 azimuth lines and 384 range bins, need not be printed. The corner reflector can usually be roughly located using a measurement of a map photograph. Figure 6 illustrates the procedure. The filter magnitude value next largest to the maximum is used in azimuth, and in range, to obtain the difference. T larger range difference is away from the radar, 15 filter magnitude values. Entering the range straddling correction curve "away from the radar" the upper curve of Figure 5, gives a correction in filter magnitude values to be added to the maximum. The filter magnitude values can be converted to dB by multiplying by the factor .376 or approximately 3/8.

This is because the recorded filter magnitude logarithmic data is

$$M_R = 16 \ Log_2 \sqrt{f_I^2 + f_Q^2} = 16 \ Log_2 \ f \qquad (5)$$

ignoring computer function algorithm error. The digital filter magnitude data are recorded in an 8-bit format with a maximum possible recorded value of 199. In decibels the filter magnitude is given by

$$M_{dB} = 20 \ Log_{10} \sqrt{f_I^2 + f_Q^2} = \left(\frac{20}{16}\right) \left(Log_{10} 2 \right) M_R \qquad (6)$$

$$= .376 \ M_R$$

2.1 OBTAINING THE CALIBRATION FACTOR

The straddling correction curve may be either in dB or in filter magnitudes. Figure 6 illustrates how the value of K is reached with straddling corrections and corrections for off-bore site aspect of the radar to the corner reflector.

2.2 DETERMINING AN AREA FACTOR FOR σ°.

The effective area for the resolution cell is required in calculations of reflectivity for different types of terrain. The usual procedure is to average the values for a representative sample of pixels, apply the calibration factor and then divide by the effective area of a pixel.

$$\sigma^\circ \ (dB) = \sigma \ (dBm^2) - 10 \ Log \ Area \ (m^2) \qquad (7)$$

The effective area is the effective range dimension times the effective azimuth dimension, found by integrating the areas under the impulse response curves and dividing by the peak response. Table 1 provides these values as obtained for the FLAMR System.

TABLE 1

ORIGINAL PAGE IS
OF POOR QUALITY

EFFECTIVE RESOLUTION CELL AREA

RESOLUTION	NOMINAL DIMENSIONS				BALDWIN HILLS TEST RESULTS			
	AZ (m)	RNG (m)	Area (m^2)	Area (dBm^2)	AZ (m)	RNG (m)	Area (m^2)	Area (dBm^2)
LOW	24	24	576	27.6	28.6	18.3	523.4	27.1
MEDIUM	12	12	144	21.6	14.3	9.1	130.1	21.1
HIGH	6	6	36	15.6	7.2	4.6	-3.1	15.2

3.0 OBTAINING THE RANGE AND AZIMUTH FILTER RESPONSE

The system was measured using a large ($30,000$ m^2) corner reflector situated
on a hill (Baldwin Hills) about 10 kilometers from the Los Angeles
International Airport with a clear radar line-of-sight. Figure 7 is a view
of the test bed aircraft on the ramp at its operating base. The system is
put under manual control and with the corner reflector return positioned in
the zero doppler (d.c.) filter, the range is incremented by .75 meters by
changing the start range window. The start range is moved through at least
three range bins, and the data recorded from d.c. filter. Of course, system
power is monitored and various system parameters are recorded for any con-
figuration variables, such as number of pulses per array, pulse compression
length, code and sequence. The data obtained may then be plotted as a
function of range and several of the curves averaged to obtain the average
response of the system in range for the different bandwidths (resolutions)
available. The doppler filter shape may be measured in much the same way,
by adjusting the frequency synthesizer in approximately 1/10 filter width
increments over a range of from at least the center of filter fc-4 to the
center of fc + 4. The digital doppler filter is well behaved, and for FLAMR
is characterized by the expression

$$f(x) = \frac{\text{Sin}\left(\frac{\pi x}{12}\right)}{\left(\frac{\pi x}{12}\right)} \left[\frac{1 + .06\left(\frac{x}{12}\right)^2}{1 - \left(\frac{x}{12}\right)^2} \right] \tag{8}$$

which may be squared and the area obtained in watt-seconds by integrating under the curve using the method of residues. The curves for range response may be integrated using Simpson's Rule or some other procedure.

4.0 TYPICAL RESULTS

Without going into detail, some typical results are provided in Figure 8, for the reflectivity of various types of scene content from Figure 1. These values were obtained by use of the calibration factor obtained using the corner reflector data of Figure 3. Aspect angle data were obtained from the aircraft data tapes (altitude), from the radar map (azimuth lines vs. road directions), and ground truth information regarding the orientation of the reflector.

5.0 REFERENCES

1. Griffin, C. R., Amendment to ARL:JT Technical Report TR-76-8 "Radar Reflectivity Study", APL-ITM-77-1, 6 January 1976

2. Rasco, W. A., and Griffin, C. R., Radar Reflectivity Study, ARL-TR-76-8, Air Force Avionics Laboratory, March 1976

Figure 1.   FLAMR Map of Barstow Vehicle Array

Reference Corner
Reflector

Figure 2.   FLAMR Doppler Beam Sharpened Map,
San Joaquin Valley Rural Scene

**EIGHTEEN INCH
TRIHEDRAL CORNER REFLECTOR**
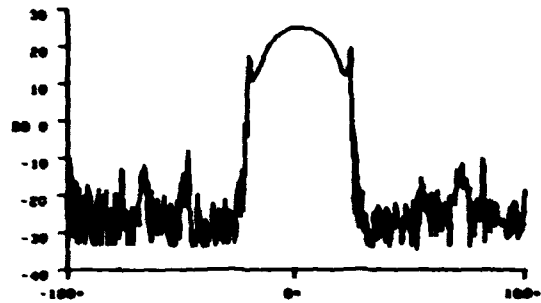
Figure 3.   Measured RCS of a 45.72 cm Trihedral Corner Reflector
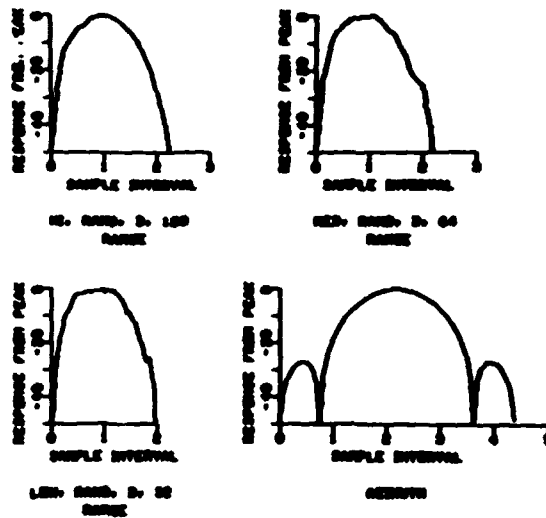
FLAMR IMPULSE RESPONSE

Figure 4.   Range Bin and Doppler Filter Response Curves for FLAMR

STRADDLING CORRECTIONS FOR
RANGE AND AZIMUTH FILTER SHAPES
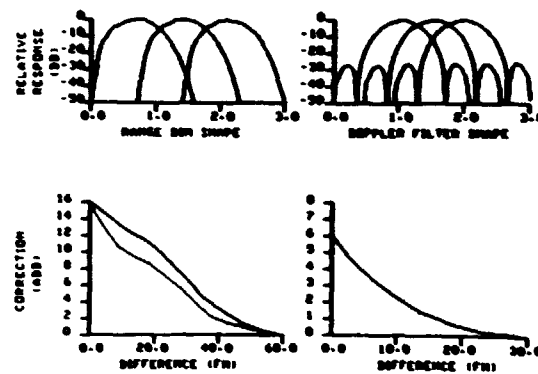
Figure 5. Adjacent filter overlap and Derived Straddling Correction Curves

Filter Magnitude   Original Value   163
Data in Region of   Azimuth Straddling Correction   001
Corner Reflector   Range Straddling Correction   012
                                                         ───
                                                         176

       ↑

               148

       128   163   149   σ CR = 27.4 dB

Range   105   Az/El correction = −2.1 dB

       ◄── Azimuth   σ CR = 25.3 dB

              K = (.376) (176) − 25.3 = 40.7 dB

Figure 6. Establishing the value of K using straddling and
           Aspect Angle Corrections.
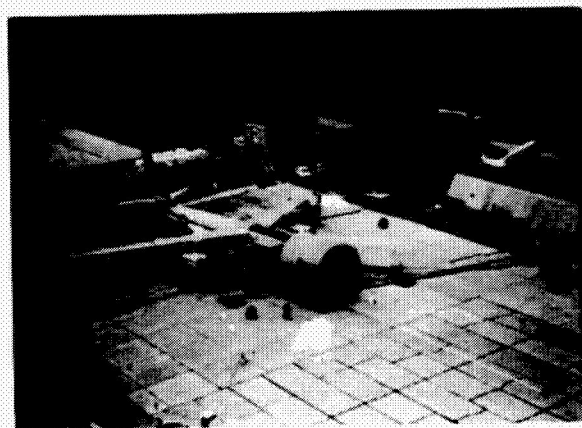
Figure 7. FLAMR System Test Bed, Ramp Ground Testing.
Los Angeles International Airport

REFLECTIVITY VALUES DERIVED FROM
FLAMR DATA

Urban or Built-up Areas (Winery)

Fig Orchard	(-14.8)
Mature Vineyard	(-15.2)
Grape Vineyard	(-16.0)
Razed Vineyard	(-18.2)
Cotton	(-18.7)
Maize	(-19.1)
Clover	(-20.4)
Plowed Field	(-20.9)
Harrowed Field	(-23.0)
Bare Field	(-24.1)
Canal	(-25.2)

f = 16.4 GHz
Vertical Polarization
Grazing Angle = 5.5 Degrees
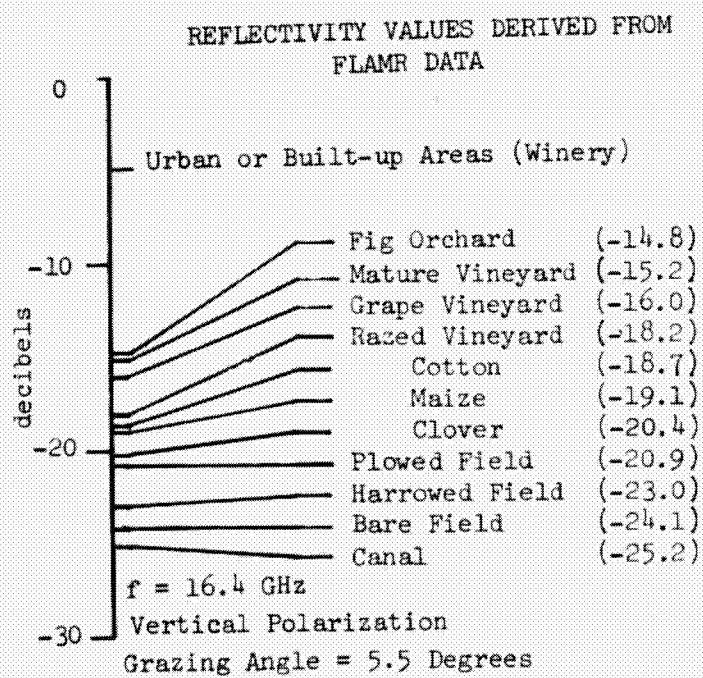
Figure 8. Typical Reflectivity Values

ELECTRONIC SAR PROCESSORS FOR SPACE MISSIONS*

CHIALIN WU
JET PROPULSION LABORATORY
CALIFORNIA INSTITUTE OF TECHNOLOGY
PASADENA, CALIFORNIA 91103

SUMMARY

This paper reports some interim results relating to an on-going effort to develop an electronic processor for real-time processing of synthetic aperture radar data. An experimental laboratory processor is being developed as a testbed for design of on-board processors for future space missions. This paper describes the configuration of the experimental processor and discusses technical factors pertaining to the design.

1.0 INTRODUCTION

The utility of airborne synthetic aperture radar (SAR) [1] [2] has been extensively investigated in the past two decades. Because of the capability of microwaves to penetrate through clouds and the unique contrast characteristics in SAR imagery, radar imaging is considered particularly useful for· surface topographic mapping and for all-weather sea state observations. To extend the utility of airborne SAR so that the imaging radar could also be used as a global environmental monitoring device, NASA is planning to launch a series of earth and planetary spacecraft with on-board imaging radars. The SEASAT-A satellite which will be launched in May 1978, is the first in the series. The SEASAT-A radar is designed to be able to produce imagery with 25 meter resolution and 100 km swath width on the earth's surface [3].

The high resolution and wide swath coverage called for by the SEASAT-A SAR imply an extremely high data acquisition rate. SEASAT-A will use a newly developed ground-based digital tape recorder with 120M bits per second recording capability. The large amount of SAR data acquired must be processed

---

to produce images in a satisfactory format. Due to various peculiarities in the doppler characteristics of spaceborne SAR data, the SAR processing and associated compensation procedures can be very involved. Currently available SAR processors are not able to produce the imagery in a timely and economic manner.

Although SEASAT-A SAR sets a data acquisition rate from the spaceborne sensor that is unprecedented, future earth orbit imaging radars may adopt similar performance criteria and data acquisition requirements. An effective way to meet the data processing needs in future anticipated operational radar imaging missions is to employ on-board SAR processors. Such on-board processors would produce SAR imagery from echo signals in realtime. Not only can the transmission bandwidth for imagery data be reduced by a large factor (compared with the unprocessed raw data transmission rate), but direct image transmission to users in the vicinity of the sensor also simplifies the data handling and distribution procedures.

To achieve the goal of on-board SAR processing, JPL initiated a phased development task in the beginning of FY 77. The first phase involves develcp-ment of a ground based experimental SAR processor. This processor will have the capability to perform realtime SAR processing. The processor architecture and device technology will be chosen to be amenable to future on-board implementation. After its completion, scheduled for the end of FY 79, the performance of the processor will be evaluated by processing a 20 km swath of the then available SEASAT-A SAR data at the real-time data rate. The output image data will comprise 4 looks and exhibit 25M resolution. The next phase of the work involves the design and construction of a SAR processor to be used in an on-board processing experiment on a future Shuttle Imaging Radar (SIR) mission. Also, it is anticipated that a simple low-resolution on-board SAR processor will be developed for a 1983 Venus Orbital Imaging Radar (VOIR) Mission. The development of these two on-board processors may begin prior to the completion of the ground based experimental processor. Nevertheless, concepts, details of the design, and perhaps some specially developed devices will be directly applicable to these follow-on activities. Although the emphasis has been placed on the development of on-board SAR processors, the

ground-based experimental SAR processor naturally will serve also as a model for real-time ground station processing of future spacecraft-gathered SAR data.

The task of developing the experimental SAR processor was divided into the following three phases: the system design, the detailed design, and the implementation. The system design phase was concluded near the end of FY 77. The task is currently in the phase of detailed design. Major issues resolved in the system design phase include the formulation of the design requirements, the selection of the correlator architecture, and the development of real-time processing control procedures. This paper reports some results related to the processor system design and analysis. A brief description of the overall system will be given first. Study results related to the spaceborne SAR doppler characteristics will be discussed to establish the design requirements for the azimuth correlator. Discussion then proceeds to the criteria for selecting a correlator architecture, the clutterlock approach, and the procedures for generating processing parameters in real-time.

2.0 SAR PROCESSOR REQUIREMENTS

An important reason for developing the experimental SAR processor is to obtain a breadboard applicable to several future operational spaceborne SAR missions. To meet this objective, the data processing needs for several anticipated future spacecraft SAR missions were analyzed to establish a set of design requirements and guidelines for the experimental processor. Those anticipated missions include the Shuttle Imaging Radar (SIR) flights, the 1983 Venus Orbital Imaging Radar (VOIR), and the SEASAT follow-up missions. Most of these missions are still in the planning stage. The radar parameters and the performance criteria are not yet fully established. The mission objectives, however, are expected to require a high resolution imaging mode, which provides multiple-look images at a spatial resolution comparable to the 25 meter resolution required by SEASAT-A. This observation in conjunction with the fact that SEASAT-A SAR data will be the only spaceborne SAR data available by the end of 1979 lead to the selection of the SEASAT-A SAR as the reference radar sensor for the development. The sensor characteristics and the performance requirements of the experimental processor (adopted from the SEASAT-A specifications) are tabulated in Table 1. A modular approach was chosen to simplify the problem of processing data over a wide swath. A swath width of 20 km, which is one-fifth of the SEASAT-A SAR swath, was chosen for the experimental SAR processor.

TABLE 1

SENSOR CHARACTERISTICS AND THE PERFORMANCE REQUIREMENTS
OF THE EXPERIMENTAL SAR PROCESSOR

SAR System Parameters (SEASAT-A SAR)

SAR Orbit	SEASAT-A Orbit
Nominal Altitude	794 km
Nominal Speed	7450 m/sec
Transmitter Frequency	1275 MHz
Pulse Repetition Frequency	1463,1537,1645 Hz
Pulse Width	33.8 μ sec
Pulse Bandwidth	19 MHz
A/D Rate for Range Offset Signals	45.03 MHz
A/D Window	288 μ sec
Antenna Dimension	2m X 10.5m
Antenna Look Angle	20° cone, 90° clock
Attitude (roll, pitch, yaw) Accuracy	$\pm 0.5^{\circ}$

Experimental Processor Performance Requirements

Image Swath	20 km
Image Resolution	25 m
Number of Looks	4
Image Dynamic Range	50 dB
Data Processing Speed	Real-Time Rate

3.0 EXPERIMENTAL SAR PROCESSOR CONFIGURATION

A block diagram of the experimental SAR processor is shown in Figure 1. The three major elements in the processor are the range correlator, the azimuth correlator, and the control processor. The range correlator compresses the transmitted pulse waveform into a short pulse. The synthetic aperture processing which refines the antenna azimuth beamwidth is performed in the azimuth correlator. The control processor is mainly responsible for the generation of a target response function which is matched to the received echo signals. The control processor also produces various timing signals to synchronize the data processing operations. The block diagram shown in Figure 1 also indicates that the range correlation is performed prior to the azimuth correlation. This order can not be altered since the azimuth Doppler response of a target is range dependent. A more detailed discussion of this requirement is given in [4].
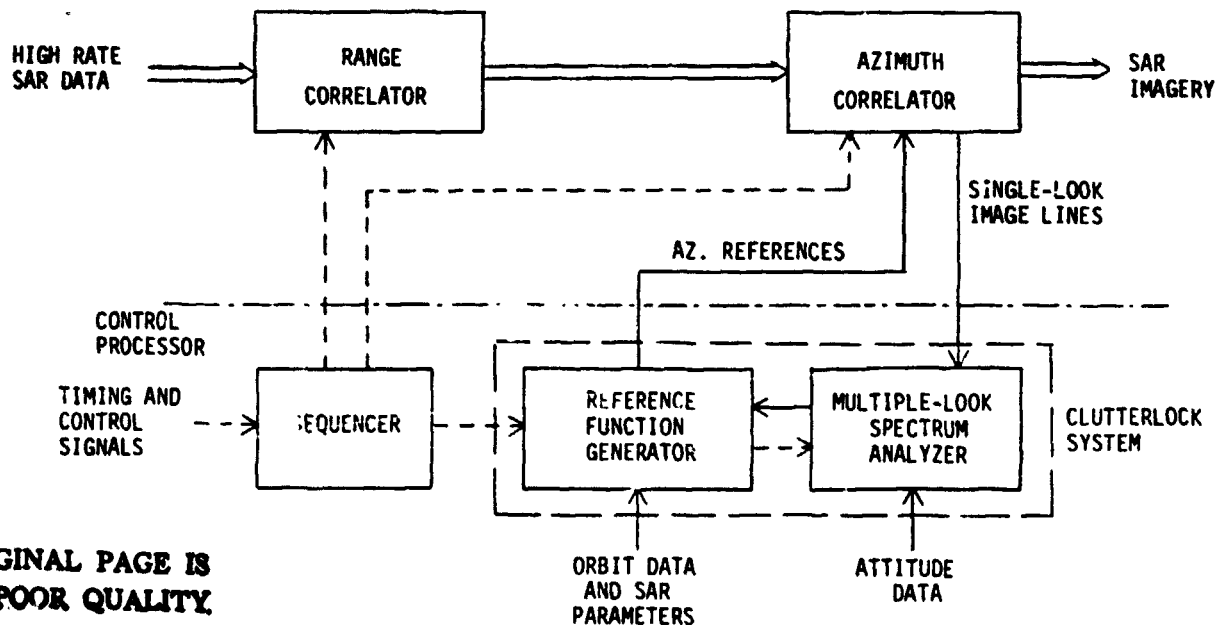
Fig. 1   The Experimental SAR Processor Blockdiagram

ORIGINAL PAGE IS
OF POOR QUALITY

The design of the data flow rate in the processor also needs some special consideration. It is necessary to accommodate different pulse repetition frequency (PRF) values. The sampling frequency of the received echo is determined by the radar bandwidth, and thus is independent of the PRF. To make the system tolerant of changes in the value of the PRF, a harmonic of the PRF is used to synchronize the data processing operations. In multi-look processing, the image data output from the overlay register occurs in bursts.

Time expansion to achieve a near uniform output rate is desirable. A constant
clock rate derived from the input sample clock can be used to produce a uniform
output data rate. In this arrangement, the input and o   data rates are
properly matched and are independent of PRF changes.

The range c   elation in SAR processing is a relatively straightforward
function compared with the synthetic aperture processing. Also, it is antici-
; ted that future missions will use transmitter codes other than the linear
FM chirp of SEASAT-A SAR. For these two reasons, it is planned to utilize
programmable digital matched filters for the experimental SAR processor.

The development emphasis is on the synthetic aperture processing. Detailed
discussions relating to the azimuth correlator and the control processor are
given in the following sections.

4.0 SYNTHETIC APERTURE PROCESSING FOR THE SPACEBORNE RADARS

Accurate knowledge of the target Doppler characteristics is essential to
produce high quality spaceborne SAR imagery. The factors which determine the
target Doppler characteristics are therefore discussed in detail.

4.1 THE SPACEBORNE SAR DOPPLER CHARACTERISTICS

In a coherent radar system such as a SAR, the variation of phase in the
returned signals is directly related to the distance history between the
sensor and the target. The analysis of doppler phase history thus is equiv-
alent to the study of the relative motion between the sensor and targets on
the planet surface. The relative motion problem for a spaceborne SAR is
usually more complex than that for an airborne SAR. For the spaceborne SAR,
both the sensor and targets must be treated as moving bodies. The problem in
many cases is further complicated by the fact that the curvature of the planet's
surface causes the target velocity vector to depend upon the position of the
target in the swath. To analyze the problem, we have assumed an elliptical
spacecraft orbit and an oblate planet surface. The position of the spacecraft
in the orbit is first chosen according to a specified orbit latitude angle.
The position of the target then can be determined by specifying a radar attitude
angle. Assuming that $\overline{R}o$, $\overline{V}o$, and $\overline{A}o$ are respectively, the relative position,
velocity, and acceleration vectors over a very short period of synthetic
aperture integration then the distance history, R(t), can be approximated by
the following expression:

$$R(t) \cong |\vec{R}_o| + \left(\frac{\vec{V}_o \cdot \vec{R}_o}{|\vec{R}_o|} \right) t + 1/2 \left(\frac{|\vec{V}_o|^2}{|\vec{R}_o|} + \frac{\vec{A}_o \cdot \vec{R}_o}{|\vec{R}_o|} \right) t^2 \qquad (1)$$

With the distance history shown above, the phase history, $\phi(t)$, can be approximated as follows:

$$\phi(t) \cong \phi_o + F \cdot t + 1/2 \; \dot{F} \; t^2 \qquad (2)$$

where
$$F = \frac{2}{\lambda} \frac{\vec{V}_o \; \vec{R}_o}{|\vec{R}_o|} \qquad (3)$$

$$\dot{F} = \frac{2}{\lambda} \left(\frac{|\vec{V}_o|^2}{|\vec{R}_o|} + \frac{\vec{A}_o \; \vec{R}_o}{|\vec{R}_o|} \right) \qquad (4)$$

and λ is the radar wavelength. The two factors F and $\dot{F}$ shown above are the instantaneous doppler frequency and the doppler chirp rate at the center of the aperture. Eqs. 2 and 3, show that the doppler center frequency is a function of relative speed along the radial direction, whereas the doppler chirp rate is a function of the relative acceleration. The first term in the radial acceleration can be referred to as the centrifugal acceleration. The second term is a direct result of the acceleration vector which is mainly due to the gravitation effect on the spacecraft free orbit motion.

A numerical study of the sensor-target relative motion problem showed that Eq. 2 provides an accurate measure of the phase history over the full 2.5 second SAR integration time required by SEASAT-A. This leads to the conclusion that the doppler frequency and the doppler chirp rate are the two most important parameters for azimuth correlation. Assuming a plus and minus one degree variation in the antenna roll, pitch, and yaw altitude, the range of doppler frequencies and chirp rates that the azimuth correlation must accept are plotted in Figures 2 and 3. These two figures show that the doppler frequency and chirp rate are dependent upon both the spacecraft position and the target
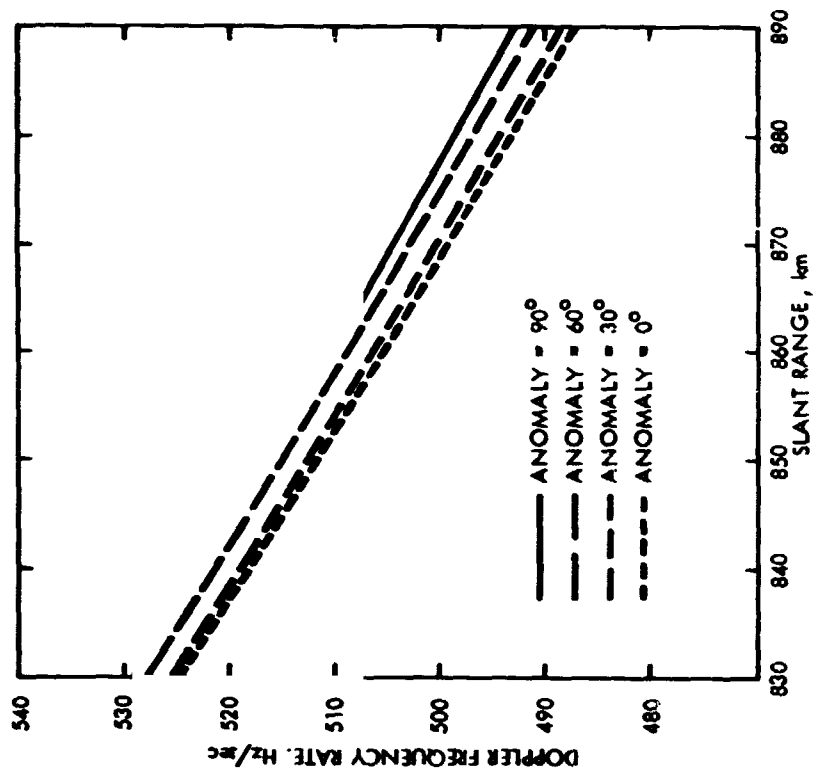
Fig. 3   SEASAT-A SAR Doppler Frequency
          Rates at Four Orbit Positions
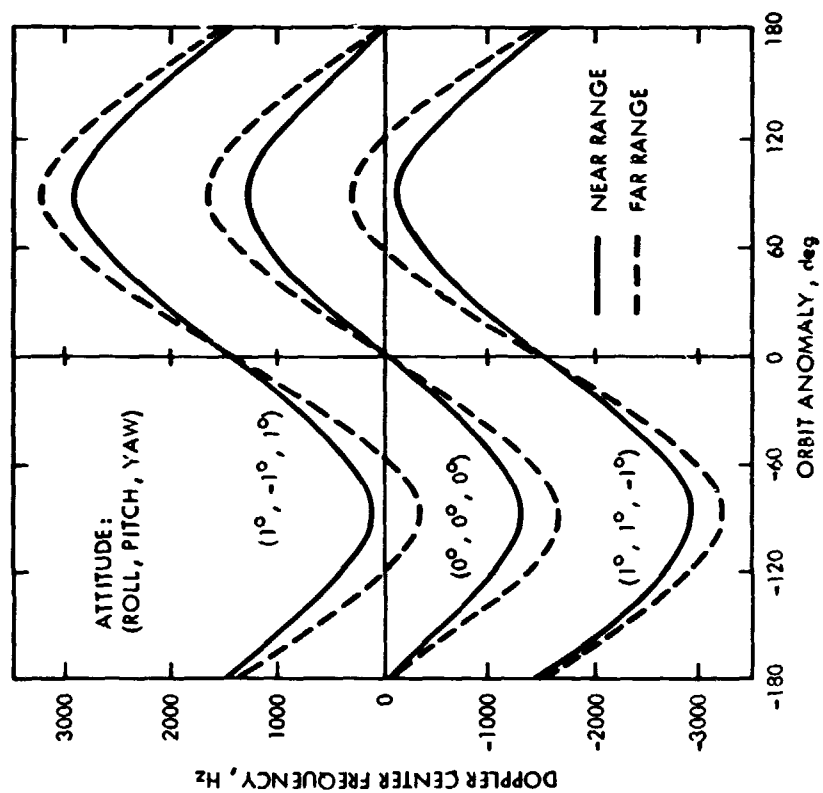
Fig. 2   SEASAT-A SAR Doppler Frequency
          Characteristics

slant range. The azimuth correlator, therefore, must be designed to accommodate such variations in the processing parameters.

Two major design requirements of particular importance are the synthetic aperture integration time and the amount of range migration to be compensated over the aperture width. The required integration time is determined based on the following factors: the doppler chirp rate shown in Figure 2, the sensor speed relative to the planet's surface, and the azimuth resolution requirement. It was determined that a 0.62 second-per-look integration time meets the 25m resolution requirement. The number of range pulses to be integrated per look is about 1020 at the highest PRF value. An attitude variation of $\pm 1^{\circ}$ in roll, pitch, and yaw corresponds to a doppler frequency range of approximately ± 3000 Hz. Such a doppler frequency range calls for a range walk compensation capability of 128 range bins (complex samples) over the total four-look integration time.

The accuracy required for the doppler frequency and the doppler chirp rate used for azimuth correlation was investigated. A small error in the doppler center frequency causes a slight degradation in the image signal-to-noise ratio. To avoid double features in the processed imagery which result from spectrum foldover, the error must be kept within the difference between the PRF and the processing bandwidth. The doppler chirp rate is a slowly varying function with respect to the target slant range. For single-look high resolution processing, the criterion is that the phase error at both ends of the synthetic aperture, as caused by an incorrect estimate of the chirp rate, must be within $\pm 90^{\circ}$. For multiple-look processing, an error in the chirp rate directly results in misregistration of the pixels produced from single-look processing. To produce 25m resolution 4-look imagery from SEASAT-A SAP, and to limit the misregistration error to within one-quarter of a resolution element, the accuracy of the predicted doppler chirp rate must be within 0.5 Hz per second.

4.2 THE DESIGN OF THE AZIMUTH CORRELATOR

4.2.1 A TIME DOMAIN CORRELATOR ARCHITECTURE

The azimuth correlator performs the correlation between the radar signals and the predicted point target response. The architecture selected must have:

(1) the capability to accommodate the varying doppler characteristics in real-time, (2) simplicity in the processing control, and (3) amenability to future on-board implementation. A number of processor architectures are available. Those using electronic processing techniques include the one-stage and two-stage fast Fourier transform approaches [5, 6], the time-domain correlation approaches [7, 8, 9], the digital matched filters [4], etc. For the space-borne SAR processing application, where high resolution multiple-look imaging is required, the time-domain correlation approach was selected for implementation. Two major advantages associated with the time-domain approach are the high degree of parallelism that facilitates custom large-scale-integrated (LSI) circuit implementation, and the relatively simple control for the processing and multiple-look registration. The selected time-domain architecture, shown in Figure 4, involves many phase shifters and data accumulators. A more detailed discussion of this architecture and the associated LSI implementation consideration is provided in [10].

INPUT SIGNAL

RANGE
MIGRATION
CORRECTION

GATE

REFERENCE
FUNCTION

MULTIPLIER

ADDER

LINE
STORAGE
FOR
COHERENT
INTEGRATION

ACCUMULATOR

MUX
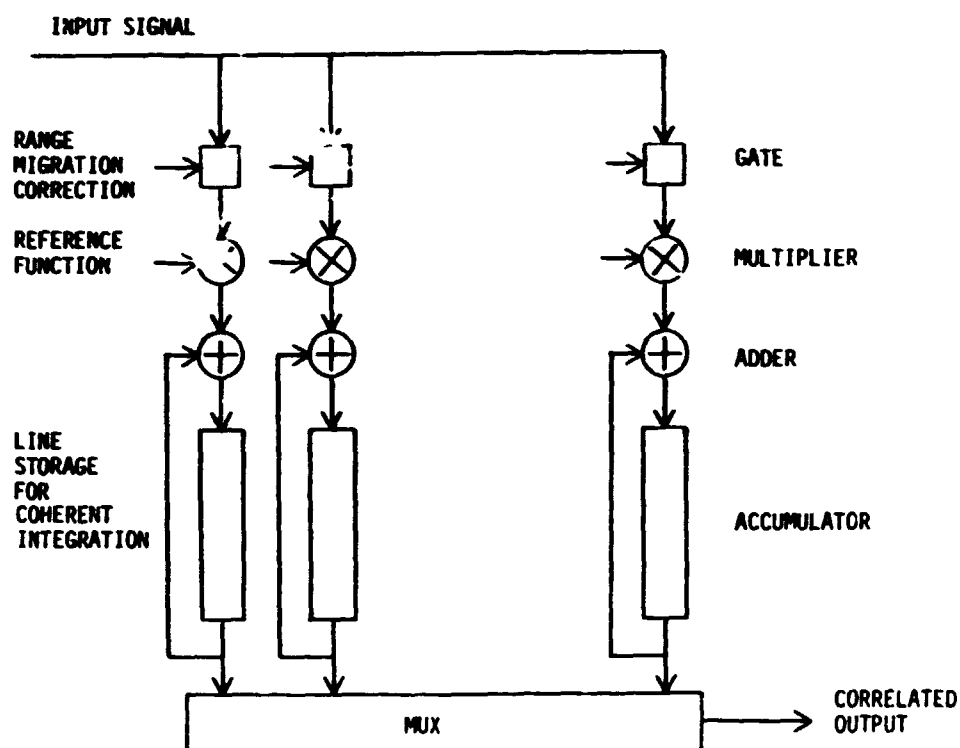
CORRELATED
OUTPUT

Fig. 4   A Time-Domain Azimuth Correlator Architecture

4.2.2 MULTIPLE LOOK REGISTRATION

To produce multiple-look imagery, the time-domain correlators are structured into a number of modules, each producing single look imagery. Assuming that the doppler center frequency and the doppler chirp rate are known, the phase reference function over the total synthetic aperture is determined by Eq. 2. This function will be partitioned into several segments of equal length. Each segment of the reference function is then used to produce single-look imagery. This method causes the different looks at each target location to correspond to data acquired at different times relative to the center of the synthetic aperture. To overlay the separate looks at the image element, the proper time delay must be applied to the output of single-look image lines. Using the right parameters in Eq. 2 for the reference, and assuming that the length of synthetic aperture is set to be a constant for each look, the timing delay to register the image lines from adjacent looks is a constant throughout the swath. (This is much simpler than the multiple-look registration problem associated with the doppler frequency filtering processing approach. That approach requires two-dimensional resampling to accomplish accurate registration of the separate looks at each pixel.)

4.2.3 AZIMUTH CORRELATION WITH PREFILTERING

Each single-look azimuth correlator module is designed to process a portion of the azimuth bandwidth. The data rate for the correlation processing can be reduced by implementing prefilters to reduce the data bandwidth. Two kinds of prefiltering approaches can be used. One approach inserts a bandpass filter in front of each azimuth correlator. The other approach uses a set of mixers and lowpass filters to perform the prefiltering.

The time domain correlator architecture shown in Figure 4 can be used to perform both the prefiltering and the azimuth correlation functions. Reference function generation is easier to accomplish for the bandpass approach than for the mixing approach. Using the proposed correlator architecture, the bandpass filter can be implemented by applying a reference function which is the product of a finite stage lowpass response and a sinusoidal wave with a frequency equal to the center frequency of the passband. The reference function for the azimuth correlator is merely a section of the original phase history of Eq. 2

sampled at a lower rate because of the reduced azimuth bandwidth. Over a wide
swath, the references for both prefiltering and azimuth correlation must be
adjusted to account for the fact that the doppler center frequency and the
doppler chirp rate are dependent on slant range.

The prefiltering approach implemented by mixers has the advantage that ref-
erences for both the front lowpass filtering and the azimuth correlation are
independent of the doppler center frequency. The calculation of the references,
however, is complicated by the fact that variation of the doppler center
frequency along the swath coupled with the target range walk effect introduces
another chirped phase factor into the radar echo signals. To produce high
quality imagery, it would be necessary to compensate for this effect.

The calculation of the reference function has a large effect on the SAR image
quality, therefore, it must be treated very carefully. More detailed descrip-
tion of the reference function and discussions relating to the effects of
phase angle quantization and the number of samples integrated are intended to
be treated in a subsequent paper.

4.2.4 RANGE INTERPOLATION FUNCTION

The input data represent discrete samples of the radar echo signal. The
timing of the sampling pulses is such that they form a rectangular grid in the
two-dimensional range and azimuth plane. However, the range delay history of
a point target follows a near parabolic curve. Therefore, the discrete digital
samples do not coincide with the loci of maximum power return from a point tar-
get. If the processor operated upon the set of discrete samples comprising the
nearest-neighbor approximation of the curved target delay history, it would
cause a loss in the pixel signal-to-noise ratio as well as a broadening of
the target response. Use of range interpolation to introduce points nearer to
the target return curves would perform better than the nearest-neighbor
approach. Both analysis and simulation regarding to the effect of range
interpolation were conducted. Simulation results indicated that a single in-
terpolation which involves the weighted sum of four original range samples and
introduces only one mid point between two samples is as effective as higher
order range interpolation methods. Two fundamental reasons for suggesting

this relatively simple interpolator can be stated as follows: 1) The range spectral response may not be known exactly. 2) The data input for correlation are often quantized to only a few binary bits. These two factors imply that both the interpolation model and the input data will be imperfect. Therefore, the performance of an interpolator will not be a monotonically increasing function of its complexity [11]. Note that interpolation is conducted only along the range direction. The interpolator outputs one i terpolated data sample in addition to each original data sample, and it therefore doubles the data rate at the input to the azimuth correlators. The range gates shown in Fig. 4 select the right data sample to be used in subsequent processing.

It has been determined that coherent speckle noise is a major source of distortion on SAR imagery. Error associated with imperfect interpolation is small compared to the speckle noise.

4.3 CORRELATOR DESIGN SUMMARY

Current baseline design of the azimuth correlator uses single-look correlator modules. Each module produces a 20 km swath of 25 m resolution imagery. The time-domain correlator architecture shown in Fig. 4 will be implemented for the single-look modules.

It is also required that the implementation be flexible enough such that a prefiltering operation later can be easily incorporated after real-time processing using the time-domain approach has been demonstrated.

The compatibility between the 20 km correlator module and the overall 100 km swath processing was also considered. Using this 20 km ath correlator as a building block, five modules would be needed for real-time pro ssing of SEASAT-A SAR data. Each module would be associated with its own input and output interface buffers. The data system design incorporating the requirements set forth by the range compression ratio and the synthetic aperture length are summarized in Table 2.

TABLE 2

DATA RATE AND STORAGE DESIGN FOR

REAL-TIME SEASAT-A SAR PROCESSING

Input Interface	
Input Data Rate	45.53 MHz
Width of Input Gating	4096 Samples
Gating Delay Between 20 km Modules	2304 Samples
Double Buffer Data Storage	4096x2 Samples
Output Data Rate	4096xPRF
20 km Correlator Module	
Input Data Rate	4096xPRF
Input Pulse Width	4096 Samples
Range Correlated Pulse Width	1280 Complex
Azimuth Correlator Input Data Rate	1408xPRF
Synthetic Aperture Integration per look	1020 pulses
Range Samples after Azimuth Correlation	1152 Samples
Output Burst Data Rate	1408xPRF
Output Interface	
Input Burst Rate	1408xPRF
Double Buffer Data Storage	1152x2 pixels
Output Data Rate	2.5 MHz

4.4 THE CONTROL PROCESSOR

The main function of the control processor is to derive accurate phase refer-
ences for the synthetic aperture processing. From the previous discussion it
is clear that the doppler center frequency and the doppler frequency rate are
the two major parameters in defining the phase delay history. There are two
ways to determine these two parameters. The first approach which is considered
an exact approach calculates those two parameters based on the relative
position, velocity and acceleration vectors as described in Eq. 1. For an
earth satellite, accurate spacecraft position and velocity vectors may be

derived using the Global Positioning System [12] which is planned to be operational in the 1980 time frame. Once the sensor position is established, the target positions will be determined by a complicated footprint procedure with the antenna attitude as another input. This exact approach appears difficult to perform in real-time because of its complicated arithmetic procedures. For the experimental processor, a simpler approach is proposed which is commonly used on aircraft SAR processing. This approach treats the doppler center frequency and the doppler chirp rate separately. The procedure to determine the doppler center frequency and to generate compensation phase factors is generally referred to as clutterlock.

In spaceborne SAR processing, the uncertainty in the real-time predicts for the antenna attitude may be comparable to the antenna beam width. The purpose of the clutterlock thus is to refine the antenna attitude prediction and thereby maximize the utility of transmitted energy in the azimuth dimension.

For the experimental processor, four-look processing is required. The spectrum selected for processing will be equally partitioned into four parts, each for a single look. It is possible to set the gains of the four single-look correlators to be equal to each other. The image energy of each look thus is proportional to the energy in the corresponding spectral band. The azimuth spectrum will resemble the antenna pattern in that dimension. Let E_i be the energy of the i-th look. A measure which indicates the symmetry of the energy on the looks relative to the center of the processing band can be written as

$$M = (E_1 + E_2 - E_3 - E_4)/(E_1 + E_2 + E_3 + E_4)$$

where the look numbers are ordered as shown in Fig. 5.

By applying proper delay in accumulating the E_j values, it is possible to have the E_i values all correspond to the same target area, therefore the measurement M is independent of any target scene variation. The M value is expected to be zero if a perfect match between the estimated and the true center frequencies is achieved. The integrated value of M can be used to drive a digital version of a voltage controlled oscillator (VCO) to generate a new sinusoidal signal to be mixed with the range correlated signal (to offset the doppler
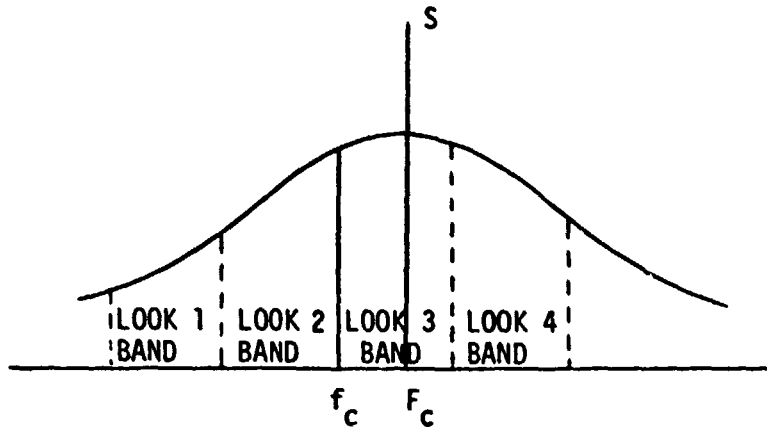
Fig. 5   The Partitioning of a SAR Azimuth
Spectrum for Four-Look Processing

center frequency) or to form a new set of the phase references for azimuth
processing. After this is completed, a new M value will be integrated to the
previously stored M value to generate another offset frequency. The feedback
control in this scheme indeed resembles that of a phase-locked-loop. Since
the M measurement is independent of scene content, convergence can be attained
by properly scaling the integrated M values.

The proposed approach utilizes available single-look image data and it there-
fore minimizes the hardware required to perform this azimuth spectrum anal-
ysis. Preliminary simulation results have indicated that this method can
tolerate a large noise/ambiguity level on the input signals. An example is
briefly discussed here. The original azimuth spectra of four different
signal-to-noise ratios are plotted in Fig. 6. With a processing bandwidth of
approximately 0.8 PRF for a total of four looks, the M values of different
center frequency estimates (normalized to PRF) are plotted in Fig. 7. The
position of zero crossings all agree well with the spectral peaks.

SPECTRUM
INTENSITY

35(db)

DATA SET NO. 1

30

DATA SET NO. 2

25

DATA SET NO. 3

DATA SET NO. 4

20

15

-.5   -.4   -.3   -.2   -.1   0   .1   .2   .3   .4   .5 PRF
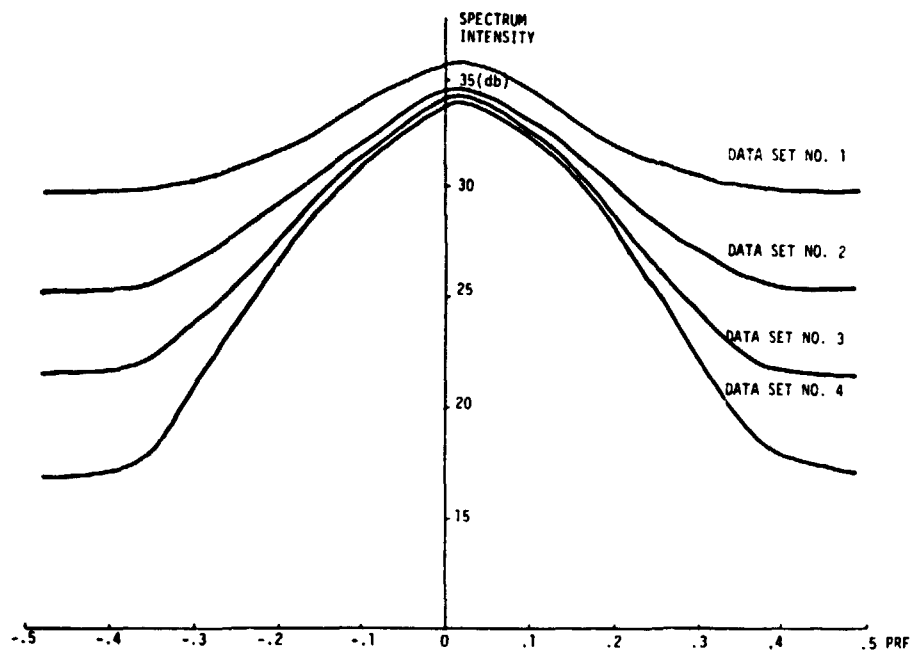
FIG. 6   THE FOUR SPECTRAL PATTERNS BEING EVALUATED IN THE SIMULATION.

M

.4

.3

X   DATA SET NO. 1
△   DATA SET NO. 2
+   DATA SET NO. 3
·   DATA SET NO. 4

.2

.1

f_c

-.3   -.2   -.1   0   .1   .2   .3

-.1

-.2
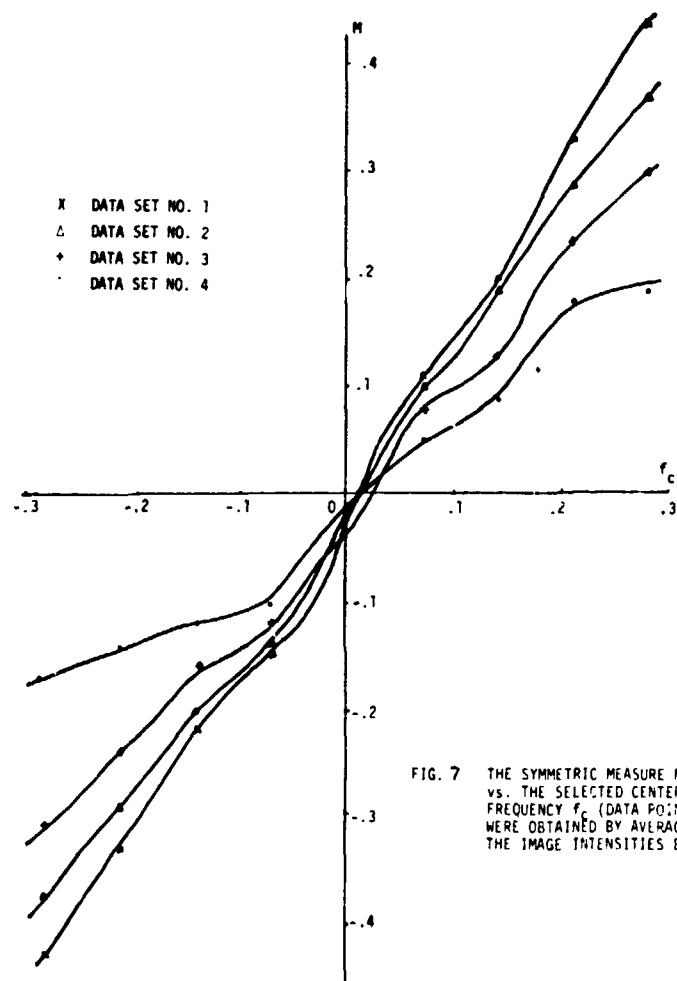
FIG. 7   THE SYMMETRIC MEASURE M
vs. THE SELECTED CENTER
FREQUENCY f_c (DATA POINTS
WERE OBTAINED BY AVERAGING
THE IMAGE INTENSITIES E_i).

-.3

-.4

V-3-17

The clutterlock approach described above measures and reduces the center-band doppler frequency. The remaining parameter, the doppler chirp rate, may be estimated by substituting values of the wavelength, slau range, relative speed, the gravitational acceleration, and the look angle, into the expression of Eq. 4. Among those quantities, the wavelength is a constant and the slant range for each range sample can be determined from the sample delay. Also, the gravitation and look angle are usually known. The relative speed is a function of both the sensor and target positions. If the spacecraft position and velocity are known, the sensor-target relative speed can be estimated using the basic trigonometric operations.

With both the doppler frequency and the frequency rate determined, the phase reference functions to be fed to the azimuth correlator for synthetic aperture processing are well defined. Using the interpulse period as another input, the quadratic phase history is easily obtained by a simple two-step integration of the doppler parameters.

5. CONCLUSION

Real-time processing of spaceborne SAR data is by no means an easy task. Further detailed analysis and simulation are being pursued in an effort to search for better solutions to the SAR processing problem. It is anticipated that this development will serve as a stepping stone toward the implementation of future on-board SAR processors. The utility and practicality of microwave remote sensing from space platforms will be enhanced by the development of high-performance on-board SAR processors.

REFERENCES

[1]   Cutrona, L. J., Synthetic Aperture Radar. Radar Handbook.
       M. I. Skolnik, ed. McGraw-Hill, New York, 1970, Chapter 23.

[2]   Leith, E. N., "Quasi-Holographic Techniques in the Microwave
       Region." IEEE Proc., Vol. 59, No. 9, pp. 1305-1318, Sept. 1971.

[3]   Jordan, R. L., "SEASAT-A Synthetic Aperture Radar Design and
       Implementation." Proceedings of the Synthetic Aperture Radar
       Technology Conference. New Mexico State University, Las Cruces,
       NM, March 1978.

[4]   Wu, C., "A '   nl System to Produce Imagery from SAR Data."
       Proceedings   -e AIAA System Design Driven by Sensors Con-
       ference, Pap   . 76-968. Pasadena, California, October 1976.

[5]   Kirk, J. C., "A Discussion of Digital Processing for Synthetic
       Aperture Radar," IEEE Trans. on Aerospace and Electronic Sys-
       tems, Vol. AES-11, pp. 326-337, May 1975.

[6]   Martinson, L., "A Programmable Digital Processor for Airborne
       Radar," IEEE 1975 International Radar Conference Record,
       pp. 186-191, April 1975.

[7]   Goodyear Aerospace Corporation, Space Shuttle Synthetic Aper-
       ture Radar-- Final Report, GERA-2113, Submitted to Jet Pro-
       pulsion Laboratory, California Institute of Technology,
       August 1975.

[8]   Arens, W. E., "The Application of Charge-Coupled Device Tech-
       nology to Produce Imagery from Synthetic Aperture Radar Data."
       Proceedings of the AIAA System Design Driven by Sensors Con-
       ference, Paper No. 76-967, Pasadena, California, October 1976.

[9]   Søndergaard, F., "A Dual Mode Digital Processor for Medium Re-
       solution Synthetic Aperture Radar," Paper presented at the
       RADAR-77 Conference, London, October 1977.

[10]   Tyree, V. C., "Custom Large Scale Integrated Circuits for Space-
       Borne SAR Processors," Proceedings of the Synthetic Aperture
       Radar Technology Conference, New Mexico State University, Las
       Cruces, NM, March 1978.

[11]   Allais, D. C., "The Selection of Measurements for Prediction,"
       Technical Report No. 6103-9, Stanford Electronics Laboratories,
       November 1964.

[12]   Smith, D. and Criss, W., "GPS Navstar Global Positioning System,"
       Astronautics and Aeronautics, Vol. 14, No. 4, pp. 26-32, April
       1976.

CUSTOM LARGE SCALE INTEGRATED
CIRCUITS FOR SPACEBORNE SAR PROCESSORS *

V. C. TYREE
JET PROPULSION LABORATORY
CALIFORNIA INSTITUTE OF TECHNOLOGY
4800 Oak Grove Dr.
Pasadena, California   91103

SUMMARY

Future space missions are expected to require real-time on-board SAR processors. Large scale integrated (LSI) circuit devices will play an important role in enabling development of SAR processors which meet the severe weight and power constraints associated with on-board processing applications. This paper discusses the application of modern LSI technology to the development of a time-domain azimuth correlator for SAR processing.

General design requirements for azimuth correlators for missions such as SEASAT-A, Venus Orbital Imaging Radar (VOIR), and Shuttle Imaging Radar (SIR) are summarized. Several azimuth correlator architectures that are suitable for implementation using custom LSI devices are described. Technical factors pertaining to selection of appropriate LSI technologies are discussed, and the maturity of alternative technologies for spacecraft application are discussed in the context of the expected space mission launch dates. Finally, the paper describes the preliminary design of a custom LSI time-domain azimuth correlator device (ACD) being developed for use in future SAR processors. Over 1000 of these ACD's are planned to be used in a laboratory model SAR processor to be built in 1979.

1.0 INTRODUCTION

The first space mission to use a SAR instrument is SEASAT-A which will be launched early in 1978. In this earth orbiting spacecraft the raw SAR instrument data will be sent to the ground where it will be processed into images. The primary goals of the SEASAT-A mission are adequately satisfied by using earth based processing. Non-real-time SAR processing is planned for this mission primarily because the cost of development of a real-time SAR processor would not fit within the SEASAT budget. Since SEASAT-A is primarily a research tool in a feasability study and it was not intended to be used for operational radar observations, it was deemed acceptable to require several hours to process data which are collected in a few minutes.

In the future, SAR data from orbiting satellites must be processed to images in real time in order to avoid an ever increasing back-log of unprocessed data. Even ground based real-time processing is not without formidable problems. The spacecraft unprocessed SAR data rates for some identified SAR instrumented missions range from $5x10^6$ bits per second to $120x10^6$ bits per second with higher rates likely for more advanced SAR instruments. There are substantial functional and economic benefits associated with real-time on-board processing of SAR data. It is therefore likely that on-board spacecraft SAR processing will play an increasing role in future SAR spacemissions.

On-board SAR processing has the advantage that the down link data rate is reduced by at least the number of looks. In addition, since the processed SAR data is in the form of images it is possible to do on-board image feature extraction similar to the type planned for LANDSAT images and further reduce the down link data rate and volume. However, these benefits are not easily attained. A on-board SAR processor must be designed within the severe weight, volume and power restrictions of a spacecraft. A way (perhaps the only way) to implement high-performance on-board SAR processors is through the use of custom large scale integrated (LSI) circuits for major portions of the SAR processing circuitry.

The portions of the SAR processor that will most benefit from custom LSI are the range correlator and the azimuth correlator. Custom LSI devices have been used to perform the range correlation for several years in aircraft SAR

processors. Range correlation devices have been constructed using analog charge coupled devices (CCD) and surface wave devices (SWD). Both of these devices depend upon the stable range chirp parameters to permit the use of fixed tap weights in the correlator devices. If the correlation coefficients must be adjustable, as is required in the azimuth correlator, conventional CCD and SWD devices cannot be used. The remainder of this paper will briefly describe a few different azimuth correlator architectures that permit variable coefficients, and will discuss the detail specification of a custom LSI device for one of these architectures.

2.0 TYPICAL SPACEBORNE SAR INSTRUMENTS

A summary of some typical spaceborne SAR instrument characteristics is given in table 1. They represent a fairly broad range of resolutions and radar frequencies and provide a baseline for the range of azimuth correlator complexity. The radar center frequencies range from L-band to X-band. Swath width varies from 12.5 km to 100 km and resolution varies from 20 m to 200 m. The requirements specified for VOIR and SIR are preliminary and may change as their respective mission goals are defined more fully. The requirements for SEASAT-A, however, are well defined and are discussed in considerable detail in a companion paper [1]. The experimental electronic SAR processor described in [1] is being designed to produce 20 km swath 25 m resolution, four look, SAR imagry.

3.0 AZIMUTH CORRELATOR ARCHITECTURE AND LSI TECHNOLOGY

Since the laboratory SAR processor is required to perform real-time processing of SEASAT-A data, the selection of an azimuth correlator architecture was heavily influenced by SEASAT-A requirements. "Simple" frequency domain azimuth processors have been devised which use an FFT to obtain the intensity of image elements along isodoppler lines on the surface of the earth. However, these "simple" frequency domain processors exhibit substantial geometric distortion requiring complex processing to solve registration problems associated with formation of multilook images. The use of custom LSI circuits to implement FFT function have been described in other papers [2] [3] and will not be discussed any further in this paper. The primary thrust of the remainder of this paper will be to discuss a few

candidate time-domain azimuth correlator architectures that are implement-
able in custom I"I circuits reasonable chip size.

<div align="center">

TABLE ?

SAR PROCESSOR FUNCTIONAL REQUIREMENTS

</div>

	SEASAT-A	SIR-B		VOIR
	L-BAND	C-BAND	X-BAND	L-BAND
GROUND RANGE RESOLUTION (M)	25	70,25,20	70,25,20	200, 25
AZIMUTH RESOLUTION (M)	25	70,25,20	70,25,20	200, 25
NUMBER OF LOOKS	4	15, 5, 5	15, 5, 5	30, 4
SWATH WIDTH (KM)	100	50,25,55	50,25,55	100, 12.5
PIXELS PRODUCED ACROSS SWATH	5760	1039,1604 3755	1039,1604 3755	770, 1115
BEAM CENTER SLANT RANGE (KM)	870	230,335 480	230,335 480	550
RANGE TIME-BANDWIDTH PRODUCT	646	339	10	42.3, 338
AZIMUTH SAMPLES PER LOOK	1020	28, 122 176	16,64,92	60, 475
RANGE WALK ACROSS BEAM (BINS)	128	10	10	2, 10
STALO FREQUENCY (MHz)	91.06	91.06	91.06	91.06
RADAR CENTER FREQUENCY (GHz)	1.275	4.75	9.1	1.275
RADAR PRF (MAX.) (Hz)	1645	2218	2218	1304
PULSE DURATION (µSEC)	33.8	33.9	1	33.8
PULSE CODING	CHIRP	PN	PN	PN
BANDWIDTH	10	10	10	10, 1.5(3)
SAMPLING FREQUENCY (I,Q)(MHz)	22.76	11.38	11.38	11.38, 1.42
ANTENNA DIMENSION (AZ.) (M)	10.5	8	8	12
ANTENNA LOOK ANGLE (DEG)	20	15,49,64	15,49,64	49
NOMINAL RADAR ALTITUDE	795	225	225	375
NOMINAL RADAR SPEED (M/SEC)	7450	7700	7700	7150

3.1   TWO AZIMUTH CORRELATOR ARCHITECTURES

In selecting a suitable time-domain azimuth correlator architecture imple-
mentable in custom LSI, one of the first characteristics to look for is a
high degree of regularity in the arithmetic and memory hardware requirements.
One of the first architectures considered was a pipeline processor shown in
figure 1. It has the property that both the data and the partial s' ', lea-
ding to image pixels, flow through the processor in nice regular ("laminar")
manner. It also is nicely modular in which each LSI device would contain the
range line memory, coefficient storage, multiplier, adder, and etc., as shown
enclosed in the dashed lines. It has the advantage that it uses a minimum
number of bits of on-chip storage which is a significant factor in minimizing
chip size. Small chip size has a very close relationship to the chip yield
in fabrication. Chip yield reduces dramatically as chip size increases. A
disadvantage of this architecture is that it is not possible to include any-
thing more than the simplest range interpolation without greatly increasing
the complexity and size of the chip. Since it was considered important to
have the option of using multipoint range interpolation for the SEASAT-A la-
boratory processor, this correlator architecture was not adopted for the ex-
perimental processor.

Another azimuth correlator architecture was considered that permitted paral-
lel image line processing for all looks. Figure 2 is a block diagram of this
azimuth correlator architecture. It is modular, as indicated by the dashed
lines, and allows range interpolation to be done centrally, eliminating the
necessity for interpolation logic on the chip. A disadvantage is that there
is a larger amount of memory required on the chip because the complex image
line is accumulated on the chip rather than accumulated over the array of
chips as in figure 1. However, since multipoint range interpolation was con-
sidered to be an important option for the SEASAT-A laboratory processor, this
second azimuth correlator architecture was preferred. A deciding factor in
confirming this architecture choice is the availability of a suitable LSI
technology which can implement the additional memory required without a sig-
nificant power penalty.

3.2 SELECTION OF APPROPRIATE LSI TECHNOLOGIES

In order to implement an LSI device of the complexity required for one of the above azimuth correlators, one needs to consider only technologies that exhibit minimum area per gate properties. Also, for spacecraft application, the amount power required to operate the chips must be minimum. Fortunately minimum power and minimum area per gate are compatible requirements. Table 2 is a comparative summary of the area, power, and speed of several common LSI technologies. These are: Complementary-Metal-Oxide-Semiconductor-Silicon-on-Sapphire (CMOS-SOS), Integrated Injection Logic (I^2L), N-channel Metal-Oxide-Semiconductor (NMOS), and Digital Charge Coupled Device (DCCD). They are representative of the most common high speed, low power and small area devices available. The areas for a logic gate and a data storage element (shift register) are useful in assessing the amount of circuitry that can be placed upon a chip of moderate size (3×10^7 square micrometers). Speed-power product is a figure of merit used to indicate the amount of energy required to change the state of a typical logic element. As can be seen under the shift register power per bit column, the speed power product is not an absolute indicator of the relative power required to operate these LSI circuits. Topological factors can override the apparent speed-power product ratios as can be seen by comparing CMOS-SOS and NMOS. The speed-power product ratio of NMOS to CMOS-SOS is 2 but the ratio of power per bit for the shift register is 3.

All of the values in Table 2 assume that the minimum on-chip conductor widths are 5 micrometers, which is currently a standard photolithographic capability within the integrated circuit industry. In the next five to ten years, the minimum line widths can be expected to reduce to one-tenth of today's limits which will allow proportional scaling of the figures in Table 2.

Selection of an LSI technology for a spacecraft application requires careful assessment of the proposed application. In applications requiring high chip complexity, it is clear from Table 2 that DCCD has a significant advantage. DCCD, however, has less radiation resistance that either I^2L or CMOS-SOS. If the spacecraft must spend a large amount of time in trapped radiation fields, it would be necessary to shield the DCCD processor circuits. Also,

DCCD technology can only be used in pipe-line processor architectures [4].
A high spacecraft radiation environment would probably require the higher
radiation tolerance of either CMOS-SOS or I^{2}L. The larger logic element di-
mensions of these technologies may require a multiple custom LSI implementa-
tion in azimuth correlators of high complexity. NMOS has about the same ra-
diation restistance as DCCD.

It is not practical to discuss all possible tradeoffs involved in selecting
a custom LSI technology in this paper. The above discussion is a brief out-
line of some of the factors that must be considered in technology selection.
The next section of this paper will describe an example azimuth correlator
architecture and will discuss an LSI technology selection. This will illus-
trate some of the practical problems encountered in using custom LSI for SAR
processors.

TABLE 2

HIGH DENSITY LSI TECHNOLOGIES

DIGITAL (5 μm GEOMETRY)

	LOGIC GATE		SHIFT REGISTER	
	AREA	SPEED-POWER	POWER/BIT 1 MHZ	AREA/BIT
CMOS SOS	12903 μm^2	5 pJ	100 μW	49387 μm^2
I^{2}L	6452 μm^2	2 pJ	50 μW	19455 μm^2
NMOS	9677 μm^2	10 pJ	300 μW	41935 μm^2
DCCD	645 μm^2	0.2 pJ	0.3 μW	129 μm^2

NOTE: A MODERATE SIZE LSI CHIP AREA IS: 3×10^7 μm^2

4.0 EXAMPLE AZIMUTH CORRELATOR LSI DEVICE

JPL is presently involved in the development of an experimental electronic
SAR processor [1] which will use a custom LSI device to implement the azimuth
correlator. This processor, called the Developmental Model SAR Processor
(DMSP), will be used to demonstrate real-time, time domain processing of SAR
data from the SEASAT-A spacecraft. Unprocessed data from the spacecraft will

be sent to the DMSP which will produce a 20 km swath image at 25 m resolution at the real-time rate. Data given in Table 1 are the baseline requirements for this processor. The azimuth correlator uses the architecture described in Figure 2 and is implemented with a set of identical custom LSI devices specified for use in this azimuth correlator. This LSI device is called the azimuth correlator device (ACD).

4.1 GENERAL REQUIREMENTS FOR THE ACD

The DMSP functional block diagram, Figure 3, shows the relationship of the azimuth correlator to the other elements of the DMSP. The DMSP requires an array of 1020 ACD's to perform a 20 km swath azimuth correlation with 4 looks. The relationship of the ACD's to the complete SAR processor is shown in Figure 4 and 5 which are, respectively, a block diagram of the complete azimuth correlator and a block diagram of a single-look azimuth correlator module. The ACD receives data from the range correlator via the ACD input sample bus as a contiguous sequence of "range-lines". Each range-line comprises 5120 complex data samples accompanied by several sync signals. The basic operation performed by the ACD during a range-line processing cycle is to select the appropriate set of 1152 complex data samples from each range-line, multiply each data sample by the appropriate complex azimuth reference function (ARF) coefficients, and to add this product to the appropriate cell in the accumulato register. (New sets of reference function coefficients are needed for each new set of range-line date samples input to the ACD during an image-line processing cycle.) In the DMSP, an image-line processing cycle will involve 1020 range-lines. The final value of the complex image-line sample stored in the jth accumulator cell takes on the value

$$P_j = \sum_{i=0}^{1019} C_{im} S_{ij} \quad \text{for } j = 0,1151 \quad (1)$$

where

C_{im} = complex reference function coefficient (where $m = [j/16]$, the integer portion of $j/16$) for the jth data sample from the ith range-line in the image-line processing cycle.

$$S_{ij} = \text{the } j^{th} \text{ complex data sample from}$$
$$\text{the } i^{th} \text{ range-line in the image-}$$
$$\text{line processing cycle.}$$

At the end of an image-line processing cycle, the output of the complex adder is switched to the output driver and the 1152 complex image-line samples are read out. The image-line memory is filled with zero levels during the image-line read out process. An ACD functional block diagram is shown in Figure 6. The functional characteristics of each element of the ACD is described in the following subsections.

4.1.1 **Data sample format.** The ACD input sample bus will supply data in word-serial (8-bits-per-word) fashion at word rates in the range from 400 kHz to 14.0 MHz. These data samples will be organized into sets of 5120 samples corresponding to individual SAR range-lines, and these range-line sample sets are subdivided into contiguous subsets of four interpolated samples each. Each data sample is a complex quantity. The first four bits of each sample report the sign and magnitude of the real part of the input sample, and the last four bits report the sign and magnitude of the imaginary part.

4.1.2 **Coefficient formats.** The following set of coefficients is provided to process the data samples corresponding to one range-line:

Coefficient Type	No. Coefficient Per Set	No. Bits Per Coefficient
RMC - Coarse	1	10
RMC - Fine	72	2
ARF	72	8

The first three bits of the Range Migration Compensation (RMC)-coarse coefficients have no effect on the processing. For convenience, the RMC-fine coefficient is appended to the end of the ARF coefficient to form a ten-bit composite coefficient. A coefficient bus sync is provided which controls and synchronizes the transfer of coefficients from ACD-to-ACD. (See Figure 5).

4.1.3 <u>Coefficient buffers</u>. Two levels of on-chip coefficient buffering are provided within the ACD. The first level provides for a set of 288 composite coefficients plus four RMC-coarse coefficients sufficient to process a set of four range-lines. The second level of buffering provides an eight word first-in-first-out (FIFO) buffer for the composite coefficients and a single word buffer register for the RMC-coarse coefficients. The organization of these buffers is described in Figure 6. The input coefficient mx switch routes the coefficient bit stream to the appropriate storage register. The internal mx switches enable the buffers to be operated in either a full-capacity mode or a one-quarter capacity mode which is useful in some applications. The output coefficient mx switch causes the normal coefficient bit stream to be re-formed from the output of the first level buffers so these coefficients can be passed on to another ACD in an azimuth correlator module (see Figure 5). The passage of coefficients from ACD-to-ACD occurs under the control of timing signals common to all of the ACDs in the azimuth correlator. The second level of buffering holds coefficients to be used in delayed range-line processing. This delay in processing is due to the action of the RMC-coarse coefficient which causes up to 127 sample subset periods of delay (realtive to coefficient transfer timing) is range line processing within an ACD. Each RMC-coarse coefficient is used once at the start of the corresponding range-line processing cycle. Each composite coefficient will be used with 16 consecutive range-line data sample subsets.

4.1.4 <u>Input control</u>. The input control (see Figure 6) selects an appropriate group of 1152 data samples from each range-line sample set. The applicable RMC-coarse coefficient determines how many of the input sample subsets (four samples each) of the range-line sample sets shall be passed-over before beginning selection of the data samples to be processed. The number of subsets passed-over can be any value from zero to 127. The four samples of each subsequent subset shall be stored in a sample buffer memory. The value of the appropriate RMC-fine coefficient will determine which on of the four samples to select for input to the complex multiplier element. (An RMC-fine coefficient value of zero shall cause the selection of the first sample of the subset, etc.)

4.1.5 <u>Complex multiplier</u>. The complex multiplier performs the following computation:

$$P = X \cdot Y; \qquad\qquad (2)$$

where

$$X = a + ib \text{ and } Y = c + id$$

This product (P) can also be expressed as $P = (ac - bd) + i(ad + bc)$. The quantities a and b are, respectively, the real and imaginary parts of the ARF coefficients. Quantities c and d are respectively the real and imaginary parts of the ACD input data samples. The real and imaginary parts of P each have a dynamic range of 8 bits.

4.1.6 <u>Image line accumulator</u>. The image-line accumulator comprises the functional equivalent of a complex adder and a recirculating image-line memory (Figure 6). The complex adder accepts the output of the complex multiplier (8 bit real component and 8 bit imaginary component) and the corresponding accumulator sample (16 bits I and 16 bits Q). The sum is passed through a multiplexer which will either route the complex sum to the image-line memory or to output driver circuits. This multiplexer, when in the output mode, shall enter zero levels into the image-line memory. The recirculating image-line memory is a shift register with a total capacity of 1152 complex image-line samples.

4.1.7 <u>Control and timing</u>. The control and timing circuitry provided on the ACD, accepts control and timing signals from the control processor and provides all of the necessary control and timing to all of the rest of the circuitry on the chip. Some of the functions to be provided by the control and timing circuitry are:

    a. Clock signals to all elements of the ACD

    b. Controls data input and sample selection

    c. Controls coefficient buffer capacity and coefficient routing to and from internel coefficient buffers

    d. Controls output of image-line pixels.

    e. Controls selection of the 11 most significant or 11 least significant portion of the complex image-line sample magnitude at the

accumulator output.

4.2   ACD LSI TECHNOLOGY SELECTION

Taking an inventory of the circuitry required for the ACD, we observe the following:

a)   There is a memory requirement of the order of 40,000 bits. Fortunately all of it is sequential (shift register) memory.

b)   A 4 bit x 4 bit complex multiplier is required, which is comprised of four multipliers and two adders.

c)   A complex adder is required which consists of two 16 bit adders.

d)   Some random logic circuits for on-chip control and timing.

Assuming the chip size is to be kept within the 6mm x 6mm size category and that the total operating power for the chip must be kept under 0.5 watt, the LSI technology choice must be DCCD. The other three technologies would only be viable if the conductor widths were reduced to about 1.7 microns. Fortunately the radiation environment for a SEASAT-A type spacecraft is in the order of 10^5 rad (Si) per year, which is within the radiation tolerance range of DCCD with some shielding.

5.   CONCLUSIONS

It has been concluded from the above that a custom LSI device is practical for a system as complex as the DMSP. Certainly SAR processing systems less complex than the DMSP could also benefit from LSI technology [5]. In the case of SEASAT-A type spacecraft, custom LSI is an enabling technology for spaceborn SAR processors.

REFERENCES

1. Wu, C., <u>Electronic SAR Processors For Space Mil jions</u>, Proceedings of The Synthetic Aperture Radar Technology Conference, New Mexico State University, New Mexico, 1978.

2. P.. cinson, L. W. and Lunsford, J. A., <u>A CMOS/SOS Pipeline FFT Processor - Construction, Performance and Application</u>, NAECON Convention Record, 1977.

3. Wu, C., <u>A-Digital Approach To Produce Imagry From SAR Data</u>, AIAA System Design Driven By Sensor Conference, October 1976.

4. Zimmermann, T. A., <u>The Digital Approach To Charge Coupled Device Signal Processing</u>, IEEE International Symposium on Systems and Circuits, 1975.

5. Arens, W. E., <u>Real-Time SAR Image Processing Onboard a Venus Orbiting Spacecraft</u>, Proceedings of The Synthetic Aperture Radar Technology Conference, New Mexico State University, New Mexico, 1978.
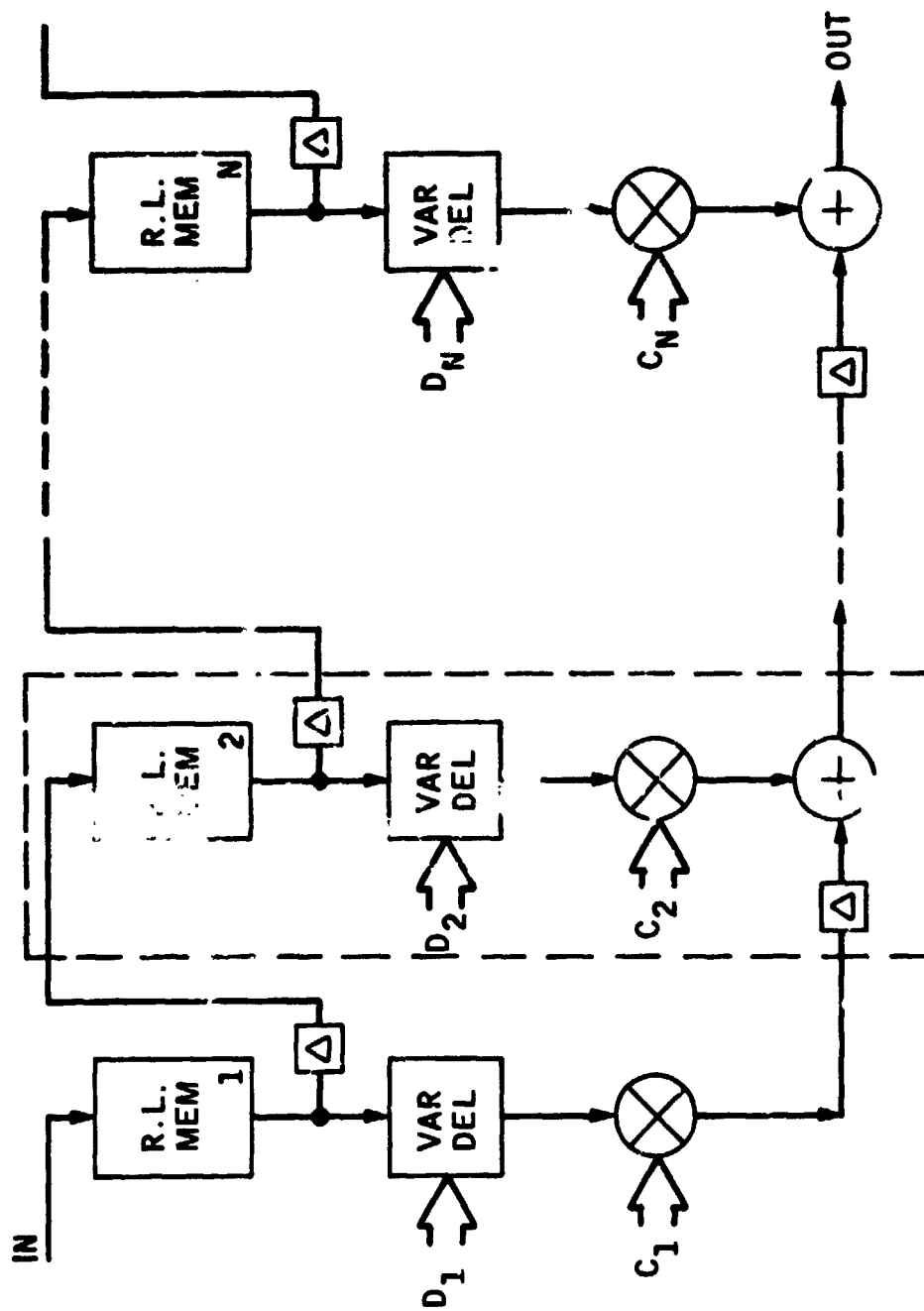
Figure 1. Time Domain Azimuth Correlator Architecture A
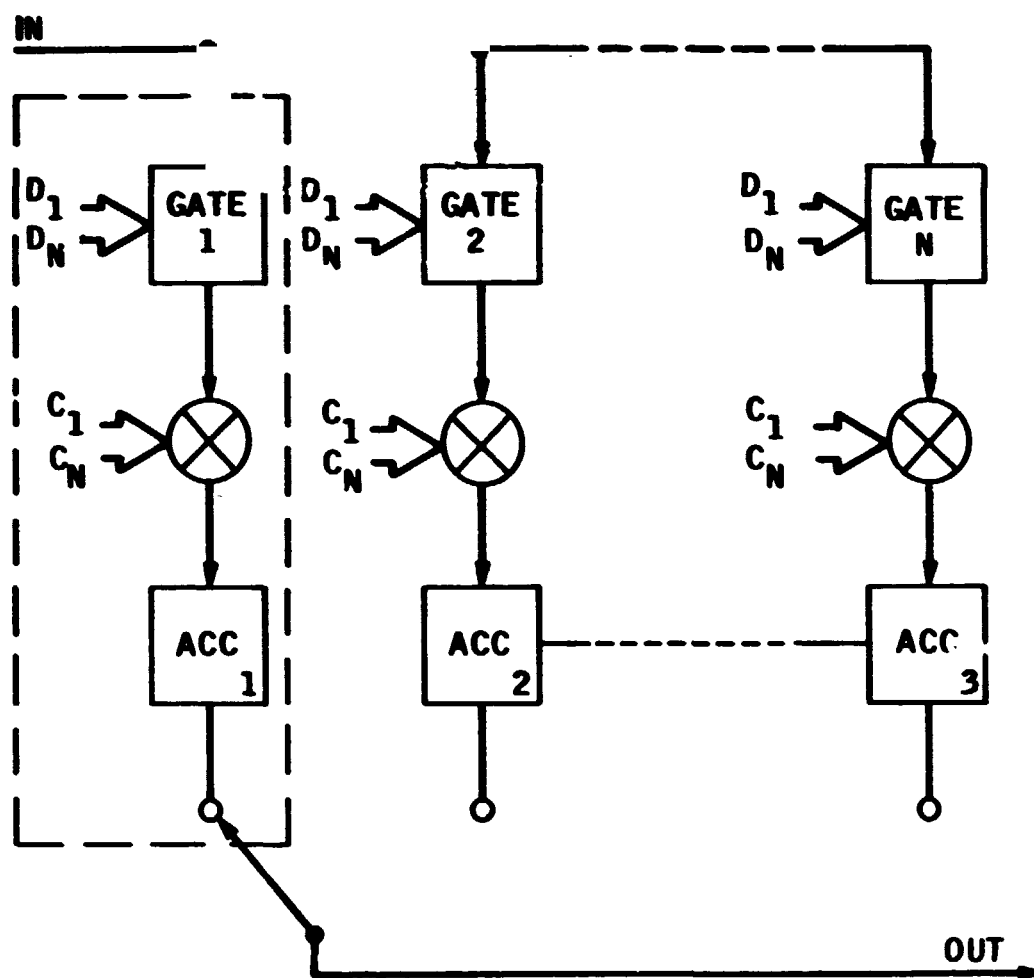
Figure 2. Time Domain Azimuth Correlator Architecture B
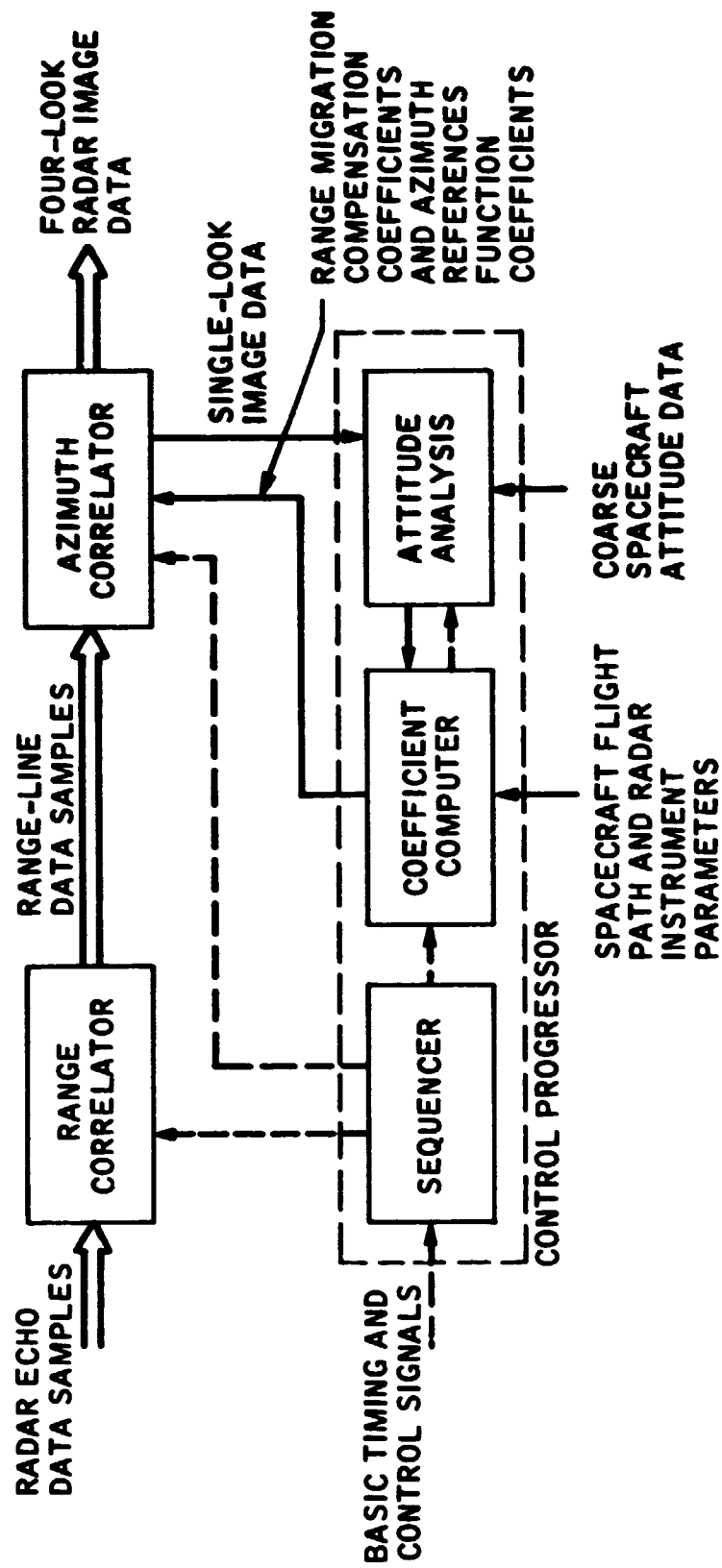
Figure 3. Developmental Model SAR Processor Block Diagram

RADAR ECHO DATA SAMPLES

RANGE CORRELATOR

RANGE-LINE DATA SAMPLES

AZIMUTH CORRELATOR

FOUR-LOOK RADAR IMAGE DATA

SINGLE-LOOK IMAGE DATA

RANGE MIGRATION COMPENSATION COEFFICIENTS AND AZIMUTH REFERENCES FUNCTION COEFFICIENTS

ATTITUDE ANALYSIS

COARSE SPACECRAFT ATTITUDE DATA

COEFFICIENT COMPUTER

SPACECRAFT FLIGHT PATH AND RADAR INSTRUMENT PARAMETERS

SEQUENCER

CONTROL PROGRESSOR

BASIC TIMING AND CONTROL SIGNALS

Figure 4. Azimuth Correlator Block Diagram
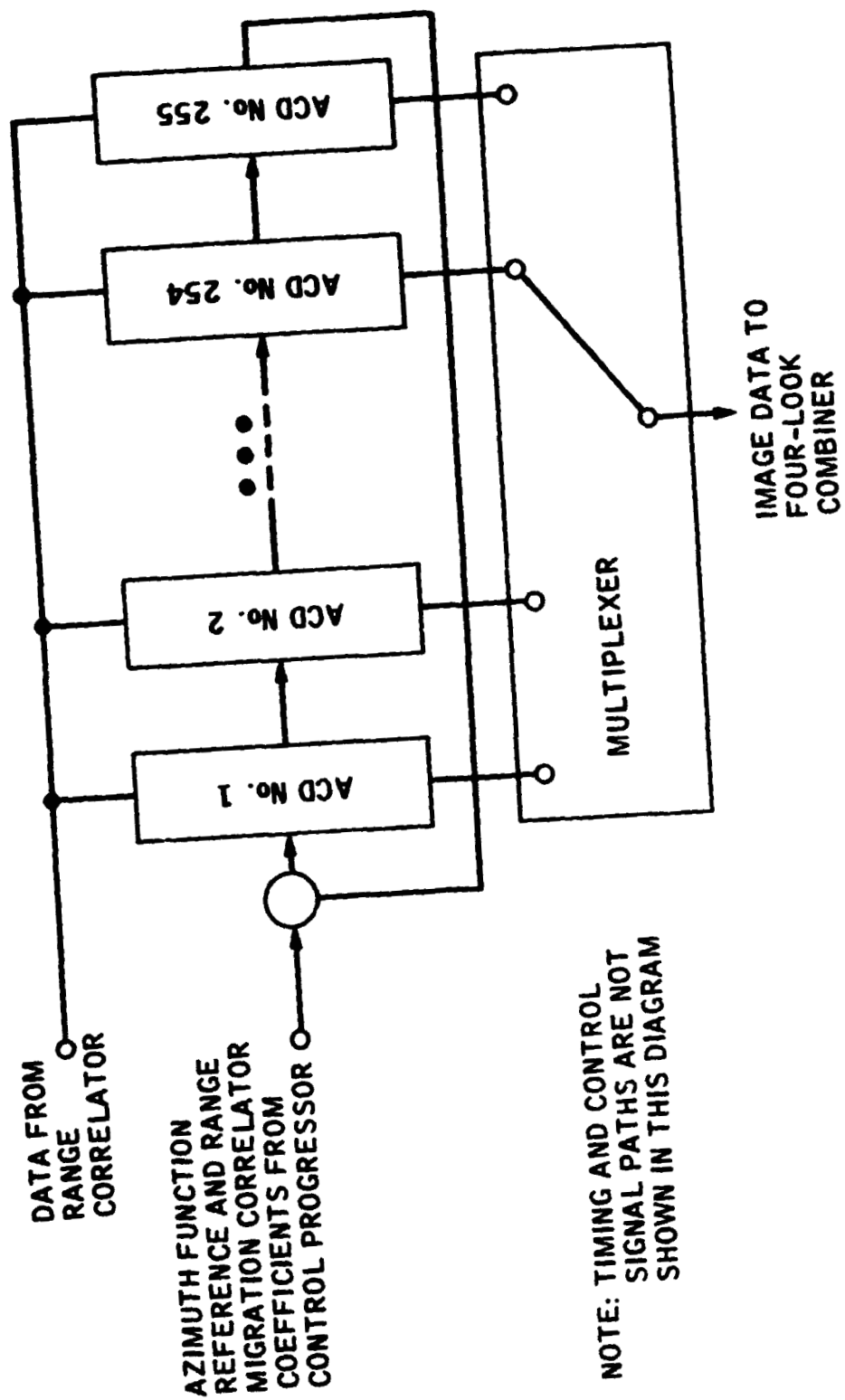
Figure 5. Block Diagram of One-Look Azimuth Correlator Module

DATA FROM RANGE CORRELATOR

AZIMUTH FUNCTION REFERENCE AND RANGE MIGRATION CORRELATOR COEFFICIENTS FROM CONTROL PROGRESSOR

ACD No. 1

ACD No. 2

ACD No. 254

ACD No. 255

MULTIPLEXER

IMAGE DATA TO FOUR-LOOK COMBINER

NOTE: TIMING AND CONTROL SIGNAL PATHS ARE NOT SHOWN IN THIS DIAGRAM

V-4-18

Figure 6. Azimuth Correlator Device Functional Block Diagram

REAL-TIME SAR IMAGE PROCESSING
ONBOARD A VENUS ORBITING SPACECRAFT*

WAYNE E. ARENS
MEMBER OF THE TECHNICAL STAFF
INFORMATION SYSTEMS DIVISION
JET PROPULSION LABORATORY
PASADENA, CALIFORNIA 91103

SUMMARY

This paper describes the potential use of real-time synthetic aperture radar (SAR) processing to produce 200-meter resolution imagery cnboard a 1983 Venus Orbiter Imaging Radar (VOIR) spacecraft. In the introductory section, the current NASA SAR processor development program and its relationship to the VOIR application is described. The VOIR SAR processing requirements are then defined in terms of a nominal baseline design evolving from a 1977 VOIR mission study by the Caltech Jet Propulsion Laboratory (JPL) [3]. A candidate on-board SAR processor a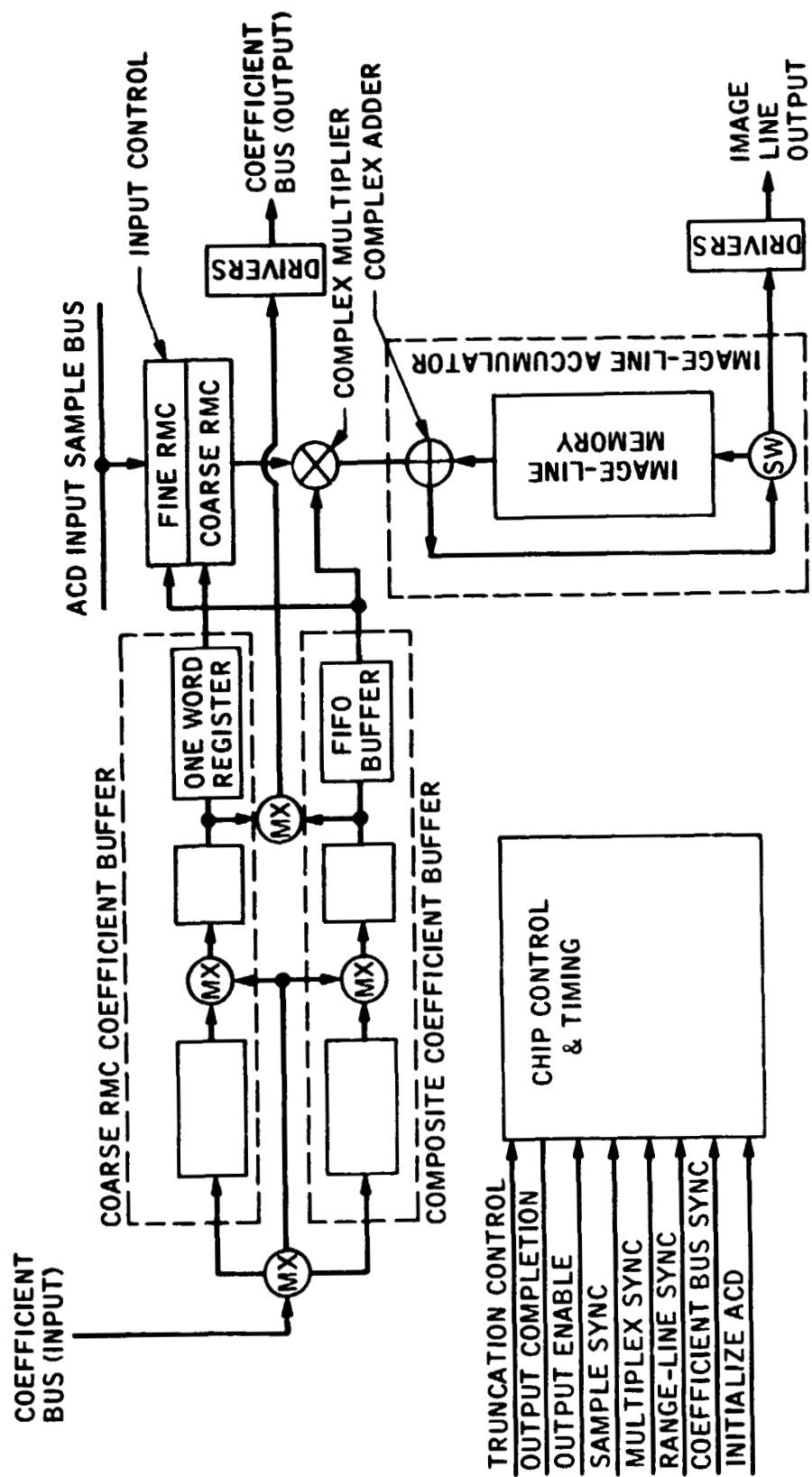rchitecture compatible with the VOIR requirements is next described. Finally, detailed implementation characteristics, based upon currently available integrated circuits, are estimated in terms of chip count, power, and weight.

1.0 INTRODUCTION

JPL is conducting a SAR processor advanced development program as part of an existing NASA Research and Technology Objective and Plan (RTOP). In turn, this RTOP is an approved and vital element of the NASA End-to-End Data System (NEEDS) program.

The current RTOP is funded to design and build a real-time stand-alone Developmental Model SAR Processor (DMSP) for operation in a laboratory environment. The DMSP will have the capability to process SEASAT-A SAR data at real-time rates to produce four-look, 25 meter resolution radar images covering a 20 Km swath. The objective is to demonstrate this capability by the end of FY'79.

Since the NEEDS program is emphasizing the development of a future on-board processing capability, it is essential that the DMSP architecture be designed to be amenable to implementation for on-board SAR processing applications. A major feature of the DMSP task is the development of a custom LSI device to be used in the azimuth correlator. This device will employ current state-of the-art charge-coupled device (CCD) technology [1].

Following the DMSP development, it is planned to design and build a SAR processor for use in an SAR processing experiment on-board a future space shuttle flight. This experiment would demonstrate the ability of a space-borne processor to produce high-resolution multi-look radar imagery in real-time. The detail functional requirements imposed on this processor are intended to be representative of those anticipated on future earth observation missions [2].

A study of a complete SAR system for VOIR was performed during 1977. This paper reports on the results of that study pertaining to the feasibililty of developing an on-board SAR processor for VOIR. Although the SAR processor functional requirements assumed for that VOIR study were much less demanding than those imposed on the DMSP design, the VOIR processor design was adapted from the preliminary design developed from the DMSP. It is expected that many results from the DMSP development program will be directly applicable to the final design of an on-board SAR processor for VOIR.

2.0 NOMINAL VOIR SAR PROCESSING REQUIREMENTS

The VOIR mission study conducted during 1977 assumed a 1983 launch date. This study produced a baseline mission definition and design in support of the current FY'78 VOIR pre-project activity. The baseline scenario provides for 200-meter low resolution mapping of the entire planetary surface and 25-meter high resolution imagery of selected areas. An on-board real-time synthetic aperature radar (SAR) image processor was included in the proposed baseline design, for the low resolution mode, in order to achieve a SAR data rate reduction commensurate with the available telecommunications line capability [3].

Nominal radar system design values applicable to establishing the necessary SAR processing design parameters are tabulated in Table 1. Using the values of Table 1, the nominal processing design parameters of Table 2 have been derived using the equations of Table 3. As noted from Table 2, coherent

TABLE 1
NOMINAL VOIR RADAR SYSTEM DESIGN VALUES

Design Parameter		Value
Transmitter Frequency	f	1275 MHz
Radar Wavelength	λ	0.235 m
Pulse Repetition Frequency	PRF	1225 Hz
Interpulse Period	IPP	816 μsec
Spacecraft Velocity	V	7.14 Km/sec
Altitude	H	375 Km
Look Angle	θ	46°
Incidence Angle	θ_i	49°
Range	R	559 Km
Swath Width	SW	100 Km
Antenna Width	W	2.0 m
Range Beamwidth	Ω_r	6.73^o
Range Pulsewidth	T_r	33.8 μsec
Range Bandwidth	Δf_r	1.25 MHz
Antenna Length	L	12.0 m
Azimuth Beamwidth	Ω_a	1.12^o
Time in Beam	T_{beam}	1.54 sec
Azimuth Bandwidth	Δf_a	1.19 KHz
Oversample Factor	f_{os}	1.2

TABLE 2

NOMINAL VOIR RADAR PROCESSING PARAMETERS

Processing Parameter		Value
Range Resolution	ρ_r	191 m
Range Time-Bandwidth Product	TB_r	42.25
Range Compression Ratio	RCR	60
Sampling Rate	SR	3 Msps
Samples Per Echo	N_s	1320
Sampling Window	T_s	440 μsec
Pulses Coherently Integrated	N_{coh}	60
Coherent Integration Time	T_{coh}	0.049 sec
Azimuth Resolution	ρ_a	225 m
Pulses Per Data Dump	N_{dump}	30
Time Per Data Dump	T_{dump}	0.0245 sec
Distance Per Data Dump	Δ_{dump}	175 m
Pulses in Beamwidth	N_{total}	1886
Looks	N_{look}	30
Filter Channels Per Look	N_{chan}	2

integration over 60 pulses is necessary to achieve a single-look image of approximately 20C-meter resolution.

Analysis conducted during the FY'77 VOIR mission study has shown that range migration correction is not required for the 200-meter low resolution mode[3]. This significantly simplifies the on-board computational requirements. However, azimuth focusing computations must be updated and effected commensurate

TABLE 3
RADAR EQUATIONS

Range Processing

$$\rho_r = \frac{(f_{os})\ C}{2(\Delta f_r)\ \sin\theta_i} \qquad SR = 2(\Delta f_r)\ (f_{os})$$

$$TB_r = (T_r)\ (\Delta f_r) \qquad \Omega_r = \frac{\lambda}{W}$$

$$RCR = (TB_r)(f_{os}) \qquad SW = \frac{\lambda R}{W\ \cos\theta_i}$$

Azimuth Processing

$$N_{coh} = (T_{coh})(PRF) \qquad T_{beam} = \frac{R\lambda}{VL}$$

$$T_{coh} = \frac{(f_{os})\ R\lambda}{2\ V\ \rho_a} \qquad N_{total} = (T_{beam})(PRF)$$

$$\rho_a = \frac{(f_{os})\ R\lambda}{2\ V\ T_{coh}} \qquad N_{look} = \frac{N_{total}}{N_{coh}}$$

$$N_{dump} = \frac{\Delta_{dump}\ (PRF)}{V} \qquad N_{chan} = \frac{N_{coh}}{N_{dump}}$$

$$T_{dump} = (N_{dump})\ (IPP) \qquad \Omega_a = \frac{\lambda}{L}$$

$$\Delta_{dump} = (T_{dump})\ V \qquad \Delta f_a = \frac{2V}{L}$$

with orbital variations in Doppler chirp rate and antenna beam pointing angle. The parametric data that must be provided in real time to effect these computations is defined in Figure 1. Referring to Figure 1, outside information defining the spacecraft attitude, antenna beam angles, and the spacecraft state-of-motion are necessary in order to generate the proper azimuth reference coefficients. To reduce the accuracy requirements of the spacecraft attitude information, the proposed design of Figure 1 incorporates the capability to compute a refined measure of the spacecraft attitude based on the characteristics of the SAR data itself. This Doppler centroid information is derived by means of energy spectral analysis of single-look images following azimuth correlation. These calculations would be performed by appropriate microprocessors which are part of the on-board SAR processor.

The detailed outside information requirements with respect to parameter and accuracy are tabulated in Table 4. The criteria for resolution is a nominal 200 meters ±25 percent. It should be noted that the ±1 Km position accuracy is based on satisfactorily meeting the resolution requirements. This does impose a pixel registration error of that magnitude which may or may not be acceptable.

3.0 ON-BOARD SAR PROCESSOR ARCHITECTURE

A functional block diagram of the proposed on-board SAR processor is defined in Figure 2. Referring to Figure 2, the data interface unit receives, conditions, and distributes incoming raw SAR video and parametric engineering data required to process SAR images. The range correlator performs the range correlation function. The azimuth correlator performs the azimuth correlation function, antenna beam pointing correction, digital magnituding, and multi look superposition. The microprocessor controller computes the necessary corrections and effects control functions for all functional elements of the processor.

Referring to the processing requirements listed in Table 2, the range correlation function could be achieved with four 60-stage transversal filters as shown in Figure 3. The block diagram of Figure 3 assumes real (I) and quadrature (Q) channels from the radar receiver. If the output data from the SAR receiver is "range offset" so that it only contains real components over a
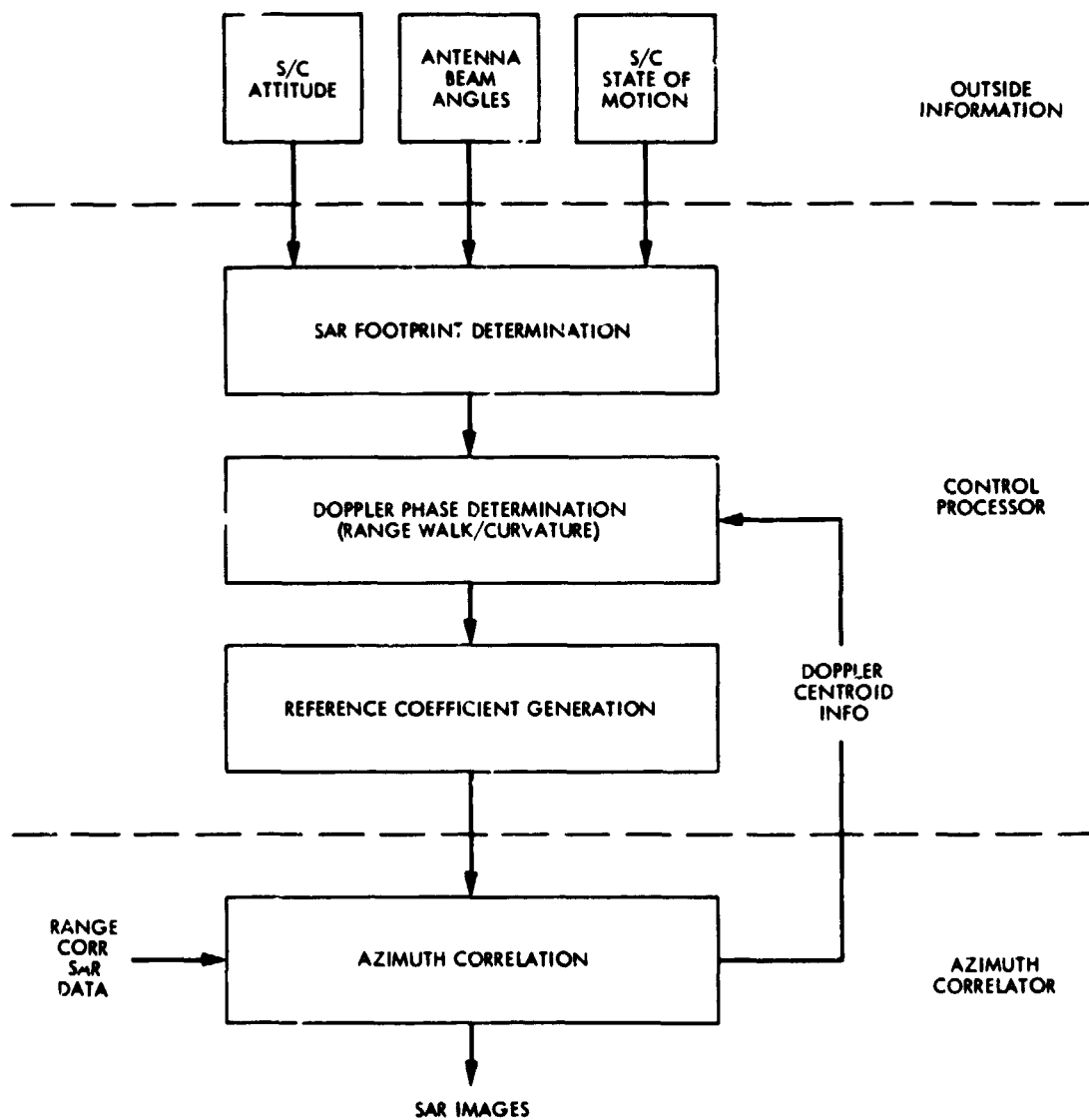
Figure 1. VOIR Azimuth Reference Function Generation

TABLE 4
OUTSIDE INFORMATION REQUIREMENTS

Parameter	Accuracy	Effects of Inaccuracy
S/C Attitude		
Roll	$\pm 1^{\circ}$	Reduced SNR
Pitch	$\pm 0.4^{\circ}$	Reduced SNR + Doppler Ambiguity
Yaw	$\pm 0.4^{\circ}$	Reduced SNR + Doppler Ambiguity
Antenna Beam Angles		
θ_{look}	$\pm 0.4^{\circ}$	Reduced SNR + Doppler Ambiguity
ϕ_{az}	$\pm 0.4^{\circ}$	Reduced SNR + Doppler Ambiguity
S/C State of Motion		
Position	± 1 Km In Three Directions	Pixel Registration Error of that Magnitude + Resolution Degradation
Velocity	± 60 m/sec In Three Directions	Resolution Degradation
Acceleration	± 0.1 m/sec^2 In Three Directions	Resolution Degradation

single channel, the range correlator implementation of Figure 4 could be used. Use of two 120-stage transversal filters (one cosine filter and one sine filter) would provide an output equivalent to that from Figure 3.

The azimuth correlator of Figure 2 could be implemented to meet the requirements listed in Table 2 using 60 parallel azimuth filter channels as shown in Figure 5. Two filter channels are required to process a single look.
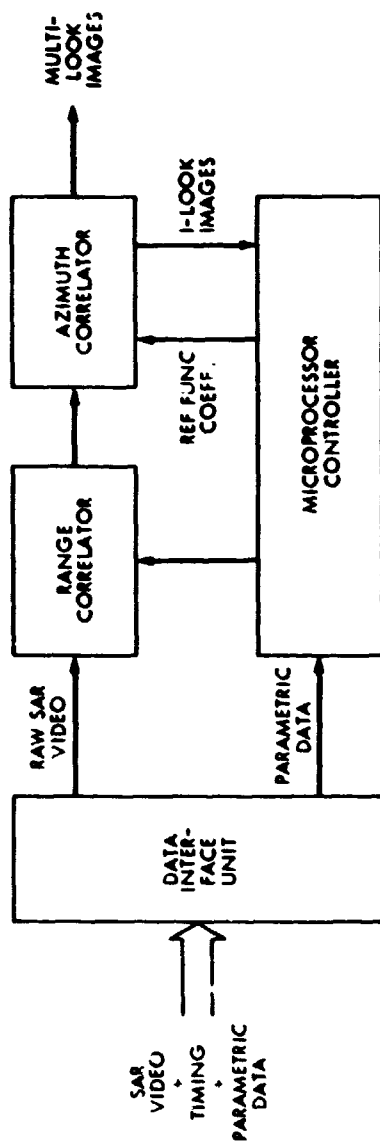
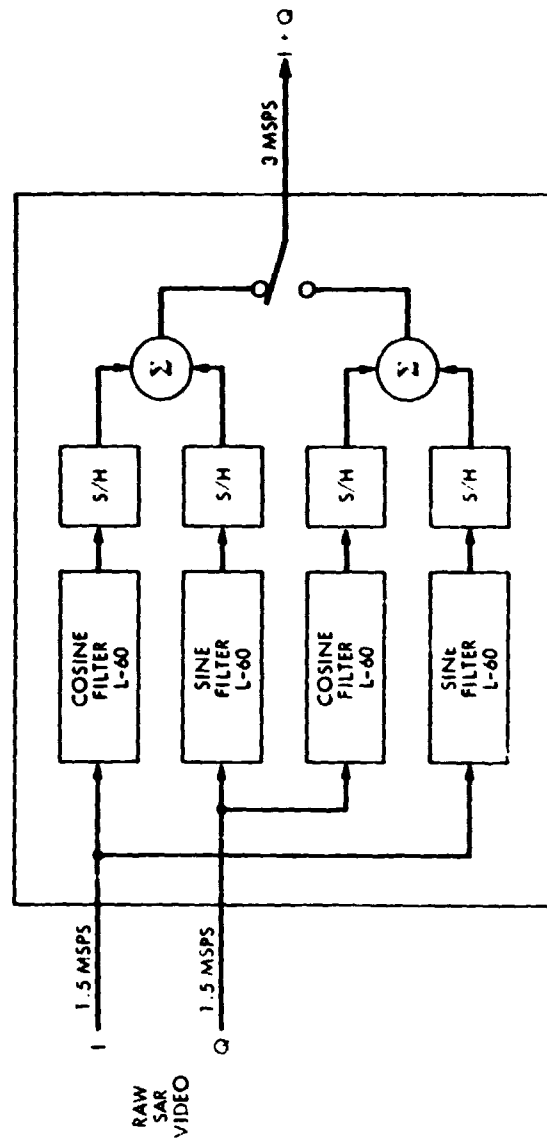Figure 2. VOIR On-Board SAR Processor Block Diagram

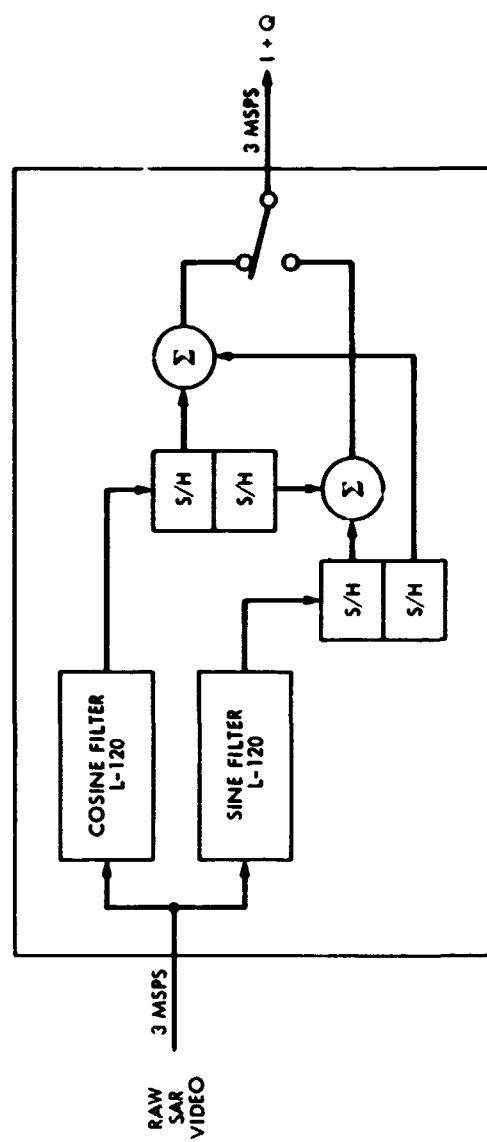Figure 3. VOIR Range Correlator (Complex Input)

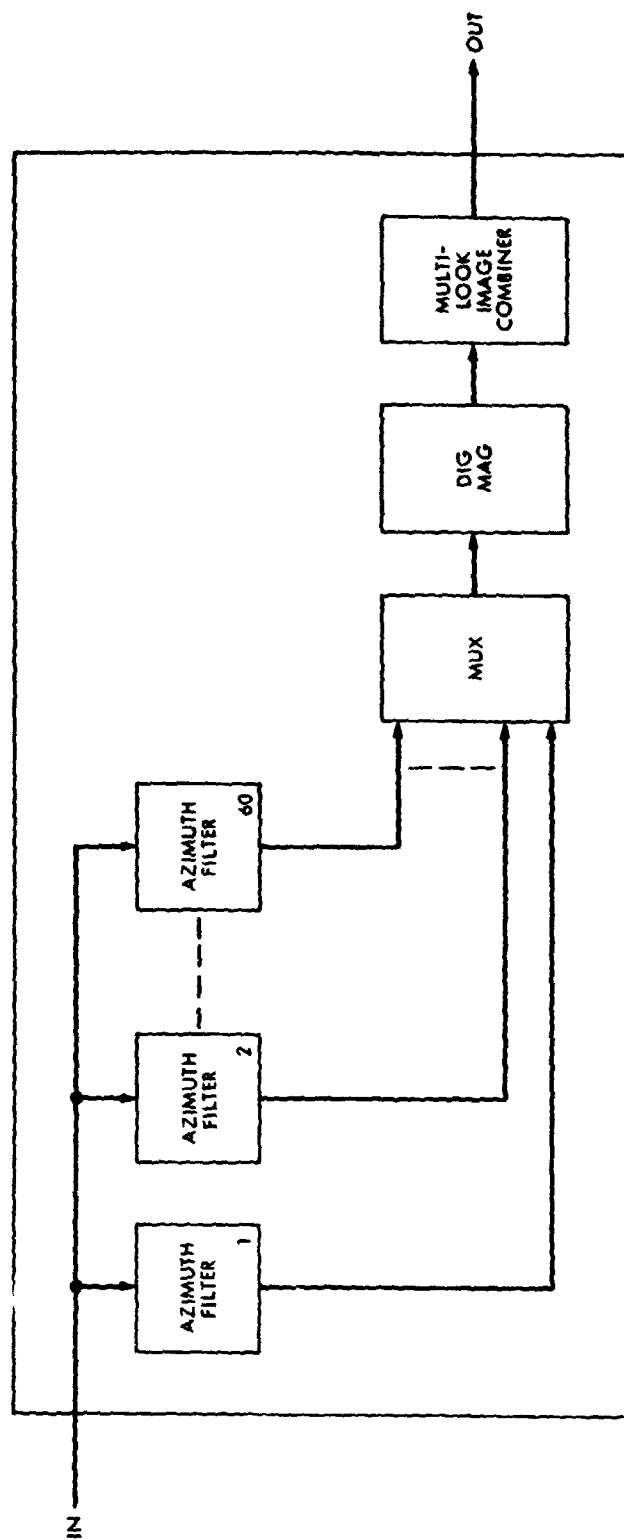Figure 4. VOIR Range Correlator (Range Offset Input)

Figure 5. VOIR Azimuth Correlator

Therefore, the implementation of Figure 5 is capable of processing and superimposing 30 looks. The digital magnituding and multi-look combining functions of Figure 5 are achieved as defined in the FY'77 JPL VOIR mission study report [3].

A functional block diagram of a single azimuth filter channel is given in Figure 6. The complex multiplier must accommodate 8-bit complex words containing 4 bits of I and 4 bits of Q. The accumulator register must accommodate 600 complex words of up to 28 bits. If there is no transfer of coefficients between channels, a reference table would have to accommodate 120 complex coefficients assuming there are 2 coefficients per range line. An alternative design approach would be to store only 60 coefficients per channel and transfer sets of coefficients between channels.

4.0 IMPLEMENTATION CHARACTERISTICS

Referring to Figure 1, the baseline design assumes CMOS-SOS technology for implementation of the data interface unit and the microprocessor controller. It appears that two 16-bit CMOS-SOS microprocessors will accommodate the computational load for the controller.

Charge-coupled device (CCD) transversal filter chips are assumed for the range correlator implementation. This is based on having a fixed digital reference function.

Implementation of the azimuth correlator is assumed to be accomplished with existing CMOS-SOS chip designs so that it is not dependent upon the custom digital CCD chip being developed for the DMSP. Assuming a mask change is made to two existing universal array CMOS-SOS chips to accomplish the complex multiply and add function of Figure 6, 15 chips would be required per azimuth filter channel with a per channel power requirement of 0.35 watts.

Based upon the foregoing assumptions, a chip count has been made for implementation of each functional block of Figure 1. The required number of chips, with the associated power and weight estimates to implement the VOIR on-board SAR processor of Figure 2, are tabulated in Table 5.
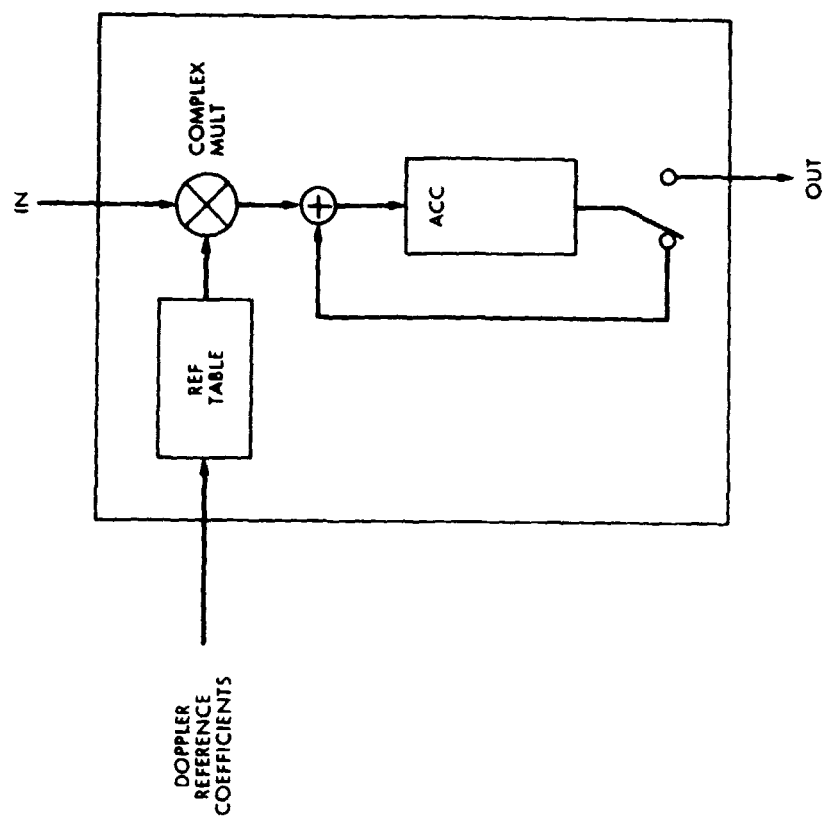
Figure 6. VOIR Azimuth Filter

TABLE 5
IMPLEMENTATION CHARACTERISTICS

Function	Chips	Power (Watts)	Weight (Kg)
Data Interface Unit	60	4	1.5
Range Correlator	10	1	0.5
Azimuth Correlator	1050	30	24
Controller	170	20	4
Totals	1290	55	30

5.0 REFERENCES

1. Arens, W.E., The Application of Charge-Coupled Device Technology to Produce Imagery from Synthetic Aperture Radar Data, Proceedings of the AIAA System Design Driven by Sensors Conference, Pasadena, California/ October, 1976.

2. Arens, W.E., CCD Architecture for Spacecraft SAR Image Processing, Proceedings of the AIAA Computers in Aerospace Conference, Los Angeles, California/October, 1977.

3. Beal, R.C., Venus Orbiter Imaging Radar FY'77 Study Report - Radar Studies, Document No. 660-60, Jet Propulsion Laboratory, California Institute of Technology, Pasadena, California/May, 1977.

APPLICATIONS AND LIMITATIONS OF VERY LARGE-SCALE INTEGRATION IN SAR AZIMUTH PROCESSING

DENNIS G. KUHLER
GOODYEAR AEROSPACE CORPORATION
P. O. BOX 85
LITCHFIELD PARK, ARIZONA 85340

SUMMARY

By using digital CCD's for data storage and single-chip multiplier accumulators, a low-power, high-density convolution processor may be designed. The memory tradeoffs involving chip design and speed are related to the operation of the processor and several optimum memory organizations are given. The major limitation of a convolution processor designed with CCD memory chips is the inability to operate in real time except for slow aircraft speeds or coarse resolutions. Two methods of summing the products are evaluated with respect to speed, power, and space requirements. A convolution processor is designed, and the number of chips as well as the power and volume requirements are determined using 4-, 6-, and 8-bit data words. The processor is flexible because range samples may be traded for additional azimuth samples by altering the control signals. The processor is also modular, and additional range or azimuth samples may be processed by adding more cards. Additional azimuth looks may be obtained by duplicating the single-look processor.

1.0 INTRODUCTION

The largest amount of hardware and the highest power requirement in a SAR data processor have been used to process the data in the azimuth or along-track dimension. The prefiltered azimuth data are stored in a corner-turning memory for the length of a synthetic aperture and convolved with the azimuth reference function to obtain processed azimuth samples. All range samples for a given azimuth position are processed before processing the

next group of range samples. The convolution operation performed on N azimuth samples may be expressed by the equation:

$$S_0(mT) = \sum_{n=(N-1)/2}^{n=(N+1)/2} h(nT)S_i(mT - nT) \quad , \quad (1)$$

where

$$S_0(mT) = \text{complex output samples}$$
$$N = \text{samples in synthetic aperture}$$
$$h(nT) = \text{complex reference}$$
$$S_i(mT - nT) = \text{complex input samples.}$$

From eq. (1), the number of complex multiplications required per output sample is N, and the number of summations is N - 1. The in-phase and quadrature samples representing digitized radar returns collected for a synthetic aperture are stored in the CCD memories, multiplied by the complex reference function, and accumulated to give the azimuth-compressed signal (see Fig. 1). Convolution processing requires a continuous stream of data with the oldest data sample being replaced by the newest sample after each azimuth output.

2.0 CCD MEMORY CHARACTERISTICS

The first element in the data path of Fig. 1 is the CCD memories, which store the samples until a synthetic aperture length of data has been collected. Three types of 65K CCD memories are presently available from different sources. The 65K CCD memories from Fairchild, F464, and Texas Instruments, TMS 3064, are organized as sixteen 4K shift registers which operate at a maximum speed of 5 MHz. The single-bit output is selected from one of the 16 shift registers by a 4-bit address. The Intel device, 2462, is organized as 256 registers of 256 bits each, and the maximum clock rate is 1 MHz. All three memories have a read-circulate, write, and read-modify-write mode. When performing the convolution operation, the read-
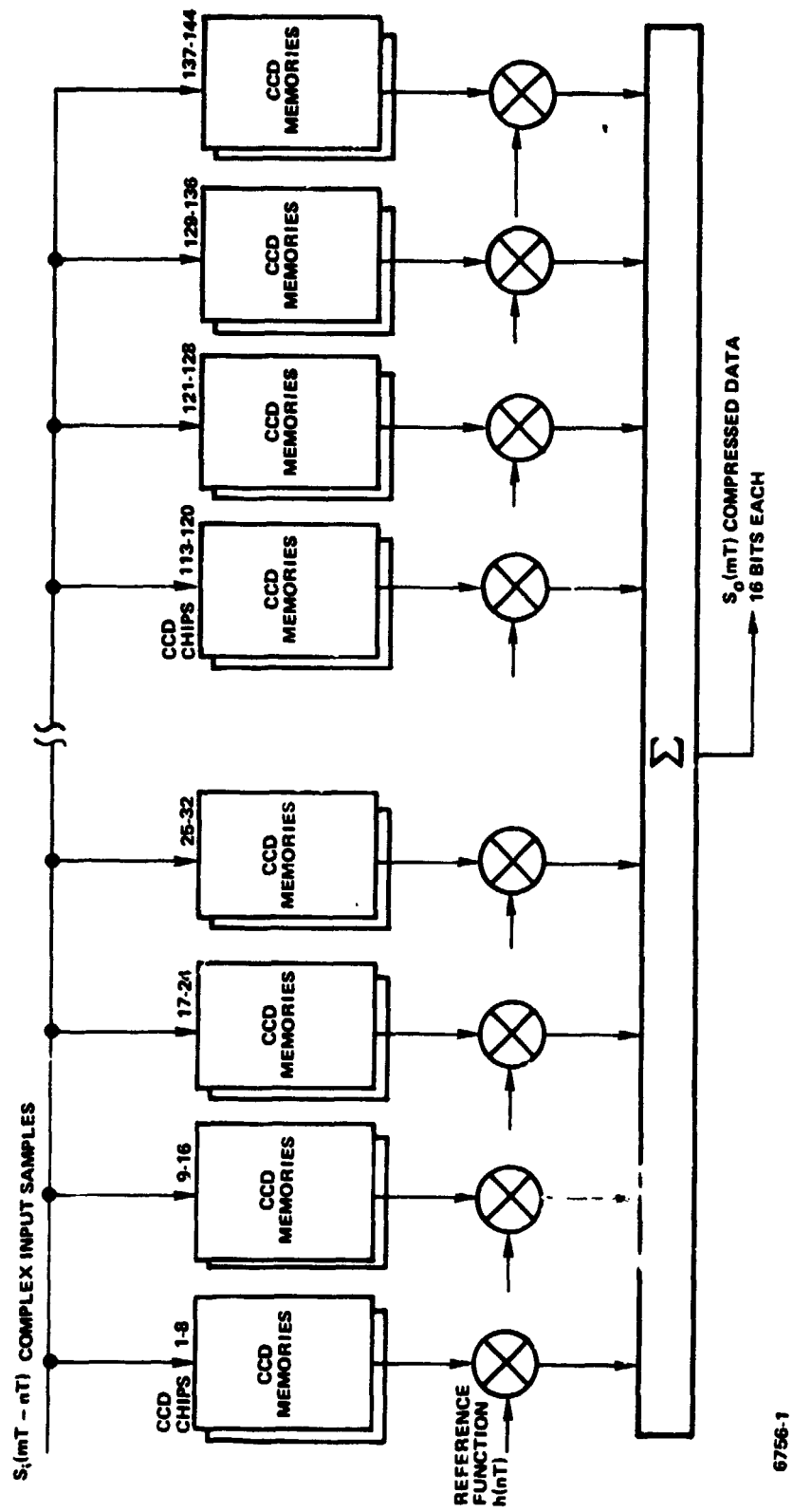
Fig. 1. Azimuth Convolution Processor

recirculate and write modes are used. The TMS 3064 and the F464 chips require 12-V clock drivers, while T^2L clocks are used on the 2462. The time required to output all 65K bits from the CCD memories (T_o) is 13.1×10^{-3} s for the TMS 3064 and the F464 when operating at a 5-MHz clock rate and 65.5×10^{-3} s from the 2464 when operating at a 1-MHz clock rate. This is the minimum time to process all range samples for a particular azimuth position and provides a real-time azimuth resolution, W_a, of

$$W_A = 1.25 T_o V_a \quad , \qquad (2)$$

where V_a is the aircraft velocity, and 1.25 azimuth samples per resolvable element are processed to give 30-dB azimuth sidelobes.

Assuming an aircraft speed of 1000 ft/s, the best azimuth resolution available in real time is 16.4 ft from the F464 and TMS 3064 devices and 81.8 ft from Intel's 2464. Better azimuth resolution may be obtained by recording the data on magnetic tape in real time and using a lower speed for playback. Five-ft resolution may be obtained by reducing the tape playback speed by a factor of 3.3. This assumes enough complex multipliers are used so that the shift rate in the CCD memory is the limiting parameter.

3.0 PROCESSOR MEMORY ORGANIZATION

Many combinations of bit length, range samples, and azimuth samples for a CCD memory chip are available as shown in Table 1. To avoid complex timing or address record keeping, the product of the bits per data word and the range samples should equal some multiple of the shift register length. Because the chips are organized as single-bit input and output, several bits of the same word may be stored sequentially in each shift register. However, if parallel multipliers are used in the correlator, a serial-to-parallel converter must be used at each CCD output. Such an organization is desirable only if the number of range samples is less than the CCD shift register length, in which case part of the shift register would remain unused. The number of bits per data word, N_B, column 1 of Table 1, is determined by

TABLE 1 - OPTIMUM CHIP ORGANIZATIONS

N_B Bits in I or Q	C_P Clock pulses/ word	N_R Range samples/ range line	N_{AZ} Azimuth samples/ chip
4	1 2 4	$\dfrac{N_{sh} \cdot m}{CP}$	$\dfrac{2^{18}}{N_{sh} \cdot m}$
6	1 2		
8	1 2 4 8		

the dynamic range requirements and will be considered fixed at 4, 6, or 8 bits, although there is some interest in single-bit processors. The number of clock pulses per data word, C_P, determines how many bits of each data word are stored on a chip. The most practical combinations are a single-clock pulse, $C_P = 1$, in which case a single bit is stored in each chip and N_B parallel chips are required; and $C_P = N_B$, in which case all bits of a data word are stored on a single chip and the data are output serially. The number of range samples, N_R, stored for each azimuth sample (column 3 of Table 1) is given by

$$N_R = \frac{N_{sh} \times m}{C_P} \quad , \tag{3}$$

where N_{sh} is the number of bits per shift register in the CCD, and m is the number of shift registers filled by a range line of data. The upper limit

of m is the number of shift registers in the CCD, 16 in the TMS 3064 and F464, and 256 in the Intel 2462. The number of range samples per PRF is given by

$$N_R = \frac{K \Delta S}{W_r} \quad , \tag{4}$$

where ΔS is the slant range swath and W_r is the slant range resolution. The number of shift registers in a CCD required to store a range sample is given by combining eq. (3) and (4) and solving for m:

$$m = \frac{K \Delta S C_P}{W_r N_{SH}} \quad . \tag{5}$$

The number of azimuth samples stored in a CCD memory, column 4 of Table 1, is given by:

$$N_{AZ} = \frac{N_{CCD}}{N_R \cdot C_P} = \frac{2^{16}}{N_{SH} \cdot m} \quad , \tag{6}$$

where N_{CCD} is the number of bits in a CCD (64K). The number of azimuth samples across the synthetic aperture, N_{LS}, required to process the data to an azimuth resolution, W_a, is given by.

$$N_{LS} = L_S \cdot \frac{K}{W_a} = \frac{K^2 R \lambda}{2 W_a^2} \quad . \tag{7}$$

The number of chips required to store a fraction C_P/N_B of the data is determined by dividing eq. (7) by eq. (6):

$$\frac{N_{LS}}{N_{AZ}} = \frac{K^2 R \lambda}{2 W_a^2} \cdot \frac{N_R C_P}{N_{CCD}} \quad . \tag{8}$$

The total number of memory chips, N_{CH}, is then obtained by multiplying eq. (8) by N_B/C_P to give:

$$N_{CH} = \frac{K^2 R \lambda}{2W_a^2} \cdot \frac{N_R C_P}{N_{CCD}} \cdot \frac{N_B}{C_P} = \frac{N_{LS} N_R N_B}{N_{CCD}} \quad . \qquad (9)$$

The number of chips required varies inversely as the range resolution, inversely as the square of the azimuth resolution, and directly as the range and range swath.

4.0 PROCESSOR DESIGN

As an example of azimuth processor design, a slant range swath of 10 mi is imaged at a maximum range of 30 mi with azimuth and range resolution of 10 ft with I and Q data channels of 4 bits each. The displacement caused by range curvature may be determined from the equation:

$$D = \frac{L_S^2}{8R_o} \quad , \qquad (10)$$

which for an X-band radar, $\lambda = 0.1$ ft, is 1.75 ft. This is sufficiently small so that range curvature correction is unnecessary. The value of m is, from eq. (5) when using $N_{SH} = 4096$, and $C_P = 1$,

$$m = \frac{K \Delta S C_P}{N_{sh} W_r} = \frac{1.25 \times 10 \text{ NMI} \times 6000 \text{ ft/NMI} \times 1}{4096 \times 10 \text{ ft}} = 1.83 \quad .$$

Because m must be an integer, the next highest value, m = 2, is chosen. This increases the slant range swath from 10 NMI to 10.9 NMI. The number of range samples is, from eq. (3),

$$N_R = \frac{N_{SH} \cdot m}{C_P} = \frac{4096 \times 2}{1} = 8192 \quad .$$

The number of azimuth samples stored per chip is, from eq. (6),

$$N_{AZ} = \frac{N_{CCD}}{N_R \cdot C_P} = \frac{65\ 536}{8192} = 8 \quad .$$

The number of azimuth samples across the synthetic aperture, N_{LS}, is determined from eq. (7) to be:

$$N_{LS} = \frac{K^2 R \lambda}{2 W_a^2} = \frac{(1.25)^2 \times 30 \text{ NMI} \times 6000 \text{ ft/NMI} \times 0.1 \text{ ft}}{2 \times (10 \text{ ft})^2} = 140.6 \qquad .$$

Because 8 azimuth samples are stored per chip, the number of azimuth chips required is $140/8 = 17.5$, so 18 azimuth chips are used, increasing the number of azimuth samples, N_{LS}, to 144. The total number of CCD chips required for azimuth processing may be determined from eq. (9) to be:

$$N_{CH} = \frac{N_{LS} \cdot N_R \cdot N_B}{N_{CCD}} = \frac{144 \times 8192 \times 8}{65\ 536} = 144 \qquad .$$

The power required is approximately 0.25 W/chip, or 36 W total, for the memory and 19 W for the 42 clock drivers. The memory and clock drivers require three printed-circuit boards.

5.0 MULTIPLIER ACCUMULATOR

The data are output from the memory to the multipliers (see Fig. 1). The product of the complex signal and the complex reference is formed and summed for all azimuth data point. The four products which are formed to give the in-phase and quadrature components are:

$$\left. \begin{array}{l} \text{In-phase} = S_i R_i - S_Q R_Q \\[2mm] \text{Quadrature} = S_i R_Q + S_Q R_i \end{array} \right\} \qquad (11)$$

The choices of integrated circuits to perform the complex multiplications are an 8-bit multiplier from Monolithic Memories and an 8-bit multiplier-accumulator from TRW. The multiplier chip requires an output latch as well as an adder stage and an accumulator to equal the capability of the 8-bit TRW multiplier accumulator. The combined space and power requirements of the multiplier, latch adder, and accumulator combination are greater by

a factor of 2 than the space and power required by the TRW chip, which uses
1.2 W to accomplish a multiply-accumulate operation in 70 ns. Because the
multiplier accumulator operates at greater than a 10-MHz rate, a single
chip can accumulate the products of either the in-phase or quadrature com-
ponents of eq. (11) by forming the first product and then adding or sub-
tracting the second. The multiplier accumulator output is a 19-bit sum of
products which may accommodate sixteen 15-bit products without overflow.
Fifteen-bit products result from the multiplication of two 8-bit words.
Sixty-four products of 11 bits each may be accumulated without overflow
when there are 6 bits in the signal and the reference, and 256 products of
7 bits each when there are 4 bits in the signal and the reference. If the data
rate to the compression filter is slowed sufficiently so that 256 products of
7 bits each may be stored in the accumulator, only a minimum number of
accumulators are required to do the convolution indicated in eq. (1).

Assuming a 5-MHz shift rate in the CCD's, a single accumulator may store
the in-phase or quadrature products for the eight azimuth samples stored in
a CCD memory. The required number of multiplier accumulators is then
144/8 × 2 = 36. The required power is 1.2 W/chip × 36 chips = 43 W.
An additional 8 W is required to multiplex the CCD outputs to form the two
products indicated in eq. (11) for the in-phase and quadrature channels.
The final operation in performing the convolution operation is to add the out-
puts of the multiplier accumulators (18 I and 18 Q accumulators). The num-
ber of its output from each accumulator in the example used is 11 (16
products of 7 bits each). The power required to accumulate the final
products is 20 W, and the number of chips required to sum the accumulator
outputs is 260, consisting of latches and adders. The output is a 16-bit sum
of products in I and Q, occurring each 1.6 μs. The power and chip require-
ments for each function are listed in Table 2. The reference function
generator is not included in the table, but a reasonable estimate would be
two cards and a total power consumption of 10 W.

TABLE 2 - SUMMARY OF PROCESSOR REQUIREMENTS

Bits I or Q input	Chips (W)					Power required (W)	Volume require-ments	Bits I or Q output	Output data rate (Mbs)
	Mem-ory	Clock driver	Multi-plexer	Multi-plier accumu-lator	Final accumu-lator				
4	144 (36)	42 (19)	36 (8)	36 (43)	260 (20)	126	11 boards 0.35 cu ft	16	20×10^6
6	216 (54)	60 (27)	72 (16)	36 (43)	334 (26)	166	19 boards 0.604 cu ft	20	25×10^6
8	288 (72)	78 (36)	72 (16)	36 (43)	422 (32)	199	19 boards 0.604 cu ft	24	30×10^6

6.0 CONCLUSIONS

Modern CCD n. :mories and signal processing chips provide the capability to design and build radar signal processors using a fraction of the volume and power required by present processors. As a comparison with current technology as exemplified by the SAPPHIRE processor, the size of an azimuth processor employing CCD memories and signal processing chips would occupy seven percent of the volume and use five percent of the power. It would have applications where near-real-time processing was satisfactory and where low power, size, and volume were desirable.

Other desirable attributes include a reduction in the number of individual printed circuit card types and the number of interconnections which enhance the reliability and reduce the cost. The processor is flexible because range and azimuth tradeoffs may be performed within each chip as given in Table 1. The processor is also modular with the basic module consisting of a single processor card which includes both the memory and the multiplier accumulator. As a result of fewer parts and simpler design, the life cycle costs of operation and maintenance are also reduced.

FRIDAY, MARCH 10, 1978

VI. SYSTEM DESIGN (8:00 - 11:20), Chairman: D. Held, Jet Propulsion
                                        Laboratory

**Withdrawn

SYNTHETIC APERTURE RADAR IN GEOSYNCHRONOUS ORBIT

KIYO TOMIYASU
GENERAL ELECTRIC COMPANY
VALLEY FORGE SPACE CENTER
PHILADELPHIA, PA. 19101

Radar images of the earth can be taken with a synthetic aperture radar (SAR) from geosynchronous orbital ranges by utilizing satellite motion relative to a geostationary position. See Figure 1. A suitable satellite motion can be obtained by having an orbit plane inclined relative to the equatorial plane and by having an eccentric orbit. Potential applications of these SAR images are topography, water resource management and soil moisture determination. Preliminary calculations show that the United States can be mapped with 100-m resolution cells in about 4 hours. With the use of microwave signals the mapping can be performed day or night, through clouds and during adverse weather.

Synthetic aperture radars have been flown in aircraft [3] and one is scheduled to be flown in the low-orbit NASA SEASAT satellite [1]. The antenna beam is usually oriented broadside (normal) to the radar platform velocity vector, although the beam can be oriented at other oblique angles [5]. The SAR image plane is defined by the platform velocity vector and radar antenna beam axis. A geometrical constraint requires that the normal of the object scene plane must not lie in the SAR image plane. In vector notation,*

$$(\overline{v} \times \overline{R}) \cdot \hat{n} \neq 0$$

where $\overline{v}$ = radar platform velocity vector

$\overline{R}$ = radar range vector along antenna beam axis

$\hat{n}$ = object scene plane normal

The track of a satellite in geosynchronous orbit depends on the orbit inclination angle and orbit eccentricity. In Figure 2a, a track is shown for an example of orbit inclination angle only. The long dimension is oriented in the North-South direction. If a small amount of orbit

* Other identities are $\overline{v} \cdot (\overline{R} \times \hat{n})$ and $\overline{R} \cdot (\hat{n} \times \overline{v})$.

eccentricity is added the track will tilt as shown in Figure 2b, and a
greater eccentricity will produce the track shown in Figure 2c. With an
inclination angle of $\pm 1°$, an orbit eccentricity of 0.009, and an argument
of perigee of 90°, a near circular subsatellite track [2] can be produced
as shown in Figure 2d, and the satellite scanning speed is about 48 m/se
relative to a nominal geostationary position. The maximum range rate is
about 30.4 m/sec to a 40° latitude ground location at the same longitude.
A radar frequency of 2450 MHz, an antenna beamwidth of 1° and a ground
resolution of 100 meters are assumed.

The following values were computed:

antenna diameter	7.3 m
incidence angle	46.3°
beam footprint	1063 km N-S by 654 km E-W
differential slant range across footprint	690 km
range ambiguity	217 pulses/sec, max
azimuth ambiguity	13 pulses/sec, min
radar PRF	54 pulses/sec, nominal
integration time	476 secs, min
radar bandwidth	2.08 MHz
radar Doppler shift	500 Hz, max

Depending on the viewing angle, an integration time of up to 700 seconds
per beam footprint may be required. To achieve 100-m azimuth resolution
to cover the United States, 3 East-West rows and 7 North-South columns of
footprints will be required and this will take about 4 hours. The number
of pixels is 10^9. An ambiguity due to a radar Doppler shift of 500 Hz can
be removed by ground processing which relies upon accurate ephemerides data.
An oscillator stability of better than 1 part in 10^{11} is required over the
integration time. The time-delay Doppler shift signal processing technique
required to produce images is quite similar to that used in radar astronomy
[4].

The transmitter power was calculated assuming a system noise temperature
of 600°K, a system loss of 6 dB and a resultant S/N = 10 dB. The average
powers as a function of normalized radar cross section $\sigma°$ are:

σ°, dB	P_{ave}, watts
-10	800
-20	8,000
-30	80,C00

Other sets of parametric values can be assumed to achieve different performance characteristics.

REFERENCES

[1] Brown, Jr., W. E., C. Elachi and T. W. Thompson, "Radar Imaging of Ocean Surface Patterns", J. Geophysical Res., Vol. 81, pp. 2657-2667, May 20, 1976.

[2] Chestek, J. H., General Electric Co., private communication.

[3] Cutrona, L. J., "Synthetic Aperture Radar," in Radar Handbook edited by M. I. Skolnik, New York: McGraw-Hill, 1970, Ch. 23.

[4] Green, Jr., P. E., "Radar Measurements of Target Scattering Propert es," in Radar Astronomy edited by J. V. Evans and 1. Hafgc s, New York: McGraw-Hill, 1968, Ch. 1.

[5] Kirk, Jr, J. C., "A Discussion of Digital Processing in Synthetic Aperture Radar," IEEE Trans. Aerosp. Electron. Syst., vol. AES-11, pp. 326-337, May 1975.
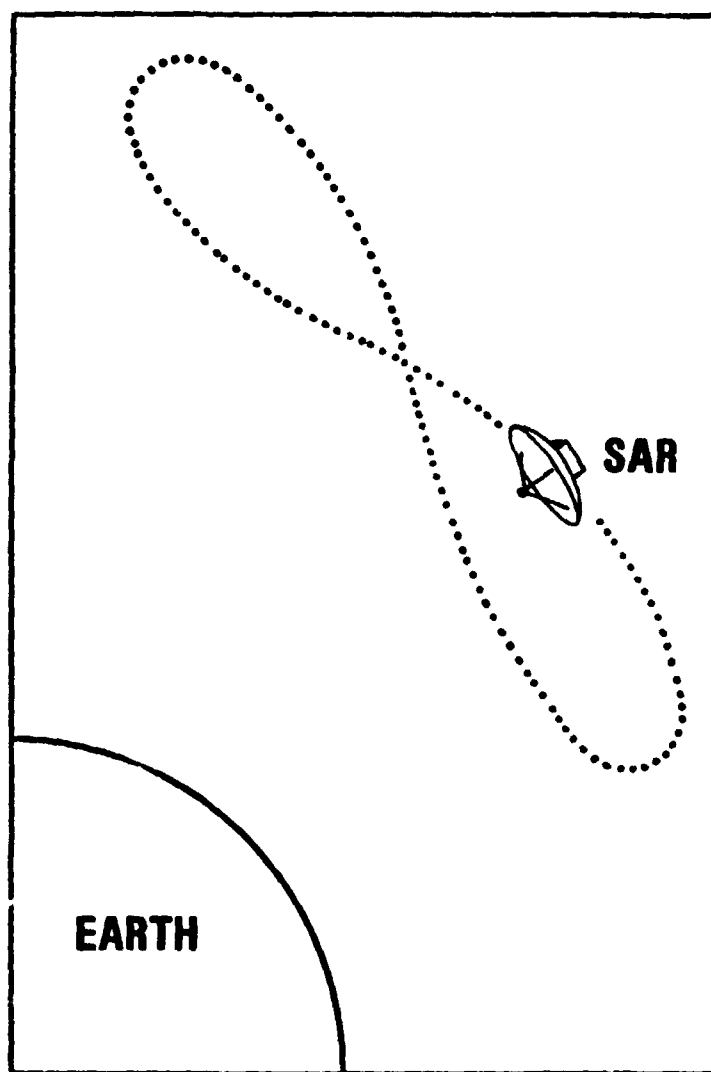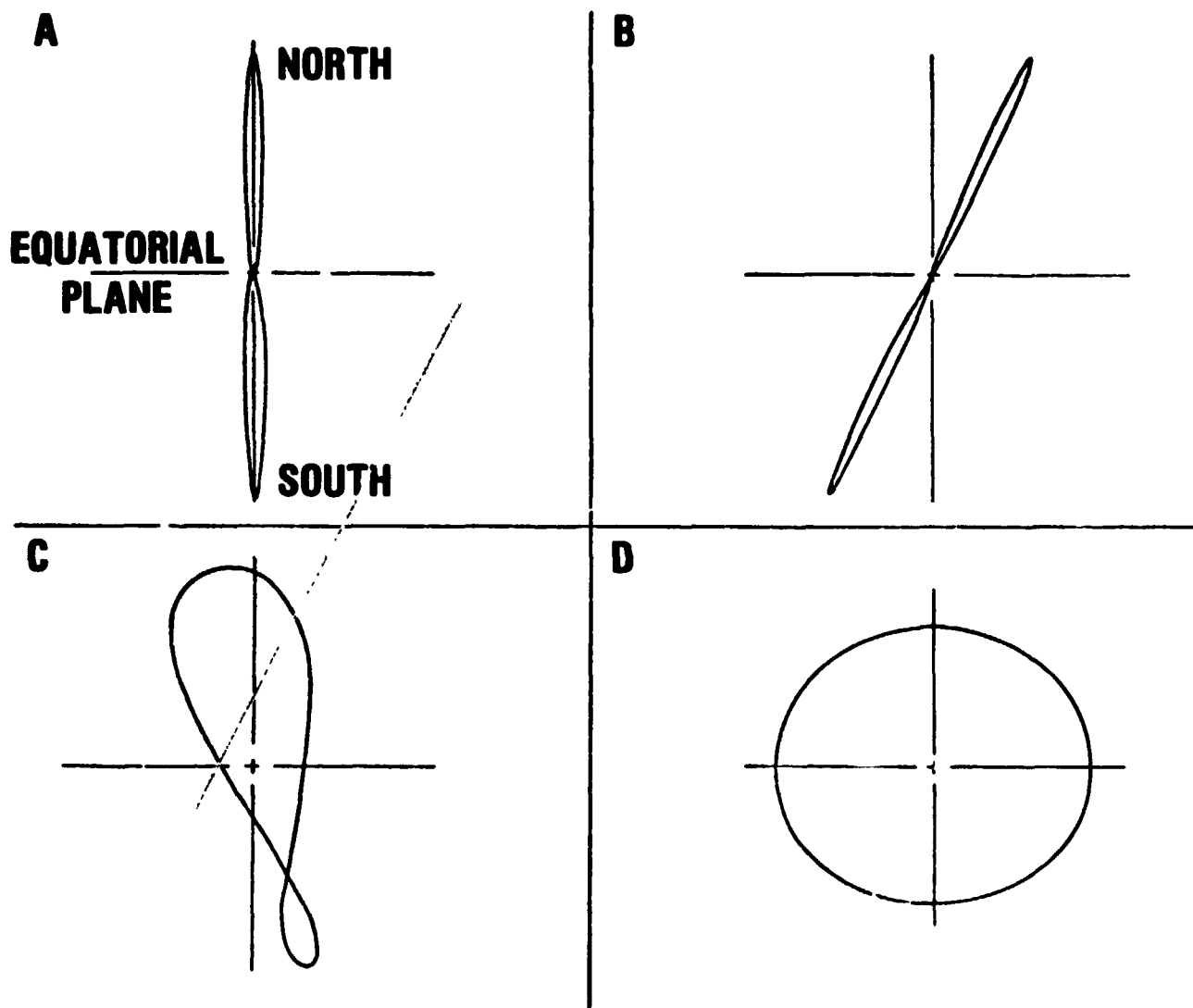
FIG.1   SAR GEOMETRY

FIG.2 SUBSATELLITE TRACK

D20(32)

A SYSTEM CONCEPT FOR WIDE SWATH CONSTANT
INCIDENT ANGLE COVERAGE

J. P. CLAASSEN
REMOTE SENSING CENTER
TEXAS A&M UNIVERSITY
COLLEGE STATION, TX   77843

J. ECKERMAN
NASA/GODDARD SPACE FLIGHT CENTER
GREENBELT, MD. 20771

SUMMARY

User requirements and inherent system constraints dictate that operational
synthetic aperture (SAR) systems for observations at orbital heights should
have the following characteristics:

1) Wide Swaths
2) Coverage at Nearly Constant Incident Angles
3) Programmable Incident Angles
4) Low Transmitter Power
5) Reasonable Antenna Size

Conventional designs fail to achieve these objectives.

A multiple beam radar is proposed as a solution meeting these requirements.
The multiple beam approach readily overcomes the radar ambiguity constraints
associated with orbital systems and therefore permits imagery over swaths
much wider than 100 kilometers. Furthermore, the antenna technique per-
mits imagery at nearly constant incident angles. When frequency scanning
is employed, the center angle may be programmed. The redundant use of
the antenna aperture during reception results in lower transmitted power
and in shorter antenna lengths in comparison to conventional designs.
Compatibility of the approach with passive imagery is also suggested.

The system concept is developed and illustrated by means of examples.
One design example is thought to be suitable for hydrological monitoring
while the other is thought to be suitable for monitoring vegetation re-
sources.

1.0 INTRODUCTION
The role for the imaging radar as an orbital sensor for earth oriented ob-

observations has emerged in recent years. Efforts are underway to demonstrate radar's capability from space using conventional design approaches to minimize development costs and risks. Although conventional radar imaging systems should be flown aboard spacecraft on an interim basis to demonstrate their capability and utility, ultimately operational systems should be based on advanced radar concepts motivated by user requirements and by inherent system constraints. An examination of these requirements indicates that a calibrated operational system should, among other factors, have the following general characteristics:

1) Wide Swath Coverage
2) Nearly Constant Incident Angle
3) Programmable Incident Angle
4) Low Transmitter Power
5) Reasonable Antenna Length

In addition to these it is also desirable that the radar system be compatible with a radiometer system so as to permit active and passive imagery simultaneously.

Swath width is necessary for frequent and timely observations. In conventional systems wide coverage is limited by practical antenna lengths, by available transmitter power, and by other factors. Crosstrack oriented systems typically image over a large domain of incident angles. Quantitative interpretation of these returns will require removal of the incident angle behavior, particularly at the smaller incident angles. Broad beam systems which generate wide swaths typically require high peak transmit powers since the PRF rate must be reduced to meet range ambiguity constraints. In some cases this can shorten the transmitter's lifetime.

To overcome swath width limitations Moore, et al. [1] have suggested and investigated a scanning synthetic aperture radar. Another technique to improve swath width while imaging at nearly a constant incident angle is suggested by a multiple beam antenna concept advanced by Bucknam, et al. [2] for a different application. This antenna concept is examined here to demonstrate its applicability in a synthetic image formation system.

2.0 THE MULTI-BEAM SAR CONCEPT

2.1 REAL BEAMS

The multi-beam antenna in its mapping mode is illustrated in Figure 1. The antenna consists of two horizontal arrays of vertical elements. This planar composite array faces at an azimuthal angle ϕ_0 between the uptrack and crosstrack directions. One array serves as the transmitting antenna and the other as the receiving antenna. The vertical elements in the arrays are identically phased to create in the elevation plane a narrow beam which points downward at an incident angle θ_0. By using a frequency scanning technique the angle of incidence may be changed as illustrated in Figure 2. The width of transmit antenna is sufficiently small to illuminate a circular swath to the right of the ground track. The vertical elements in the receive array are the same height as the elements in the transmit array. The output signals from the receive elements are processed simultaneously to form N_B real beams. The real beams overlap to provide receive coverage over the entire illuminated area.

2.2 SYNTHETIC BEAMS

The translation of the real aperture together with range gating is employed to generate high resolution synthetic beams in each real receive beam. The intersection of these synthetic beams with the scene forms pixel elements as suggested by Figure 3. A mosiac of radar images may be created by appropriately combining the synthetic resolution elements in all receive beams.

It is advantageous to image in the uptrack sector defined by the azimuthal interval $0° < \phi < 45°$. More swath is generated per unit azimuthal beamwidth in the uptrack sector in comparison to the crosstrack sector $(45° < \phi \leq 90°)$. Therefore, fewer receive beams per unit of swath length are required. In addition the multi-look strategies differ significantly between the two sectors. The choice of one sector, consequently, simplifies the SAR processing.

To generate multiple looks in the uptrack sector processed returns are sampled in azimuth at identical cross-track distances at all range intervals as illustrated in Figure 3. The detected samples at identical
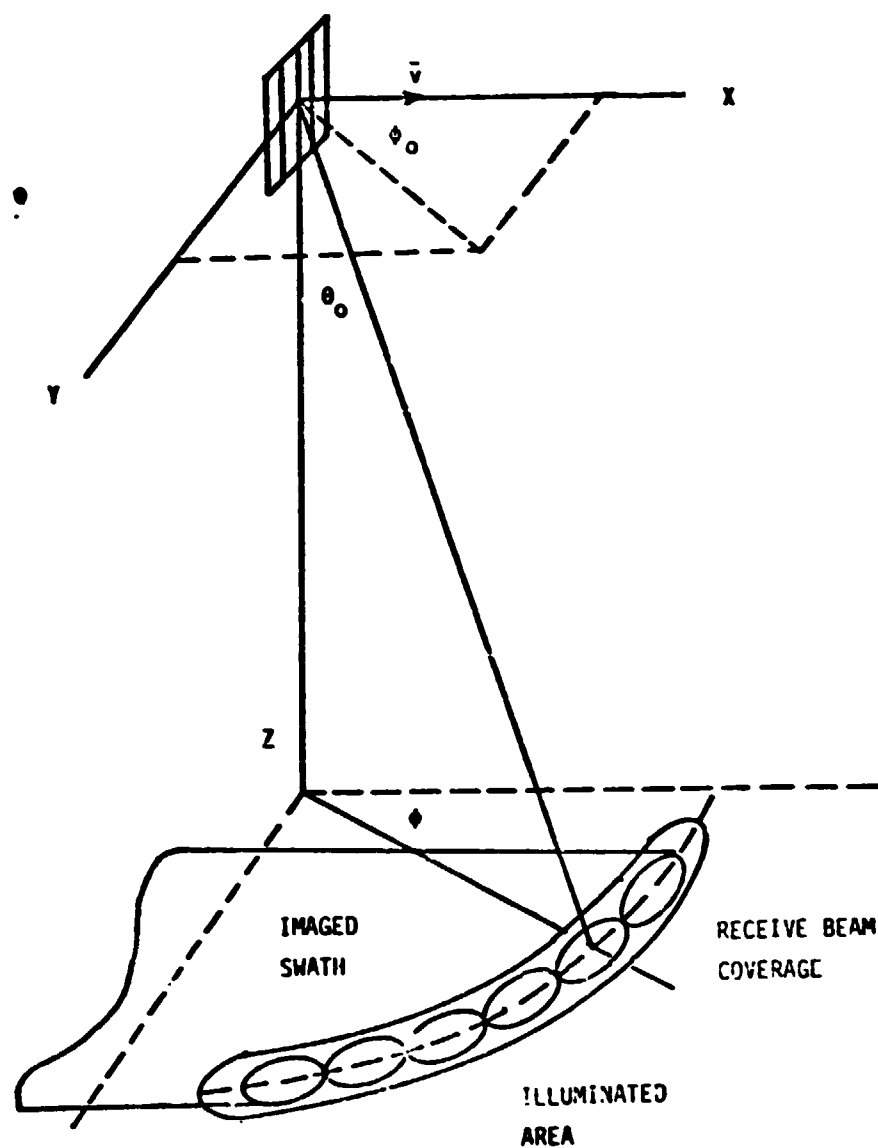
FIGURE 1. THE GEOMETRY OF THE MULTIPLE BEAM SAR
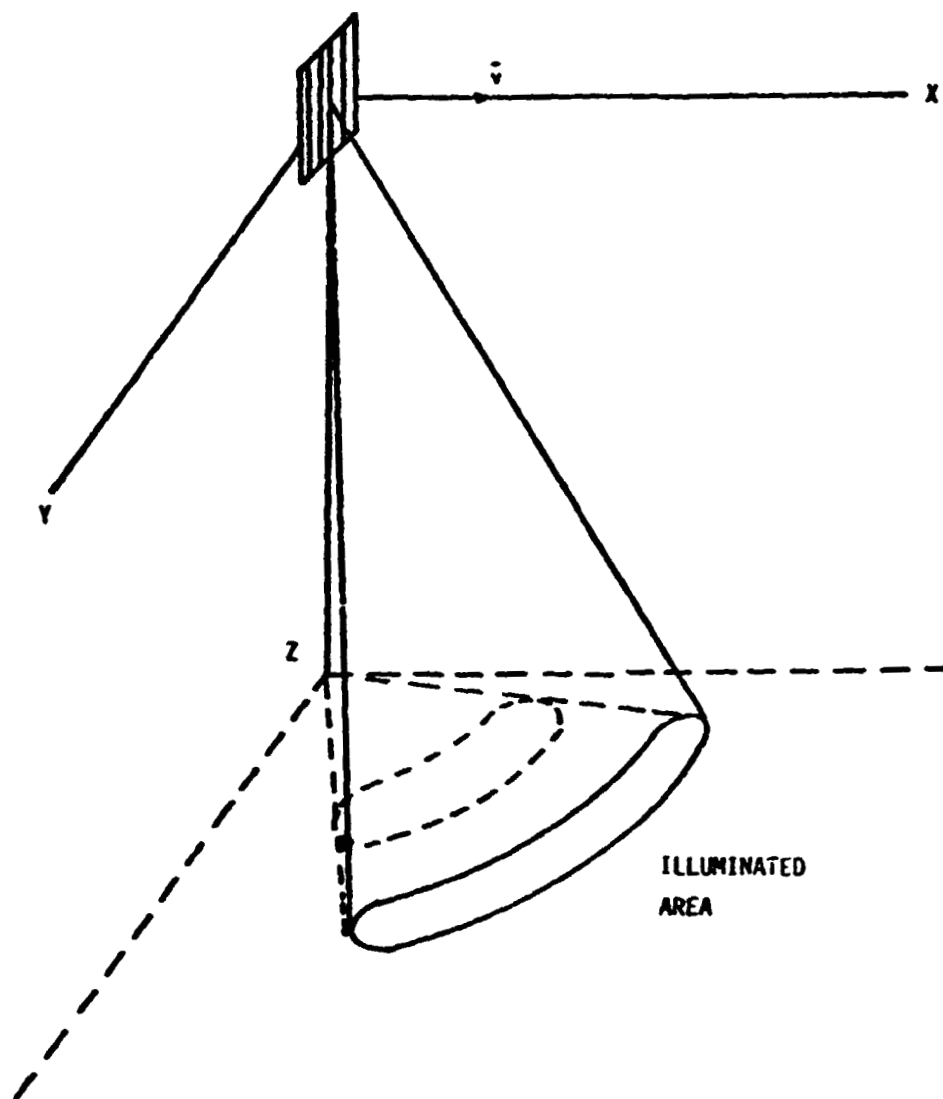
FIGURE 2.   THE EFFECT OF A PROGRAMMABLE INCIDENT ANGLE
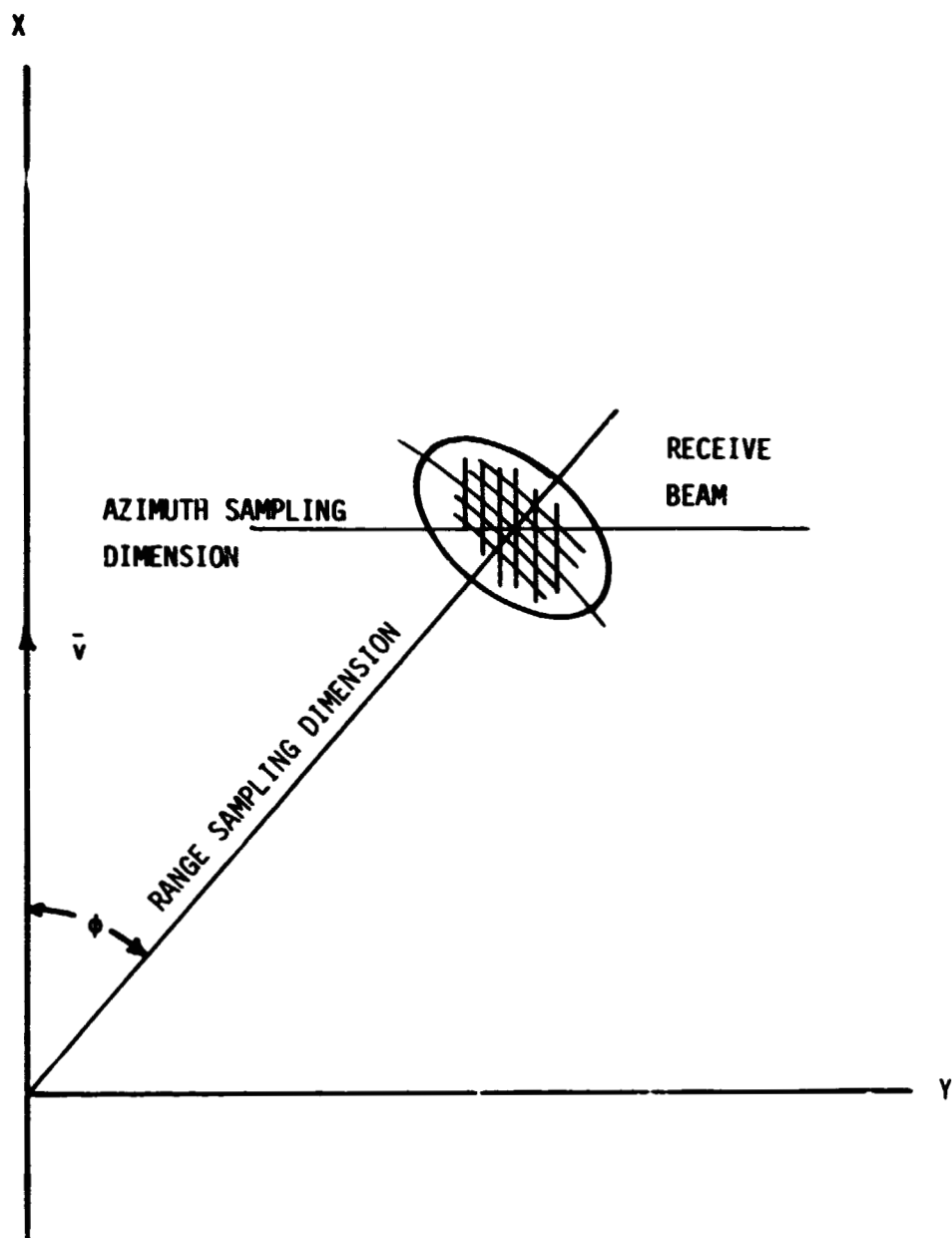
FIGURE 3. AZIMUTHAL SAMPLING STRATAGEM FOR GENERATING
          MULTIPLE LOOKS

crosstrack distances are then summed on the same cell but from different range bins as made possible by the translation of the aperture. Therefore multiple looks are created "in elevation" rather than "in azimuth" as is the case with systems looking crosstrack.

2.3 TRANSMITTER CONFIGURATION

The transmitter architecture is illustrated in the block diagram of Figure 4. A bank of frequency synthesizers provide the frequency scanning capability. The output of a frequency source is modulated, amplified and directed to the transmit antenna. A small portion of the transmitter power is sampled for internal calibration of the system.

2.4 RECEIVER CONFIGURATION

A receiver block diagram representing a processing approach for the multi-beam SAR is illustrated in Figure 5. Amplified signals from the elements of the receive antenna are combined with appropriate phase shifts to produce return signals within each real beam. The output of each beam is then coherently demodulated to zero IF using quadrature local oscillators Range compression is performed on the I and Q channels. The range sampling is performed in such a manner to track the range walk in each beam. The samples are then stored in a corner turning memory. Two such memory banks are provided to store samples from overlapping synthetic apertures.

As one memory bank fills, the samples in the other undergo azimuthal compression. Signals generated by the azimuthal processor are appropriately sampled in accord with the multi-look strategem described above. Detected samples are stored in the post processor memory. The processor registers and overlays the multiple looks. From the post processor memory the pixel elements are directed into the telemetry link.

3.0 CONCEPT VERIFICATION

3.1 INTRODUCTION

A design approach for the multi-beam SAR is presented in this section to confirm the acceptability of the concept. In the approach it is assumed that the radar wavelength λ, the elevation beamwidth β_H, the incident angle θ_o, the swath width S_w and spatial resolution ρ are specified by
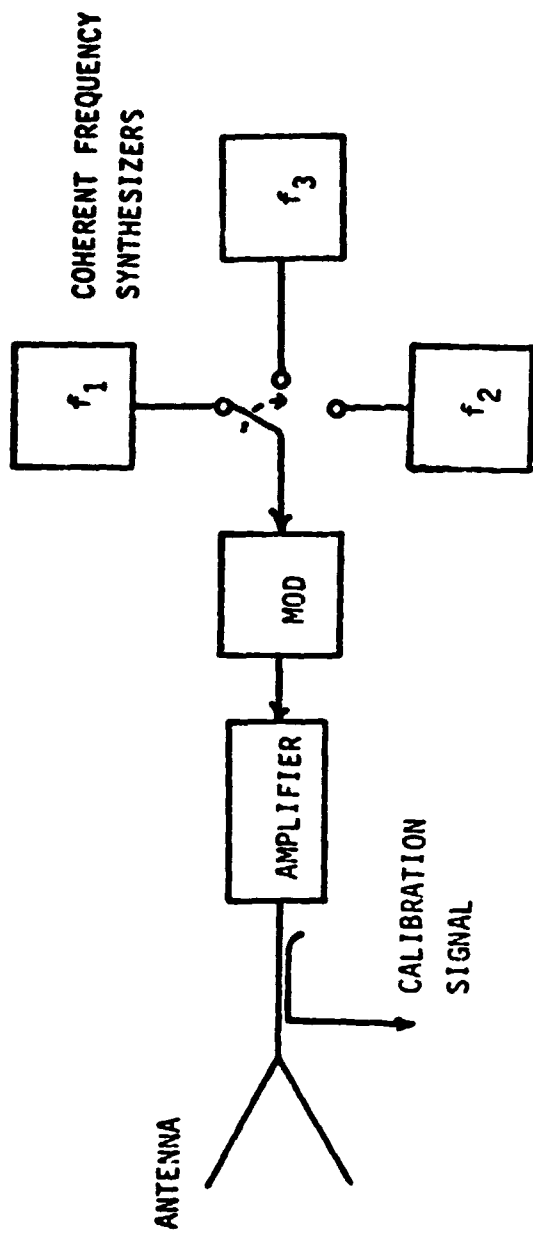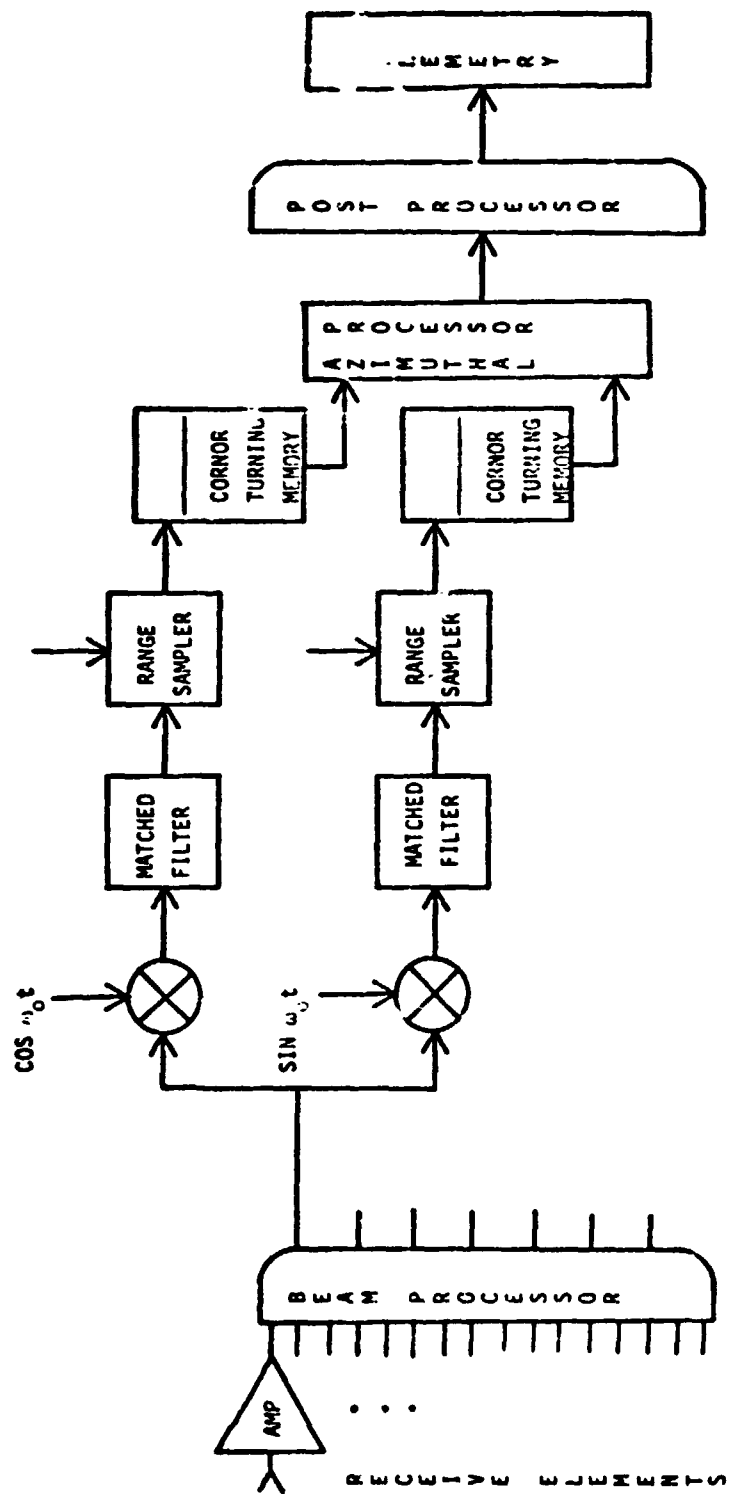
FIGURE 4.   TRANSMITTER BLOCK DIAGRAM

FIGURE 5.   RECEIVER BLOCK DIAGRAM

VI-4-9

the user application. Furthermore, it will be pragmatically assumed that the swath will be generated in the azimuthal sector between 10° and 45°. The antenna will, therefore, point at ϕ_0 = 27.5°. Throughout the concept verification a planar earth will be used to simplify the analysis.

3.2 ORBITAL ALTITUDE

The orbital altitude z is dependent upon the swath width desired. The parametric dependence of the swath width on the altitude is illustrated as a function of incident angle in the graphs of Figure 6. At small incident angles it may be necessary to image on both sides of the ground track with separate systems to improve the swath width.

3.3 RADAR AMBIGUITIES

An important consideration in designing orbital SAR systems is providing sufficient ambiguity suppression. To achieve satisfactory suppression in this design verification a guard factor of 1.7 will be used in the range and azimuth sampling requirements. When these requirements are combined, the following restriction on the beam widths is derived:

$$\beta_L \; \beta_H \; \leq \; .088\lambda c/zv \; \tan^2 \theta_0 \; \sin\phi \qquad (1)$$

where c is the speed of propagation and v is the ground track velocity. The above expression can be used to determine an acceptable azimuthal beam width β_L since β_H has been specified.

The suitability of such guard factors is dependent on reasonably low sidelobe levels. In view of the two-way characteristic in the range dimension, a 17.6 dB sidelobe level is chosen. The associated beam width is given by [3]

$$\beta_H \; = \; \frac{1.02\lambda}{H\sin\theta_0} \qquad (2)$$

where H is the antenna height. A sidelobe level of 40 dB is chosen in the azimuth dimension in view of the one-way characteristic there. The azimuthal beam width is given by [3]

$$\beta_L \; = \; \frac{1.66\lambda}{L \; \sin\theta_0 \; \cos \; (\phi-\phi_0)} \qquad (3)$$

where L is the antenna length. To illuminate the entire 35° sector, the width of the transmit antenna must be given by
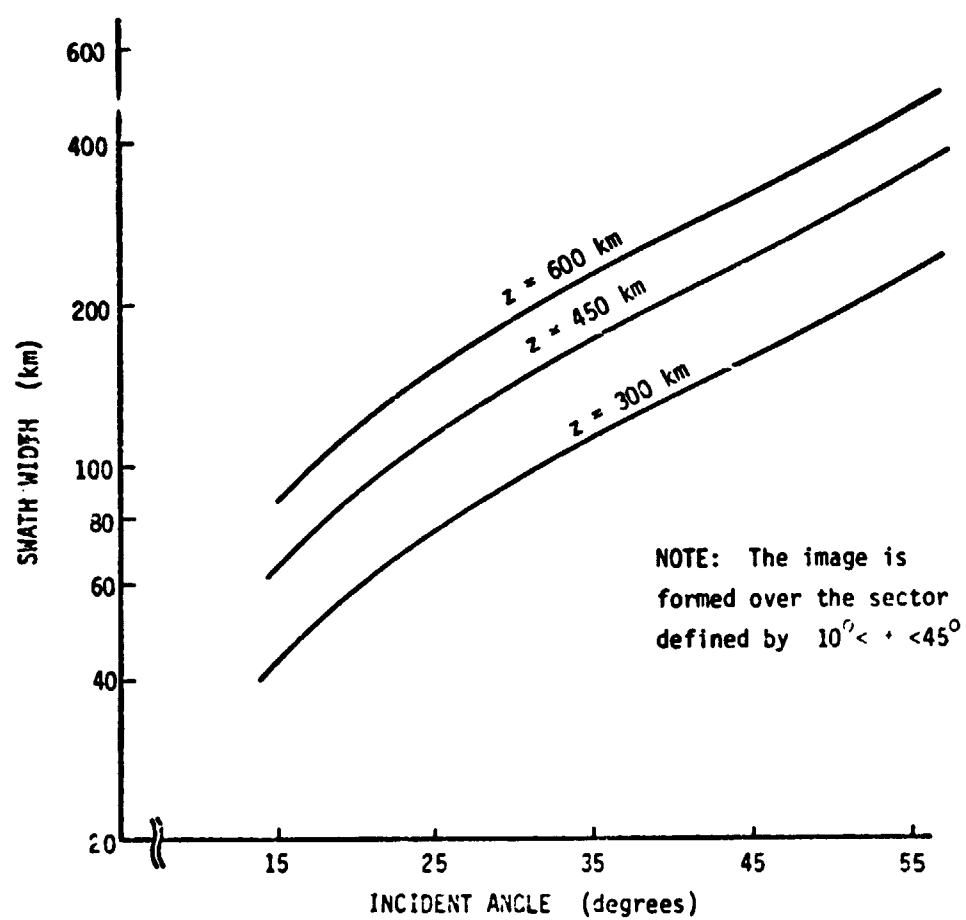
FIGURE 6. THE MULTI-BEAM SAR SWATH WIDTH CHAI ACTERISTIC

$$W = 1.7\lambda/\sin\theta_o \qquad (4)$$

The above relationships specify the antenna dimensions.

From β_L the number of receive beams can be computed approximately as

$$N_B = 0.61/\beta_L (\phi = \phi_o) \qquad (5)$$

A PRF which includes the 1.7 guard factor is given by

$$PRF = 5.9 \ v/L \qquad (6)$$

3.4 TRANSMITTER POWER

It is well known that the average transmitter power is given as

$$W_{ta} = \frac{4\pi\lambda^2 R^4 L_s FkT \ S/N}{T_a A_t A_r \eta_t \eta_r \sigma^o \rho^2} \qquad (7)$$

where

R = radar range

L_s = system loss factor

F = receiver noise figure

kT = noise power per unit bandwidth

S/N = signal to noise ratio

$A_t A_r = LWH^2 \sin^2\theta_o \cos(\phi-\phi_o) \qquad (8)$

$\eta_t \eta_r$ = product of antenna efficiencies

σ^o = scattering coefficient

$T_a = 1.28 \ \lambda R/2v(1 \ \sin^2\theta_o \cos^2\phi)^{1/2} \rho \qquad (9)$

The corresponding peak power is given by

$$W_{tr} = B_{rf} W_{ta}/PRF \ C_r \qquad (10)$$

where

C_r = range compression factor

$B_{rf} = 0.5c/\rho\sin\theta_o \qquad (11)$

The range compression factor C_r cannot be increased indefinitely since the sum of the transmit and receive durations must be less than the PRF interval. When a guard space of four transmit pulse lengths is added to the interval to allow for receiver gate rise and fall times and for variations

In altitude, a range compression constraint can be established

$$Cr \leq \frac{Brf}{6} \left[\frac{1}{PRF} - \frac{2\Delta R}{c}\right]$$ (12)

where ΔR is the range interval over the illuminated area.

The above expressions are helpful in specifying the transmitter power requirements.

3.5 RANGE MIGRATION CONSIDERATIONS

Since the multi-beam SAR is a squinted system, the changing range to a resolution cell must be compensated. To keep a resolution cell within the same processing bin, the range gate must be advanced

$$t = \frac{2 \sin^{\theta}o \cos \phi v}{c \; PRF}$$ (13)

every radar pulse. This will track the so-called range walk.

In addition, there is range curvature also induced by the advance of the spacecraft. The azimuthal coverage is restricted by this curvature as illustrated in Figure 7. To keep the azimuthal elements in focus throughout the beam the following inequality

$$\frac{z \; \beta_L}{\cos\theta_o} < \frac{3.1\rho^2 \sin \theta_o}{\lambda}$$ (14)

must be satisfied. This restriction will impact the beam size or resolution if the processing is to be kept simple.

3.6 SAR PROCESSING REQUIREMENTS

To minimize the telemetry data rate on wide swath systems, it is important to perform the SAR processing on-board the spacecraft. The feasibility of such a processor is dependent on its adaptability, speed and memory requirements. Various processing techniques having sufficient speed and adaptability have been advanced [4]. The SAR processing memory size for the multi-beam SAR is nominally given by

$$M = 4.6 \; PRF \; v \; T_a^2 \; N_L \; N_B/\rho$$ (15)

where N_L is the number of independent looks. This estimate is based on I and Q memories and two memory banks as described in Section 3.4.

3.7 TELEMETRY B RATE

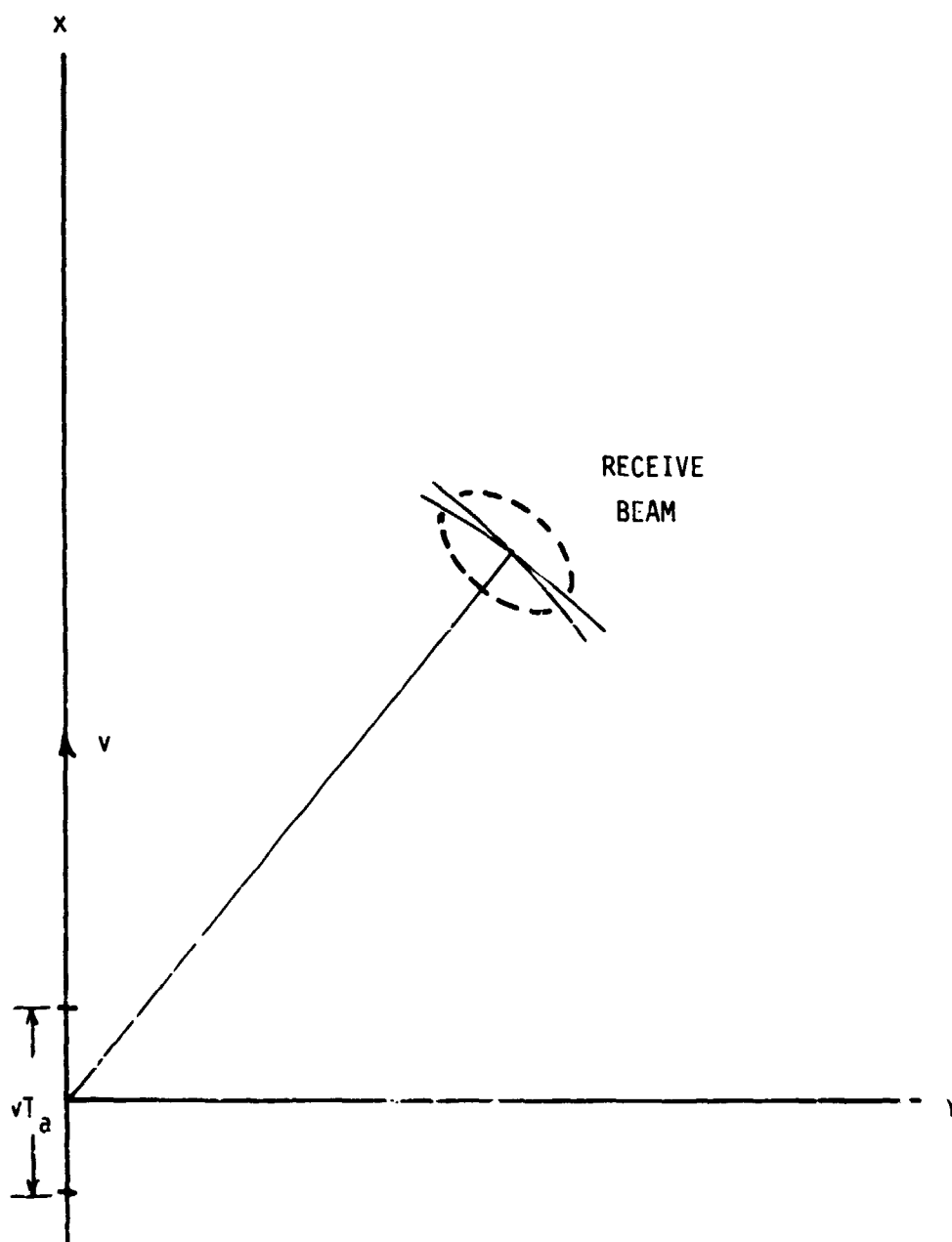If the processed data is logarithmically converted and if eight bits of

FIGURE 7.   RANGE CURVATURE AS APPLIED TO
            A SQUINTED SYSTEM

dynamic range are employed, then the telemetry bit rate is given by

$$B_T = 5.5 \text{ v z } \tan\theta_o/\rho^2 \qquad (16)$$

This rate estimate does not include the bits required for housekeeping, synchronization, control, error recovery codes, etc. These will add slightly to the above estimate.

4.0 DESIGN ILLUSTRATIONS

To illustrate the potential of the multi-beam SAR concept two designs are presented. One design is based on system parameters thought to be suitable for hydrological monitoring [5]. The second design is appropriate for monitoring vegetation resources [6]. The design guidelines are presented in Table 1. The resulting designs are presented in Table 2.

4.1 DISCUSSION OF THE DESIGN RESULTS

It is apparent from the power entries of Table 2 that the redundant use of the receiving aperture has reduced the average and peak transmitted powers considerably in comparison to conventional systems offering comparable swaths. The peak power requirement was further reduced by the high PRF permitted by the multi-beam approach. This low peak power will significantly increase the life of the transmitter.

As a point of reference a comparison of the SIR-B X band design [7] with the multi-beam X band design is presented in Table 3. It is clear from these entries that the mult'-beam SAR can achieve identical resolution, more looks, larger swath, and a comparable S/N ratio with less transmitter power at much higher altitudes.

Also from the entries of Table 3 it is noted that the antenna length has been shortened considerably while achieving a larger swath with the multi-beam system. Had the SIR-B system obtained a similar swath its antenna length would have been 29 meters long. The area of the multi-beam antenna is considerably larger than conventional systems. This arises because the physical aperture is considerably larger than the projected aperture. This feature may become bothersome at the small incident angle and longer wavelengths. However, the aperture size for the C band design is within the capability of a free flying system; consequently, its size is not objectionable.

TABLE 1
DESIGN GUIDELINES

Parameter	Application		Units
	Hydrology	Vegetation	
λ	6	2.5	cm
θ_o	15	45	deg
β_H	2	0.5	deg
S_w	86	160	km
ρ	50	25	m

TABLE 2
NOMINAL DESIGN RESULTS

z	600	300	km
H	6.8	4.1	m
L	6.8	3.4	m
W	0.39	0.06	m
β_L	3.2	1.1	deg
PRF	4.5	9.3	KHz
B_{rf}	11.6	8.5	MHz
T_a	65.4	46.5	ms
S/N	10	10	dB
$n_t n_r$	-2.0	-2.0	dB
σ^o(min)	-10	-20	dB
L_s	6	3	dB
C_r(max)	390	150	-
W_{ta}	22	128	watts
C_r(design)	200	100	-
W_{tp}	280	450	watts
N_B	11	32	beams
N_L	10	10	looks
M_w	1.5×10^6	2.3×10^6	words
B_t	2.7×10^6	19.8×10^6	bits/sec

TABLE 3
COMPARISON OF MULTI-BEAM AND CONVENTIONAL ORBITAL SARS

Parameter	Multi-Beam	SIR-B	Units
λ	2.5	3.6	cm
z	600	185	km
W_{ta}	128	800	w
W_{tp}	.450	20	kw
L	3.4	12	m
H	4.1	.24	m
ρ_r	25	25	m
σ^0	-20	-23	dB
S/N	10	14	dB
S_w	160	68	km
N_L	10	8	
C_r	100	400	

It is encouraging to note that the memory sizes and telemetry bit rates are more than within the capabilities of current technology. The telemetry bit rates demonstrate the advantages of on-board processing. The reduction, among other factors, results from overlaying the multiple looks aboard the spacecraft.

5.0 CONCLUSIONS

A unique and novel approach to radar imaging has been identified. The results of the verification analysis have demonstrated that the multi-beam SAR exhibits sytem properties compatible with free flying satellites. The constant incident angle (particularly at the smaller angles) and the large swath are attractive features to experimenters and users requiring quantitative data over large areas.

The multi-beam approach allows flexibility in designing orbiting systems. The radar ambiguity constraints are more easily satisfied through the use of multiple beams on reception. The redundant use of the receiving aperture reduces the transmitter power by a sizeable factor. This allows the

designer more choices in power amplifiers and assures him a more reliable transmitter section. It is also anticipated that real-time SAR processing within a multi-beam system will be easier to implement. The constant incident angle and narrow receive beams make clutter locking more effective and simplifies focusing of the processor associated with each beam. In particular, the depth of focus and range curvature are both easily managed within the confines of narrow beams.

The multiple beam approach is also compatible with a passive imaging system. A portion of the PRF interval not occupied by the transmission or the return can be used as a quiet listening time. The beam processor may be employed to form radiometer pixel elements. Concurrent passive and active imagery is a very attractive alternative, particularly when the radar images can be used to show the internal composition of the radiometer pixel element.

6.0 REFERENCES

[1] Moore, R.K., J.P. Claassen, R.L. Erickson, R.K.T. Fong, B.C. Hansen, M.J. Komen, S.B. McMillan, S.R. Parashar, "Radar Systems for the Water Resources Mission," Final Report, RSL-TR-295-3, University of Kansas Center for Research, Inc., Lawrence, Kansas, NASA Contr. NAS5-22384, June 1976.

[2] Bucknam, J., R. Dooley, A. Fredrickson, and F. Nathanson, "A Meteorological Satellite (METSAT) Radar for Space Shuttle," TSC-W3-27, Technology Service Corporation, Silver Spring, Md, NASA Contr. NAS5-20058, Jan. 1975.

[3] Sherman III, J.W., "Aperture-Antenna Analysis," Chapter 9 of Radar Handbook edited by M. Skolnik, McGraw-Hill, 1970.

[4] Rouse, J.W., Jr. (Editor), "Microwave Remote Sensing Workshop Report," Microwave Remote Sensing Workshop, Host International Hotel, Houston, Sponsored by NASA Johnson Space Center, Dec. 8-9, 1977.

[5] Ulaby, F.T. and P.P. Batlivala, "Optimum Radar Parameters for Mapping Soil Moisture," IEEE Trans. on Geoscience Electronics, Vol. GE-14, No.2, pp. 81-92, April 1976.

[6] Matthews, R.E. (Editor), "Active Microwave Workshop Report," NASA SP-376, Active Microwave Workshop, NASA Johnson Space Center, July 1974.

[7] Mehlis, J.G. "Shuttle Synthetic Aperture Radar Implementation Study," Report No. 750-73, Jet Propulsion Laboratory, California Institute of Technology, Pasadena, California, Oct. 1975.

RANDOM SAMPLING ADAPTIVELY FOCUSING
SYNTHETIC APERTURE RADAR

EARL N. POWERS
RAYMOND S. BERKOWITZ
VALLEY FORGE RESEARCH CENTER
MOORE SCHOOL OF ELECTRICAL ENGINEERING
UNIVERSITY OF PENNSYLVANIA
PHILADELPHIA, PENNSYLVANIA 19104

SUMMARY

Valley Forge Research Center is designing a high resolution narrow angle of
view imaging radar system. It will employ an airborne synthetic aperture of
600 meters operating at X-band to produce a beamwidth of approximately 0.05
mr. This system differs from a conventional SAR in that only a smaller num-
ber of wavefront samples, spaced randomly over the aperture are processed,
and adaptive beamforming with open loop scanning is used. As a result, the
processing requirements are reduced to within the capability of present day
small computer technology, and the tolerance on flight path stability is
loosened by about 100:1. The system will be described and initial analysis
and evaluation results will be presented.

INTRODUCTION

The system design to be described is a product of the ongoing research pro-
gram to study the application of the theory of large, random, adaptive arrays
to the implementation of high resolution airborne ground surveillance radars.
This design combines adaptive beamforming and synthetic aperture techniques
to provide a 100-fold improvement in the resolution capability of a helicop-
ter radar system. The assumed helicopter radar has a beamwidth of about 5
milliradians; the high resolution system will sharpen the beamwidth to 0.05
milliradians. This increased resolution will be provided over only a limited
field of view as this high resolution system is designed to be used in a man-
ner analogous to a telephoto lens. The conventional radar will be used to
identify a small region of interest, perhaps 5 mr in angular extent and a few
hundred meters in depth; at the assumed range of about 60 km this target area
would be about 300m on a side. The high resolution 0.05 mr array pattern
will be scanned over this region providing a resolution cell 3 meters wide.

The depth of the resolution cell will be determined by the range gate of the radar and is assumed to be about 15m. It is advantageous to limit the angular extent of the area of high resolution imaging (scanning) since this permits much greater uncertainty in the position of the radar platform without loss of resolution. Also, if pipeline processing is used, the amount of data to be stored will be greatly reduced, since for the parameters assumed above there would be only about 100 resolution cells in the azimuthal direction and about 20 range bins in depth.

High resolution imaging requires that the effective aperture of the receiving antenna is very large; 0.05 milliradian beamwidth demands an aperture size of about 20,000 wavelengths. This corresponds to a physical dimension of 600 meters (about 2,000 ft) if the system is operating at X-band (a wavelength of approximately 3 centimeters) [1]. The system uses a single helicopter which moves along a path to construct the large array sequentially. When the small area to be imaged has been selected, the helicopter will maneuver so that its position is coincident with a line determined by a prepositioned cooperative corner reflector and the target region. The corner reflector will serve as an aiming point for adaptive focusing of the array.

The use of a corner reflector for adaptive beamforming results in major differences between this adaptive synthetic aperture radar (ASAR) and a conventional SAR system. Adaptive beamforming will be accomplished by cophasing the corner reflector returns as measured at each of the sample points of the array to place the peak of the main lobe of the array's receive pattern in the direction of the corner reflector. Adaptive beamforming thus permits forming a beam without knowledge of the positions of the sample points of the array. The aiming point reflector must be readily identified in spite of the normal ground clutter; consequently, this "corner reflector" might be implemented as a high power transponder beacon or perhaps a coded retrodirective array offering a large time-bandwidth product. Once the helicopter has established its position along the line determined by the aiming point and the target region, it will move horizontally in a direction perpendicular to this line, sampling the signal returns from the target region as it is illuminated by the helicopter radar. The samples of the target wavefront will be collected at random intervals over the entire pathlength (600m at X-band).

Random sampling permits thinning the array to reduce the amount of data required to image the target region. The collected target wavefront data will then be processed to yield an image of the target region. This will be accomplished by first organizing the array through adaptive beamforming on the aiming point corner reflector. Once the array pattern has been established adaptively, phase shifts can be added to each of the wavefront samples to shift the focus of the array from the corner reflector out to the target range. Then sequences of phase shifts can be added to the wavefront samples to scan the array beam over the target region. The last two operations require an approximate knowledge of the locations of the array sample points. It is assumed that this position determination will be supplied by a separate independent system. It can be shown that the position data need not be precise; only the relative positions of the sample points are needed and accuracy on the order of 1 meter is adequate. An inertial navigation system can provide this precision with ease.

BASIC SIGNAL PROCESSING CONCEPTS

The adaptive synthetic aperture system uses the adaptive beamforming corner reflector to compensate for the motion induced effects of the helicopter. Figure 1 shows the geometry which exists if a linear random array is focused on a near field target. If the target is illuminated from the ith element,
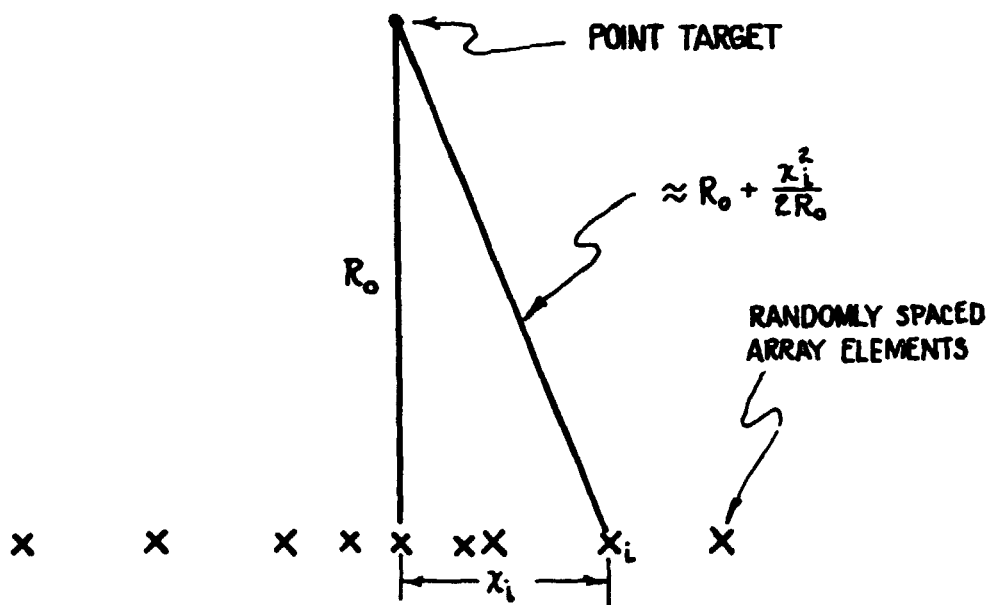

$\approx R_o + \dfrac{x_i^2}{2R_o}$

POINT TARGET

R_o

RANDOMLY SPACED ARRAY ELEMENTS

x_i

FIGURE 1. RANDOM ARRAY GEOMETRY

the phase of the target return at that element relative to reference element x_o is

$$2K_\lambda R_o + \frac{K_\lambda x_i^2}{R_o} \qquad (1)$$

The second term exhibits the quadratic phase variation required to focus the array on a near field target.

The storage and processing requirements for digital computation in the case of the ASAR are much less than those of the conventional SAR. A primary source for this reduction is the use of random sampling to thin the array. Random sampling is used to eliminate grating sidelobes and the sampled array will be thinned to a high degree. The number of samples taken along the 600m flight path will be approximately 1,000; this number of samples implies an average sidelobe level of approximately -30 dB [2]. Thus if the wavelength is assumed to be about 3 centimeters, then on the average, samples will be taken every 20 wavelengths, and the array is thinned below that of a filled array by a factor on the order of 40 to 1. At each sample point, three types of information will be stored, the phase of the transmitted pulse, the return from the corner reflector and the values from the 20 target range bins. If quadrature components are stored for 22 range bins for each of the 1,000 sample points, a maximum of 44,000 words of memory would be required. This amount of storage would permit off-line processing; however, the memory requirements can be reduced still further making real time processing practical for the ASAR.

The required multiplication rate for the ASAR would be similar to that of the conventional SAR if it were necessary to complete the processing during a single interpulse period; however since the ASAR array is highly thinned, additional time is available for processing. For example, if a helicopter traverses a 600m path at 50 m/s while collecting 1000 samples of the target wavefront, the average interval between samples would be about 12 milliseconds. A fraction of this time might be required for sweep integration or other processing, but on the average an interval of about 10 ms is available for processing. If the processing is accomplished while the data are being collected, the data memory could be reduced to 2000 words, one for each resolution element in the target image (100 azimuth cells x 20 range bins). The

processing and memory requirements for the sampled random array are quite compatible with modern small computer technology; the same can not be said for the SAR technique.

Thus there are important differences between the conventional SAR and the ASAR. The conventional synthetic aperture approach uses the quadratic phase history arising from the doppler shift to compress the target signal in azimuthal beamwidth. The ASAR array described herein will compensate the signal to remove the doppler offset so that the target and the array can be treated as stationary. Furthermore in the case of this randomly sampled array, the number of samples is kept small compared to a usual synthetic aperture array. The ASAR array will beamform adaptively on the signal return from a corner reflector. The use of this technique greatly increases the tolerance permitted on the uncertainty in the position of the sampling points. It will be shown later that the uncertainty in sample point position can be as much as 20λ. The helicopter motion need not be regular, and the system can tolerate relatively large position errors. The characteristic is in sharp contrast to an SAR approach where it is desired to hold phase errors to less than 1 radian and preferably less than 1/10 radian [3].

The number of corner reflectors required will depend upon how rapidly the high resolution image must be constructed. Figure 2 shows a typical airborne surveillance situation. The area of surveillance is assumed to extend over a sector 120° wide by 30 km in depth. N corner reflectors will be placed on the accessible side of the surveillance area boundary. The conventional low resolution helicopter radar will be used to identify a small target region to be scanned with the high resolution array pattern. The helicopter will then move from its initial point 0 to point A to place a convenient corner reflector, reflector i, in the vertical plane defined by the helicopter and the center of the target region. If it is assumed that the N corner reflectors are evenly spaced and that the helicopter has a reasonable top speed of perhaps 50 m/s, the number of reflectors required to limit the maximum time required to move the helicopter to an imaging point is readily computed since the greatest helicopter movement will be a distance equal to 1/2 the segment BC. The length of the arc segment BC at the maximum distance is

$$BC = \frac{60 \times 10^3 m}{N} \times \frac{2\pi}{3} = \frac{125 km}{N} \tag{2}$$
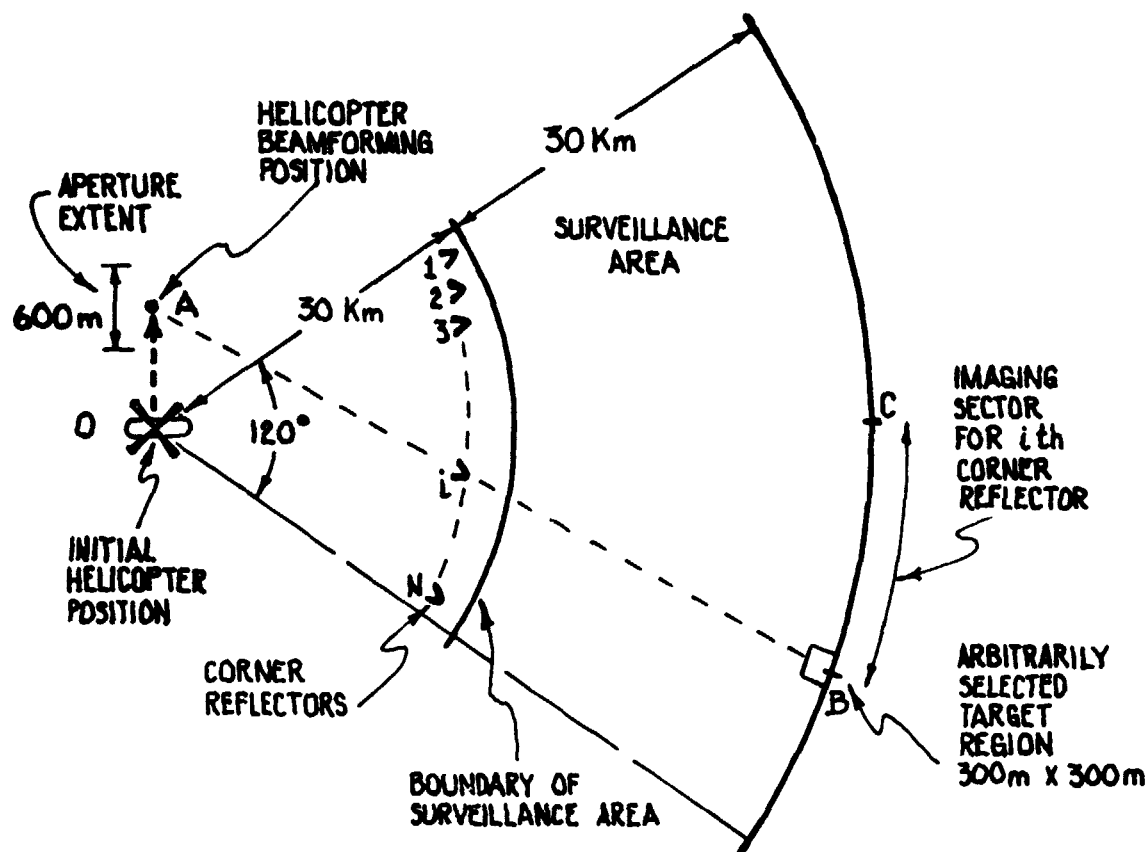
FIGURE 2. AIRBORNE RADAR ENVIRONMENT

The time required for the helicopter to move the maximum required distance on the other side of the surveillance area boundary at 50 m/s is

$$t_A = \frac{125}{2N} km \times \frac{1}{50 m/s} = \frac{1.25 \times 10^3}{N} \text{ seconds} \qquad (3)$$

Thus if four corner reflectors are used, about 5 minutes would be required for the initial positioning of the helicopter in the worst case. It should be noted that knowledge of the exact position of the reflector is not required for beamforming. Thus the use of adaptive beamforming via a corner reflector need not be a large disadvantage if the required rate of imaging is low.

The details of the system will be developed by considering the simplest case where helicopter motion is ignored and it is assumed that both the corner reflector and the target are in the far field of the array. The subsequent section will consider the corrections required to focus the array when the target region is in the near field of the array, and the effects of heli-

copter motion.

FAR FIELD SYSTEM

Figure 2 shows typical geometry. Initially it will be assumed that the heli-
copter is stationary at each of the sample points; consequently no doppler
correction will be required. It will also be assumed for the initial discus-
sion that the corner reflector and the target region are both located in the
far field of the array. (Both of these restrictions will be removed after
the basic system description has been deve .oped.)

It is assumed that the helicopter will move from point to point along its
flight path as indicated in Figure 3. At each of the sample points, for ex-
ample, point i, the helicopter will transmit a number of pulses that will il-
luminate the corner reflector and then at a later time the target region.

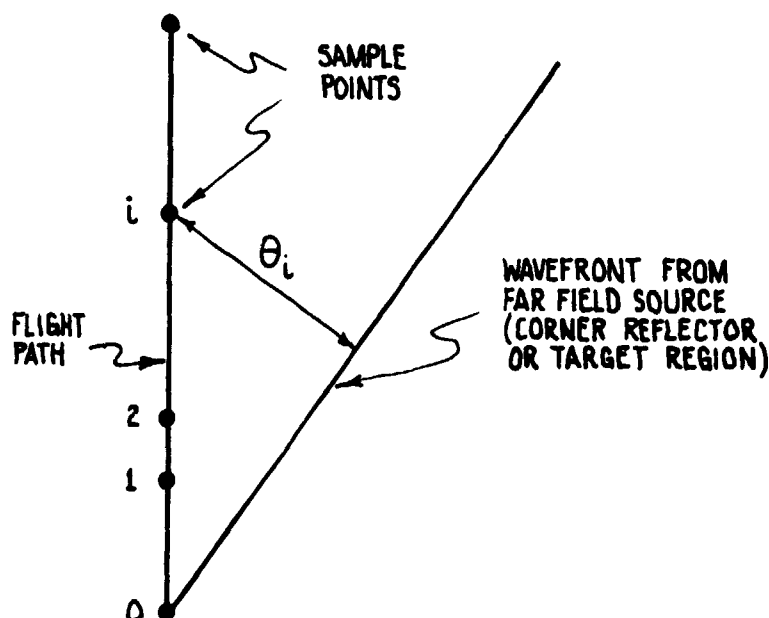FIGURE 3. PHASE RELATIONSHIPS, FAR FIELD

The first return of interest received by the radar set at point i will be a
return from the corner reflector. This return will be phase detected against
a local reference signal. The return from the corner reflector θ_{CRi} as mea-
sured against a local stable reference is

$$\theta_{CRi} = \theta_{oi} + \theta_{pc} = \theta_{oi} + 2\theta_i \tag{4}$$

where θ_{oi} is the phase of the transmitted pulse relative to the local reference, θ_{pc} is the phase accumulated by propagation from the transmitter to the corner reflector and return, and $2\theta_i = \theta_{pc}$ mod 2π. The phase detection process will not be sensitive to integral wavelengths, and θ_{pc} may be replaced by $2\theta_i$. The phase of the return from the corner reflector can be expressed as the sum of the phase delay from the element to a planar wavefront from the far field reflector, θ_i, and the transmitted phase θ_{oi} (see Figure 3).

At a slightly later time the signal return from the target region will be compared against the same local phase reference. The phase of this return is given by (5)

Measured phase from target region = ϕ_{Ti} =

$$\theta_{oi} + \theta_{pT} + \theta_\epsilon = \theta_{oi} + 2\theta_i + \theta_\epsilon + n2\pi \qquad (5)$$

θ_{pT} = propagation phase for the target signal

This equation is similar to (4) except that (5) also contains a quantity θ_ϵ which represents phase drift which might occur in the phase reference against which incoming signals are measured during the time between the reception of the return from the corner reflector and the detection of the return from the target region. For the geometry shown in Figure 2, the difference in propagation time between the corner reflector and the target will result in a maximum delay of approximately 200 microseconds. If we demand that the oscillator stability in the receiver system be such that maximum phase error is on the order of 10°, then as indicated by (6) the stability required of the receiver LO (the most critical of the phase determining components) will be on the order of 1 part in 10^8.

$$\frac{\Delta f}{f} = \frac{((1/36) \text{ cycle}/(200\mu\text{sec})}{10^{10} \text{ Hz}} = 1.38 \times 10^{-8} \qquad (6)$$

Assuming X-band operation $(f = 10^{10} \text{ Hz})$

This is a severe requirement but not beyond the capability of present-day hardware. The stability required of the lower frequency portions of the system, for example IF detection reference sources, will be substantially less due to the lower operating frequency.

It is apparent from (4) and (5) that if the error signal θ_ϵ is small, then

the information exists in the phase measurement of the returns from the corner reflector to permit cophasing the target returns at least in the far field case. It should be noted that the transmitter phase θ_{oi} is independent from pulse to pulse, consequently it would not be possible to combine successive phase returns from the target region for the purpose of sweep integration unless a correction is made for this fluctuation. This correction can be accomplished by storing θ_{oi} and comparing it against the corner reflector return. Upon reception of the return from the corner reflector, the transmitted phase will be subtracted to obtain the quantity $2\theta_i$. The same correction would be performed on the target return phase measurement, thus the transmitted phase variation is removed and successive returns from the target region can be added for sweep integration and the reduction of noise components.

In summary, three phase quantities will be measured at each sample point. The first is the transmitter phase. This information will provide a reference phase correction to permit combining successive returns from the target region. The second quantity to be measured will be the return from the beamforming in the direction of the corner reflector; and since the position of the helicopter has been deliberately chosen to place the corner reflector in the direction of the target region, a beam can be formed in the direction of the desired angle of view. The third set of data to be recorded will be returns from the target region. The number of pieces of information to be recorded will depend upon the desired number of range bins. It has been assumed as typical that the range gate duration will be approximately 100 nanoseconds corresponding to a two-way propagation distance of 50 ft. Then approximately 20 range bins will be required to cover the target region depth of about 300 meters.

When these three sets of information have been collected from all of the sample points, it will be possible to beamform and scan over the target region assuming only that the approximate locations of the sampling points are known. The precision required on the determination of the position of the sampling points is low. Since the maximum scan angle required of the array will be of the order of 5 milliradians, the uncertainty in the sample point positions can be high; the 5 milliradian scan angle implies that scanning can be accomplished even with an uncertainty in element position, on the order of 20

wavelengths [4]. A 20 wavelength uncertainty at X-band corresponds to about
0.6 meters. Position determination to this accuracy can be obtained from a
variety of distance or position determining equipments. The most desirable
would probably be an inertial navigation system since this would permit self-
contained operation within the helicopter system. It should be noted that
the position determination is particularly nonrestrictive since absolute val-
ues are not required. Only the relative position of the helicopter at each
of the sampling points will be stored along with the phase data. The amount
of memory required might be reduced if the sequential array is constructed as
the data are collected. That is, there are only 2000 resolution cells in the
target region (100 azimuth cells x 20 range bins), if the processing can be
performed in a pipeline fashion it would not be necessary to store more than
one word per resolution cell. This type of operation would involve the fol-
lowing operations at each sample point. The first step would require sub-
traction of the phase of the transmitted pulse from the target returns
followed by beamforming as the data are collected by using the corrected cor-
ner reflector phase. This phase could be subtracted from the corresponding
target values, i.e., a new array of numbers identified only by the element
number and range gate position would be constructed. Open loop scanning
would result in a final array of numbers identified by azimuth and range.

NEAR-FIELD CORRECTIONS

Several additional considerations arise from study of the near-field model.
These include the necessity for increasing the beamwidth of the transmitter
antenna and for refocusing the array. As shown in Figure 2 the target region
is assumed to be about 300 meters on a side. The flight path required for
the generation of the array is approximately 600 meters. Consequently the
center of a 5 mr transmit antenna beam from the helicopter will sweep over a
transverse distance of 600 meters at the maximum target range, and the target
region will not be uniformly illuminated for all positions along the flight
path. It will be necessary to increase the beamwidth by a factor on the or-
der of 4 to 1; a beamwidth of 20 milliradians would have cross-section at a
distance of 60 km of 1200 meters. This beamwidth will be adequate to illumi-
nate the target region continuously and uniformly as the helicopter moves.

A focused array will be required. The far-field boundary as given by (7) is

located approximately 12,000 kilometers away from the array [5].

$$\text{Far Field Boundary} \simeq \frac{L^2}{\lambda} = 12 \times 10^6 \text{ m}$$

$$L = \text{array extent} = 600\text{m}, \ \lambda = 3 \text{ cm for X-band} \tag{7}$$

Consequently the target region will be in the extreme near field. Also, the depth of field will not be great enough to achieve simultaneous focus on the target region and the corner reflector. The depth of field as given by (8) is approximately 525 me· rs at a distance of 30 km from the 600 meter array operating at a 3 centimeter wavelength [6].

$$\text{Depth of field} = 7\lambda \ (\frac{P_o}{L})^2 = 525\text{m} \tag{8}$$

$$P_o = 30 \text{ km, helicopter to beacon}$$
$$L = 600\text{m, array extent}$$
$$\lambda = 3 \text{ cm wavelength}$$

It will be necessary to refocus the array after beamforming by adding phase corrections to the data received at the sequential sampling points.

HELICOPTER MOTION

The next topic to be considered in this description of the high resolution imaging radar system is the effect of helicopter motion. Fortunately, the corner reflector provides a means of compensating for the , :se change arising from radial motion of the helicopter, that is if the transmitted phase is compared with the phase return from the corner reflector, an indication of the pathlength between the helicopter and the corner reflector is obtained. Comparing this length on a pulse-to-pulse basis will permit generating a history of the motion of the helicopter in the radial direction with respect to the corner reflector. This measurement of pathlength change can be used to correct the measured phase of the returns from the target region. The phase shifts due to the helicopter's radial motion can be predicted if the rate of movement is not so large that the helicopter can move an ambiguous number of wavelengths during an interpulse period. If we assume a pulse rate of 1 KHz, then the motion of the helicopter must be such that it moves less than 1/2 of the assumed wavelength of 3 centimeters in the interpulse period of 1 milli-second. This corresponds to a maximum radial velocity on the order of 15 me-

ters per second.

CONCLUSION

An adaptive SAR system has been described which may be used with a helicopter radar to provide high resolution imaging over a limited target region (e.g., appr ximately 300m on a side at 60 km). Array organization will be accomplished by adaptive beamforming on a corner reflector in the direction of the target region. Since the corner reflector is nearby relative to the target, refocusing after beamforming will be required. The array will be formed sequentially by moving the helicopter and sampling at random intervals. Random sampling is used to permit data reduction through array thinning while preventing grating sidelobes. Approximately 10^3 sample points will be recorded along a 600 meter flight path. These data will be used to construct an image by adaptive beamforming and then open loop scanning. Since the maximum scan angle will be about 5 mr, the element position uncertainty can be high, e.g., 20λ. This thin, random adaptive array offers several advantages over a conventional SAR approach. First, the amount of storage required for realistic processing rates is much lower, (at least 10:1) and the processing rates are within the capability of modern small computer technology. Secondly, the operation of a conventional SAR is much more sensitive to motion uncertainties of the platform, i.e., 100:1. These advantages arise because the ASAR array is highly thinned relative to a filled array (40:1), and the use of adaptive beamforming on a corner reflector permits greatly increased uncertainty in sampling point positions.

REFERENCES

[1] Bernard D. Steinberg, Principles of Aperture and Array System Design, John Wiley & Sons, New York, 1970, p. 42.

[2] Ibid., p. 142

[3] Robert O. Harger, Synthetic Aperture Radar Systems, Academic Press, New York, 1970, p. 20.

[4] Steinberg, Principles of Aperture and Array System Design, p. 249.

[5] Ib .., p. 12

[6] Ibid., p. 53

THE SEASAT-A SYNTHETIC APERTURE RADAR DESIGN AND IMPLEMENTATION

ROLANDO JORDAN
JET PROPULSION LABORATORY
PASADENA, CALIFORNIA 91103

SUMMARY

The Seasat-A Synthetic Aperture Imaging Radar System is the first imaging radar system intended to be used as a scientific instrument designed for orbital use. The requirement of the radar system is to generate continuous radar imagery with a 100 kilometer swath with 25 meter resolution from an orbital altitude of 800 kilometers. These requirements impose unique system design problems and a description of the implementation will be given. The end-to-end data system will be described, including interactions of the spacecraft, antenna, sensor, telemetry link, recording subsystem, and data processor. Some of the factors leading to the selection of critical system parameters will be listed. The expected error sources leading to degradation of image quality will be described as well as estimates given of the expected performance from data obtained during ground testing of the completed subsystems.

1.0 SYSTEM DESCRIPTION

The design of the Seasat-A Synthetic Aperture Radar System was driven by the limitations imposed by the satellite system. In particular, the following constraints played a significant role in the system configuration determination.

1. No on-board data storage could be accommodated of the unprocessed radar signal.

2. The standard satellite system telemetry could not accommodate the large data volume generated by the SAR system.

3. Telemetry link bandwidth allocation was limited to 20 MHz.

4. The average raw power from the spacecraft for the SAR was limited to 500 watts.

With these factors in mind the system configuration evolved as that shown in Figure 1. A tabulation of the principal system parameters is given in Table 1.

The radar antenna consists of a deployable 10.7 meter long by 2.16 meter wide planar array. The antenna in its stowed configuration consists of eight panels each 1.3 meters by 2.16 meters, these panels are folded into an accordion configuration. Upon reaching orbit the antenna structure is folded up from the spacecraft and the elements allowed to deploy into a long planar configuration. Subsequent to deployment the antenna cannot be retracted.

The deployed antenna is configured to fly with the long dimension along the spacecraft velocity vector. The antenna boresight is at an angle of 20° from the nadir direction in elevation.

The antenna dimensions are dictated by the desire to limit range and azimuth ambiguities to acceptably low levels. At a nominal 20° look angle from nadir in order to illuminate 100 kilometers swath on the Earth's surface from an 800 kilometer high orbit, a total beamwidth elevation of 6.2° is required. Thus the antenna cross track dimension is 2.16 meters in order to limit the radiation to these sets of angles.

The antenna elements in elevation are weighted in illumination to limit side lobes in the cross track direction. The resulting area illuminated on the surface of the Earth is from 240 to 340 kilometers to the right of the sub-satellites point. The arrival of radar echos from near and far range prevents the radar transmitter pulses from being too close together in order to prevent overlapping the returns, from near and far range, of subsequent pulses. Thus, the pulse repetition rate is limited to a maximum level by the antenna cross track dimensions.

The antenna along track dimensions is limited on the low end by a desire to keep azimuth sample ambiguities at an acceptably low level. In order to avoid sampling ambiguities of the radar data the antenna azimuth beamwidth must be kept small enough so that the set of azimuth frequencies do not exceed the sampling rate. However, if the azimuth beamwidth is kept too small it is not possible to generate the synthetic aperture large enough to attain the desired resolution for the four independent

TABLE 1

SEASAT-A SAR SYSTEM CHARACTERISTICS

Satellite altitude	800 km
Wavelength	0.235m
RF bandwidth	19 MHz
Transmit pulse length	33.4 µsec
Pulse repetition rate	1463 to 1640 pps
Time-bandwidth product	634
Radar transmitter peak power	1000W
Telemetry transmitter power	10W
Telemetry frequency	2265 MHz
Radar transmitter average power	55W
Sensitivity time control range	9 dB
Data recorder bit rate	110 megabits/sec
Data recording pass duration	10 min
Radar DC power	500W
Radar antenna dimensions	11 by 2.3m
Radar antenna gain	35 dB
Telemetry antenna	Quadrufilar Helix
Telemetry antenna gain	4 dB

looks. These two requirements limit the antenna length along velocity vector to be between 10.5 and 14 meters in length. The antenna length of 10.74 meters was dictated by the available volume within the spacecraft shroud.
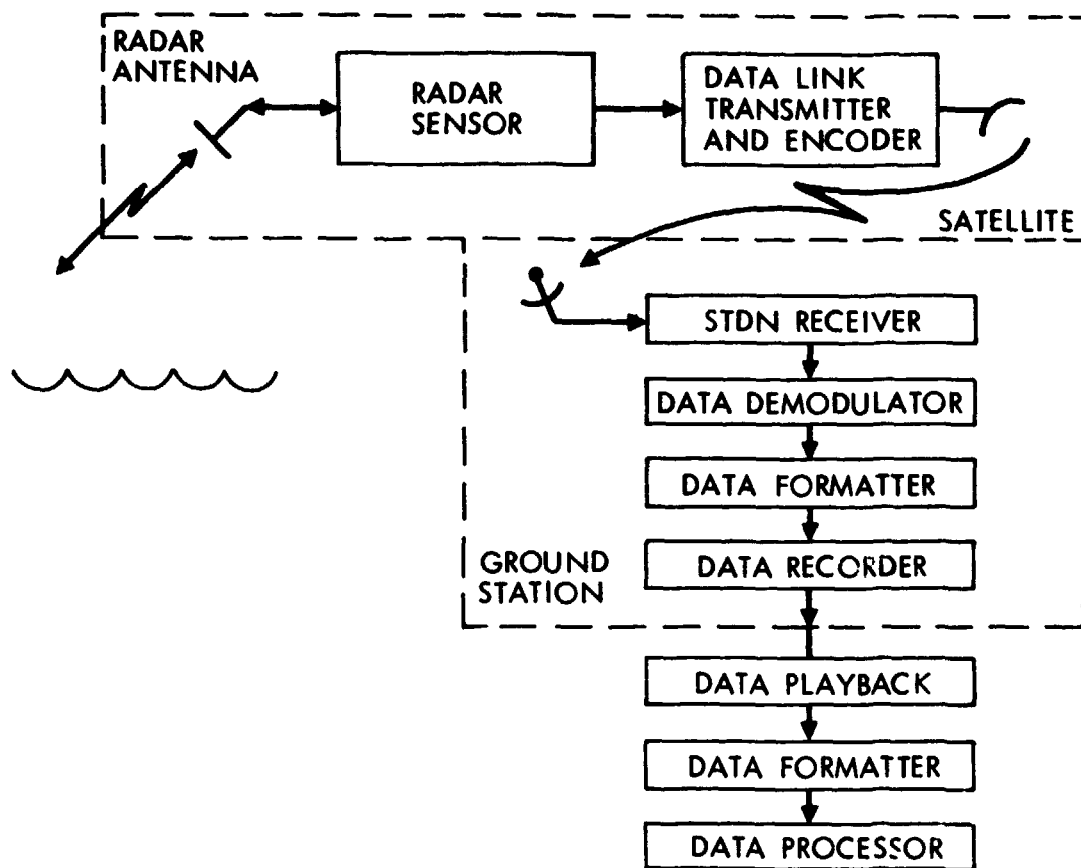
Figure 1. SEASAT-A SAR System Configuration Diagram.

The sensor electronics derives its signal from a surface acoustic wave line which generates a linear FM chirp signal with a bandwidth of 19 MHz and a duration of 33.4 microseconds. The signal is up converted to the L-band carrier frequency amplified to a power level of 1000 watts peak and transmitted to the ground. Upon reception the echo is amplified and up converted to an S-band carrier frequency for telemetering the data to the ground.

Prior to the data transmission a sample of the stable local oscillator is encoded into the S-band spectrum along with a dispersed version of the pulse repetition frequency event. The resultant spectrum of the data link is as shown in Figure 2.

Figure 2. Composite SAR Data Link S Band Transmitted Spectrum
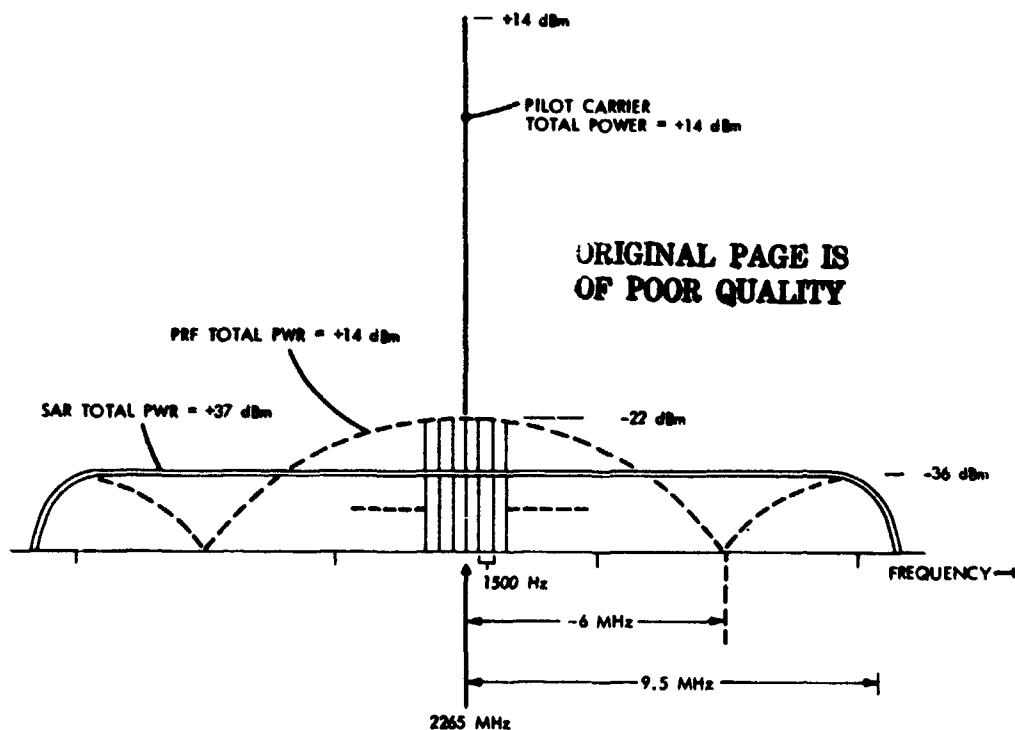
The signal at this point has an analog form with a carrier at the S-band telemetry carrier spectrum. The telemetry signal is transmitted to the ground via a 5 watt solid state transmitter and a omni directional antenna. On the ground the data is received using a 9 meter dish of the STDN network. Upon reception of the composite spectrum by the STDN multifunctional receiver

and parametric amplifier the stable local oscilator pilot tone enables phase-lock tracking of the signal spectrum and a 45.5 MHz signal is derived from this pilot carrier. This signal is then utilized to generate a separate 11 MHz signal for performing the synchronous demodulation operation on the entire carrier. The signal is also passed to the cross correlation device which provides the retreval of the PRF pulse to a high level of time accuracy required for reconstituting the signal on the spacecraft. Last, at the output of the data link the signals are as follows:

1. A range offset video with a frequency spectrum of approximately 2 to 21 MHz.

2. A PRF pulse which is coincident with the PRF pulse on the spacecraft except for the one way delay of the spacecraft to ground station.

3. A clock signal which is derived from the spacecraft stable local oscillator.

These signals are then passed on to a recording subsystem at the STDN network. The recording subsystem consists of a analog to digital converter which is controlled by the clock derived from the spacecraft stable local oscillator to an accuracy of 5 bits per word. The data is next stored in a high speed buffer for subsequent recording in a high density digital tape recorder.

A total of 302 microseconds of data is recorded which corresponds to a 104 kilometer swath width operation at the maximum pulse repetition rate of 1645 pulses per second. The resulting data rate into the high density digital tape recorder is approximately 107 Megabits per second. The data recorder has the capability to record a maximum of 15 minutes of data which corresponds to one station pass. The high density digital tape is then used at the ground data processor to convert the radar video signals in digital form to a radar image.

The function of the data processor is to convert the radar video signals stored in the high-density digital tape format into the radar image in a format equivalent to a map coordinate system. The task of converting the radar signal into a radar image from the orbiting spacecraft to the Earth is a significant one. One must take into account the effect of the Earth rotating beneath a satellite which is stationary with respect to inertial space. As the spacecraft orbits the Earth, the antenna will, in practice,

not point in a direction exactly normal to the velocity vector of the spacecraft in inertial space or normal to the velocity of the spacecraft relative to the points being imaged. Consequently, during the generation of a synthetic aperture which has a 15 km nominal length, any one point in the area that is being imaged will undergo an effect termed range migration.

This effect causes a point on the surface to either approach or recede from the spacecraft by as many as 70 resolution elements. The exact amount of range migration that any one point will undergo is a function of the range of that point to the spacecraft, as well as the direction that the antenna is pointing in respect to the true zero doppler direction from the spacecraft.

In practice the knowledge of the location of the antenna bore sight is not good enough to compute the range migration characteristics of e   e of the 8000 resolution elements in the cross track directions that are   , imaged. Thus, spectrum analysis of the radar signal must first be accomp...shed in order to determine the range migration characteristics. Once the range migration characteristics are known and compensated for, then both the range and azimuth compression operations can take place.

The processing of the Synthetic Aperture Radar Data for <u>Seasat A</u> will be done in an optical correlator. The information from the high-density digital tape format is first converted into a two-dimensional photographic signal film as shown in Figure 3. This signal film is then illuminated with a coherent beam of light. A two-dimensional transform of the signal film is then accomplished by observing the light intensity after the transmitted light beam goes through a spherical lens. The light then passes through a set of lenses which deflect the light beams in proportion to the azimuth spatial frequency and thus perform a range migration correction. The inverse transform is then accomplished by passing the light through another spherical lens.
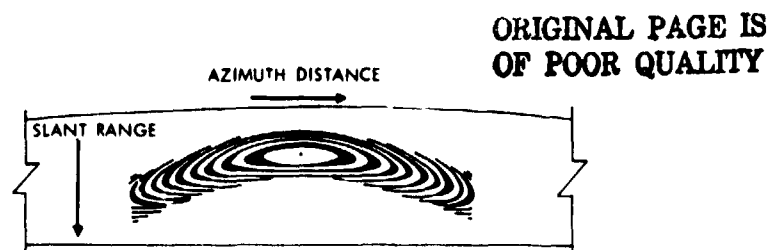
Fig. 3. Signal Film Showing Point Target Phase History

A set of cylindrical lenses then allow the light conversion from targets of all ranges to come into focus at the output plane.

An examination of the characteristics of the radar parameters yields that the resolution equal to approximately 4 times better than the 25 meter resolution required is possible along-track or that the synthetic aperture length required to obtain the 25 meter resolution is 1/4 of that length that the real aperture antenna illuminates the ground. It is therefore, possible to generate a total of 4 separate radar images of the surface and consequently the concept of multiple looks becomes possible when trying to image the surface of the Earth at the 25 meter resolution with the antenna selected. A radar image, because it is generated by observing the surface with a monochromatic source of light has a speckly nature to it. This speckle gives an inability for the data user to accurately estimate the strength of the return. In order to give a better estimate of the return from each individual resolvable element, the image is observed a number of times and the results of each of these measurements is averaged. Thus, the standard deviation of the measurement is reduced. The result to the radar image is that as the number of independent looks is increased, the texture of the radar image becomes a smooth one or a more pleasing one to the eye.

The SEASAT SAR is capable of processing data up to a maximum of 4 independent looks, consequently the radar data processor must be capable of processing the data 4 times, generating 4 separate images and registering the images to a sufficient accuracy so that the resultant image has a low standard deviation for a uniform target field and not have a loss of resolution due to misregistration.

2.0 SPACECRAFT PECULIAR SOURCES OF ERROR

Operations of the synthetic aperture radar in orbit gives rise to some errors or peculiarities that are not found in conventional aircraft borne synthetic aperture radars. A spacecraft, because it operates in inertial space and the Earth rotates beneath the sensor, results in a geometry that is peculiar to imaging radars. First the effects of imaging from an orbiting platform will be described and then the effects of imaging from an orbiting platform discussed.

If the Earth were not rotating and the antenna was pointed exactly normal to the spacecraft velocity vector the return spectrum would be the spectrum of the transmitted waveform convolved with the effects of the pulse repetition frequency and effects of the antenna along track beamwidth. The centroid of the doppler spectrum would be along zero doppler. If either an antenna pointing error is introduced or the Earth rotates, the spectrum would no longer be centered above zero doppler but would shift to some other frequency determined by the doppler effect. Since range migration correction is dependent upon the knowledge of the doppler spectrum, the direction in which the antenna is pointed must be known to within an angle:

$$\Delta\theta \leq 1/2 \ \sin^{-1} \ \{\frac{\lambda (PRF)}{2V}\}$$

where $\Delta\theta$ is the antenna pointing angle uncertainty, λ is the radar wavelength and V is the velocity of the spacecraft.

To define the ambiguity a priori, the implication for SEASAT is that at some point the antenna angle must be known to within 0.65^o in order to be able to correctly process the data. If not, the images will be blurred as the data will be processed about an ambiguity. Since the spacecraft operates with reference to inertial space, and the earth rotates beneath the sensor orbit, the effect of th earth's rotation crosses a predictable shift in the azimuth doppler spectrum, and consequently, the range of the target migrates in the signal domain. In the absense of any antenna pointing errors if the target latitude is known, it is easy to correct for the azimuth shift caused by the earth's rotation because the earth's rotation is very well known.

Imperfect spacecraft attitude control also effects the data because of changes in the ground area, which is illuminated by the antenna. The effects of the doppler spectrum by yaw pitch and roll error is shown in Figure 4. Since there there is a one to one relationship between the doppler frequency and range migration once the doppler spectrum is known, the range migration correction can be completed exactly. The quadrangled bracket by (b) represents the doppler frequency versus ground range spectrum in the absence of any errors for an equatorial crossing. In this case, the doppler spectrum is not centered around the zero doppler because of the earth's rotation. The doppler frequency bandwidth occurs between -650 Hz and -800 Hz for the near range targets. In far

range, the frequency will go from -1100 Hz to -2000 Hz. In presence of a yaw error of +0.5° the spectrum will shift up to (a). If the yaw and pitch errors are negative, the doppler frequencies will increase in the negative direction as shown by (c). The main effect is that the spectrum is shifting when the antenna is yawing, pitching, or rol ing. There is a skew because the antenna ground pattern is pointed normal to the spacecraft velocity while the iso doppler lines are oriented perpendicular to the relative velocity composed of the spacecraft velocity and the earth's rotation. The predicted doppler centroid versus latitude is shown in Figure 5. The lines bracketed indicate
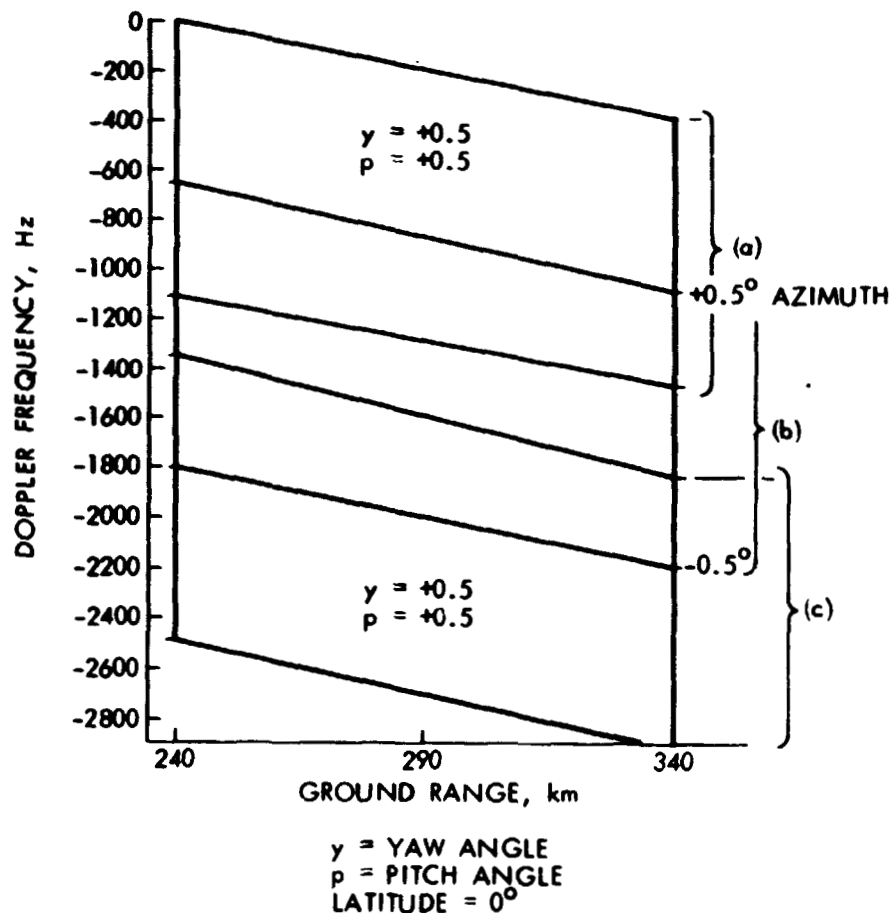

Figure 4. Effect of Pitch and Yaw Errors on Doppler Spectrum.

the center of the spectrum in the absence of any spacecraft added to the
errors. As the latitude increases when the spacecraft travels north from
the equator, the effect of the earth's rotation gets smaller and smaller until
the spacecraft reaches 72° north latitude. At that point, the spacecraft is
at the top of the orbit and the earth's rotation is exactly parallel to the
flight path. Consequently, there is no doppler centroid shift at this point
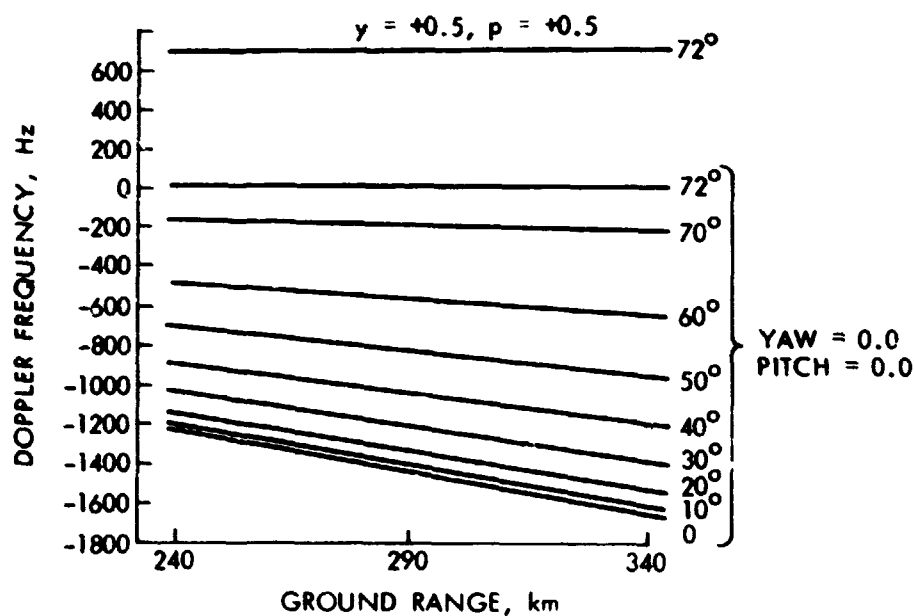again in absence of any pointing errors.

Figure 5. Predicted Doppler Centroid Versus Latitude.

3.0 EXPECTED RADAR PERFORMANCE

The synthetic aperture radar system gives a pictorial representation of the radar backscatter of the Earth surface in a maplike representation. The radar backscatter is defined as the ratio of reflected power per unit area to that which is incident on the terrain that is being illuminated. The ability of the radar system to give an adequate representation of the radar backscatter will be limited on the lower end by the sensitivity of the radar system and on the upper end by the dynamic range of the components comprising the radar system. Furthermore, the sensitivity of the radar system will depend on the location of the area beam map with respect to the assigned swath width of the radar system. The predominant element which determines the radar sensitivity as a function of the swath is the radar antenna. The radar antenna has a gain which will have a peak value at boresight, and as the angle changes from boresight, the antenna gain will drop with angle, and consequently the ability of the radar system to image the Earth's surface will vary with angular position.

The Seasat-A SAR system design is based on measuring the sea backscatter which has a model as shown in Figure 6 . This model is based on measurements taken with the JPL L-Band imaging radar as well as numerous other irvestigations. This model is based on average sea conditions and as the sea state becomes rougher, higher values of radar backscatter are to be expected and as the sea becomes smoother, lower values in radar backscatter will be observed.

The overall radar system designed allows nominal operation with a surface whose backscatter model follows this curve along the nominal gain of the overall radar system. This radar sensitivity curve is applicable for targets which are extended in nature. If on the surface there are target areas whose average backscatter differs substantially from the expected model, they will be imaged properly if the extent of this specular target is significantly smaller than 15 by 15 km in dimension. The reason for this increase is dynamic range of the system is that the radar signal which is transmitted is dispersed in time and also in azimuth because of the changing doppler frequency of each of the targets. The extent of the dynamic range and improvement which can be expected is a function of this dispersion and for the SEASAT-A SAR can reach values as high as 50 dB.
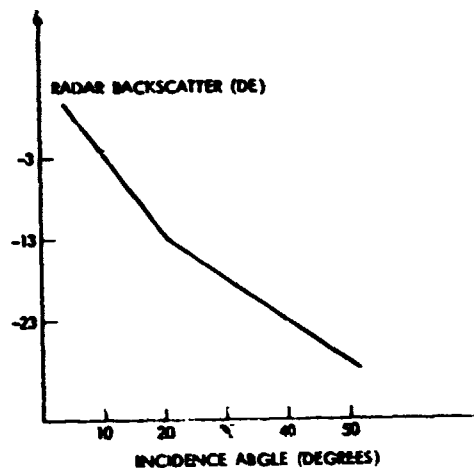
Figure 6. L-band Average Sea Backscatter Model.

In order to compensate for the expected varying signal strength due to effects of the antenna pattern, the radar system incorporates a sensitivity time control as an attempt to maintain a constant sensitivity to a radar backscatter. This is possible because the returns from different angles arrive at different intervals of time. The price paid for this time dependent radar sensitivity is that the radar noise becomes time varying, and consequently the dynamic range that the overall radar system will have will again change with angular precision or swath that is being imaged. If the radar returns are too strong, because the radar backscatter is high, then the radar system will exhibit saturation, and consequently the dynamic range or the ability of the radar system to image over varying values of radar backscatter will be limited.

In the SEASAT-A synthetic aperture radar system, the predominant element which exhibits saturation is the analog data link. On the lower end the radar sensitivity for regions that correspond to the beginning and end of the radar swath, the radar system or radar receiver noise is predominant. At the center of the swath where the sensitivity time control puts a minimum gain, then the data link equivalent noise predominates. In order to accommodate radar signals that are beyond the instantaneous dynamic range of the radar system, the radar receiver incorporates a variable gain control system to accommodate varying values of radar backscatter. Since the radar system noise as seen by the data link is dependent on the gain state of the radar receiver, the overall system

sensitivity to measure radar backscatter becomes dependent on the receiver gain state.

For the nominal gain, the performance of the SEASAT-A SAR system is as shown in Figure 7. The upper curve represents the values of radar backscatter which would drive the overall radar system to saturation. As seen from this figure, this curve varies with position that is being imaged. As seen from the curve, for the beginning and end of the radar swath, the values of radar backs... .ter which will drive the system to saturation represent targets where radar backscatter is very high. The lower curve represents the threshold for the minimum values of radar backscatter, which would appear to have a level that is representative of the overall system noise. Again, the same curve has a higher value at the beginning and end of the area being imaged.

With the radar receiver a low gain state, as shown in Figure 8 it can be seen that the overall dynamic range of the system is quite high. However, the values of radar backscatter that result in a normal radar image correspond to surfaces having a high radar backscatter or reflectivity. This area will correspond primarily to strong reflectors, such as areas which are mountainous or forested. If the radar system gain is increased, the radar sensitivity curve is as shown in Figure 9. In this case, it will be noted that the system dynamic range is quite limited since the radar gain is such that the radar noise is approaching the level required to saturate the data link. However, in the case, areas of radar backscatter which are quite weak will be detectable, and these areas are representative of rather quiet ocean wave conditions.

In summary, the performance of the SEASAT-A SAR system should allow adequate imaging of ocean surfaces from orbital altitudes and in time may prove to be a significant remote sensing instrument capable of measuring ocean swell wavelength and direction from orbit around the Earth.
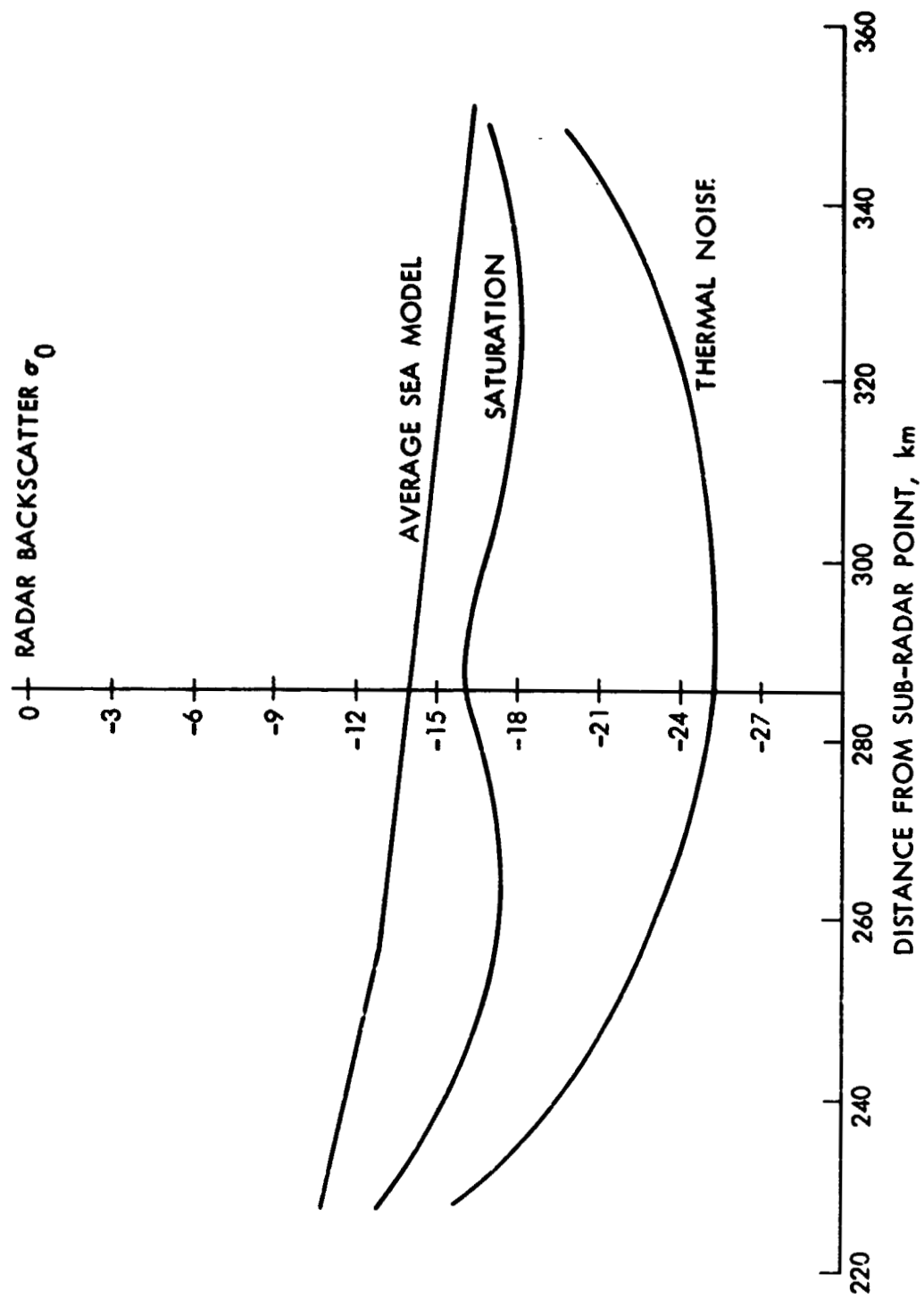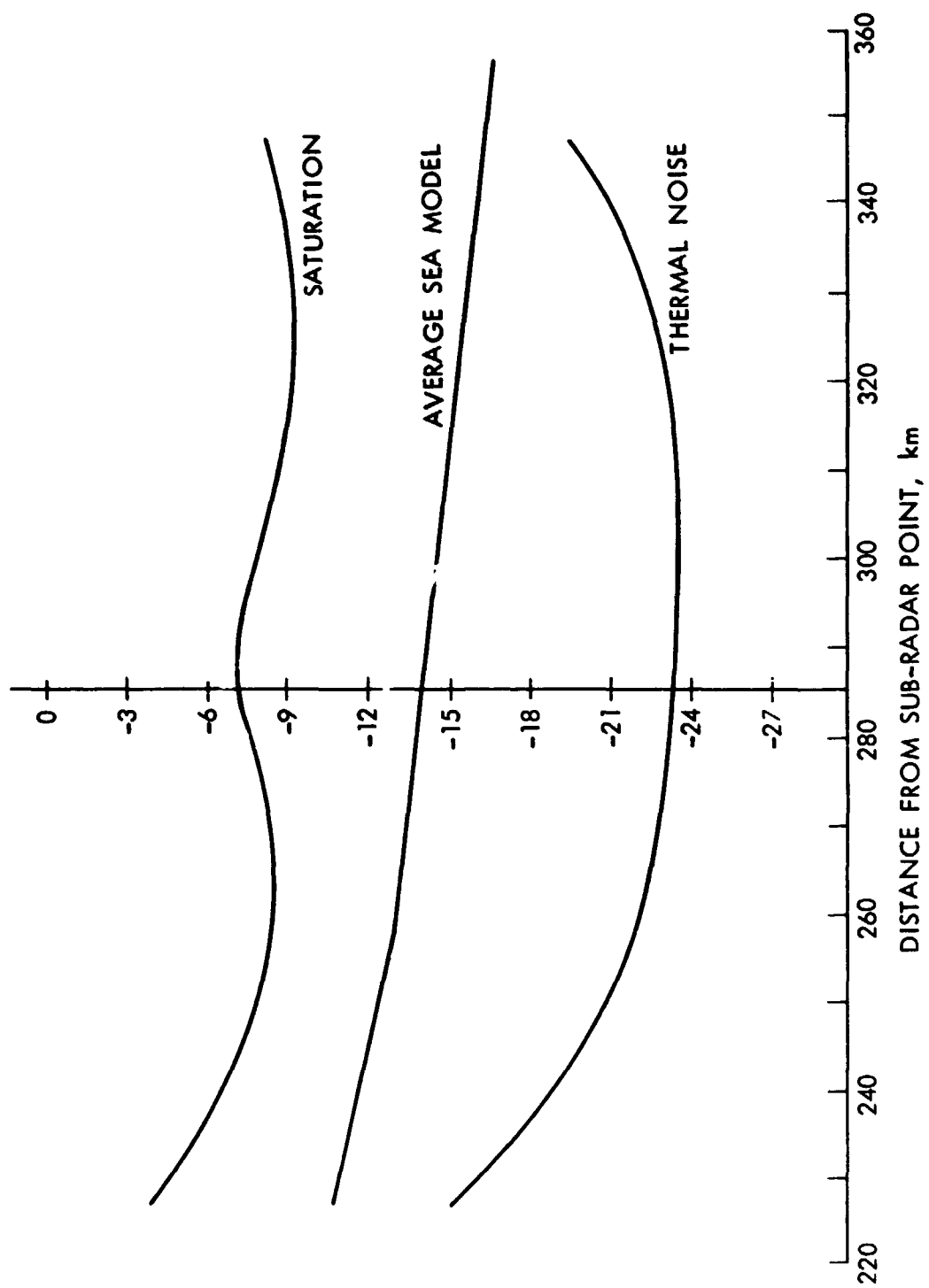
Figure 9. SEASAT-A SAR System G = 95 db
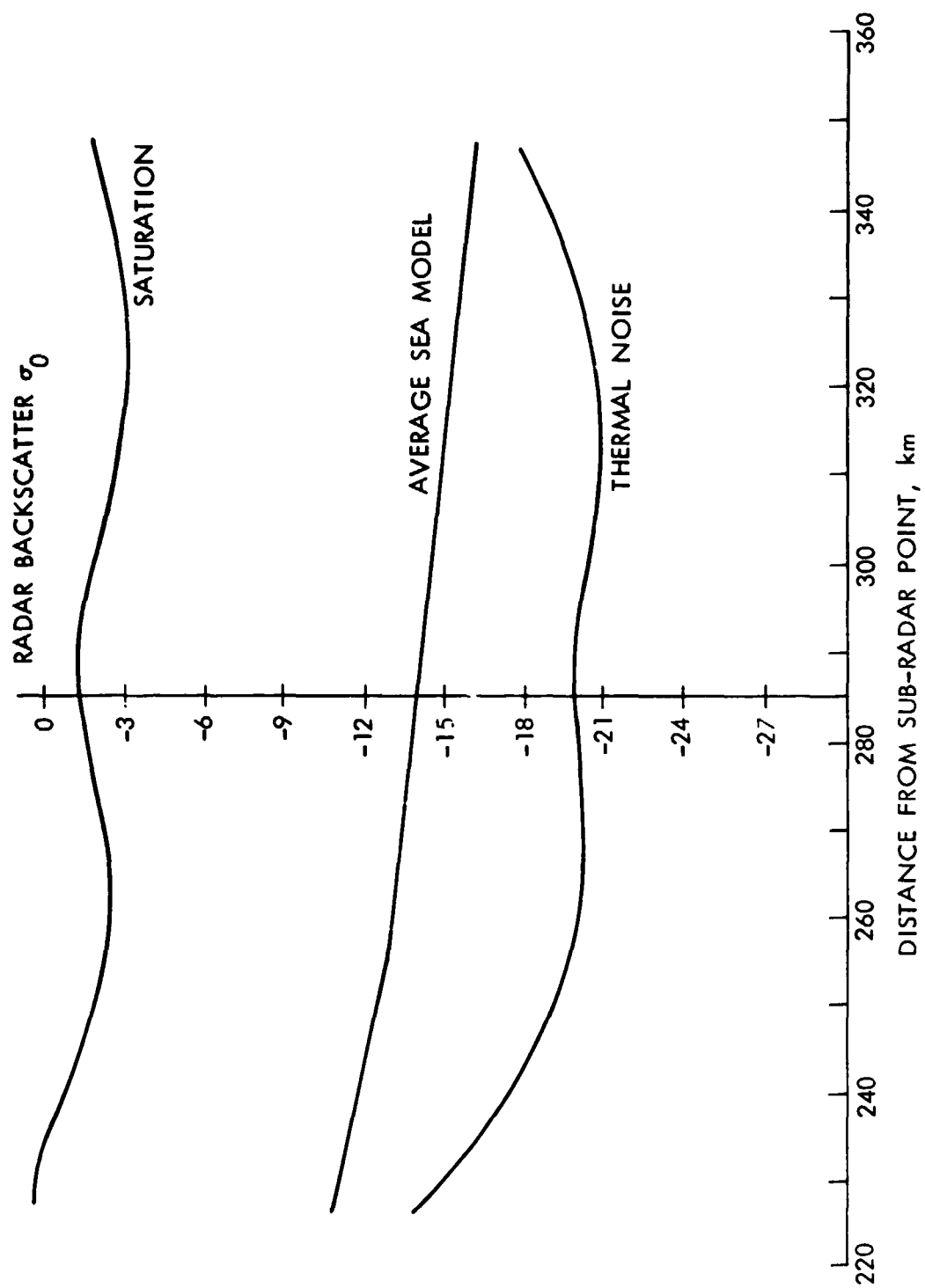
Figure 7. SEASAT-A SAR System G = 86 db

DISTANCE FROM SUB-RADAR POINT, km

SATURATION

AVERAGE SEA MODEL

THERMAL NOISE

Figure 8. SEASAT-A SAR System G = 80 db